Measurement of the $\eta \to e^+e^-e^+e^-$ double Dalitz decay and the search for new physics beyond the Standard Model in $\eta \to e^+e^-$ with WASA-at-COSY

I n a u g u r a l - D i s s e r t a t i o n
zur
Erlangung des Doktorgrades
der Mathematisch-Naturwissenschaftlichen Fakultät
der Universität zu Köln

vorgelegt von

Patrick Wurm

aus Olpe

Köln, 2013

Berichterstatter: Priv.-Doz. Dr. Markus Büscher
Prof. Dr. Jan Jolie

Tag der mündlichen Prüfung: 13.11.2012

Zusammenfassung

Der Wide Angle Shower Apparatus (WASA) – der am Cooler Synchrotron COSY-Jülich betrieben wird – ist ein nahezu 4π-Detektor, der die Untersuchung der Produktionsmechanismen und die Zerfälle von leichten Mesonen ermöglicht. In den vergangen Jahren wurde eine große Menge an Daten mit η Meson Zerfällen aufgenommen, die die Messung von seltenen Zerfallskanälen ermöglicht. Einer dieser Kanäle ist der doppelte Dalitz Zerfall, bei dem das η Meson über zwei virtuelle Photonen in zwei Elektron-Positron-Paare zerfällt. Basierend auf QED-Rechnungen ist das erwartete Verzweigungsverhältnis $\mathcal{BR}(\eta \to e^+e^-e^+e^-) = 2{,}6 \cdot 10^{-5}$.

In dieser Arbeit wird die Analyse von $3 \cdot 10^7$ η Ereignissen von $p\,d \to {}^3\mathrm{He}\,\eta$ Reaktionen präsentiert. Basierend auf $49{,}7 \pm 12{,}5_{\mathrm{stat}}$ identifizierten Signalkandidaten beträgt das gemessene Verzweigungsverhältnis $\mathcal{BR}(\eta \to e^+e^-e^+e^-) = (3{,}2 \pm 0{,}8_{\mathrm{stat}} \pm 0{,}8_{\mathrm{syst}}) \cdot 10^{-5}$. Dieses Ergebnis ist konsistent mit dem Wert $\mathcal{BR}(\eta \to e^+e^-e^+e^-) = (2{,}9 \pm 1{,}1_{\mathrm{stat}}) \cdot 10^{-5}$, der von L. Yurev in einer früheren Arbeit ermitteltet wurde, wobei nur das erste Drittel des Datensatzes mit anderen Selektionskriterien analysiert wurde. Das Ergebnis ist ebenfalls in Übereinstimmung mit dem Wert $\mathcal{BR}(\eta \to e^+e^-e^+e^-) = (2{,}4 \pm 0{,}2_{\mathrm{stat}} \pm 0{,}1_{\mathrm{syst}}) \cdot 10^{-5}$, welcher kürzlich von der KLOE Kollaboration veröffentlicht wurde.

Weitgehende Analysemethoden wurden entwickelt und auf die Suche nach dem sehr seltenen Zerfall $\eta \to e^+e^-$ abgestimmt, der gemäß dem Standardmodell ein Verzweigungsverhältnis in der Größenordnung von 10^{-9} hat. Jede erhebliche Abweichung von diesem Wert wäre ein Hinweis für neue Physik. Im Rahmen dieser Arbeit wird eine obere Grenze für das Verzweigungsverhältnis dieses Kanals von $\mathcal{BR}(\eta \to e^+e^-) < 6 \cdot 10^{-6}$ (Vertrauensbereich von 90 %) bestimmt. Dieser Wert ist nah an der kürzlich veröffentlichten oberen Grenze von der HADES Kollaboration: $\mathcal{BR}(\eta \to e^+e^-) < 4{,}9^{+0{,}7}_{-1{,}2} \cdot 10^{-6}$ (Vertrauensbereich von 90 %).

Abstract

The Wide Angle Shower Apparatus (WASA) – operated at the Cooler Synchrotron COSY-Jülich – is a close-to-4π-detector used for the study of the production mechanisms and decay modes of light mesons. A huge amount of η meson data has been accumulated over the last few years and these allow one to measure even rare decay channels. One of these channels is the double Dalitz decay, where the η meson decays via two virtual photons into two electron-positron pairs. According to QED calculations, the expected branching ratio is $\mathcal{BR}(\eta \to e^+e^-e^+e^-) = 2.6 \times 10^{-5}$.

In this work the analysis of 3×10^7 η events from $p\,d \to {}^3\mathrm{He}\,\eta$ reactions is presented. Based upon $49.7 \pm 12.5_{\mathrm{stat}}$ identified candidates, the branching ratio for $\eta \to e^+e^-e^+e^-$ is measured to be $\mathcal{BR}(\eta \to e^+e^-e^+e^-) = (3.2 \pm 0.8_{\mathrm{stat}} \pm 0.8_{\mathrm{syst}}) \times 10^{-5}$. This is consistent with the value $\mathcal{BR}(\eta \to e^+e^-e^+e^-) = (2.9 \pm 1.1) \times 10^{-5}$ reported in the earlier PhD thesis of L. Yurev, where only the first third of the data set was analyzed but with different selection criteria. The result is also in agreement with the recently published value from the KLOE collaboration: $\mathcal{BR}(\eta \to e^+e^-e^+e^-) = (2.4 \pm 0.2_{\mathrm{stat}} \pm 0.1_{\mathrm{syst}}) \times 10^{-5}$.

Sophisticated analysis methods have been developed and tuned to search for the very rare decay channel $\eta \to e^+e^-$ which, according to the Standard Model, has a branching ratio on the order of 10^{-9}. Any significant deviation from this value would be a sign for new physics. Within the framework of this thesis, an upper limit for this branching ratio has been determined as $\mathcal{BR}(\eta \to e^+e^-) < 6 \times 10^{-6}$ at the 90 % confidence level. This is close to the recently published upper limit measured by the HADES collaboration: $\mathcal{BR}(\eta \to e^+e^-) < 4.9^{+0.7}_{-1.2} \times 10^{-6}$ at the 90 % confidence level.

Contents

List of Figures

List of Tables

Chapter 1

Introduction

This work aims to identify $\eta \to e^+e^-e^+e^-$ events in a data sample which comprises more than $3{\times}10^7$ η-meson decays from $p\,d \to {}^3\mathrm{He}\,\eta$ reactions taken with the WASA-at-COSY experiment. The challenge of the measurement of this rare channel is the huge amount of background events. The expected ratio between the number of signal events and those from other η-decay channels is around 1/40000. For that reason, sophisticated selection criteria and particle identification algorithms must be developed to obtain a clean sample of $\eta \to e^+e^-e^+e^-$ events. Based on the identified signal events the branching fraction is calculated and compared with the results from previous studies of this decay. Theoretical predictions for the branching ratio lie in the range 2.41×10^{-5} to 3.45×10^{-5} (*cf.* Refs. [1, 2, 3, 4, 5, 6, 7]).

Until recently there existed only experimental upper limits for the branching fraction of this channel, where the smallest bound was 6.9×10^{-5} (90 % confidence level) [8]. During the course of this PhD work there was a publication from the KLOE collaboration reporting the first measurement of a finite value for the branching ratio [9]. Their result is $\mathcal{BR}(\eta \to e^+e^-e^+e^-) = (2.4 \pm 0.2_{\mathrm{stat}} \pm 0.1_{\mathrm{syst}}) \times 10^{-5}$, and the number of identified $\eta \to e^+e^-e^+e^-$ decay candidates is 362 ± 29. The branching ratio agrees with an earlier analysis from WASA-at-COSY of a smaller data sample (10^7 events) [10], where 30 ± 10 identified $\eta \to e^+e^-e^+e^-$ events lead to $\mathcal{BR}(\eta \to e^+e^-e^+e^-) = (2.9 \pm 1.1_{\mathrm{stat}}) \times 10^{-5}$. With the present measurement the branching ratio from KLOE can be verified with an independent experiment, and for that reason it gives an important contribution to the understanding of a rare η-decay channel.

The second topic of this thesis is the search for the extremely rare decay $\eta \to e^+e^-$. This channel can serve as a probe for processes beyond the SM. The new physics would be reflected in an unexpectedly large value for the branching ratio compared to the theoretical predictions, which are in the order of 10^{-9} (based on SM calculations). The goal of this analysis is to reduce the gap between these predictions and the upper bounds which were set from former experiments.

In this chapter, the theory behind the channels and $\eta \to e^+e^-e^+e^-$ and $\eta \to e^+e^-$ will be presented, and the former works on these decays will be summarized.

1.1 Standard Model of particle physics

The Standard Model (SM) of particle physics is a relativistic quantum field theory, which describes elementary particles and their interactions. Within the SM, the particles can be divided into two groups: the matter particles and the force carriers. The former are fermions

with spin 1/2 and can be further grouped into quarks and leptons. There are three families of quarks and leptons, where each generation includes one quark doublet and one lepton doublet. The three quark doublets are

$$\begin{pmatrix} u \\ d \end{pmatrix} \quad \begin{pmatrix} c \\ s \end{pmatrix} \quad \begin{pmatrix} t \\ b \end{pmatrix}$$

There is the up, down, charm, strange, top, and bottom quark. The quarks in the upper row have an electric charge of $+(2/3)$ times the elementary charge, and the lower ones have an electric charge of $-(1/3)$ times the elementary charge.

The six leptons are

$$\begin{pmatrix} \nu_e \\ e \end{pmatrix} \quad \begin{pmatrix} \nu_\mu \\ \mu \end{pmatrix} \quad \begin{pmatrix} \nu_\tau \\ \tau \end{pmatrix}$$

The e (electron), μ (muon), and τ (tau) have an electric charge of -1 times the elementary charge. The ν_e (electron neutrino), ν_μ (muon neutrino), and ν_τ (tau neutrino) are uncharged. For each matter particle there exists an antiparticle with identical mass. A particle and its corresponding antiparticle differ in the sign of the charge-like quantum numbers, like the electric charge, quark number, or lepton number.

The interactions between the elementary particles are mediated by gauge bosons, which are listed in Table 1.1. In the following, the three different interactions of the SM are briefly summarized, ordered by their strength.

Table 1.1: Gauge bosons in the Standard Model.

gauge boson	force	coupling to...
photon γ	electromagnetic	electrically charged particles
W^+, W^-, Z^0	weak	quarks/leptons/W^+/W^-/Z^0
eight gluons	strong	colored particles

The weakest interaction is the weak force. It is described by the exchange of W^+, W^-, and Z^0 bosons which couple to quarks and leptons. The $W^\pm$ bosons have a mass of $80.4\,\mathrm{GeV}/c^2$, and the Z^0 has a mass of $91.2\,\mathrm{GeV}/c^2$. Their lifetimes are in the order of 3×10^{-25} s [11]. Due to the large masses of the gauge bosons, the weak interaction has only a short range in the order of 10^{-18} m [12]. An example where the weak interaction occurs is the β^- decay. Here, a down quark converts into an up quark under the emission of a W^-, which finally decays into an electron and electron antineutrino.

The next interaction is the electromagnetic force, where the exchange particles are photons. They couple to all particles with an electromagnetic charge. Since photons are massless, the range of the electromagnetic force is infinite. The theory of electromagnetic interactions is called quantum electrodynamics (QED). An example for a QED process is the Coulomb scattering or the conversion of a photon into an electron-positron pair. The weak and the electromagnetic interactions are unified to the electro-weak interaction. The corresponding theory is named quantum flavordynamics, or also named as the Glashow-Weinberg-Salam (GWS) model. The unification of the electromagnetic and weak forces is one of the main successes of the SM.

The strongest interaction is the strong force. The exchange particles are eight massless gluons which couple to quarks and to themselves as well. The range of the strong force is

limited to a distance in the order of the radius of a nucleon [12], with a remaining van-der-Waals-force like long range interaction, the nuclear force. The theory of the strong interaction is called quantum chromodynamics (QCD). The exchange of gluons between quarks, which is described within the QCD, is responsible for the existence of hadrons. These are particles which are built of quarks, bound by gluons. One of these hadrons is the η meson, which will be described in the next section in more detail.

Although the SM is a very successful theory which can be used to calculate physical quantities that can be measured and verified in experiments, it does not include gravity, which is the fourth interaction. However, when regarding processes on the sub-atomic level as it is the case of the processes which are discussed and analyzed in this thesis, gravity plays a negligible role.

1.2 The η meson

1.2.1 General properties

Mesons are unstable particles, which, together with the baryons, belong to the hadrons. Baryons are built from three quarks, which results in total in an half-integer spin. Therefore, these particles are fermions. Mesons, however, are built up from a quark-antiquark pair; thus, they are bosons with an integer spin. Since there are many possibilities to combine the different quarks, there exist a large number of mesons. One of these is the η meson, which was discovered in pion-nucleon collisions by a team from the John Hopkins University at the Lawrence Radiation Laboratory Bevatron accelerator in 1961 [13]. This particle is a mixture of up, down and strange quarks and their antiquarks. Due to the quark composition and its charge of zero, the η meson is its own antiparticle. The mass of the η meson is $(547.853 \pm 0.024)\,\mathrm{MeV}/c^2$, and the mean lifetime is $(5.0 \pm 0.3) \times 10^{-19}\,\mathrm{s}$ [11]. The isospin quantum number is zero, its total angular momentum J is zero, its P parity [1] is -1, and its C parity [2] is $+1$ [11]. Because of its spin and parity, the η meson is classified as a pseudoscalar meson (*cf.* Table 1.2).

Table 1.2: Classification of the mesons [1].

Type	S	L	P	J	J^P
pseudoscalar meson	0	0	$-$	0	0^-
pseudovector meson	0	1	$+$	1	1^+
vector meson	1	0	$-$	1	1^-
scalar meson	1	1	$+$	0	0^+
tensor meson	1	1	$+$	2	2^+

[1] The parity operator $\hat{P}$ is the product of the intrinsic parity of a particle and the flip of the spatial coordinates of a wave function: $\hat{P}\psi(\vec{x}) = P\psi(-\vec{x})$, where ψ is the quark Dirac wave function.

[2] The $\hat{C}$ parity operator transforms a particle into its antiparticle: $\hat{C}\psi = C\bar{\psi}$

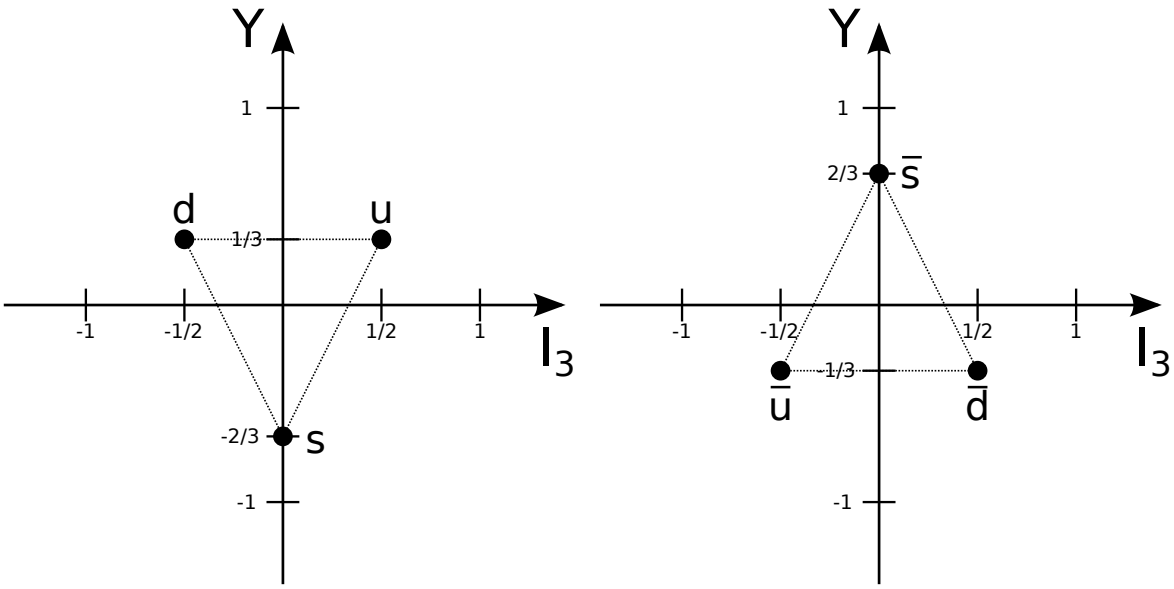

(a) quarks (b) antiquarks

Figure 1.1: The triplets of the three lightest quarks and antiquarks. Y is the hypercharge, and I_3 is the third component of the isospin vector.

1.2.2 Description in the static quark-model

The three lightest quarks (namely the up, down, and strange quark) and the antiquarks can be grouped into two triplets, where the particles are characterized by two independent quantum numbers: the hypercharge Y ("counting" the number of s quarks) and the third component of the isospin vector I_3 (proportional to number of u minus d quarks). Figure 1.1 shows the triplets of the three lightest quarks and antiquarks.

There are nine quark-antiquark pairs which can be constructed from the three lightest quarks. These are the π^0, π^+, π^-, η, η', K^0, $\bar{K}^0$, K^+, and K^-, which built the nonet of pseudoscalar mesons, described by the SU(3) symmetry group. The nonet can be decomposed into an octet and singlet (written in group notation $\{3\} \otimes \{\overline{3}\} = \{8\} \oplus \{1\}$). The SU(3) octet and singlet are shown in Fig. 1.2.

The observed particles η and the η' are mixtures of

$$\eta_8 = \frac{u\bar{u} + d\bar{d} - 2s\bar{s}}{\sqrt{6}} \,, \tag{1.1}$$

which is a member of the octet, and the singlet state

$$\eta_1 = \frac{u\bar{u} + d\bar{d} + s\bar{s}}{\sqrt{3}} \,. \tag{1.2}$$

These flavor states mix to the η and η' according to

$$\begin{pmatrix} \eta \\ \eta' \end{pmatrix} = R_{\theta_P} \begin{pmatrix} \eta_8 \\ \eta_1 \end{pmatrix} = \begin{pmatrix} \cos\theta_P & -\sin\theta_P \\ \sin\theta_P & \cos\theta_P \end{pmatrix} \begin{pmatrix} \eta_8 \\ \eta_1 \end{pmatrix} \,, \tag{1.3}$$

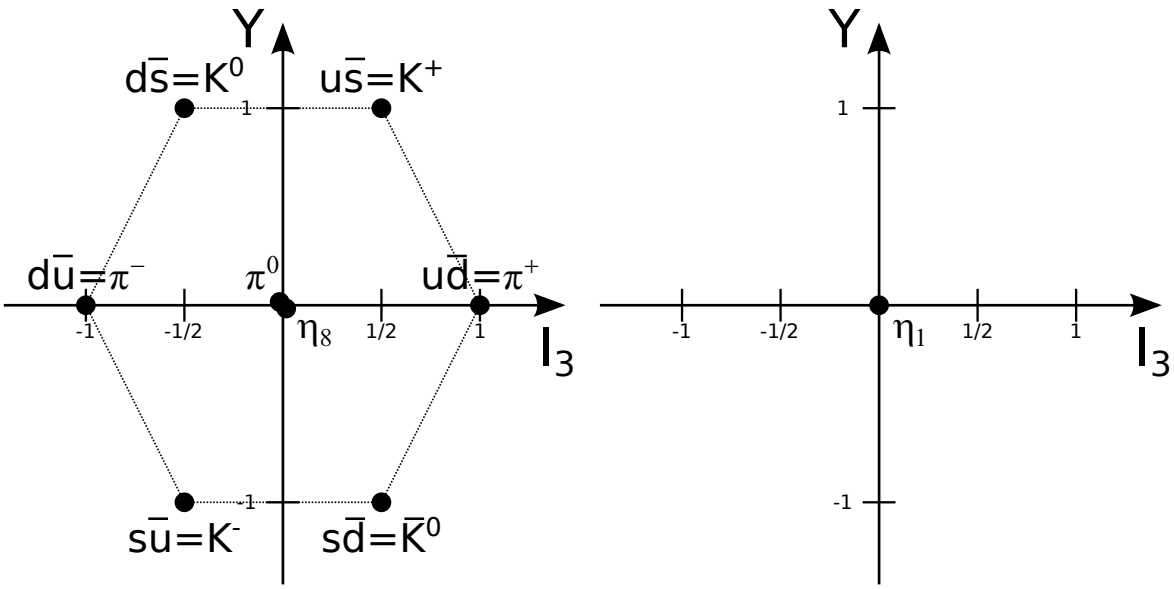

(a) octet (b) singlet

Figure 1.2: SU(3) nonet. The π^0 is composed of $\pi^0 = (1/\sqrt{2})(u\bar{u} - d\bar{d})$. The octet state η_8 is composed of $\eta_8 = (1/\sqrt{6})(u\bar{u} + d\bar{d} - 2s\bar{s})$. Besides the eight states of the SU(3) octet, there exists the singlet state η_1, which completes the SU(3) nonet. It is composed of $\eta_1 = (1/\sqrt{3})(u\bar{u} + d\bar{d} + s\bar{s})$ and has the quantum numbers $I_3 = 0$ and $Y = 0$.

where R_{θ_P} is a rotation matrix in the Euclidean plane $\mathbb{R}^2$ with a mixing angle θ_P. η and η' can be written as

$$\eta = \left(\frac{\cos\theta_P}{\sqrt{6}} - \frac{\sin\theta_P}{\sqrt{3}}\right)(u\bar{u} + d\bar{d}) - \frac{1}{\sqrt{3}}\left(\sqrt{2}\cos\theta_P + \sin\theta_P\right)s\bar{s} \tag{1.4}$$

and

$$\eta' = \left(\frac{\sin\theta_P}{\sqrt{6}} + \frac{\cos\theta_P}{\sqrt{3}}\right)(u\bar{u} + d\bar{d}) + \frac{1}{\sqrt{3}}\left(\cos\theta_P - \sqrt{2}\sin\theta_P\right)s\bar{s} \tag{1.5}$$

The mixing angle was measured as $\theta_P = -15.5° \pm 1.3°$ [14]. Since it is quite small, the rotation matrix is nearly diagonal and $\eta \approx \eta_8$ and $\eta' \approx \eta_1$.

1.3 η-meson decays

The η meson decays via the electromagnetic and the strong force. In about 70 % of the time, it decays into neutral particles, while in the other 30 % there are charged particles in the final state. The most abundant decay modes and their corresponding branching ratios are listed in Table 1.3.

Table 1.3: Measured η-meson branching ratios (from the Particle Data Group (PDG) [11]). The decay channels where only an upper limit exists are not listed.

decay mode	branching ratio
$\eta \to \gamma\gamma$	$(39.31 \pm 0.20)\,\%$
$\eta \to \pi^0\pi^0\pi^0$	$(32.57 \pm 0.23)\,\%$
$\eta \to \pi^0\gamma\gamma$	$(2.7 \pm 0.5) \times 10^{-4}$
$\eta \to \pi^+\pi^-\pi^0$	$(22.74 \pm 0.28)\,\%$
$\eta \to \pi^+\pi^-\gamma$	$(4.60 \pm 0.16)\,\%$
$\eta \to e^+e^-\gamma$	$(6.9 \pm 0.4) \times 10^{-3}$
$\eta \to e^+e^-e^+e^-$	$(2.40 \pm 0.22) \times 10^{-5}$
$\eta \to \mu^+\mu^-\gamma$	$(3.1 \pm 0.4) \times 10^{-4}$
$\eta \to \pi^+\pi^-e^+e^-(\gamma)$	$(2.68 \pm 0.11) \times 10^{-4}$
$\eta \to \mu^+\mu^-$	$(5.8 \pm 0.8) \times 10^{-6}$

Already the four most frequent decay modes sum up to more than 99 % of the total branching fraction. These are modes where the η meson decays either solely into photons, or decays with pions. The most frequent decay channel with an electron-positron pair in the final state is the single Dalitz decay $\eta \to e^+e^-\gamma$. However, compared with the sum of the four most common η-decay channels, it is suppressed by more than a factor of hundred.

The listed η-decay channels and their branching ratios are mostly based on measurements from different experiments. However, besides the shown decays there are also channels where the experimental data are scarce, resulting in less established branching fractions. One of these decays is $\eta \to e^+e^-e^+e^-$, which is suppressed by a factor of hundred compared to $\eta \to e^+e^-\gamma$. An even rarer channel is $\eta \to e^+e^-$, which has according to SM predictions a branching ratio in the order of 10^{-9}. The study of the two channels $\eta \to e^+e^-e^+e^-$ and $\eta \to e^+e^-$ is the main topic of this work. The theoretical background and the motivation to measure these channels will be presented in the following sections.

1.4 The decay $\eta \to e^+e^-e^+e^-$

The first channel which was analyzed within the framework of this thesis is the decay $\eta \to e^+e^-e^+e^-$. It is called the η double Dalitz decay. Here, the η meson decays via two virtual photons into two electron-positron pairs. The Feynman diagram for this fourth order electromagnetic process is shown in Fig. 1.3. The channel is closely related to the decay $\eta \to \gamma\gamma$ with the difference that the two photons are off-shell in case of the double Dalitz decay.

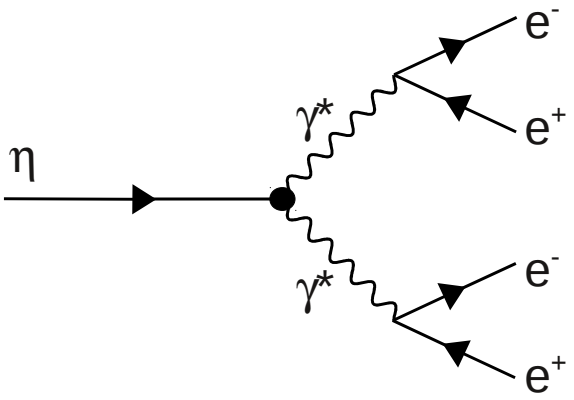

Figure 1.3: Simplified Feynman diagram for $\eta \to e^+e^-e^+e^-$. The η-meson is assumed as a point-like particle which decays via two virtual photons into two electron-positron pairs. The time axis goes from the left to the right.

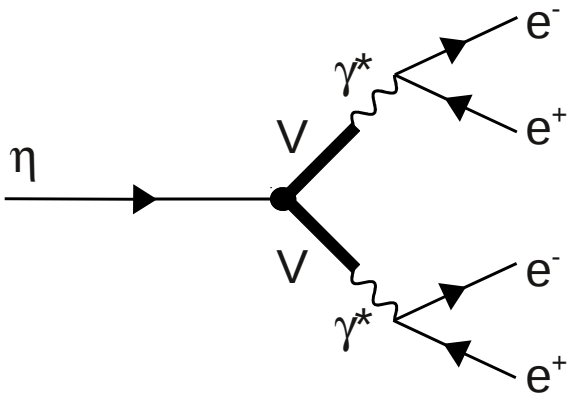

Figure 1.4: Feynman diagram for $\eta \to e^+e^-e^+e^-$ in the vector meson dominance (VMD) model. The transition of the η meson into the electron-positron pairs is described by a superposition of the virtual photon and the three lightest vector mesons V, namely the ρ, ω, and ϕ. The time axis goes from the left to the right.

Different theoretical descriptions for this decay exist, which predict that the branching fraction of this channel should be in the order of 10^{-5}. This makes the double Dalitz decay to one of the rare decay channel of the η meson. Due to the small branching fraction, the experimental data are quite scarce and a precise measurement of the branching ratio is needed in order to verify the predictions from theory.

Another motivation to study the double Dalitz decay is the possibility to measure the transition form factor of the η-meson: QCD calculations for the transition of a meson into two photons are very challenging, since the strong coupling constant α_s is large, which makes perturbative approaches impossible. In the chiral limit, however, the decay can be described by the triangle term of the Wess-Zumino-Witten Lagrangian [1, 15, 16], which describes the coupling of the two photons to the pseudoscaler field. It has the form [17, 18]

$$\mathcal{L} = \mathcal{L}_{AAP} = -\frac{N_C e^2}{4\pi^2 f_\pi} \epsilon^{\mu\nu\alpha\beta} \partial_\mu A_\nu \partial_\alpha A_\beta \mathrm{Tr}[Q^2 P] \,, \tag{1.6}$$

where N_C is the number of colors in the SM, e is the electric charge, f_π is the pion-decay

constant, A_ν and A_β are the photon fields, Q is the quark charge matrix

$$Q = \begin{pmatrix} \frac{2}{3} & 0 & 0 \\ 0 & -\frac{1}{3} & 0 \\ 0 & 0 & -\frac{1}{3} \end{pmatrix} , \tag{1.7}$$

and P is the bare pseudoscalar field matrix [1, 19], which is

$$P = P_8 + P_1 = \frac{1}{\sqrt{2}} \begin{pmatrix} \frac{1}{\sqrt{2}}\pi^0 + \frac{1}{\sqrt{6}}\eta_8 + \frac{1}{\sqrt{3}}\eta_1 & \pi^+ & K^+ \\ \pi^- & -\frac{1}{\sqrt{2}}\pi^0 + \frac{1}{\sqrt{6}}\eta_8 + \frac{1}{\sqrt{3}}\eta_1 & K^0 \\ K^- & \bar{K}^0 & -\sqrt{\frac{2}{3}}\eta_8 + \frac{1}{\sqrt{3}}\eta_1 \end{pmatrix} . \tag{1.8}$$

Since the transition of a meson into two photons in reality is far away from the chiral limit, the Lagrangian from Eq. 1.6 must be extended by terms which describe the decay in a more realistic way. Instead of expanding the Lagrangian, all additional effects are summarized in a form factor which is multiplied to the vertex.

The form factor depends on the squares of the energy-momentum four-vectors of the two photons and can thus be defined as $F(q_1^2, q_2^2)$, where q_1 is the energy-momentum four-vector of the first photon, and q_2 of the second, respectively. At extreme values for the squared energy-momentum four-vectors it is possible to extract constraints for the shape of the form factor from QCD calculations (*cf.* Ref. [2]), but the exact shape of the form factor is not known yet.

Theoretical predictions for $F(q_1^2, q_2^2)$ can be found in Refs. [1, 2, 3, 4, 5, 6]. One description for the form factor is given by the phenomenological vector meson dominance (VMD) model. According to VMD, the virtual photon is a superposition of an electromagnetic photon and the three lightest vector mesons, namely the ρ, ω, and ϕ. This results then in a hadronic contribution to the photon propagator and could be a more reasonable approach to describe the decay of a pseudoscalar particle into photons. The mixing between the virtual particles is possible, since the electromagnetic photon and the three mesons all have quantum numbers $J^P = 1^-$.

The Lagrangians which describe the additional couplings of the vector meson fields to the pseudoscalar meson must be added to the Eq. 1.6, which leads then to the Lagrangian [17, 18]

$$\mathcal{L} = \mathcal{L}_{AAP} + \mathcal{L}_{AVP} + \mathcal{L}_{VVP} \tag{1.9}$$

with the term [17, 18]

$$\mathcal{L}_{AAP} = -\frac{N_C e^2}{4\pi^2 f_\pi}(1 - c_4)\epsilon^{\mu\nu\alpha\beta}\partial_\mu A_\nu \partial_\alpha A_\beta \mathrm{Tr}[Q^2 P] \tag{1.10}$$

which describes the coupling of the two photon fields to the pseudoscalar field. The coupling of a photon and a vector meson field to the pseudoscalar field is described by [17, 18]

$$\mathcal{L}_{AVP} = -\frac{N_C g e}{8\pi^2 f_\pi}(c_4 - c_3)\epsilon^{\mu\nu\alpha\beta}\partial_\mu A_\nu \mathrm{Tr}[\{\partial_\alpha V_\beta, Q\}P] , \tag{1.11}$$

where g is the vector meson coupling and V is the vector meson field. The coupling of two vector meson field to the pseudoscalar field can be described by [17, 18]

$$\mathcal{L}_{VVP} = -\frac{N_C g^2}{4\pi^2 f_\pi} c_3 \epsilon^{\mu\nu\alpha\beta}\mathrm{Tr}[\partial_\mu V_\nu \partial_\alpha V_\beta P] . \tag{1.12}$$

The Feynman diagram corresponding to this full VMD term is shown in Fig. 1.4 for $\eta \to e^+e^-e^+e^-$. More information about the presented Lagrangians can be found in Refs. [1, 17, 18, 19].

The contributions of the individual Lagrangians, which are expressed by the parameters c_3 and c_4, must be derived from experiments by measuring the shape of the form factor. This can be achieved by precisely measuring the invariant mass distribution of the two electron-positron pairs. At the moment, different measurements for the form factor exist based on studies of the single Dalitz decay $\eta \to e^+e^-\gamma$ (for example in Ref. [20]), but no experiment has measured the double off-shell form factor with the decay $\eta \to e^+e^-e^+e^-$.

Due to the limited statistics, the data set which was analyzed within the framework of this thesis does not allow for the measurement of the form factor. For that reason, this work was focused on a precise determination of the branching fraction of $\eta \to e^+e^-e^+e^-$. Former works (from theory and experimental groups) on this decay will be presented in the following subsections.

1.4.1 Theoretical calculations

The branching ratio for the decay $\eta \to e^+e^-e^+e^-$ relative to the decay $\eta \to \gamma\gamma$ was calculated for the first time by C. Jarlskog and H. Pilkuhn [3]. Their result was $\mathcal{BR}(\eta \to e^+e^-e^+e^-)/\mathcal{BR}(\eta \to \gamma\gamma) = \rho_{\eta\to e^+e^-e^+e^-} = 6.6 \times 10^{-5}$ and was based on QED calculations. By inserting the measured value for the branching ratio of $\eta \to \gamma\gamma$ (with $\mathcal{BR}(\eta \to \gamma\gamma) = 0.3931 \pm 0.0020$, see Table 1.3), one obtains $\mathcal{BR}(\eta \to e^+e^-e^+e^-) = 2.59 \times 10^{-5}$.

T. Miyazaki and E. Takasugi found $\rho_{\eta\to e^+e^-e^+e^-} = 6.14 \times 10^{-5}$, which leads to $\mathcal{BR}(\eta \to e^+e^-e^+e^-) = 2.41 \times 10^{-5}$. Their calculations were based on a combination of QED calculations with a momentum dependent form factor [4].

J. Bijnens and F. Persson studied the decay rate for the double Dalitz decay relative to $\eta \to \gamma\gamma$ for different form factor models [2]. When transforming the values in absolute values, the branching ratios lie in the range between 2.52×10^{-5} and 2.65×10^{-5}. The different form factors and the calculated relative and absolute branching ratios are listed in Table 1.4. The given errors are from the used Monte Carlo integration program.

Table 1.4: Relative and absolute branching ratios for $\eta \to e^+e^-e^+e^-$ for different form factors [2].

form factor $F(q_1^2, q_1^2) = ...$	$\rho_{\eta\to e^+e^-e^+e^-}$ $[\times 10^{-5}]$	$\mathcal{BR}(\eta \to e^+e^-e^+e^-)$ $[\times 10^{-5}]$
1	6.40 ± 0.02	2.52 ± 0.02
$\frac{m_\rho^4}{(m_\rho^2-q_1^2)(m_\rho^2-q_2^2)}$	6.73 ± 0.02	2.65 ± 0.02
$\frac{m_\rho^2}{(m_\rho^2-q_1^2-q_2^2)}$	6.71 ± 0.02	2.64 ± 0.02
$\frac{m_\rho^4-\frac{4\pi^2 f_\pi^2}{N_c}(q_1^2+q_2^2)}{(m_\rho^2-q_1^2)(m_\rho^2-q_2^2)}$	6.64 ± 0.02	2.61 ± 0.02

C. Terschluesen found for the branching ratio in leading order calculations $\mathcal{BR}(\eta \to$

$e^+e^-e^+e^-) = (3.45 \pm 0.19) \times 10^{-5}\,\mathrm{GeV}$ (the error includes the error of the experimental total decay width of the η meson) [6, 7]. The calculation was based on a power counting scheme by M. F. M. Lutz and S. Leupold [21].

T. Petri calculated for the relative branching fraction without a VMD model $\rho_{\eta\to e^+e^-e^+e^-} = 6.463 \times 10^{-5}$ (*i.e.* $\mathcal{BR}(\eta \to e^+e^-e^+e^-) = 2.541 \times 10^{-5}$), with a hidden gauge model $\rho_{\eta\to e^+e^-e^+e^-} = (6.800 \pm 0.013) \times 10^{-5}$ (*i.e.* $\mathcal{BR}(\eta \to e^+e^-e^+e^-) = (2.673 \pm 0.015) \times 10^{-5}$), and with a modified VMD model $\rho_{\eta\to e^+e^-e^+e^-} = (6.770 \pm 0.016) \times 10^{-5}$ (*i.e.* $\mathcal{BR}(\eta \to e^+e^-e^+e^-) = (2.661 \pm 0.015) \times 10^{-5}$) [1].

C. C. Lih used a light-front quark model (LFQM) to determine a momentum dependent form factor, which was then used to calculate the branching fraction [5]. The result for the branching ratio was $\mathcal{BR}(\eta \to e^+e^-e^+e^-) = 2.47 \times 10^{-5}$ [5].

1.4.2 Former experimental results

The most recent published value for the $\eta \to e^+e^-e^+e^-$ branching ratio comes from the KLOE collaboration, and is $\mathcal{BR}(\eta \to e^+e^-e^+e^-) = (2.4 \pm 0.2_{\mathrm{stat}} \pm 0.1_{\mathrm{syst}}) \times 10^{-5}$ [9]. This value was published during the course of this PhD thesis. The experiment was performed at the DAϕNE Frascati ϕ-factory, where the η mesons were produced in $e^+e^- \to \phi \to \eta\gamma$ reactions with a cross section of $(41.7 \pm 0.6)\,\mathrm{nb}$. The analysis was based on a data sample with more than 7×10^7 $\phi \to \eta\gamma$ events, where 362 ± 29 event candidates were observed

Within the framework of a PhD thesis, $\eta \to e^+e^-e^+e^-$ was studied by L. Yurev [10]. 10^7 η events from $p\,d \to {}^3\mathrm{He}\,\eta$ reactions (first third of the data which were analyzed in this thesis), measured with the WASA-at-COSY experiment, were analyzed and 30 ± 10 signal event candidates were identified. The measured branching ratio was $\mathcal{BR}(\eta \to e^+e^-e^+e^-) = (2.9 \pm 1.1_{\mathrm{stat}}) \times 10^{-5}$.

Before these measurements, there existed only upper limits for the branching fraction. CMD-2 published an upper limit of 6.9×10^{-5} at the 90 % confidence level (CL) [8]. The data were taken at the e^+e^- collider VEPP-2M using the reaction $e^+e^- \to \phi \to \eta\gamma$.

Later, the WASA/CELSIUS experiment published an upper limit of 9.7×10^{-5} (90 % CL) [22]. The result is based on the analysis of 3×10^5 η events from $p\,d \to {}^3\mathrm{He}\,\eta$ reactions. Two events passed all selection criteria, whereas the number of background events was estimated to be 1.3 ± 0.2, originating mainly from the decay $\eta \to e^+e^-\gamma$.

1.4.3 Summary of the previous works on $\eta \to e^+e^-e^+e^-$

Figure 1.5 shows a summary of the calculated and measured values for the branching ratio of $\eta \to e^+e^-e^+e^-$.

On the theory side, the predicted values for the branching ratio of $\eta \to e^+e^-e^+e^-$ lie in the range between 2.41×10^{-5} and 3.45×10^{-5}. On the experimental side, the measured branching ratios have quite large error bars due to the small numbers of identified signal events. For that reason, they lack the precision needed to determine which theoretical model is preferable. Due to the fact that the experimental results for the branching ratio of the double Dalitz decay $\eta \to e^+e^-e^+e^-$ are very scarce, an independent measurement which leads to a precise determination of its branching ratio is needed.

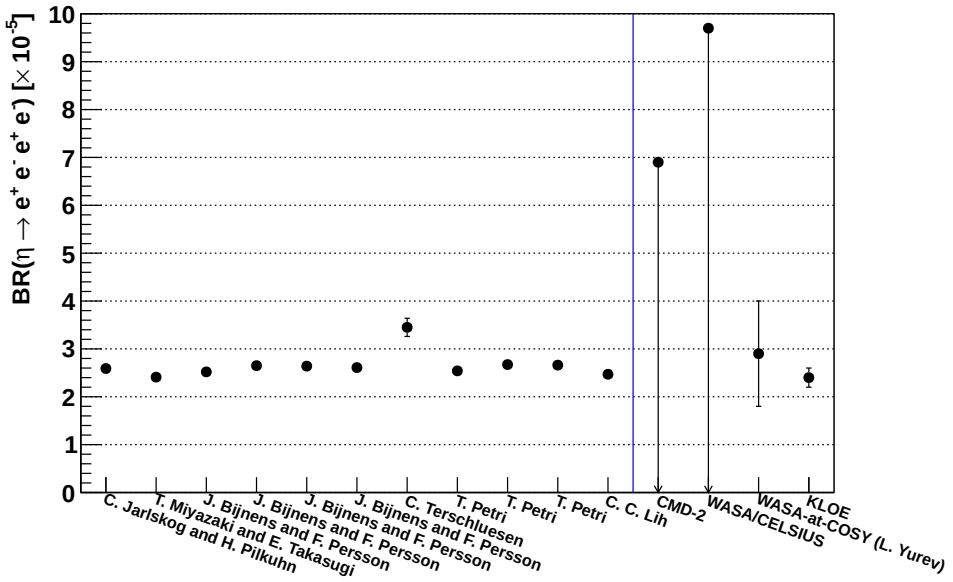

Figure 1.5: Summary of the calculated and measured values for the branching ratio of $\eta \to e^+e^-e^+e^-$. The blue solid line separates the calculated values on the left side from the experimental values on the right side. In case of the experimental results the errors shown are statistical errors. The upper limits are given at the 90 % CL.

1.5 The decay $\eta \to e^+e^-$

The dominant mechanism behind the decay of the η meson into one electron and one positron is a fourth order electromagnetic process, which proceeds at the chiral limit via the triangle anomaly term of the Wess-Zumino-Witten Lagrangian. The Feynman diagram for $\eta \to e^+e^-$ is shown in Fig. 1.6.

In the following, an estimate for the branching ratio $\eta \to e^+e^-$ will be derived, which follows the descriptions of the papers by L. G. Landsberg [23], T. E. Browder et al. [24], and A. E. Dorokhov and M. A. Ivanov [25]:

In lowest order of QED, the decay is described by a one-loop process via the two-photon intermediate state [25]. Here, the general formula for the branching ratio for the decay of a pseudoscalar meson into a lepton-antilepton pair relative to the decay of the pseudoscalar meson into two photons is

$$\frac{\mathcal{BR}(P \to l^+l^-)}{\mathcal{BR}(P \to \gamma\gamma)} = 2\left(\frac{\alpha}{\pi}\frac{m_l}{m_P}\right)^2 \beta_l \, |\mathcal{A}|^2 \,, \tag{1.13}$$

where α is the fine structure constant, m_l is the mass of the lepton, m_P is the mass of the pseudoscalar meson, $\beta_l = \sqrt{1 - 4m_l^2/m_P^2}$ (the index l denotes that the mass of the lepton l is used in this expression), and $\mathcal{A}$ is the decay amplitude. The factor $2(m_l/m_P)^2$ appears due to the approximate helicity conservation of the interaction [25].

The imaginary part of the decay amplitude is

$$\mathrm{Im}\mathcal{A} = \frac{\pi}{2\beta_l} \ln\left(\frac{1-\beta_l}{1+\beta_l}\right) \,. \tag{1.14}$$

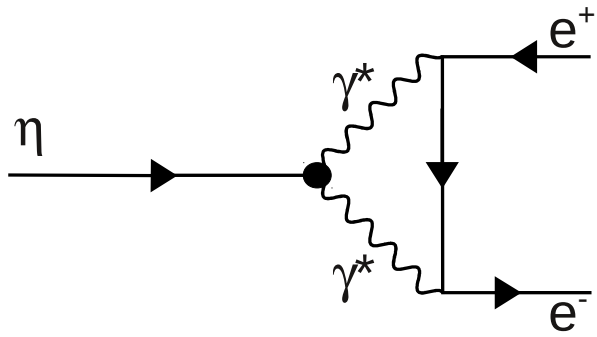

Figure 1.6: One-loop Feynman amplitude for $\eta \to e^+e^-$ in the lowest order of QED perturbation theory. The η meson decays via two virtual photons into the electron and positron. The time axis goes from the left to the right.

This model independent term comes from the contribution of the real photons in the intermediate state [25]. Due to the fact that the real part of the decay amplitude ($\mathrm{Re}\mathcal{A}$) is complicated to calculate, it can be set equal to zero in order to get an estimate for the lower limit of the branching fraction of $\eta \to e^+e^-$. Inserting the imaginary part into Eq. 1.13 and using $|\mathcal{A}|^2 \geq (\mathrm{Im}\mathcal{A})^2$ leads to the lower bound

$$\mathcal{BR}(P \to l^+l^-) \geq \mathcal{BR}(P \to \gamma\gamma) \left(\alpha \frac{m_l}{m_P}\right)^2 \frac{1}{2\beta_l} \left[\ln\left(\frac{1-\beta_l}{1+\beta_l}\right)\right]^2 . \tag{1.15}$$

By using the measured branching ratio for $\eta \to \gamma\gamma$ from the PDG ($\mathcal{BR}(\eta \to \gamma\gamma) = 0.3931 \pm 0.0020$ [11]), one can make the estimates

$$\mathcal{BR}(\eta \to \mu^+\mu^-) \geq 4.4 \times 10^{-6} \tag{1.16}$$

and

$$\mathcal{BR}(\eta \to e^+e^-) \geq 1.8 \times 10^{-9} . \tag{1.17}$$

Under the assumption that the ratio $|\mathrm{Re}\mathcal{A}|^2/|\mathrm{Im}\mathcal{A}|^2$ is the same for $\eta \to e^+e^-$ and $\eta \to \mu^+\mu^-$, the ratio of their branching fractions is

$$\frac{\mathcal{BR}(\eta \to e^+e^-)}{\mathcal{BR}(\eta \to \mu^+\mu^-)} = \left(\frac{m_e}{m_\mu}\right)^2 \frac{\beta_\mu}{\beta_e} \left[\frac{\ln\left(\frac{1-\beta_e}{1+\beta_e}\right)}{\ln\left(\frac{1-\beta_\mu}{1+\beta_\mu}\right)}\right]^2 , \tag{1.18}$$

where the subscripts e and μ refer to the electron mass m_e, and the muon mass m_μ. The first ratio $(m_e/m_\mu)^2 \approx (1/200)^2 = \mathcal{O}(10^{-5})$ is due to helicity suppression. The second term $\beta_\mu/\beta_e = \mathcal{O}(1)$, and the third part (the squared logarithmic terms) is $\mathcal{O}(10)$. Therefore, Eq. 1.18 is dominated by the helicity suppression term. After inserting the exact values into this equation one obtains

$$\frac{\mathcal{BR}(\eta \to e^+e^-)}{\mathcal{BR}(\eta \to \mu^+\mu^-)} = 4.1 \times 10^{-4} , \tag{1.19}$$

and with the measured value $\mathcal{BR}(\eta \to \mu^+\mu^-) = (5.8 \pm 0.8) \times 10^{-6}$ [11] one obtains $\mathcal{BR}(\eta \to e^+e^-) \approx 2.4 \times 10^{-9}$ as an estimate for the branching ratio of $\eta \to e^+e^-$.

The calculation of the branching ratio is based on the assumption that $|\mathrm{Re}\mathcal{A}|^2/|\mathrm{Im}\mathcal{A}|^2$ is the same for $\eta \to e^+e^-$ and for $\eta \to \mu^+\mu^-$. Any unknown process in the decay of $\eta \to e^+e^-$,

which does not occur in the decay $\eta \to \mu^+\mu^-$, could lead to a larger value for $|\mathrm{Re}\mathcal{A}|^2/|\mathrm{Im}\mathcal{A}|^2$ as compared to $\eta \to \mu^+\mu^-$. And this would lead to a larger branching ratio for $\eta \to e^+e^-$ compared with the value which has been calculated here. For that reason, the decay $\eta \to e^+e^-$ is an excellent probe to search for new physics beyond the SM.

Different models and explanations were already developed which could explain a significant deviation between the "true" branching ratio compared with the value based on conventional theory [26, 27, 28, 29]. One model explains a possible enhancement of the branching ratio by a contribution to the decay amplitude from an intermediate U boson[3] which couples to the quarks and decays into the electron-positron pair. Also discussed are CP-odd Higgs particles as they are proposed in the NMSSM[4] or axions.

In the last years, the search for the decay of a pseudoscalar meson into an electron-positron pair was encouraged again when a discrepancy between the predicted value for $\mathcal{BR}(\pi^0 \to e^+e^-)$ and the measured value was observed. The decay $\pi^0 \to e^+e^-$ is strongly related to the decay $\eta \to e^+e^-$ and has a comparably low branching ratio. Due to the fact that π^0 mesons are often more abundant than η-mesons decays, there were already measurements where a finite value for the branching ratio of $\pi^0 \to e^+e^-$ was determined. The PDG value is $(6.46 \pm 0.33) \times 10^{-8}$ [11]. In 2007, A. E. Dorokhov and M. A. Ivanov calculated $\mathcal{BR}(\pi^0 \to e^+e^-) = (6.2 \pm 0.1) \times 10^{-8}$ based on SM calculations (*cf.* the estimate for the upper limit of the branching ratio for $P \to l^+l^-$ at the beginning of this section) [25], which is in agreement with the PDG value. In the same year, a measurement with the KTeV E799-II experiment at Fermilab found $\mathcal{BR}(\pi^0 \to e^+e^-, x_D > 0.95) = (6.44 \pm 0.25_{\mathrm{stat}} \pm 0.22_{\mathrm{syst}}) \times 10^{-8}$ based on around 794 identified $\pi^0 \to e^+e^-$ decay candidates [30]. Here, $x_D = (m_{e^+e^-}/m_{\pi^0})^2$ is the Dalitz variable. In order to remove the effects of final state radiation, the KTeV collaboration extrapolated the full radiative tail beyond $x_D = 0.95$ and scaled the result back up by the overall radiative correction. In doing so, they obtained $\mathcal{BR}(\pi^0 \to e^+e^-) = (7.49 \pm 0.29_{\mathrm{stat}} \pm 0.25_{\mathrm{syst}}) \times 10^{-8}$. This result is more than three standard deviations larger than the theoretical prediction and also not in agreement with the PDG value. The discrepancy should be investigated more carefully, however, the experimental result could be a sign for new physical processes. For that reason, both the decay $\pi^0 \to e^+e^-$ and the related decay $\eta \to e^+e^-$ enables the search for effects beyond the SM.

1.5.1 Theoretical calculations

The decay $\eta \to e^+e^-$ was studied in several theoretical works. In the following, the results for the branching ratio of $\eta \to e^+e^-$ or the upper limits from different publications will be summarized.

C. Jarlskog and H. Pilkuhn found 4.5×10^{-9} for the lower limit of the relative branching fraction of $\eta \to e^+e^-$ with respect to $\eta \to \gamma\gamma$ [3]. With the measured branching ratio for $\eta \to \gamma\gamma$ (see Table 1.3) one obtains $\mathcal{BR}(\eta \to e^+e^-) > 1.8 \times 10^{-9}$. This calculation was completely based on QED calculations.

G. B. Tupper and M. A. Samuel predicted for the absolute value of the branching ratio $\mathcal{BR}(\eta \to e^+e^-) = 9.1 \times 10^{-9}$. In their calculations they used a once-subtracted dispersion relation for the decay amplitude [31, 32].

[3] U bosons are light spin-1 particles which might also occur in the annihilation of light dark matter particles. The decay of an U boson into electron-positron pairs could be then an explanation of the 511 keV line from the galactic bulge [27, 28].

[4] NMSSM: Next-to-Minimal Supersymmetric Standard Model, supersymmetric extension of the SM

M. J. Savage (et al.) calculated the branching ratio for $\eta \to e^+e^-$ in chiral perturbation theory [33]. They found $\mathcal{BR}(\eta \to e^+e^-) = (5 \pm 1) \times 10^{-9}$.

B. Margolis (et al.) determined $\mathcal{BR}(\eta \to e^+e^-) \approx 6.3 \times 10^{-9}$ by analyzing the electromagnetic amplitude for the decay in the quark model [34]. Different models for the bound state wave function were used, where their results showed that the ratio $\mathcal{BR}(\eta \to e^+e^-)/\mathcal{BR}(\eta \to \gamma\gamma)$ is insensitive to the details of the quark model wave function.

D. G. Dumm and A. Pich found $\mathcal{BR}(\eta \to e^+e^-) = (5.8 \pm 0.2) \times 10^{-9}$ by using chiral perturbation theory techniques and large N_C considerations [35].

A. E. Dorokhov and M. A. Ivanov calculated as a lower bound for the branching fraction $\mathcal{BR}(\eta \to e^+e^-) > (4.33 \pm 0.02) \times 10^{-9}$ [25]. Their calculations included the $(\eta\gamma\gamma^*)$-transition form factor, which was measured by the CLEO collaboration (from Ref. [36]). By including further constraints from operator product expansion (OPE) in QCD, the branching ratio was calculated as $\mathcal{BR}(\eta \to e^+e^-) = (4.60 \pm 0.06) \times 10^{-9}$. In a later publication, A. E. Dorokhov (et al.) aimed to improve the calculations by considering mass corrections to the decay width [37]. This led to $\mathcal{BR}(\eta \to e^+e^-) = 5.24 \times 10^{-9}$.

M. Knecht (et al.) found $\rho_{\eta \to e^+e^-} = (11.5 \pm 0.5) \times 10^{-9}$, which was obtained within the Lowest Meson Dominance (LMD) approximation to large–N_C QCD [38]. This value can be transformed into $\mathcal{BR}(\eta \to e^+e^-) = (4.5 \pm 0.2) \times 10^{-9}$.

T. Petri calculated $\mathcal{BR}(\eta \to e^+e^-) = (4.68 \pm 0.01) \times 10^{-9}$ with a hidden gauge model, and $\mathcal{BR}(\eta \to e^+e^-) = (4.65 \pm 0.01) \times 10^{-9}$ with a modified VMD model [1].

C. C. Lih found for the branching ratio $\mathcal{BR}(\eta \to e^+e^-) = 4.47 \times 10^{-9}$ by using the light-front quark model (LFQM) [5].

1.5.2 Former experimental results

The first search for $\eta \to e^+e^-$ was performed by J. D. Davies (et al.) [39]. They analyzed 1.2×10^4 η events from the reaction $\pi^+n \to p\eta$, which were detected with a heavy-liquid bubble chamber experiment. They found two electron-positron pairs with an invariant mass in the range of the η mass. However, these events were identified as background events from the reaction $\pi^+n \to pe^+e^-$, which is denoted as the inverse electroproduction of the pion. The result of the analysis was an upper limit for the branching ratio of $\mathcal{BR}(\eta \to e^+e^-) < 3 \times 10^{-4}$ at the 90 % CL.

An upper limit of $\mathcal{BR}(\eta \to e^+e^-) < 2 \times 10^{-4}$ at the 90 % CL was published by D. B. White (et al.) [40]. The upper limit for the number of signal events was 9.1 (at the 90 % CL). The measurement was carried out at the Laboratoire National Saturne with the magnetic spectrometer SPES2. The analysis was based on $(2.71 \pm 0.05) \times 10^6$ η-mesons events which were produced in $p\,d \to {}^3\mathrm{He}\,\eta$ reactions.

The CLEO collaboration searched for the decay in $e^+e^- \to$ *hadrons* reactions, which were produced at the Cornell Electron Storage Ring (CESR). They did not observe any event candidate for the signal and set an upper limit for the branching ratio of $\mathcal{BR}(\eta \to e^+e^-) < 7.7 \times 10^{-5}$ at the 90 % CL [24].

The WASA/CELSIUS collaboration extracted an upper bound for the branching ratio of $\mathcal{BR}(\eta \to e^+e^-) < 2.7 \times 10^{-5}$ at the 90 % CL [22]. The data set comprised of 3×10^5 η events from $p\,d \to {}^3\mathrm{He}\,\eta$ reactions.

The most recent result for the upper limit comes from the HADES collaboration. It was published in the course of this PhD work. From the study of inclusive dielectron spectra in pp-collisions at $T_p = 3.5\,\mathrm{GeV}$, they determined the value $\mathcal{BR}(\eta \to e^+e^-) < 4.9^{+0.7}_{-1.2} \times 10^{-6}$ [41].

1.5.3 Summary of the previous works on $\eta \to e^+e^-$

Figure 1.7 summarizes both the theoretical and the experimental results for the branching ratio of the channel $\eta \to e^+e^-$.

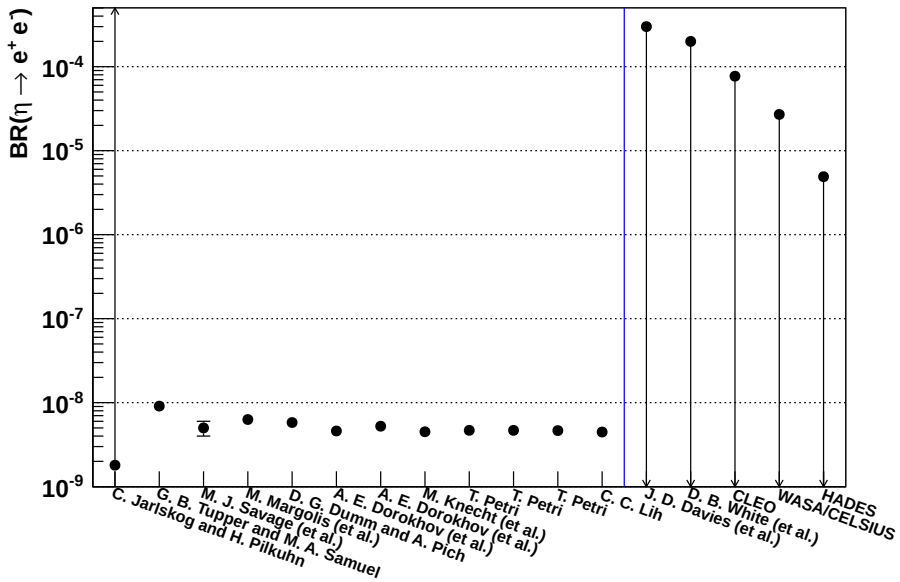

Figure 1.7: Summary of the calculated and measured values, respectively the upper limits, for the branching ratio of $\eta \to e^+e^-$. The blue solid line separates the calculated values on the left from the experimental values on the right. The experimental upper limits are given at the 90 % CL. On the theory and the experimental sides, the results are ordered by their years of publication.

The theoretical predictions for the branching fraction vary in the range between 4.47×10^{-9} and 9.1×10^{-9}. The expected lower limit for the branching ratio is 1.8×10^{-9}. On the experimental side, the upper limits for the branching ratio were reduced over the years. However, there is still a gap of three orders of magnitude between the experimental upper limits and theoretical predictions. This thesis aims to reduce this gap with a new measurement.

Chapter 2

Experimental Setup

2.1 Cooler Synchrotron COSY–Jülich

The Cooler Synchrotron COSY–Jülich is a synchrotron and storage ring which is run by the Institut für Kernphysik (IKP) of the Forschungszentrum Jülich in Germany. It consists of several ion sources, the injector cyclotron (JULIC: JUelich Isochronous Cyclotron), the injection and extraction beam lines, and the COSY-ring itself [42, 43]. A schematic top view of the complete setup can be seen in Fig. 2.1.

The COSY ring has a shape of a race track with a circumference of 184 m. It comprises of two parallel 40 m long straight sectors and two arc sections, where each arc is 52 m long. In the arc sections, the particles are redirected 180°. 24 dipole magnets keep the beam on the desired orbit. 54 quadrupole magnets are used for the transversal focusing and defocusing of the beam. Aberration effects are compensated by 18 sextupole magnets.

COSY provides both polarized and unpolarized beams of protons or deuterons. The pre-acceleration of the H^- or D^- ions takes place in the injector cyclotron JULIC, where the H^- are accelerated to energies up to 45 MeV (corresponding to a momentum of 0.29 GeV/c) and the D^- to 75 MeV (corresponding to a momentum of 0.54 GeV/c) [45]. After the pre-acceleration, the negatively charged ions are shot onto a carbon foil where they lose their electrons. Finally, the positively charged ions reach the COSY ring where they are accelerated further.

The usable beam momentum range of COSY lies between 0.295 and 3.7 GeV/c [45]. The maximum center of mass energy allows the production of hadrons up to the mass of the ϕ meson in pp-interactions.

COSY is equipped with two beam-cooling methods: electron cooling and stochastic cooling. At injection energies and momenta up to approximately 600 MeV/c electron cooling is used. For higher energies (momenta > 1.5 GeV/c) stochastic cooling is used to reduce the phase space volume of the beam. The momentum spread can be reduced by the cooling modes to values better than $\Delta p/p \lesssim 10^{-4}$. Without cooling, the momentum spread would be $\Delta p/p \approx 10^{-3}$. The maximum number of particles in the beam is around 10^{11} for unpolarized proton or deuteron nuclei. The intensity for polarized beams is about one order of magnitude smaller. With the pellet target system of WASA this leads to typical luminosities of 10^{31} to $10^{32}\,\mathrm{cm}^{-2}\mathrm{s}^{-1}$. COSY is also equipped with a barrier bucket cavity for the acceleration and to compensate the mean energy loss in beam target interactions. This is especially important for WASA due to the large target densities of around $10^{15}\,\mathrm{atoms/cm}^2$ (*cf.* Sect. 2.2.1), where

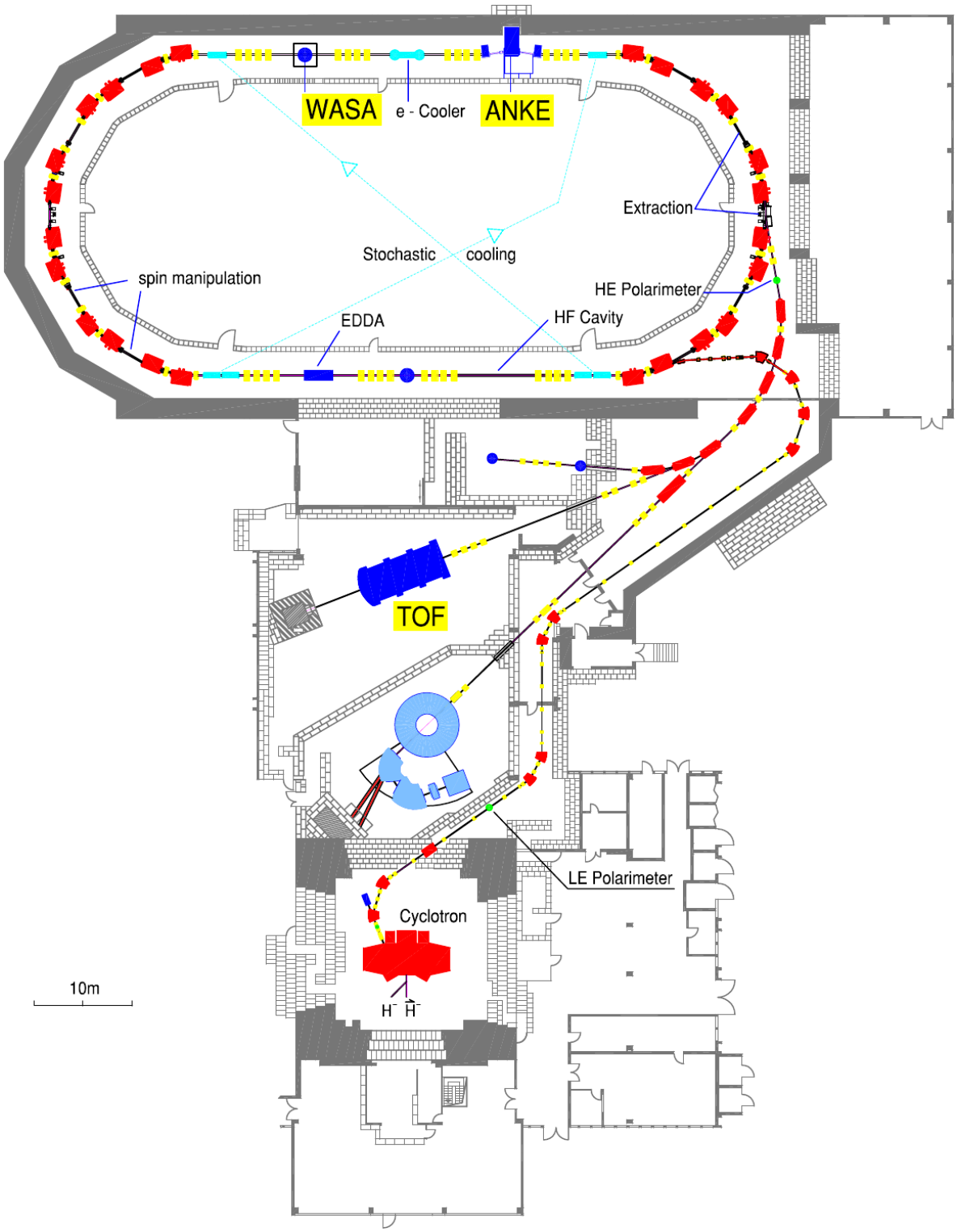

Figure 2.1: Schematic top view of the Cooler Synchrotron COSY–Jülich [44]. The ions are pre-accelerated with the injector cyclotron JULIC. After the pre-acceleration, the beam is directed via the transfer beam line and is brought into the COSY ring via stripping injection.

the energy loss can not be compensated by the beam cooling. Typical beam lifetimes in the order of a few minutes can be achieved [46].

There are both internal and external experiments being operated at COSY. At present, the internal experiments are the nearly 4π detector "Wide Angle Shower Apparatus" (WASA), the magnetic spectrometer "Apparatus for Studies of Nucleon and KaonEjectiles" (ANKE), and "Polarized Antiproton EXperiments" (PAX). These internal experiments are situated at the straight segments of the ring. The external experiment is the flight-time spectrometer "Time of Flight" (COSY–TOF). Additionally, test measurements are carried out at COSY to develop a facility for measurements of electric dipole moments (EDM) and for the High Energy Storage Ring (HESR), which is a part of the Facility for Antiproton and Ion Research (FAIR) project at the GSI Helmholtzzentrum für Schwerionenforschung [47].

2.2 Wide Angle Shower Apparatus

This section describes the Wide Angle Shower Apparatus (WASA) as it is installed in the COSY ring. Figure 2.2 shows a schematic side view of the detector. The forward part is described in Sect. 2.2.2, and the central part is described in Sect. 2.2.3. The pellet target is described in Sect. 2.2.1. The pictures which are shown within this section and the information which is given here are taken from Refs. [46, 48] and the common data pool of the WASA collaboration. More detailed information can be found in these references.

The detector was designed to study the production and the decays of light mesons [48]. It is able to measure both neutral and charged particles with a geometrical acceptance which is close to the full solid angle of 4π. WASA was built with the following design requests:

- large acceptance, close to 4π solid angle
- handling of high particle fluxes, at luminosities up to $10^{32}\,\mathrm{cm}^{-2}\mathrm{s}^{-1}$
- identification and measurement of neutral particles
- identification and measurement of charged particles
- minimum amount of structural material of the beam pipe and inside the detector to reduce the disturbances of particles and the probability for external photon-conversion

Originally, the detector was operated at the CELSIUS storage ring in Uppsala, Sweden (CELSIUS: Cooling with ELectrons and Storing of Ions from the Uppsala Synchrocyclotron) [49]. In 2005, the operation of CELSIUS stopped and WASA was moved to COSY, where in 2006 a commissioning beam time was carried out. From 2006 until the summer shutdown in 2012, WASA took data for 61 weeks[1].

2.2.1 Pellet target

The pellet-target system provides a stream of frozen hydrogen or deuterium droplets, which are called pellets. The size of such a droplet is typically $20 - 35\,\mu\mathrm{m}$ with an effective density of around $10^{15}\mathrm{atoms/cm}^2$, taking into account the overlap factor with the beam. With such a

[1]The duration of the individual beam times and their goals are documented in the Annual Reports of the Institut für Kernphysik and can be found on the website of the institute `http://www.fz-juelich.de/ikp`.

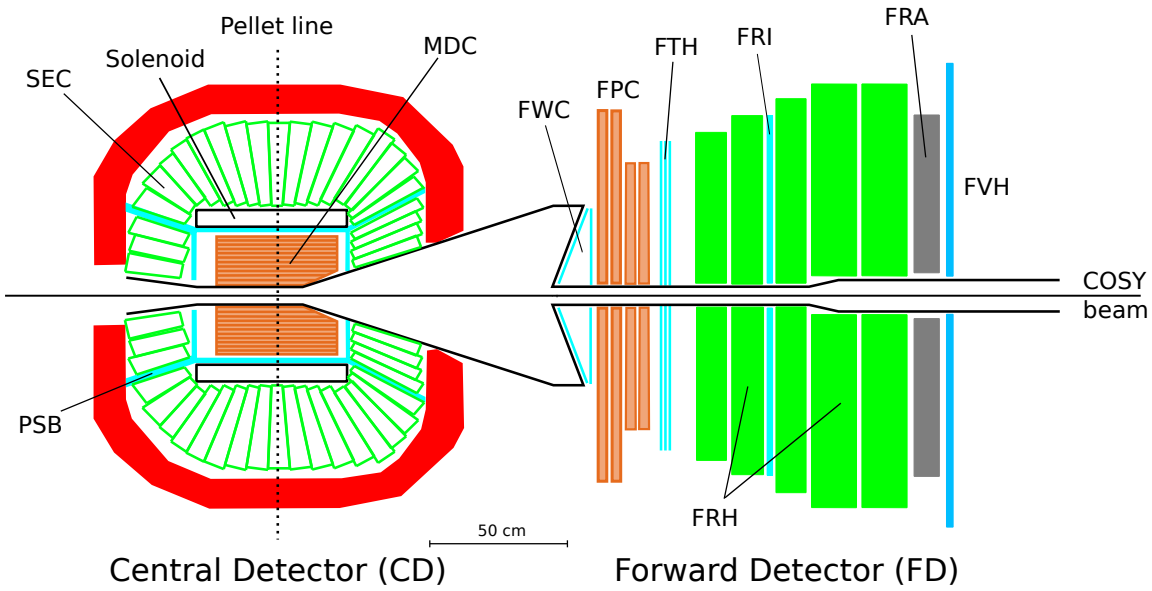

Figure 2.2: Schematic side view of the Wide Angle Shower Apparatus (WASA) as it is installed at COSY [44]. It consists of the Forward Detector (FD), where the forward scattered hadrons are measured, and the Central Detector (CD), where the meson decay products are measured. The FD consists of the Forward Window Counter (FWC), the Forward Proportional Chamber (FPC), the Forward Trigger Hodoscope (FTH), the Forward Range Hodoscope (FRH), the Forward Range Intermediate (FRI), the Forward Veto Hodoscope (FVH), and the Forward Range Absorber (FRA). The CD consists of the Mini Drift Chamber (MDC), the Plastic Scintillator Barrel (PSB), the Scintillator Electromagnetic Calorimeter (SEC), a solenoid and the pellet beam tube. The beam enters the detector from the left side.

large density high luminosities are reached at COSY, which are essential for the measurement of rare decays. The pellet stream has a spread of 2 – 3 mm at the interaction point. This small spread is important in order to have a well-defined vertex. Moreover, it reduces the probability for the occurrence of a secondary interaction.

The pellet-target system consists of the pellet generator, pumps, the pellet beam tube, and the pellet beam dump (*cf.* Fig. 2.3). To guarantee the close to 4π geometrical acceptance of WASA, most of the pellet generation system is located outside of the detector on top of the CD.

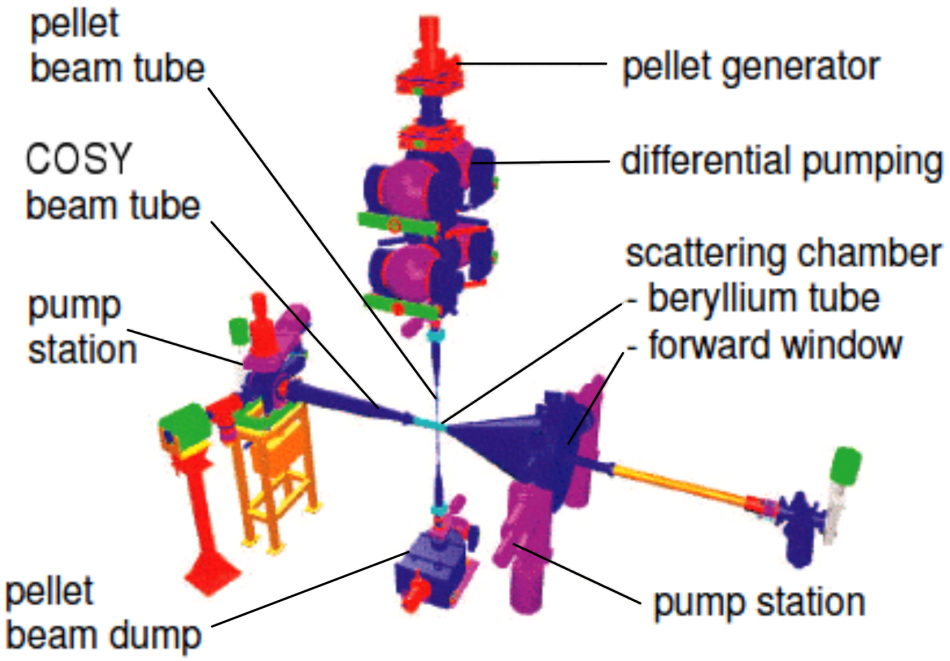

Figure 2.3: Sketch of the pellet target system with the pellet generator, pumps, the pellet beam tube, and the pellet dump [44].

In the pellet generator, a cold head liquifies the hydrogen or deuterium gas which is then pressed with 400 – 800 mbar through a thin glass nozzle (around 12 µm diameter). The nozzle vibrates with a frequency of around 50 – 80 kHz and divides the stream of liquid gas into a stream of equidistant droplets with the same size. The droplets reach the droplet chamber where the pressure and the temperature are close to the triple point of the target material (typical conditions in droplet chamber for hydrogen: 14 K, 20 mbar, deuterium: 17 K, 60 mbar). Afterwards, the droplets pass the vacuum injection capillary, where the pressure is $\sim 10^{-3}$ mbar. There, the droplets further cool by means of evaporation and freeze to solid spheres, called pellets. Before the pellets reach the pellet beam tube, they have to pass a skimmer, which separates the vacuum injection chamber from the scattering chamber. The skimmer reduces the divergence of the pellet stream and leads to a collimated beam of pellets. A well defined beam-target interaction point is important for the track reconstruction of the charged particles in the FD and the neutral particles measured in the CD, since the track reconstruction assumes for all these tracks the same vertex. Differences between the true vertex and the assumed one would lead to wrongly reconstructed angles.

The pellets reach the scattering chamber (pressure $\sim 10^{-6}$ mbar) with a frequency of

around 8 – 15 kHz. Typical droplet velocities are around 60 m/s. After the pellets have reached the interaction area, they arrive at the pellet beam dump where turbo pumps remove the gas of the evaporating pellets. This is important in order to avoid reactions between the gas and the beam which would happen outside the main interaction vertex.

The pellet flux through the COSY beam tube is switched on and off by shutters. A more detailed explanation of the pellet target system can be found in Refs. [50, 51].

2.2.2 Forward Detector

The Forward Detector (FD) of WASA is used to measure and identify the scattered projectiles and charged recoil particles. It covers a scattering angle range from 3° to 18° and has a full acceptance in the azimuthal angle. The different sub-detectors will be presented in the following.

Forward Window Counter

The Forward Window Counter (FWC) is mounted immediately behind the exit window of the vacuum chamber. Figure 2.4 shows a schematic view of the FWC.

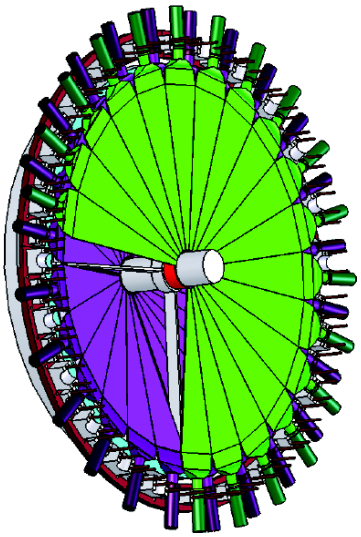

Figure 2.4: Schematic view of the Forward Window Counter (FWC) [44]. The green elements show the second layer. Some elements are here removed to show the first layer, whose elements are marked in blue.

This sub-detector consists of two planes, where each layer is made of 24 *BC408* plastic scintillators with a thickness of 3 mm. The first layer has a conical shape and the individual elements are tilted by 20° with respect to the vertical plane. This brings the FWC closer to the exit window of the vacuum chamber. The second layer is planar. To have an effective granularity of 48 elements, the layers of the two planes are rotated by half an element with respect to the elements of the other layer. Every single element is read out by an *XP3112* photomultiplier tube.

As it will be described later in Sect. 4.4, the FWC information is used in the trigger. Additionally, the energy deposit in the FWC together with the total energy deposit of a

particle in the FD can be used for particle identification ($\Delta E - E$ method). A more detailed description of the FWC can be found in Ref. [52], and an explanation about the functional principle of a plastic scintillator is given in the Sect. 2.2.3, where the Plastic Scintillator Barrel is described.

Forward Proportional Chamber

The Forward Proportional Chamber (FPC) is a straw tube tracker which is placed behind the FWC as being viewed along the beam direction. Figure 2.5 shows two schematic illustrations of the FPC.

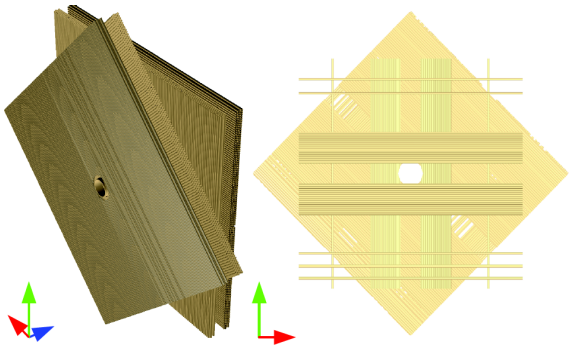

Figure 2.5: Schematic view of the structure of the Forward Proportional Chamber (FPC) [44]. Left: Three dimensional view. Right: Top view. To show the structure some straws are removed in this drawing.

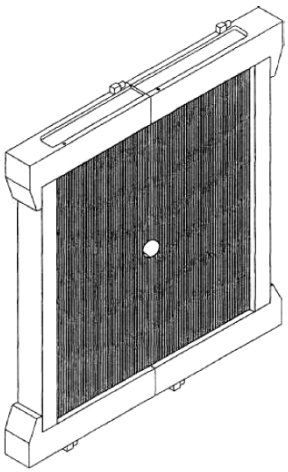

Figure 2.6: Schematic view of one module of the Forward Proportional Chamber (FPC) [44].

The FPC is used to reconstruct the coordinates and the angles of the trajectories of charged particles. It consists of four modules, where each module is built of four staggered layers. One module is shown in Fig. 2.6. Each layer consists of 122 proportional drift tubes, where the layers are shifted by one tube radius with respect to the previous layer.

The first module in beam direction is rotated by $+45°$ and the second module is rotated by $-45°$ with respect to the x-axis. The other two modules are aligned along the x- and y-axis (the coordinate system is described in Sect. 2.2.5). By combining the measured coordinates of the four modules, one obtains two points of the trajectory of a particle.

The cylindrical straws each have a diameter of 8 mm and are made of 26 µm thick aluminum-coated Mylar. The anode wire is made of 20 µm stainless steel which is stretched with a tension of 40 g. A mixture of 80 % argon (Ar) and 20 % ethane (C_2H_6) is used as drift gas. A more detailed description of straw tracking detectors is given in the Sect. 2.2.3, where the Mini Drift Chamber is described.

Forward Trigger Hodoscope

The Forward Trigger Hodoscope (FTH) consists of three layers of *BC408* plastic scintillators with a thickness of 5 mm. It is located behind the FPC as being viewed along the beam direction. The first layer of the FTH consists of 48 radial elements, whereas the other two layers consist in each case of 24 elements with a shape of an Archimedian spiral. The direction of rotation of the Archimedian spirals is counterclockwise in the second layer, while it is clockwise in the third layer. The geometry of the three layers is shown in Fig. 2.7.

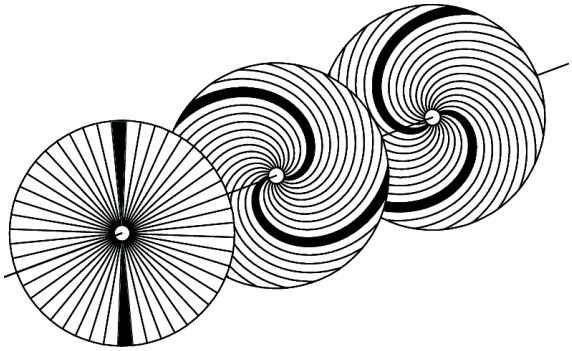

Figure 2.7: Schematic view of the Forward Trigger Hodoscope (FTH) [44]. The first layer consists of radial elements, the other two layers consist of Archimedian spiral shaped elements with opposite orientation.

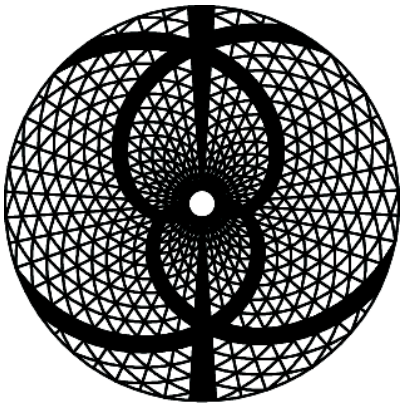

Figure 2.8: Resulting pixel structure of all three layers of the FTH [44].

Each element is read out by an *EMI/THORN 9954B* photomultiplier tube. The geometry of the three layers results in a pixel structure, which provides the hit multiplicity, azimuthal, and polar angles on the trigger level. The resulting pixel structure of the three FTH layers can be seen in Fig. 2.8. Additionally, the energy deposit in the FTH can be used together with the total energy deposit of a particle, like in case of the FWC, for particle identification ($\Delta E - E$ method).

Forward Range Hodoscope

The Forward Range Hodoscope (FRH) is installed behind the FTH. It consists of five layers of *BC400* plastic scintillators, as seen in Fig. 2.9. The first three layers have a thickness of 11 cm, while the last two layers have a thickness of 15 cm. The diameter of the layers range from 120 cm (first layer of the FRH) to 180 cm (fourth and fifth layer).

Each layer consists of 24 radial elements, which are read out individually by *XP2412* photomultiplier tubes. The energy deposit in the FRH and in the FWC or in the FTH is used for particle identification using the ΔE - E method. The particles deposit a small amount of their energy in the FWC or in the FTH (ΔE), while the rest of their energy E is deposited in the FRH. The energy deposit in the FRH is also used to determine the kinetic energy of the ^{3}He nuclei from the reaction $p\,d \rightarrow {}^3\mathrm{He}\,\eta$. This will be discussed in Sect. 3.3.1, where the reconstruction of the tracks in the FD is explained.

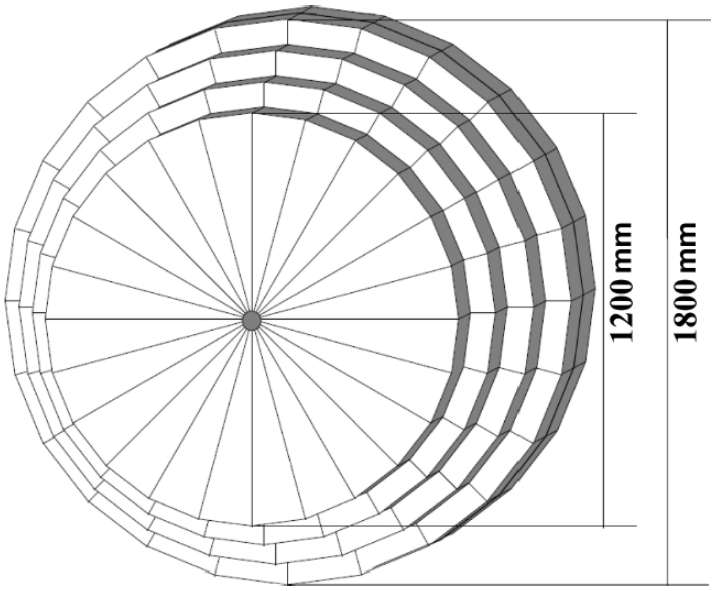

Figure 2.9: Schematic view of the Forward Range Hodoscope (FRH) [44]. Each of the five layers consists of 24 radial plastic-scintillator elements.

Forward Range Intermediate hodoscope

Between the second and the third layer of the FRH there is the Forward Range Intermediate hodoscope (FRI). A schematic view of this detector is showing Fig. 2.10.

It consists of two layers, where each layer comprises 32 rectangular plastic scintillator bars with a thickness of 5.2 cm. In the first layer, the bars are oriented horizontally and in the second vertically. Close to the beam pipe the bars have a width of 3 cm to account for the higher count rates at small scattering angles. In the outer region the bars have a width of 6 cm and a maximum length of 140.5 cm. In order to provide space for the beam pipe, the inner bars are split.

The FRI gives the opportunity to have a two-dimensional Cartesian position sensitivity within the FRH, which additionally helps to reconstruct the vertex position of the forward scattered particles. More information about the FRI can be found in Ref. [53].

Forward Veto Hodoscope

In the beam direction the last active detector component is the Forward Veto Hodoscope (FVH). A schematic illustration is given in Fig. 2.11.

The FVH consists of 12 horizontal plastic scintillator bars with a thickness of 2 cm and a width of 13.7 cm. Each bar is connected on both sides to an *XP2020* photomultiplier tube. The location where the particle hits the bar can be reconstructed by using the time difference of the signals. The FVH information can be used in the trigger to select or reject events with particles which traverse the entire FRH (and if it is installed also the Forward Range Absorber, see below).

Since fall 2008, there is a second FVH layer which is positioned in front of the first COSY quadrupole behind the FD. This layer will be used as a stop detector for Time-Of-Flight measurements which will improve the energy resolution and therefore the missing mass

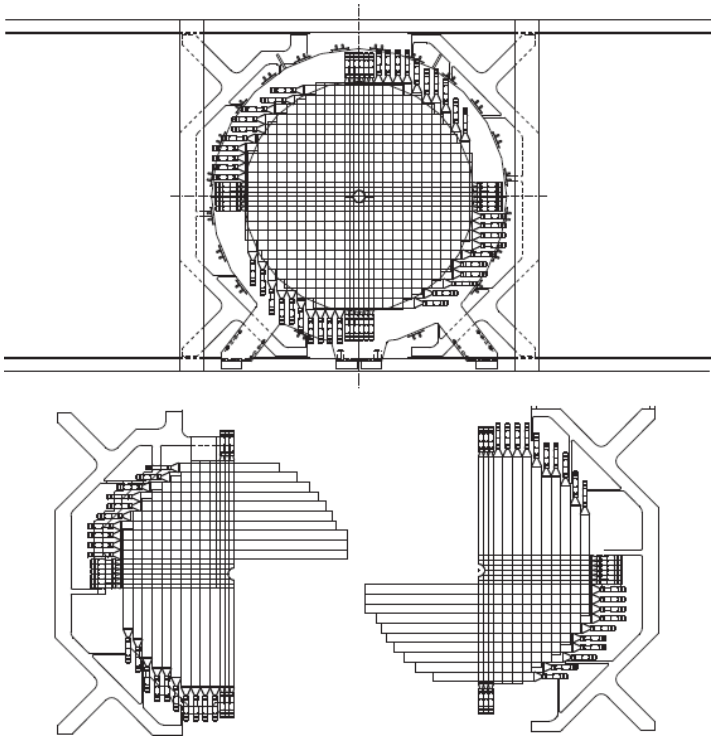

Figure 2.10: Schematic view of the Forward Range Intermediate hodoscope (FRI) [44]. Upper part: Front view of the complete hodoscope. Lower part: Two planes with orthogonally oriented scintillator bars.

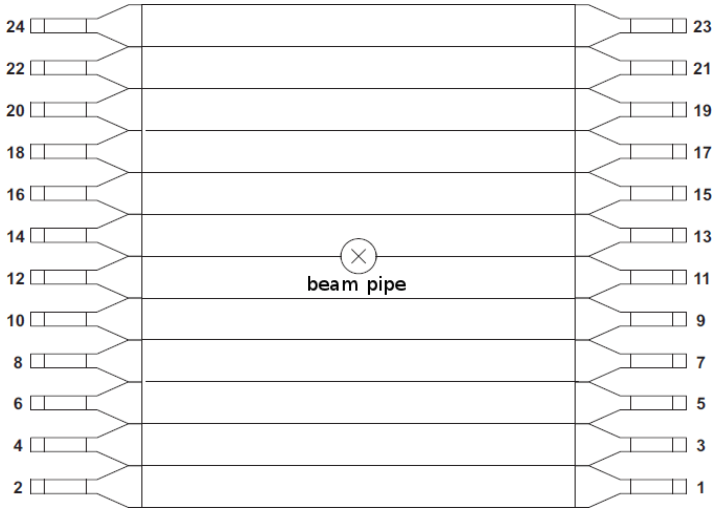

Figure 2.11: Schematic view of the Forward Veto Hodoscope (FVH) [44]. It consists of 12 horizontal plastic scintillator bars which are connected to photomultiplier tubes on both sides.

resolution (*cf.* Sect. 4.2) of particles which are scattered in forward direction [54].

Forward Range Absorber

The Forward Range Absorber (FRA) can be placed between the FRH and the FVH. It is a passive absorber made of 5 mm thick iron plates. By installing several plates behind each other, a maximum absorber thickness of 100 mm can be achieved. The FRA can be used to stop the slow protons from $pp \to pp\eta$ reactions at a beam energy of approximately 1.36 GeV. Higher energetic protons from elastic scattering reactions and from reactions with direct-pion production traverse the FRA and can be detected with the FVH. In doing so, those events can be easily identified and effectively suppressed on the trigger level.

2.2.3 Central Detector

The Central Detector (CD) is built around the interaction point and is used to measure the decay products of the produced mesons. The CD has an angular acceptance for scattering angles which lies in the range between 20° and 169°, and it has a full acceptance in the azimuthal angle. The different components will be explained in the following.

Beam pipe

In the central part of WASA the beam pipe has a radius of 30 mm and a wall thickness of 1.2 mm. In its center it is crossed perpendicularly by the pellet target tube. The beam pipe is made out of beryllium (Be) which keeps the probability for photon conversion very small. Within the Coulomb field of a nucleus a photon with an energy $E_\gamma \geq 2m_e c^2$ can produce an electron-positron pair. Here, E_γ is the energy of the photon, m_e is the electron mass, and c is the vacuum speed of light. The cross section of the pair production process is

$$\sigma \propto Z^2 E_\gamma \tag{2.1}$$

where Z is the atomic number [55]. Since for beryllium the atomic number is only $Z = 4$, the cross section for pair production is quite small. This is important, especially for WASA, since the search for decays with electron-positron pairs in the final state is one of the main objectives.

Mini Drift Chamber

The Mini Drift Chamber (MDC) is the innermost sub-detector of the central part of WASA. It is located around the beam pipe and is used for momentum measurements of charged particles. A photo of the MDC is shown in Fig. 2.12. It has the shape of a cylindrical chamber, which is built into a cylindrical aluminum-beryllium (Al-Be) cover with a thickness of 1 mm.

In total, the MDC consists of 1783 drift tubes (also named as straws). Each straw is made of a 25 µm thick Mylar foil, where the inner side is coated with a 0.1 µm thick aluminum film. The sensing wires are made of gold-plated tungsten. They have a diameter of 20 µm and are stretched with a tension of 40 g. The precision of the alignment of the wires is ±20 µm [56]. Each wire serves as the anode, whereas the aluminized mylar pipes are used as the corresponding cathodes. A high voltage produces a cylindrically symmetric electric field with $E \propto 1/r$, where r is the distance from the wire. If a particle passes through a straw it

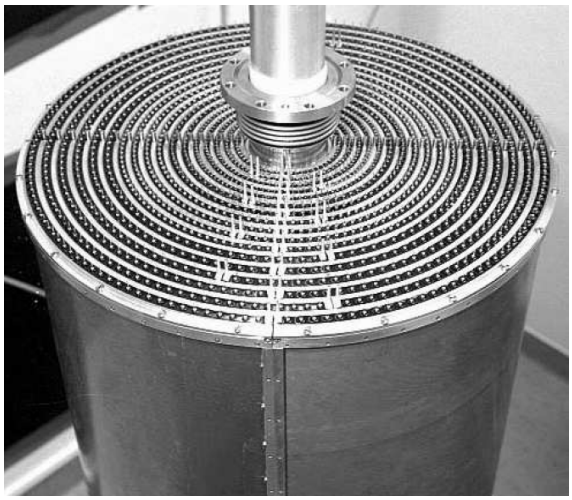

Figure 2.12: Fully assembled Mini Drift Chamber (MDC) inside the Al-Be cylinder [44].

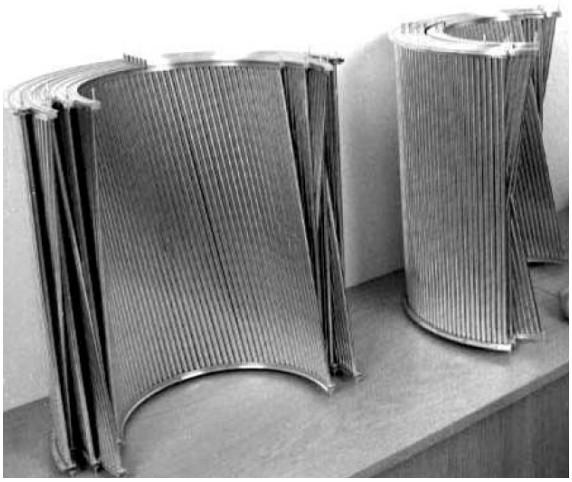

Figure 2.13: Two halves of the MDC. The MDC consists of alternating layers of parallel and skewed tubes with respect to the beam axis [44].

ionizes the filling gas. The free electrons are accelerated towards the sensing wire whereby they are able to ionize other atoms. Therefore, an avalanche of electrons arises which drifts to the anode where it can be detected as an electrical signal.

The drift tubes are disposed in 17 cylindrical layers. The five innermost layers consist of straws with a diameter of 4 mm, the following six layers with 6 mm, and the remaining six layers with 8 mm. The first layer has a radius of 41 mm, while the last layer has a radius of 203 mm. In order to avoid a mechanical deformation, there are small gaps between the adjacent straws. The drift tubes of every layer are attached on both sides to Al-Be end plates which have a thickness of 5 mm.

To get the three-dimensional information about the trajectory of a particle, the MDC consists of alternating layers of parallel and skewed tubes. This can be seen in Fig. 2.13, where the two halves of the MDC are shown. Nine layers consist of straws which are parallel to the beam axis. The other eight layers consist of tubes which are tilted by an angle in the range between 6° and 9° with respect to the beam axis.

Because of the design of the scattering chamber (*cf.* Fig. 2.2), the drift tubes of the five central layers have distinct lengths. Due to the alignment and the sizes of the straws, particles with scattering angles in the range between 24° and 159° can be measured with the MDC.

When the MDC is in operation, the straws are permanently flushed with a drift-gas mixture consisting of 80 % argon (Ar) and 20 % ethane (C_2H_6). Argon is used because of its small electron affinity, while ethane serves as a quenching gas. This is needed to absorb the photons which can be produced in the processes of excitation or dissociation of the ethane molecules. Without this absorption, the photons could also ionize other argon atoms which then would lead to an ongoing avalanche [12]. After a beam time, the MDC is further flushed solely with argon to remove the organic components which would otherwise deposit in the tubes.

Further information about the MDC is given in Ref. [56].

Plastic Scintillator Barrel

The Plastic Scintillator Barrel (PSB) surrounds the MDC and is installed inside the superconducting solenoid and the electromagnetic calorimeter. If a particle propagates through the scintillating material, it excites the atoms and molecular states. When a molecule falls back into its ground state it emits detectable light. Due to the small atomic number of the detector material, there is nearly no detection probability for photons [12]. For that reason, the fast PSB signals from charged particles can be used for the trigger logic. It also gives the timing information of the charged particles and can be used for particle identification, where the energy deposit in the PSB together with the momentum information from the MDC ($\Delta E - p$ method) and the energy deposit in the SEC ($\Delta E - E$ method) enables to separate electrons (positrons) from pions.

The PSB consists of a cylindrical part (central part: PSC) and two end caps (forward part named PSF, backward part named PSB, respectively) which can be seen in Fig. 2.14.

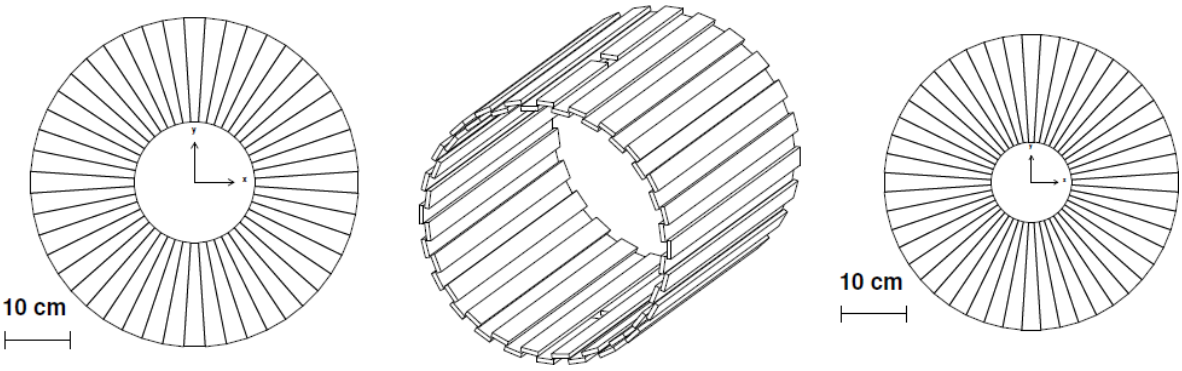

Figure 2.14: Three parts of the Plastic Scintillator Barrel (PSB): Forward part (PSF), central part (PSC), and backward part (PSB) [44].

In total, the PSB consists of 146 *BC408* plastic scintillator elements with a thickness of 8 mm. The central part consists of 50 elements with a length of 550 mm and a width of 38 mm. In order to have a high acceptance for particles, the elements have a small overlap of 6 mm with the neighboring strips (see Fig. 2.14 (center)). Each scintillator element is connected to a photomultiplier tube. The photomultiplier tubes are located outside the iron yoke in order to be shielded from the magnetic field which would disturb their functionality. The photomultipliers are connected to the scintillators via 50 cm long light guides.

The forward and backward cap of the PSB consist in each case of 48 radial elements. The forward cap of the PSB has a diameter of 42 cm, while the backward cap has a diameter of 51 cm. The radial elements of the backward cap are arranged in the way that they form a conical surface. The two end caps have a hole in their center for the beam pipe. In case of the forward part, the hole has a diameter of 19 cm, while the hole in the backward part has a diameter of 12 cm. In the central part of the PSB there are two split elements for the pellet tube.

More information about the PSB can be found in Refs. [56, 57].

Superconducting Solenoid

The Superconducting Solenoid (SCS) produces an axial magnetic field inside the MDC. This is mandatory for the momentum reconstruction and the determination of the charge sign of the particles. The SCS encloses the MDC and the PSB and protects the outer electromagnetic calorimeter from low-energy delta electrons originating from beam-target interactions. To obtain precise energy measurements with the calorimeter, the extension of the SCS plus its cryostat is quite small. The inner radius of the superconducting coil is 267.8 mm, while the outer radius is 288.8 mm. The magnetic return yoke has a weight of 5 t and is made of soft iron. Besides its function to close the magnetic flux, it shields the sensitive readout electronics and photomultipliers from the inner magnetic field. Additionally, the yoke is used as the support structure for the crystals of the electromagnetic calorimeter.

The solenoid is cooled with liquid helium with a temperature of 4.5 K. The maximum achievable magnetic field is 1.3 T. The magnetic field inside the iron yoke was measured with Hall probes and also simulated as illustrated in Fig. 2.15, where the density distribution of the magnetic flux is shown for a current of 667 A.

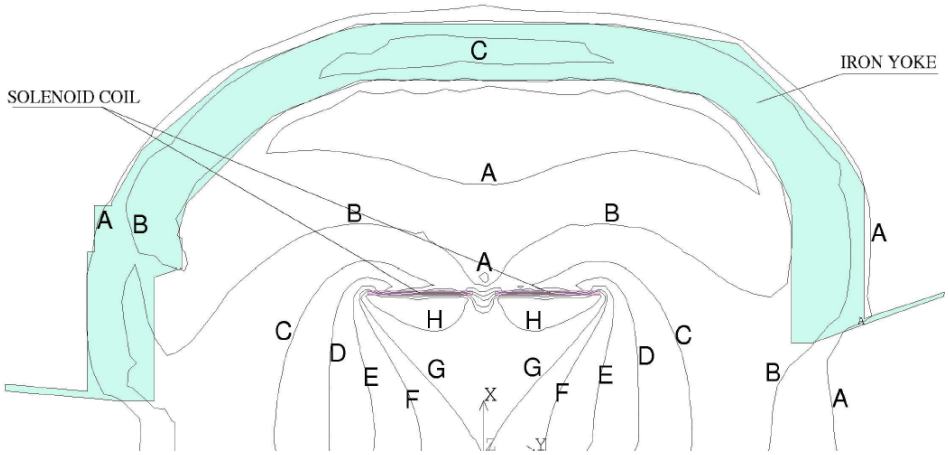

Figure 2.15: Magnetic flux density distribution for a coil current of 667 A [44, 58]. Contour maxima are indicated by lines with the labels A – H, where A = 0.10 T, B = 0.25 T, C = 0.50 T, E = 1.00 T, F = 1.20 T, G = 1.30 T, A = 1.50 T.

More information about the SCS is given in Ref. [58].

Scintillator Electromagnetic Calorimeter

The Scintillator Electromagnetic Calorimeter (SEC) surrounds the SCS. It consists of 1012 scintillating crystals which are attached to the iron yoke. The crystals are arranged in 24 rings which cover scattering angles between 20° and 169°. A schematic view of the SEC is given in Fig. 2.16.

Each crystal is connected via a plastic light guide to a photomultiplier tube, which is installed outside the iron yoke. Figure 2.17 shows a fully equipped calorimeter module.

With the SEC, the energy of charged and neutral particles can be measured. In case of charged particles the energy deposit together with the momentum information from the MDC is used to distinguish between electrons (positrons) and pions ($p - E$ method).

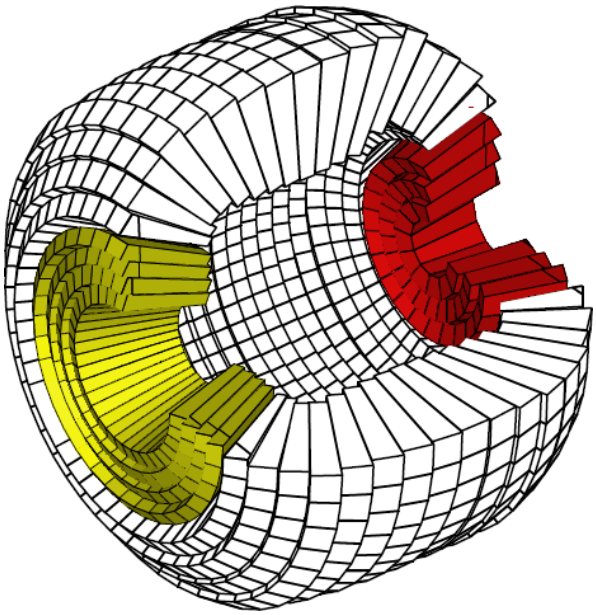

Figure 2.16: Schematic view of the Scintillator Electromagnetic Calorimeter (SEC) [44]. Some of the crystals in the foreground are removed to make the interior of the SEC visible. The forward part of the SEC is colored in yellow and the backward part of the SEC is colored in red.

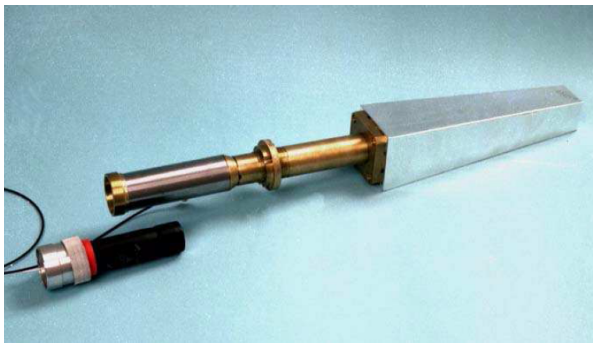

Figure 2.17: Fully equipped calorimeter module which consists of a CsI(Na) crystal, a light guide, a photomultiplier tube, and its housing [44].

The energy deposit of a particle within the SEC is measured via its produced amount of scintillation light. If a MeV-photon or an electron (positron) passes through a crystal, an electromagnetic shower occurs which is dominated by pair production

$$\gamma + {}^{A}_{Z}\mathrm{X} \rightarrow {}^{A}_{Z}\mathrm{X} + e^{+} + e^{-}$$

and Bremsstrahlung processes

$$e + {}^{A}_{Z}\mathrm{X} \rightarrow {}^{A}_{Z}\mathrm{X} + e + \gamma \; .$$

The arising shower particles produce scintillation light which is detected by the photomultipliers.

The energy of charged pions can be also measured with the SEC. These particles lose their energy in the crystals by means of excitation and ionization of the atoms. A stopped π^- is absorbed by a nucleus and the reaction products are detected, while a stopped π^+ decays mainly via $\pi^+ \rightarrow \mu^+\nu_\mu$. The e^+ which arises in the decay of the μ^+ produces a delayed electromagnetic shower.

The SEC crystals are made of sodium doped cesium iodide (CsI(Na)) which has mainly three advantages [59]:

- large light yield
- short radiation length
- good mechanical properties

Compared with the more commonly used thallium doped cesium iodide crystals (CsI(Tl)), the CsI(Na) crystals have the following advantages ([60, 61] as cited in [49]):

- the emission peak matches well with the used photocathodes resulting in good photon statistics and a sufficiently fast response
- a shorter scintillation decay time which is important for the high luminosities which are reachable at WASA
- less afterglow
- high resistance against radiation damage

In Ref. [59] the SEC is described in more detail, while a study of the characteristics of the CsI(Na) crystals can be found in Ref. [62].

2.2.4 Light pulser monitoring system

The light pulser system monitors the gain stability of the photomultiplier tubes. Two types of light sources are used to produce reference signals. For the fast organic plastic scintillators four LED-based sources are installed, whereas for the slow CsI(Na) crystals of the electromagnetic calorimeter a xenon flash lamp is used. The stability of the light pulser signals is monitored by Hamamatsu Silicon Pin Photodiodes. The light pulser monitoring system for WASA is described in detail in Ref. [63].

2.2.5 Reference frame

Each point of the WASA detector can be described by the three Cartesian coordinates x, y, z or alternatively by the spherical coordinates r, ϕ, θ. The origin of the coordinate system is at the interaction point. The positive z-axis points along the axis of the COSY beam. The positive y-axis points upwards along the pellet beam tube. The x-axis of the right-handed coordinate system points in the horizontal plane out of the COSY ring. The transformation of the Cartesian coordinates into the spherical coordinates is achieved according to the usual convention (see for example Ref. [64]): r is the radius, ϕ is the azimuth angle, and θ is the polar angle (also named as scattering angle).

2.3 Data Acquisition System

The Data Acquisition System (DAQ) comprises electronic devices, which digitize and store the detector signals. The WASA DAQ is especially designed to handle the huge amount of data which occurs during the experiments with high luminosities, and is based on the third generation of DAQ at COSY [65, 66]. The structure of the DAQ is shown in Fig. 2.18.

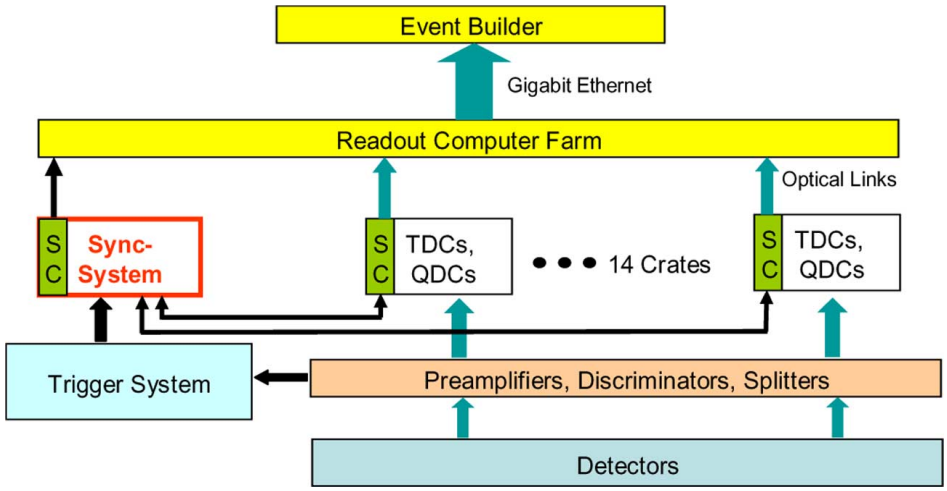

Figure 2.18: Structure of the Data Acquisition System (DAQ) system of WASA [66].

The signals from different sub-detectors are sent to the front-end electronics (preamplifier, splitters, discriminators), which are connected to the digitizing modules in the crates. The digitizing modules are based on a proprietary optimized parallel bus with LVDS[2] technology. Each of the 14 crates is connected to a PC of the readout farm via an high-speed optical link.

The synchronization system is used to control the data flow. If a trigger signal arrives, the digitized signals, which are stored in buffers, are readout. An event builder collects the data streams and writes the data to disk (RAID system[3]). The event and buffer management is FPGA-controlled[4]. The decoding of the cluster format into events is later done with the offline analysis software RootSorter, which will be described in the next chapter (*cf.* Sect. 3.3).

[2]LVDS: Low Voltage Differential Signaling
[3]RAID: Redundant Array of Independent Disks
[4]FPGA: Field Programmable Gate Array

The system runs in "common stop mode", which means that the trigger comes up to 2 µs after the digitization of the signal. For that reason, the digitizing modules work in a self-triggering mode. In doing so, the modules continuously digitize all signals of interest and store them together with a timestamp in FIFO[5] buffers [66].

The WASA DAQ system is able to cope the high luminosities and reaches the design goal of approximately 20 µs deadtime per event [67].

[5]FIFO: First In First Out

Chapter 3

Analysis Software

This section describes the software tools which are used for the data analysis and for the generation of the Monte Carlo files. The relation between the different software packages is illustrated in Fig. 3.1.

3.1 Pluto

The Monte Carlo event generator Pluto is developed for the simulation of hadronic-physics interactions and for the study of heavy ion reactions [68]. It is completely based on ROOT [69], and was originally written for the HADES experiment at GSI. However, it can be easily adapted to other nuclear and hadron physics experiments.

The user initializes the desired reaction and the kinematic variables of the beam and target particles. The event generator creates the energy-momentum four-vectors of the final state particles and all intermediate particles, which are produced in the defined reaction. The principle for the generation of phase-space distributed particles is based on the GENBOD procedures from the CERNLIB software package [70]. More sophisticated physic models can be also activated or implemented by the user.

In case of the signal channel $\eta \to e^+e^-e^+e^-$ the simple interaction model is used. The mass distributions of the dilepton pairs are based on QCD calculations for a point-like particle. The second model includes the form factor

$$F(q_1^2, q_2^2) = \frac{m_\rho^4}{(m_\rho^2 - q_1^2)(m_\rho^2 - q_2^2)} \tag{3.1}$$

where q_1 and q_2 are the energy-momentum four-vectors of the first and the second electron-positron pair, and $m_\rho = 770\,\mathrm{MeV}/c^2$ is the pole mass parameter. This form factor is proposed in Ref. [2]. In the main analysis, the model without the form factor is used. This is done in order compare the results for the branching ratio with the results found in Ref. [10], where the same model was used. However, the influences of the form factor on the final result will be discussed as well.

The other decay which is studied within the framework of this thesis is $\eta \to e^+e^-$, where the final state particles are distributed according to phase space.

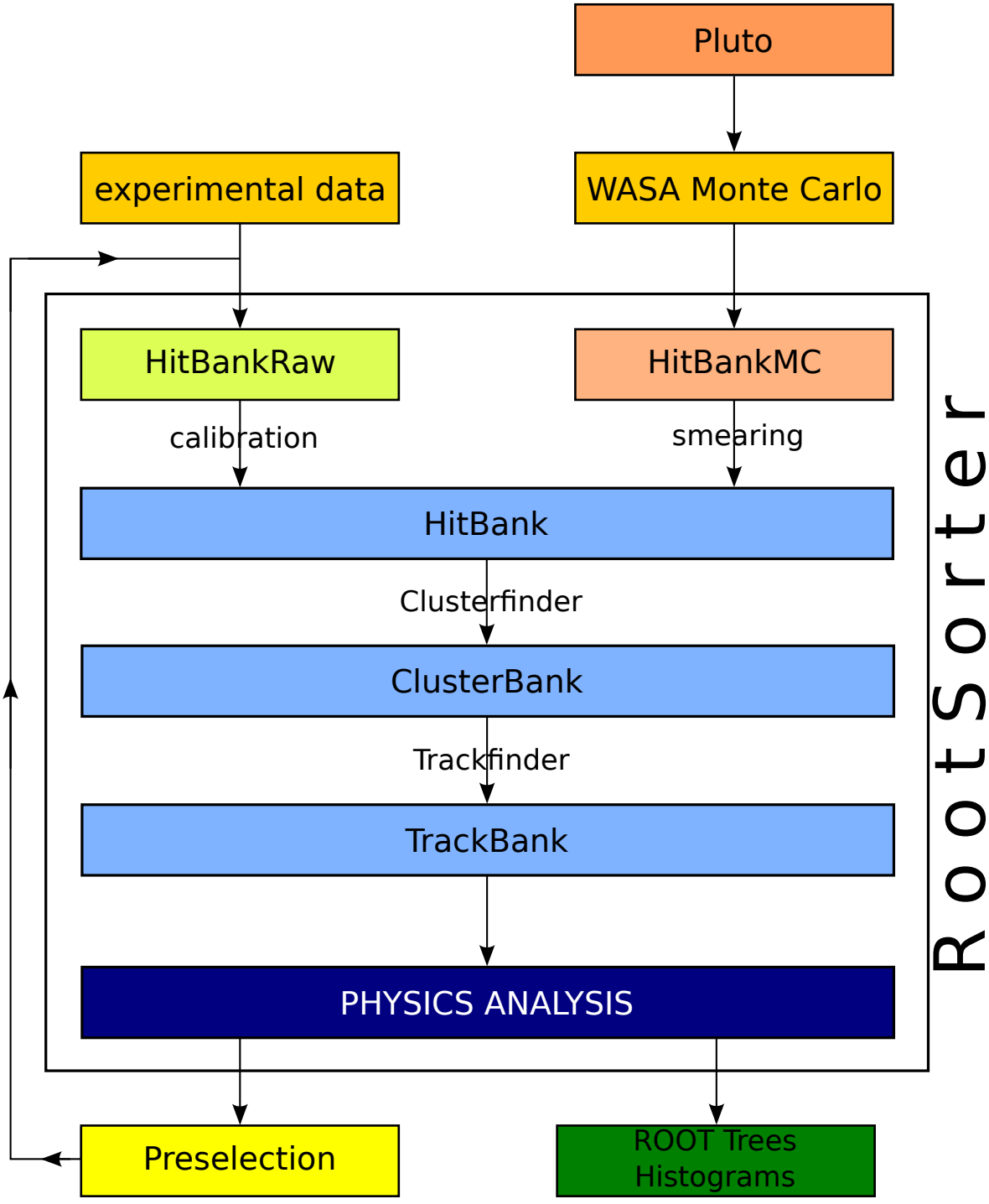

Figure 3.1: Relation between the different software tools. The experimental data are passed to RootSorter. The Monte Carlo data are generated with WASA Monte Carlo (WMC), which gets the input from the event generator Pluto. The Monte Carlo data are also analyzed with RootSorter.

3.2 WASA Monte Carlo

The WASA Monte Carlo (WMC) program simulates the propagation of particles through the detector. The software is based on GEANT3 (GEometry ANd Tracking) [71], which is a package developed at CERN. Within the WMC software, the geometry and the different materials of the entire WASA setup are implemented. The interaction with the active detector elements and also with the detector support structure and other passive elements is simulated, where physical processes like secondary and tertiary particle decays and photon conversion are included. The magnetic field provided by the solenoid is described by a three dimensional field map. To match the resolution of the simulated data with the experimental data, a smearing of the simulated data is applied. Electronic noise, electron drift behavior in the MDC and FPC, light propagation in the scintillators, or the response of the photomultipliers are not included in WMC [46]. Effects due to event overlap and chance coincidences are also not included in the simulation.

The input for WMC are the output files from the event generator Pluto. Additionally, an internal event generator is available which can be used to simulate single-track events[1]. The energy deposit of the particles and the time information is saved in `ems`-files[2], which can be read and analyzed with RootSorter. Apart from the simulated values, the output files contain the initial energy-momentum four-vectors of the particles. The Monte Carlo simulations provide a detailed understanding of the detector response and allow to determine the influence of certain selection criteria on the reconstruction efficiencies. Figure 3.2 shows two event displays for the simulated reaction $p\,d \to {}^3\mathrm{He}\,(\eta \to e^+e^-e^+e^-)$. The ^{3}He nucleus enters the FD, while the electrons and positrons are detected in the CD. They traverse the MDC, PSB, and finally reach the calorimeter, where they produce an electromagnetic shower.

3.3 RootSorter

The analysis of the data is performed with RootSorter [73], which is based on the ROOT data-analysis software [69]. Originally, the RootSorter framework was developed for the ANKE experiment at COSY. Later, it was adapted to the needs of the WASA experiment. Since RootSorter is based on an object-oriented framework, it is quite easy to modify or to extend the software to the desired requirements.

In the first instance, the data are stored in a bank which contains the energy and time information from each single detector element. In case of the experimental data, the information is stored in the `HitBankRaw`. The raw hits are calibrated and copied to the `HitBank`. The calibration constants for each run period are stored in a database. The Monte Carlo data are stored at first in the `HitBankMC`. To match the simulated data with the actual resolution of the detector elements, the Monte Carlo data are smeared according to the detector resolution while they are copied to the `HitBank`.

The hits from each sub-detector element, which could belong to the same particle, are combined into clusters and stored in a `ClusterBank`. A track is a group of all clusters from

[1] Single track events are used as a training set for the Artificial Neural Network (ANN), which is later used for particle identification (PID). Additionally, these events are used to parametrize the errors for the kinematic fit.

[2] EMS: Experimental Message Specification [72]

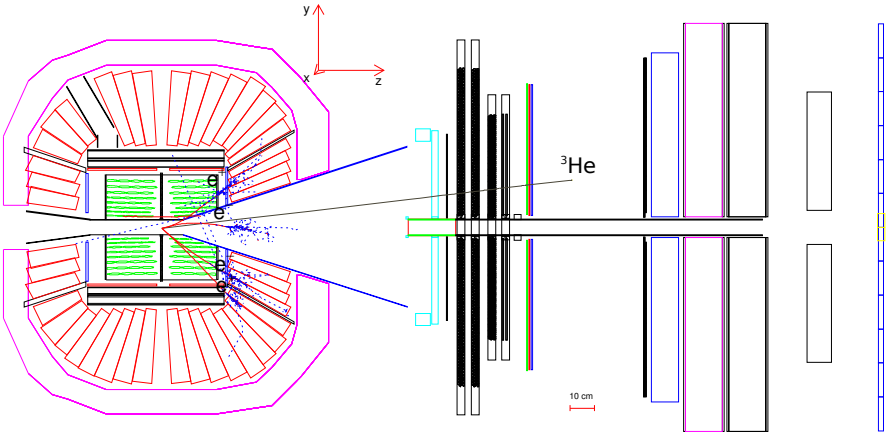

(a) Side view of WASA

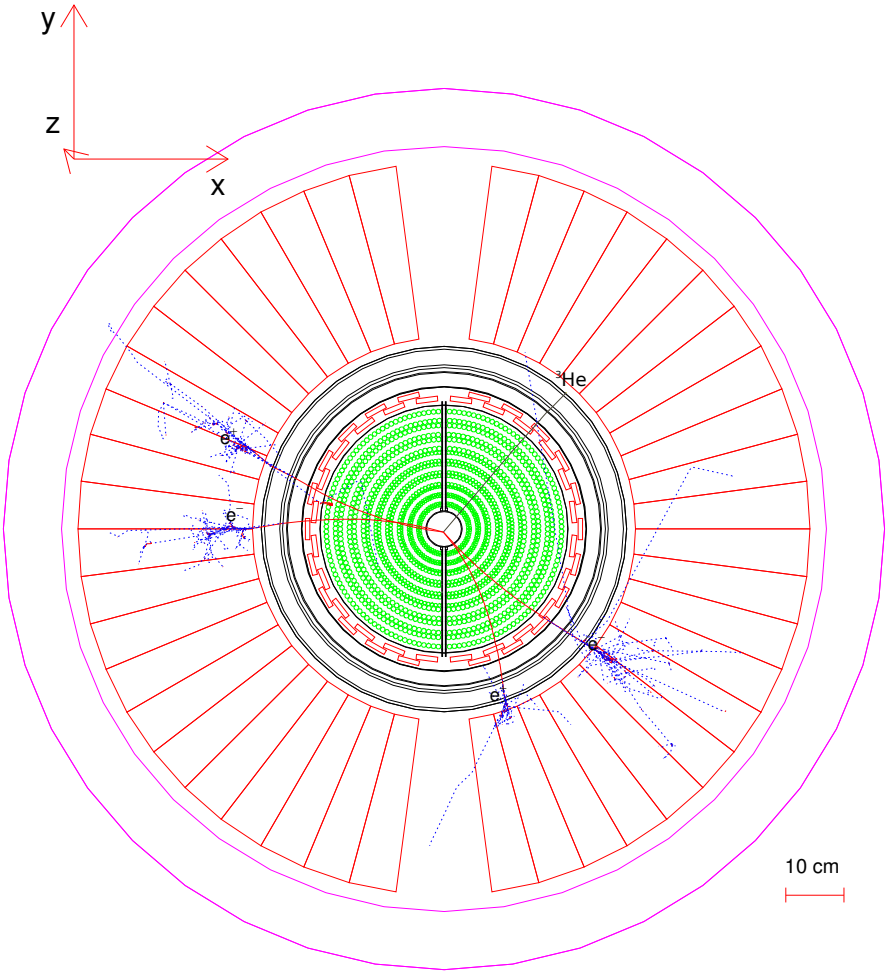

(b) Front view of the CD

Figure 3.2: Event display from WASA Monte Carlo (WMC). The simulated reaction is $p\,d \to {}^3\mathrm{He}\,(\eta \to e^+e^-e^+e^-)$. The ^{3}He track is colored in grey, and the electron and positrons are red. The blue dashed lines in the calorimeter illustrate the electromagnetic shower.

the sub-detectors, which are assigned to a physical particle. Tracks are stored in a `TrackBank`. The `HitBank`, `ClusterBank`, and `TrackBank` have the same structure and functionality both for experimental and simulated data.

A detailed description how hits are clustered and how these clusters are assigned to tracks will follow in the next subsections. Depending on whether the particles are measured in the FD or in the CD, two different reconstruction algorithms are used, which both aim to reproduce the particle trajectories with their correct energy-momentum four-vectors.

3.3.1 Track reconstruction in the Forward Detector

The track reconstruction of charged particles in the FD is based on the pixels from the FTH, where each pixel is made up of a cluster in at least two of the three FTH layers. The special geometry of the FTH layers (*cf.* Fig. 2.8) enables to obtain the azimuthal and polar angles from one reconstructed pixel together with an assumed second point on the particles trajectory, which is the origin of the WASA coordinate system (*cf.* Sect. 2.2.5).

In the next step, the algorithm checks if there is a coincidence in the azimuthal overlap, the time difference, and a minimum amount of deposited energy between the so far reconstructed track and the wedged FD scintillators (FWC and FRH). If so, the cluster information is added to the track.

The spatial resolution of the track can be further improved by the FPC. If there is a match between the trajectory reconstructed from the FTH pixel and a line constructed from the assumed vertex to the FPC cluster, the track parameters are updated, thus improving the angular resolution by a factor of approximately two [46]. The time information of the reconstructed track is the average of the FTH clusters.

More information about the track reconstruction in the FD can be found in Ref. [52].

For the analysis of the $p\,d \to {}^3\mathrm{He}\,X$ reactions it is mandatory to know the kinetic energy of the ^{3}He nucleus. It can be reconstructed using following equation [74]

$$\begin{aligned} E_{^3\mathrm{He,kin}} \;=\; & [(0.199876 + 0.640187/\mathrm{GeV} \times E_{\mathrm{dep}}(\mathrm{FRH1}) + \\ & 1.60489/\mathrm{GeV}^2 \times E_{\mathrm{dep}}(\mathrm{FRH1})^2 - \\ & 2.28946/\mathrm{GeV}^3 \times E_{\mathrm{dep}}(\mathrm{FRH1})^3) \times \\ & (1.42133 - 0.364951 \times \cos\theta)]\,\mathrm{GeV} \end{aligned} \tag{3.2}$$

where $E_{\mathrm{dep}}(\mathrm{FRH1})$ is the energy deposit in the first layer of the FRH, and θ is the scattering angle of the ^{3}He nucleus. This formula is valid for particles which are stopped in the FRH1. This is the case for ^{3}He nuclei which stem from the production reaction $p\,d \to {}^3\mathrm{He}\,\eta$ at the center-of-mass energy which is used for our experiments. The parametrization is based on a comparison between the energy deposit in the first layer of the FRH at a certain scattering angle θ and the true kinetic energy for simulated ^{3}He nuclei.

3.3.2 Track reconstruction in the Central Detector

The detector components of the central part of WASA which are used to reconstruct tracks are the MDC, the PSB, and the SEC. The different reconstruction procedures for the clusters in these individual sub-detectors will be described in the following.

Mini Drift Chamber

The recognition of helical trajectories in the MDC is based on the pattern recognition and the final fitting [46, 56, 75]. The pattern recognition extracts helices from hit patterns, which correspond to the particle trajectories within the magnetic field of the solenoid. Here, the assumption is made that the magnetic field within the MDC is homogeneous and parallel to the z-axis. This results in helices which have their axis also parallel to the z-axis. They can be parametrized with six variables, namely

- R_0: distance between origin and center of helix axis (in xy-plane)
- Φ_0: relative orientation of the helix center and coordinate center (in xy-plane)
- R: helix radius
- q: particles charge
- θ: polar angle of the particle (angle between the z-axis and track momentum)
- z_0: closest approach of the helix to the origin in z-direction

The pattern-recognition algorithm uses multi-model regression techniques to fit the helices to the hits. At first, hits coming from the axial layers are used and projected onto the xy-plane. Circles are fitted to the hit patterns, where the helix parameters R_0, Φ_0, and R are determined. The radius of the helix allows one to calculate the transversal momentum component: The Lorentz force

$$\vec{F_L} = q\vec{v} \times \vec{B} \tag{3.3}$$

bends the particles on circular paths perpendicular to the magnetic field. In this equation, $\vec{v}$ is the velocity of the particle, and $\vec{B}$ is the magnetic field along the z-axis. The centrifugal force acts against the Lorentz force. Equalizing the two forces leads to

$$\frac{\gamma m v_t^2}{R} = q v_t B_z \ . \tag{3.4}$$

The transversal momentum can be then calculated with

$$p_t = qB_z R \tag{3.5}$$

where the charge of the particle q is obtained from the direction of the curvature.

As a second step, the hit information of the inclined tubes is used to get the polar angle θ and z_0. The momentum vector can be now calculated with

$$\vec{p} = \begin{pmatrix} p_x \\ p_y \\ p_z \end{pmatrix} = p_t \begin{pmatrix} \cos\Phi_0 \\ \sin\Phi_0 \\ \cot\theta \end{pmatrix} \ . \tag{3.6}$$

After the pattern recognition, a final fitting routine is used to improve the determined helix parameters. It uses Kalman filter methods [76], where the primary helix parameters from the pattern recognition algorithm are taken as initial values. The helical trajectory is traced from the outer MDC layers back to the innermost layer, where the helix parameters are iteratively improved by taking important physical processes into account. These processes include the energy loss and multiple Coulomb scattering in the detector material. Additionally, the magnetic field map is considered instead of assuming a homogeneous field which is parallel to the z-axis.

Plastic Scintillator Barrel

The cluster finding routine checks if there are hits in overlapping PSB elements. If the energy deposit in these elements is larger than 0.5 MeV and the time difference is smaller than 10 ns, the hits are clustered. The azimuthal angle of the cluster is the average of the azimuthal angles of the contributing detector elements. The polar angle is 30° for a cluster in the PSB forward part, 90° for a cluster in the PSB central part, and 140° for a cluster in the PSB backward part. In each case, the angles correspond to the center of the detector planes. The time information of the cluster is the average time information of the clustered hits, while the assigned energy is the one from the hit with the largest energy deposit.

Scintillator Electromagnetic Calorimeter

In case of the SEC, the cluster finding routine starts from the first crystal which has an energy deposit of at least 5 MeV. Such a hit is used as the basis for the search of the first cluster. The neighboring crystals are checked for an energy deposit larger than or equal to 2 MeV. If the time difference between the hit of the reference crystal and the hit in those crystals is smaller than 50 ns, it is added to the cluster. In the next iteration step, each added crystal is regarded as the new reference crystal. Again, all neighboring crystals are checked if they fulfill the criteria concerning the minimum energy deposit and the time correlation with respect to the reference crystal. If this is fulfilled, they are added to the initial cluster. This procedure is repeated until all hits in the environment around the central crystal are found. The sum of the energy deposits must be at least 10 MeV to be actually considered as a cluster in the following.

Out of the remaining hits, the next crystal with the an energy deposit above the threshold is now regarded as the new reference crystal. Based on this crystal, the search for the next cluster starts again.

The energy of a cluster is the sum of the energies E_i of the contributing crystals. The time information of the cluster is the time information of the hit in the reference crystal. The position vector of the cluster $\vec{X}$ is the weighted mean value of the crystal position and is calculated with

$$\vec{X} = \frac{\sum_i w_i \vec{x}_i}{\sum_i w_i} \tag{3.7}$$

where $\vec{x}_i$ is the position vector of the ith cluster, which is the vector that points from the origin of the reference frame (*cf.* Sect. 2.2.1) to the center of the crystals front surface. w_i is the weight, which is defined as

$$w_i = \mathrm{MAX}\left\{0, W_0 + \ln \frac{E_i}{\sum_i E_i}\right\} \tag{3.8}$$

with the constant W_0. In the next step, the position vector is corrected for the shower depth, which improves the angular resolution. More information about the procedure can be found in Refs. [77, 78].

Track reconstruction

The track reconstruction routine checks if the identified clusters could belong to the same track. It starts with the clustered hits in the MDC and searches if there is a PSB cluster which fits to the MDC cluster with respect to an overlap of the angles. The difference of

the azimuthal angles of the cluster position in the PSB and the exit coordinate of the MDC tracklet should not be larger than 10°. In case of the polar angle it is just checked if the exit coordinate of the MDC tracklet is within the polar angle range of the PSB element. After that, the matching between the MDC cluster and one of the SEC clusters is checked. This is done by regarding the propagated MDC tracklet from the MDC exit point to the calorimeter. The MDC cluster and a SEC cluster are matched together if the angle between a vector which is parallel to the propagated tracklet and the position vector of the clustered SEC hits is at maximum is 25°. Depending if the MDC cluster matches with one the other detector elements of the CD or not, there are four different possibilities: MDC-PSB matching, MDC-SEC matching, MDC-PSB-SEC-matching, or no matching (only MDC cluster).

After checking the MDC cluster for a matching with one of the clusters in the other sub-detectors of the CD, the track reconstruction checks if one of the remaining PSB clusters match together with one of the remaining SEC clusters. This is done by regarding the difference of the azimuthal angles between the clusters, which should be smaller than or equal to 20°. Additionally, the time difference between the clusters should be at maximum 35 ns. If this is fulfilled, a track is found which consists of a PSB-SEC cluster.

So far, the identified tracks are treated as belonging to charged particles. If there is a SEC cluster which can not be assigned to a cluster in one of the CD components which are sensitive to charged particles, namely the MDC and the PSB, these clustered SEC hits are assigned to a neutral particle.

Chapter 4

Preselection of η Decays through ^{3}He Identification

This chapter describes the production reactions for the η mesons and explains how the mesons are identified (Sect. 4.1 and Sect. 4.2). The run periods which were analyzed within the framework of this thesis are summarized in Sect. 4.3. Additionally, the main experiment trigger is explained. In Sect. 4.5 the preselection is presented which is used to reduce the amount of data by rejecting events which obviously belong to background reactions. Section 4.6 illustrates how the ^{3}He nuclei are identified in the FD. Finally, Sect. 4.7 explains the storage of the preselected data for a more efficient analysis of specific η-decay channels.

4.1 η-production reactions

There are two reactions which are used in the WASA-at-COSY experiments for the production of η mesons. Both will be described in this section.

4.1.1 Proton-deuteron collisions

The first η-production reaction is the fusion reaction $p\,d \to {}^3\mathrm{He}\,\eta$. The protons have a momentum of $p_{p,z} = 1.7\,\mathrm{GeV}/c$, which corresponds to a kinetic energy of $T_p = 1.0\,\mathrm{GeV}$. Deuteron pellets are used as targets with negligible momenta and kinetic energies, respectively. The center-of-mass energy of the production reaction is $\sqrt{s} = 3.4\,\mathrm{GeV}/c^2$, and the excess energy is $Q = 60\,\mathrm{MeV}$.

Figure 4.1 shows the total cross section for the reaction $p\,d \to {}^3\mathrm{He}\,\eta$ as a function of the proton kinetic energy [79]. The cross section can be interpolated to the kinetic energy of the present experiment by averaging the measured values from the two closest data points, which leads to $\sigma = 0.41\,\mu\mathrm{b}$.

One advantage of the η-meson production with *pd*-reactions is the small background from reactions with direct-pion production. Not all cross sections for these reactions are measured at the energy of this experiment; the available data are listed in Table 4.1. Also measurements at energies differing from the used energy for the WASA-at-COSY experiment are listed. It can be seen that the cross sections for the reactions where pions are produced are in the same order of magnitude as for the η-production reaction $p\,d \to {}^3\mathrm{He}\,\eta$.

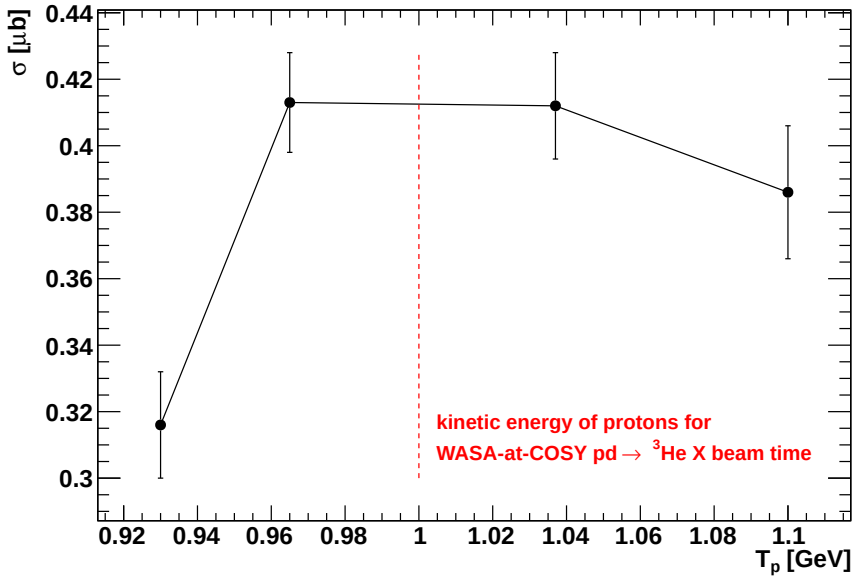

Figure 4.1: Total cross section for $p\,d \to {}^3\mathrm{He}\,\eta$ as a function of the kinetic energy of the protons. The data points are taken from Ref. [79].

4.1.2 Proton-proton collisions

The alternative reaction which is used at WASA-at-COSY to produce η mesons is the reaction $p\,p \to p\,p\,\eta$, where the proton has a momentum of $p_{p,z} = 2.1\,\mathrm{GeV}/c$, corresponding to a kinetic energy of $T_p = 1.4\,\mathrm{GeV}$. The total cross section was measured at this energy as $\sigma(p\,p \to p\,p\,\eta) = 9.8 \pm 1.0$ [83]. It is 25 times larger as compared to the $p\,d \to {}^3\mathrm{He}\,\eta$ cross section: $\sigma(p\,p \to p\,p\,\eta)/\sigma(p\,d \to {}^3\mathrm{He}\,\eta) \approx 10\,\mu\mathrm{b}/0.4\,\mu\mathrm{b} = 25$.

Due to the larger background from reactions with direct-pion production in the *pp*-reactions compared to the *pd*-reactions, it is necessary to use more selective trigger conditions. In experiments with *pd*-reactions it is sufficient to trigger on the ^{3}He in the FD. In experiments with *pp*-reactions, however, the trigger must be more selective and includes also information from the CD where the η decay products are measured. This means that certain η-decay channels are already selected on trigger level.

4.2 η-meson tagging

The very short lifetime of the η meson ($(5.0\pm0.3)\times10^{-19}$ s [11]) makes it impossible to detect it directly. Nevertheless, it is possible to reconstruct it via the missing-mass method. Here, the invariant mass of one or more unmeasured particles is calculated from the measured energy-momentum four-vectors of the detected particles. In the following, the reaction $p\,d \to {}^3\mathrm{He}\,X$ (where X stands, for instance, for η or pions) will be used to demonstrate this technique.

The kinematic variables of the proton beam and the deuteron target are given by the COSY setup and the pellet target system, respectively. The energy-momentum four-vector

Table 4.1: Total cross section for reactions with direct-pion production. The center-of-mass energies from the different experiments are rounded to the same precision.

reaction	$\sqrt{s}$ [GeV/c^2]	σ [μb]	Reference
$d\,p \to {}^3\mathrm{He}\,\pi^0$	3.3	3.6 ± 0.6	[80]
$d\,p \to {}^3\mathrm{He}\,\pi^0$	3.4	1.8 ± 0.3	[80]
$p\,d \to {}^3\mathrm{He}\,\pi^0\pi^0$	3.4	2.8 ± 0.3	[81]
$p\,d \to {}^3\mathrm{He}\,\pi^+\pi^-$	3.4	5.1 ± 0.5	[81]
$p\,d \to {}^3\mathrm{He}\,\pi^+\pi^-\pi^0$	3.6	$1.400 \pm 0.017_{\mathrm{stat}} \pm 0.370_{\mathrm{syst}}$	[82]
$p\,d \to {}^3\mathrm{He}\,\pi^+\pi^-\pi^0$	3.7	$0.910 \pm 0.007_{\mathrm{stat}} \pm 0.080_{\mathrm{syst}}$	[82]
$p\,d \to {}^3\mathrm{He}\,\pi^0\pi^0\pi^0$	3.6	$0.180 \pm 0.006_{\mathrm{stat}} \pm 0.049_{\mathrm{syst}}$	[82]
$p\,d \to {}^3\mathrm{He}\,\pi^0\pi^0\pi^0$	3.7	$0.115 \pm 0.003_{\mathrm{stat}} \pm 0.023_{\mathrm{syst}}$	[82]

of the proton is

$$\underline{\mathrm{p}}_p = \begin{pmatrix} E_p/c \\ \vec{p_p} \end{pmatrix} = \begin{pmatrix} \sqrt{p_{p,z}^2 + (m_p c)^2} \\ 0 \\ 0 \\ p_{p,z} \end{pmatrix} \tag{4.1}$$

where c is the speed of light, m_p is the proton mass, and $p_{p,z}$ is its momentum (beam momentum).

The energy-momentum four-vector of the deuteron is

$$\underline{\mathrm{p}}_d = \begin{pmatrix} E_d/c \\ \vec{p_d} \end{pmatrix} = \begin{pmatrix} m_d c \\ 0 \\ 0 \\ 0 \end{pmatrix} \tag{4.2}$$

where m_d is the deuteron mass. At a pellet velocity of around 60 m/s it can be assumed to be at rest.

The energy-momentum four-vector $\underline{\mathrm{p}}_{^3\mathrm{He}}$ of the ^{3}He nucleus can be reconstructed in the FD.

Due to energy and momentum conservation the four-vector of an undetected particle or particles X is

$$\underline{\mathrm{p}}_X = \underline{\mathrm{p}}_p + \underline{\mathrm{p}}_d - \underline{\mathrm{p}}_{^3\mathrm{He}}\,. \tag{4.3}$$

The absolute value of $\underline{\mathrm{p}}_X$ (divided by c) is commonly denoted as the ^{3}He-missing mass

$$\frac{|\underline{\mathrm{p}}_X|}{c} = \frac{1}{c}\sqrt{(E_X/c)^2 - (\vec{p_X})^2} = m_X \tag{4.4}$$

which is equal to the invariant mass of X. If X is a single particle, $\underline{\mathrm{p}}_X$ is its four-vector. Otherwise, it is the sum of the four-vectors of the system comprising particles X. This means that in case of $X = \eta$ the ^{3}He-missing mass is equal to the η mass.

Another method to tag a short-lived particle is to calculate the invariant mass of its decay products, since this value must be equal to the mass of the initial particle. While the ^{3}He-missing mass is only based on the measurement of the ^{3}He in the FD and is independent of the

decay channel of X, the invariant mass is based on the determination of energy-momentum four-vectors of the particles in the CD and generally requires the detection of more than two particles.

4.3 Run periods

The analyzed data comprise two beam times where the η mesons were produced in $p\,d \to {}^3\mathrm{He}\,\eta$ reactions. In total, more than 3×10^7 η events were recorded in twelve weeks of beam time, which also includes the pellet regeneration time. This corresponds to an averaged rate for recorded η mesons of $\sim 4\,\eta/s$ (meaning that around 9 $\eta \to e^+e^-e^+e^-$ events were recorded per day).

The COSY cycle length was 100 seconds. Each cycle started with the injection of the beam into the ring and the acceleration to a proton momentum of $p_{p,z} = 1.7\,\mathrm{GeV}/c$. Seven seconds after the beginning of the cycle the pellet vacuum shutters were opened and the data taking began. After 91 seconds, the pellet stream was stopped. Two seconds later the DAQ was also stopped and the remaining beam ($\sim 30\,\%$ for the barrier bucket mode and $\sim 70\,\%$ for the sweeping beam mode, see below) was dumped. To protect the wire chambers and photomultiplier tubes from high currents, the applied high voltages were ramped down during the acceleration and the beam dumping phases.

Figure 4.2 illustrates the beam intensity and the trigger and pellet rates as a function of time for several cycles. The lifetime of the DAQ can be determined from the ratio between the accepted trigger signals and the incoming trigger signals. It shows a time dependency, where the lifetime is around 70 % at the beginning of a cycle, while it is close to 100 % at the end.

The first beam time was in September/October 2008 and lasted four weeks (COSY experiment number 188). In this beam time an amount of data with a total size of 19.7 TB was recorded. In around half of the runs of the 2008 beam time the barrier bucket cavity was used to compensate for the mean energy loss of the COSY beam through beam target interactions (barrier-bucket mode) [46]. In the other runs the beam orbit was changed during a cycle in order to obtain longer beam lifetimes (sweeping-beam mode). However, the energy loss was not compensated which resulted in a time dependent beam momentum. If the ^{3}He-missing mass is calculated under the assumption of a constant beam momentum, the time dependent beam momentum translates into a time dependent ^{3}He-missing mass distribution. This is shown in Fig. 4.3 where the η-peak position in the ^{3}He-missing mass distribution is plotted as a function of the time in cycle. A clear time dependence can be seen, where the reconstructed η-peak position is smaller as compared to the true value at the beginning of the time in cycle, while it is larger at the end of the cycle.

The time dependence of the beam momentum was extracted from the ^{3}He-scattering angles at different cycle times. The function is also shown in Fig. 4.3. It can be described with

$$p_{p,z}(t) = 1.70013\,\frac{\mathrm{GeV}}{c} - 0.0000983915\,\frac{\mathrm{GeV}}{c} \times \frac{t}{s} \tag{4.5}$$

where t is the time in cycle [46]. For the runs where the barrier bucket cavity was in operation, a constant beam momentum of $p_{p,z} = 1.696\,\mathrm{GeV}/c$ is used for the data analysis.

The second beam time was in August/September 2009 and lasted eight weeks (COSY experiment number 188.1). In this beam time, an amount of data with a total size of 42.9 TB was taken. During the entire beam time the barrier bucket mode was used.

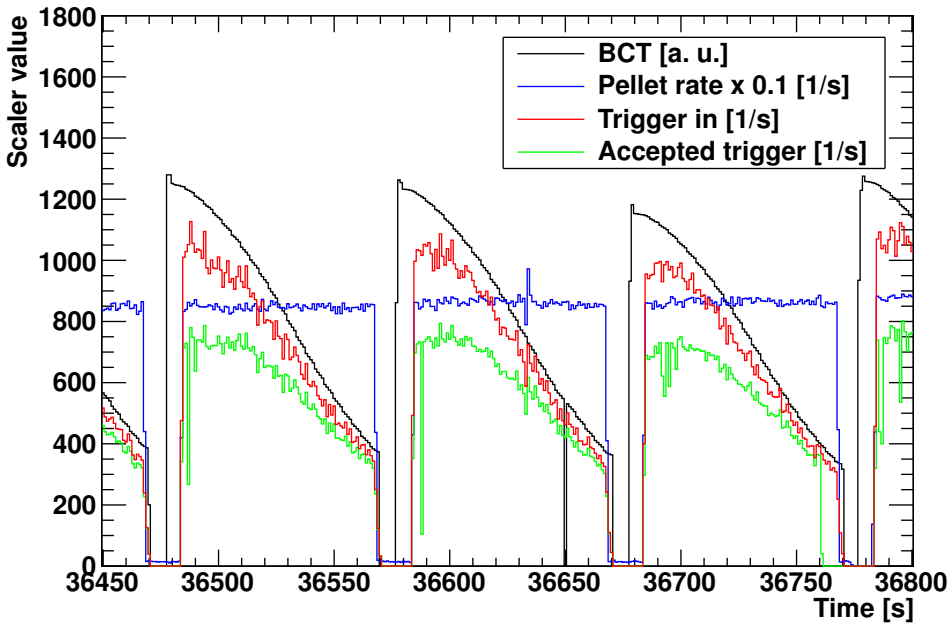

Figure 4.2: Scaler values as a function of time shown for several cycles. The Beam Current Transformer (BCT) value is proportional to the number of protons in the beam. The pellet rate is around 9 kHz (note that the true pellet rate is scaled by factor of 0.1 in the plot). During these cycles the barrier bucket cavity was used.

4.4 On-line trigger

A trigger selects events with a specific signature already during data taking. Only for those events the analog detector signals are digitized and written on disc. This reduces the amount of data significantly. The main experiment trigger for the two $p\,d \rightarrow {}^{3}\mathrm{He}\,X$ beam times has the notation

fwHea1 & fwHeb1 & fHedwr1

which is a logical conjunction of all three conditions. The individual conditions stand for:

- **fwHea1**: At least one module in the first layer of the FWC above high threshold
- **fwHea2**: At least one module in the second layer of the FWC above high threshold
- **fHedwr1**: Matching trigger: At least one module of the first or the second layer of the FWC above high threshold. At least one sector coincidence (in ϕ) between these one or two layers of the FWC, the first layer of the FTH, and the first layer of the FRH, *i.e.* matching track (*cf.* Fig. 4.4). More information about the matching trigger can be found in Ref. [84].

The main experiment trigger condition is only based on information measured with the FD. Due to the distinctive signature of the ^{3}He nuclei, it is possible to select them already on the trigger level. By using the main experiment trigger, the event rate is around 1 kHz. This is roughly a factor of one thousand smaller compared with the event rate for events with at least one fired element in the first layer of the FRH.

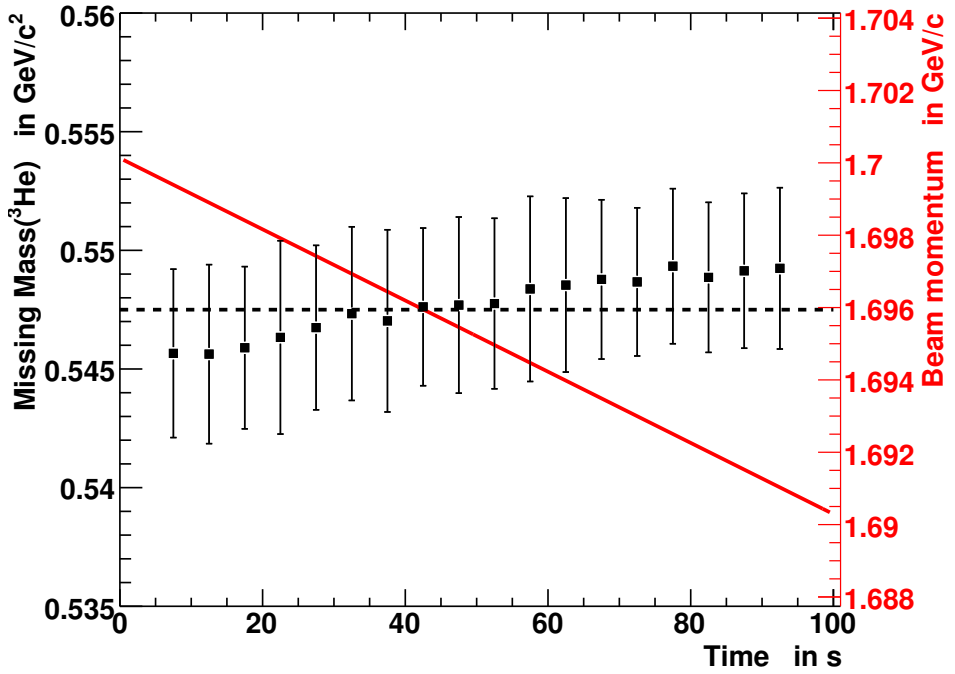

Figure 4.3: Time dependencies of ^{3}He-missing mass and beam momentum (from Ref. [46]). The ^{3}He-missing was calculated with an assumed proton momentum of $p_{p,z} = 1.696\,\mathrm{GeV}/c$. The black data points are the peak centers of the Gaussian functions which were used to fit the η peaks, while the error bars denote the standard deviation of the fit functions. The horizontal line marks the η mass. To correct for the effect of the time dependent ^{3}He-missing mass, a function was determined which parametrizes the beam momentum as a function of the time in cycle (red line).

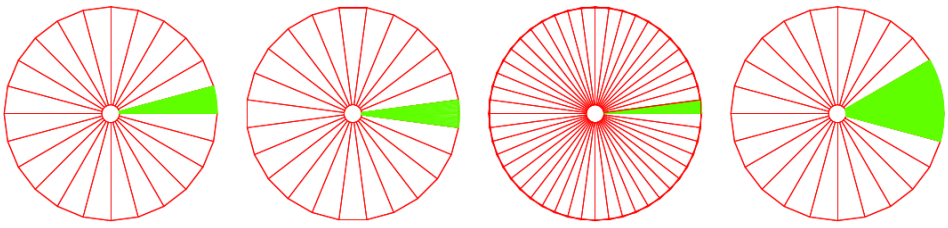

Figure 4.4: Matching trigger condition (from Ref. [84]). From the left to the right: first layer of FWC / second layer of FWC (only one FWC layer is required), first layer of FTH, first layer of FRH. The trigger condition is fulfilled if there is at least one sector coincidence (in ϕ) between the layers. Additionally, there must be at least one module of the first or the second layer of the FWC above high threshold.

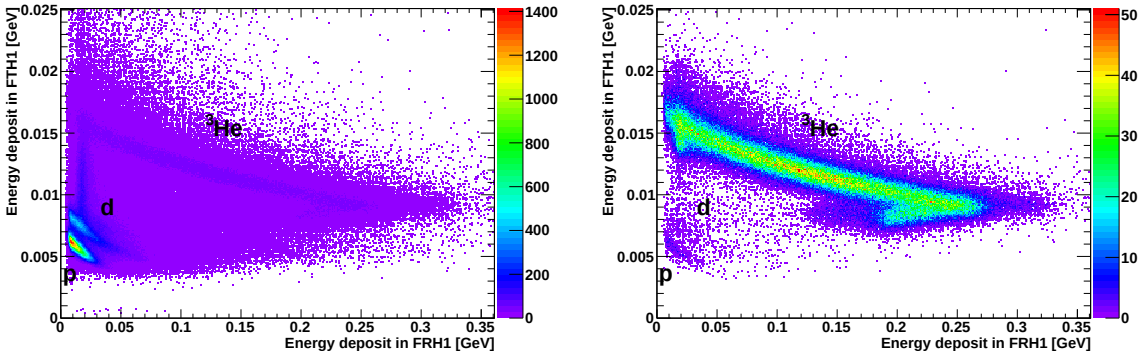

(a) before preselection

(b) after preselection

Figure 4.5: Identification of the particles in the FD via the $\Delta E - E$ method. The preselection suppresses events which obviously belong to background reactions with protons and deuterons in the FD. As an example, the first run of the 2009 data is shown (run 13969).

4.5 Preselection

A first preselection of the data was done by J. Złomańczuk [85]. This preselection suppresses events which obviously belong to background reactions, while selecting events with ^{3}He candidates from $p\,d \rightarrow {}^3\mathrm{He}\,X$ reactions. The identification of the ^{3}He candidates in the FD is achieved via the $\Delta E - E$ method. Here, the energy deposit in one of the thin plastic scintillators of the FD (FTH, FWC, or the sum of the energy deposits) is plotted as a function of the energy deposit in the thick FRH. Figure 4.5 shows the plots which are obtained from the analysis of one run before and after the preselection, respectively. The areas of protons, deuterons and ^{3}He nuclei are clearly visible in the distribution before the preselection. Compared to the ^{3}He band, the protons and deuterons are located at small energy deposits in the FTH1 and in the FRH1. Since the different bands are well separated, events with ^{3}He nuclei can be easily selected with a graphical cut. In the plot after the preselection the areas with protons and deuterons are less populated while the ^{3}He band is more pronounced. The preselection routine accepts all events where at least one particle fulfills the ^{3}He-selection criteria. There might be then also a second particle in the FD. For that reason, there remain some protons and deuterons from events where another particle in the FD was accepted as a ^{3}He candidate.

In the plot obtained after the preselection it can be seen that the ^{3}He band bends back for large energy deposits in the FRH1 towards smaller energy deposits in the FTH1. The reason for this are ^{3}He nuclei which punch through the first layer of the FRH. Those particles originate from reactions where pions are produced instead of an η meson (reactions with direct-pion production, *cf.* Table 4.1). In the later analysis such events are rejected by checking the energy deposits in the layers two till five of the FRH and using them as a veto.

As an example for the efficiency of the preselection, Fig. 4.6 shows the ^{3}He-missing mass distribution from the first run from the 2009 beam time (number 13969) before and after the preselection. In both cases it is asked for at least one positively charged particle in the FD. Due to the preselection the number of entries is reduced to 25 % (from 738503 to 182436) and the peak at the η mass gets obviously more pronounced.

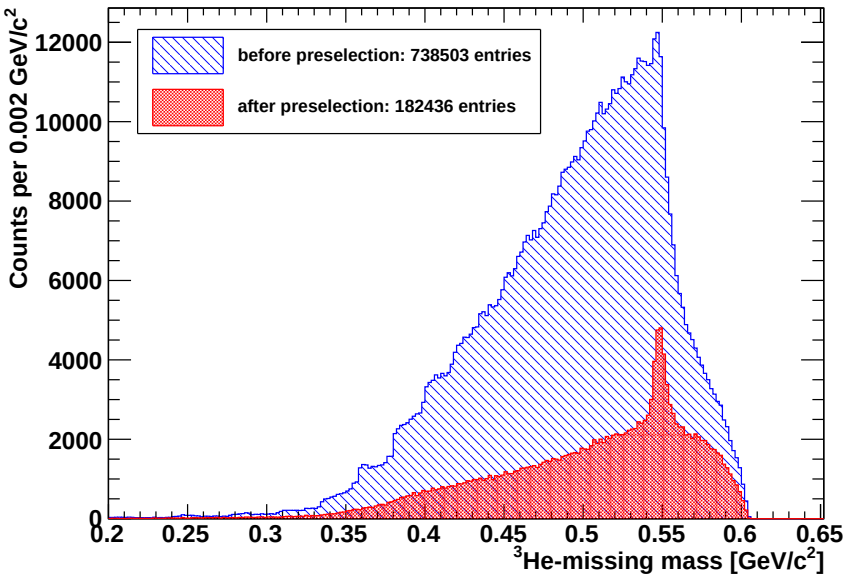

Figure 4.6: ^{3}He-missing mass distribution before and after the preselection (from the run number 13969 of the 2009 data).

4.6 Helium selection

The preselection presented in the last section is based on rough selection criteria for ^{3}He nuclei from $p\,d \to {}^3\mathrm{He}\,X$ reactions. It is used to decrease the initial amount of data by rejecting events which obviously belong to background reactions. The ^{3}He-selection criteria which will be presented in this section are more selective and focus on the identification of clean events from $p\,d \to {}^3\mathrm{He}\,\eta$ reactions.

At first, it is checked if the scattering angle of the forward-scattered particle in the lies in the geometrical acceptance of the FD. Particles with scattering angles smaller than 3° or above 18° are not considered since their polar angles were obviously wrongly reconstructed. Figure 4.7 shows the ^{3}He-scattering angle distribution from the 2009 data. The used cuts are marked in the distribution as well. The asymmetric peak around 10° comes from ^{3}He nuclei from the reaction $p\,d \to {}^3\mathrm{He}\,\eta$. The fast decrease on the right side of the peak is due to the kinematic limit which allows for a maximum ^{3}He-scattering angle of 9.8°. Because of the detector resolution, the maximum scattering angle reaches slightly larger values.

After this cut, the time correlation between the particle in the FD and trigger is checked. Particles are accepted if their time signal relative to the trigger lies in the range between 1980 ns and 2020 ns. Figure 4.8 shows the time-difference distribution for different triggers obtained from the 2009 data. The red dashed lines mark the time window for accepted particles.

The next selection criteria are requirements on the minimum and maximum energy deposit in the FWC, the FTH, and the FRH. The energy deposit in both layers of the FWC should be $E_{\mathrm{dep}}(\mathrm{FWC}) \geq 0.0035\,\mathrm{GeV}$. This value is slightly more restrictive than the highest energy threshold on the trigger level for the FWC modules. This cut is mandatory to have the same trigger condition (trigger conditions fwHea1 and fwHea2, *cf.* Sect. 4.4) for the measured data

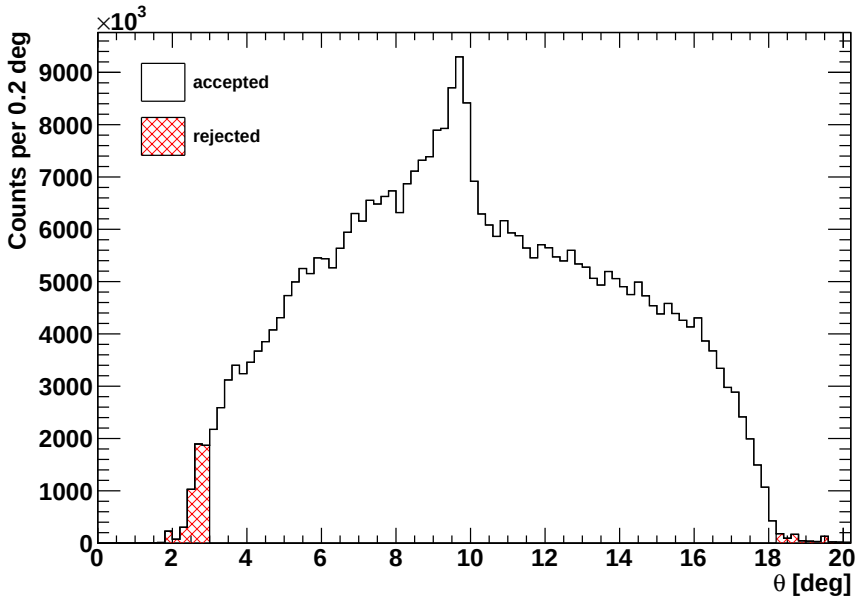

Figure 4.7: ^{3}He-scattering angle distribution (2009 data). Particles with a scattering angle outside the geometrical acceptance of the FD (namely $\theta < 3°$ or $\theta > 18°$) are rejected.

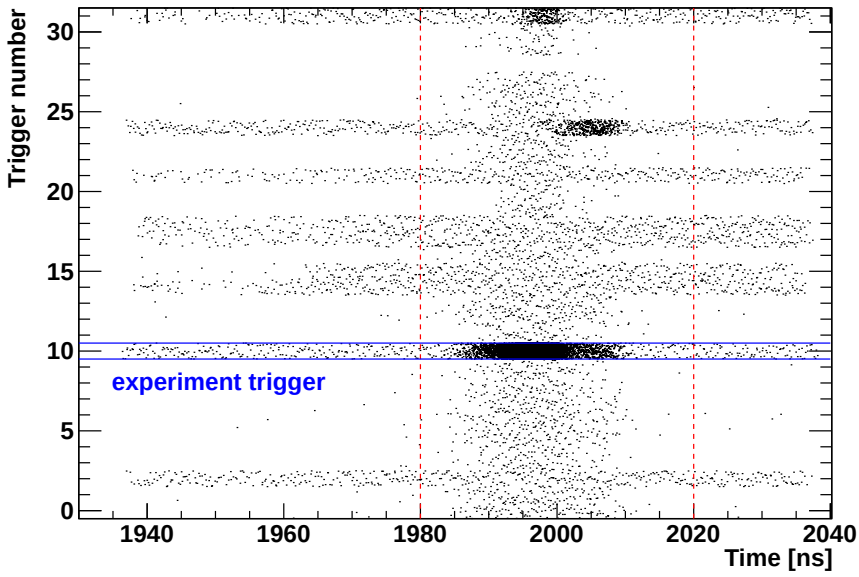

Figure 4.8: Distribution of the FD track time signal with respect to the trigger (from the 2009 data). The main experiment trigger has the trigger number 10. The red dashed lines show the used cuts. Particles are accepted if their time signal relative to the trigger lies in the range between 1980 ns and 2020 ns.

and the simulation. The energy deposit in the first layer of the FTH should be in the range $0.005\,\text{GeV} \leq E_{\text{dep}}(\text{FTH1}) \leq 0.025\,\text{GeV}$. And the energy deposit in the first layer of the FRH should be in the range $0.005\,\text{GeV} \leq E_{\text{dep}}(\text{FRH1}) \leq 0.35\,\text{GeV}$. These thresholds are motivated by the $\Delta E - E$ plot (energy deposit in the FTH1 against the energy deposit in the FRH1) and are used to reject particles which are too far away from the ^{3}He band.

At the given center-of-mass energy, the ^{3}He nuclei from the $p\,d \rightarrow {}^3\text{He}\,\eta$ reaction are stopped in the first layer of the FRH. This can be seen in Fig. 4.9, where the scattering angles of the ^{3}He nuclei from different *pd*-reactions is shown as a function of their kinetic energies. The horizontal lines mark the geometrical acceptance of the FD. By demanding that the energy deposits in the layers 2 – 5 of the FRH should be smaller than or equal to 0.005 GeV, reactions are reduced where a ^{3}He nucleus and one or more pions were produced. Especially the number of events with $p\,d \rightarrow {}^3\text{He}\,\pi^0$ reactions is reduced to less than 30 %, and $p\,d \rightarrow {}^3\text{He}\,\pi^+\pi^-$ reactions are reduced to 77 %.

Due to noise, a non-zero energy deposit in the layers 2 – 5 of the FRH is possible, although the ^{3}He is stopped in the first layer of the FRH. To avoid a rejection of such events, an energy deposit in these layers smaller than the noise level, which corresponds to 0.005 GeV, is allowed.

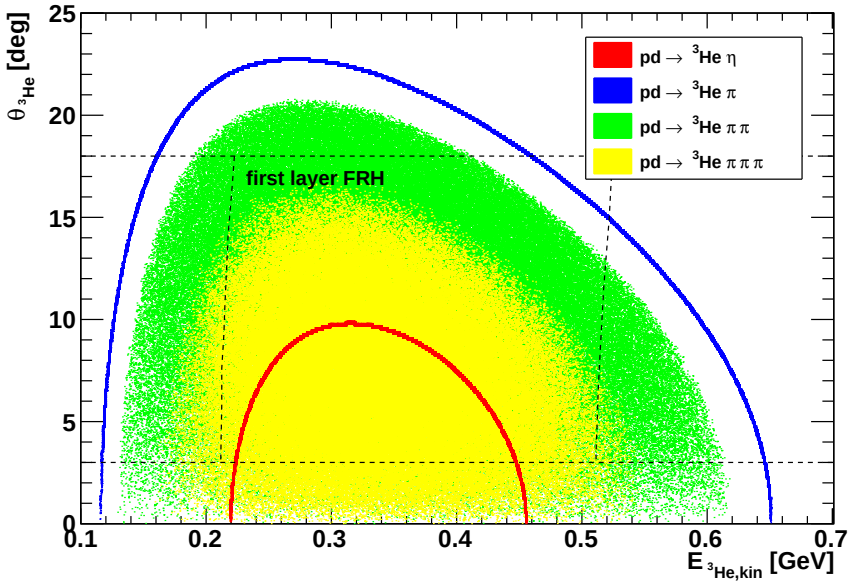

Figure 4.9: Simulation of the ^{3}He-scattering angle as a function of its kinetic energy for different reactions at $\sqrt{s} = 3.4\,\text{GeV}/c^2$. The horizontal lines mark the geometrical acceptance of the FD. The vertical lines mark the range of kinetic energies for particles which are stopped in the first layer of the FRH. A similar study can be found in Ref. [46].

The last selection criterion for ^{3}He candidates is a graphical cut on the $\Delta E - E$ plot. Figure 4.10 illustrates the simulated $\Delta E - E$ plot and also shows the plot which is obtained from the 2009 data. Particles are accepted with an energy deposit beneath the upper red dashed line and above the lower red dashed line. This means that particles with an energy deposit of

$$E_{\text{dep}}(\text{FTH1}) < -0.025 \times E_{\text{dep}}(\text{FRH1}) + 0.010\,\text{GeV} \tag{4.6}$$

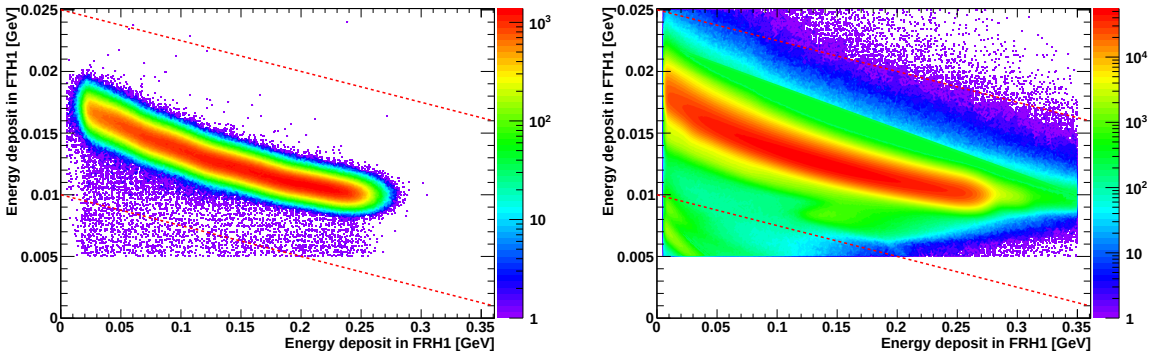

(a) MC simulation for $p\,d \to {}^3\mathrm{He}\,\eta$ reactions

(b) 2009 data

Figure 4.10: Energy deposit in the first layer of the FTH against the energy deposit in the first layer of the FRH: $\Delta E - E$ plot for ^{3}He identification. Particles with an energy deposit within the region which is bounded by the two red dashed lines are accepted.

or

$$E_{\mathrm{dep}}(\mathrm{FTH1}) > -0.025 \times E_{\mathrm{dep}}(\mathrm{FRH1}) + 0.025\,\mathrm{GeV} \tag{4.7}$$

are rejected. Due to the cuts on the energy deposits in the layers 2 – 5 of the FRH, the majority of entries in the shown figure comes from events where the ^{3}He nucleus are stopped in the first layer of the FRH. This is why there is no indication for a punch-through band. Although the preselection suppressed already events with deuterons and protons in the final state (*cf.* Fig. 4.5)), there is still an indication for a proton and deuteron band visible in the $\Delta E - E$ plot obtained from data (*cf.* Fig. 4.10). By applying the used cuts, events with these particles are suppressed.

For all measured particles in the FD it is checked whether they fulfill the described selection criteria for a ^{3}He nucleus. If the multiplicity of the charged tracks in the FD is larger than one and all of them fulfill the cuts, the event is rejected. However, this is only the case for very few events compared with the total number of events ((events with multiplicity = 2)/(events with multiplicity = 1) $\approx 10^{-5}$).

Figure 4.11 shows the missing mass distributions from the particles which fulfill the presented ^{3}He-selection criteria obtained from the 2008 and 2009 data. Since on this stage of the analysis there are no cuts on any specific η-decay channel, these distributions are used to extract the number of η events in the data sets after the preselection. Each distribution is fitted with a sum of a 5^{th} order polynomial function for the continuous background coming from reactions with direct-pion production (will be later denoted as direct-pion background), and a Gaussian function for the η peak. After subtraction of the direct-pion background, the events are counted which lie within three standard deviations around the peak center of the Gaussian function (peak center $\mu = 0.548\,\mathrm{GeV}/c^2$, $\sigma = 0.004\,\mathrm{GeV}/c^2$). The range is marked by two red lines in the inserts. There are $(11.26 \pm 0.01_{\mathrm{stat}}) \times 10^6$ η events in case of the 2008 data, and $(19.32 \pm 0.01_{\mathrm{stat}}) \times 10^6$ η events in case of 2009 data.

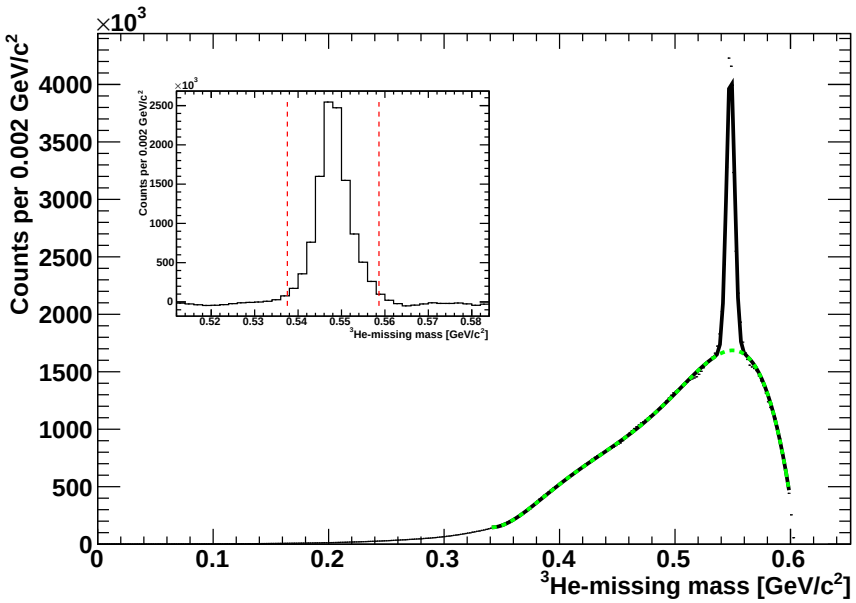

(a) 2008 data

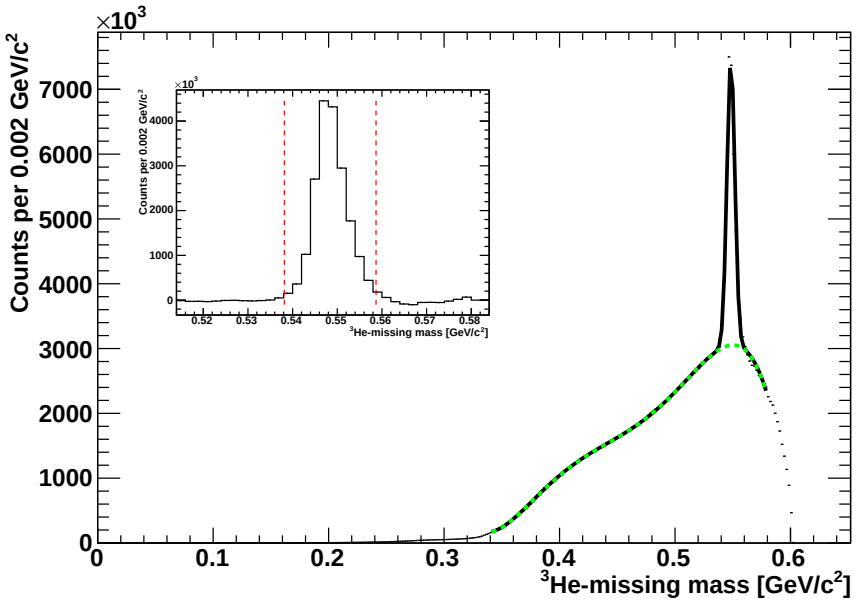

(b) 2009 data

Figure 4.11: ^{3}He-missing mass distribution after the basic ^{3}He-selection criteria. The black curve shows the fit which is composed of a Gaussian function for the η peak and a polynomial function (marked here in green) for the background from reactions with direct-pion production. The inserts show the background subtracted signal peak which contains $(11.26 \pm 0.01_{\text{stat}}) \times 10^6$ events (2008 data set) and $(19.32 \pm 0.01_{\text{stat}}) \times 10^6$ η events (2009 data set).

4.7 Filling trees

After the selection of events with a ^{3}He nuclei in the FD the data are further preselected by checking if the event has at least one positively and one negatively charged particle in the CD. The charged particle must have a cluster in the MDC in order to have access to their momenta and the sign of their charge. The selection of events with a ^{3}He nucleus and at least one positively and one negatively charged particle makes it possible to study the main signal reactions

$$p\,d \to {}^3\mathrm{He}\,(\eta \to e^+e^-e^+e^-) \tag{4.8}$$

and

$$p\,d \to {}^3\mathrm{He}\,(\eta \to e^+e^-) \tag{4.9}$$

and the monitoring channels

$$p\,d \to {}^3\mathrm{He}\,(\eta \to e^+e^-\gamma) \tag{4.10}$$

and

$$p\,d \to {}^3\mathrm{He}\,(\eta \to \pi^+\pi^-(\pi^0 \to e^+e^-\gamma)) \tag{4.11}$$

by analyzing the same preselected data set. One option for a fast data analysis would be to save the selected events in the same format as the original data sample (*i.e.* `*.ems` format). This makes the analysis of the data less time consuming since only events which possibly contain the signal- and normalization channels must be re-analyzed.

In this analysis, however, all the information which is needed for the further analysis of the selected events is saved in ROOT-trees [69]. These are data objects which consist of branches which contain the variables. Compared to the `*.ems` format, ROOT-trees enable a much faster access to the data. If the `ems`-files are read all the detector signals have to be translated into clusters and particle tracks, which is very time consuming. In case of trees, the information of the reconstructed particles, like the momentum and the energy deposit in the PSB or the SEC, is saved. Additionally, the needed disc space is significantly smaller. For example, the preselected `ems`-file of run 10392 from the 2008 data has a size of around 90 MB, whereas the tree has a size of around 5 MB.

In total, the number of events is reduced from approximately 1.4×10^8 (after ^{3}He-selection) to 5.8×10^7 (2008 data set), and from 2.5×10^8 to 1.1×10^8 (2009 data set).

Chapter 5

Monte Carlo Data Set

In order to describe the experimental data it is necessary to have a sufficient large data base of Monte Carlo events. This section lists the considered channels and the number of simulated events. In total more than 6.6×10^8 events were generated.

5.1 Monte Carlo data set for η-decay channels

In case of the η-decay channels, the signal reactions $\eta \to e^+e^-e^+e^-$ and $\eta \to e^+e^-$ and all decay modes with a finite value for the branching ratio were simulated. Only the channel $\eta \to \pi^0\gamma\gamma$ was not simulated since a contribution with charged particles to the final state is too small: The branching ratio for this channel is in the order of 10^{-4} and the probability for $\eta \to (\pi^0 \to e^+e^-\gamma)\gamma\gamma$ is in the order of 10^{-6}. Table 5.1 shows the decay modes and the number of simulated events.

Additionally, 10^7 ^{3}He-single track events and 2×10^7 electron and positron single track events were generated for the error parametrization of the kinematic fit. For the cut optimization which is used for the $p\,d \to {}^3\mathrm{He}\,(\eta \to e^+e^-)$ analysis, 10^7 signal events were simulated. The training of the artificial neural networks which are used for the particle identification is based on 2×10^7 pion single track events and the already mentioned 2×10^7 electron and positron single track events.

5.2 Monte Carlo data set for reactions with direct-pion production

Table 5.2 lists the considered reactions with direct-pion production and the number of simulated events.

Table 5.1: Simulated η-meson decays.

decay mode $\eta \to ...$	model	simulated events
$\gamma\gamma$	phase space	5×10^7
$\pi^0\pi^0\pi^0$	phase space	
$(\pi^0 \to \gamma\gamma)(\pi^0 \to \gamma\gamma)(\pi^0 \to \gamma\gamma)$		5×10^7
$(\pi^0 \to \gamma\gamma)(\pi^0 \to \gamma\gamma)(\pi^0 \to e^+e^-\gamma)$		1×10^6
$(\pi^0 \to \gamma\gamma)(\pi^0 \to e^+e^-\gamma)(\pi^0 \to e^+e^-\gamma)$		1×10^6
$(\pi^0 \to e^+e^-\gamma)(\pi^0 \to e^+e^-\gamma)(\pi^0 \to e^+e^-\gamma)$		1×10^5
$\pi^+\pi^-\pi^0$	matrix element [68, 86]	
$\pi^+\pi^-(\pi^0 \to \gamma\gamma)$		3×10^7
$\pi^+\pi^-(\pi^0 \to e^+e^-\gamma)$		1×10^6
$\pi^+\pi^-\gamma$	phase space	7×10^6
$\pi^+\pi^-\gamma$	matrix element [1]	7×10^6
$e^+e^-\gamma$	Landsberg FF [23, 68]	1×10^6
$\mu^+\mu^-\gamma$	Landsberg FF [23, 68]	1×10^5
$\pi^+\pi^-e^+e^-$	QED FF	1×10^5
$e^+e^-e^+e^-$	QED FF	5×10^5
$e^+e^-e^+e^-$	Bijnens FF [2]	5×10^5
$\mu^+\mu^-$	phase space	1×10^5
e^+e^-	phase space	1×10^5 and 10^7
sum		1.595×10^8

Table 5.2: Simulated reactions with direct-pion production. The particles are distributed according phase space.

reaction $p\,d \to {}^3\mathrm{He}\,X$ with $X = ...$	simulated events
$\pi^0 \to \gamma\gamma$	1×10^8
$\pi^0 \to e^+e^-\gamma$	4×10^6
$(\pi^0 \to \gamma\gamma)(\pi^0 \to \gamma\gamma)$	1×10^8
$(\pi^0 \to \gamma\gamma)(\pi^0 \to e^+e^-\gamma)$	4×10^6
$(\pi^0 \to e^+e^-\gamma)(\pi^0 \to e^+e^-\gamma)$	4×10^5
$(\pi^0 \to \gamma\gamma)(\pi^0 \to \gamma\gamma)(\pi^0 \to \gamma\gamma)$	1×10^8
$(\pi^0 \to \gamma\gamma)(\pi^0 \to \gamma\gamma)(\pi^0 \to e^+e^-\gamma)$	4×10^6
$(\pi^0 \to \gamma\gamma)(\pi^0 \to e^+e^-\gamma)(\pi^0 \to e^+e^-\gamma)$	4×10^5
$(\pi^0 \to e^+e^-\gamma)(\pi^0 \to e^+e^-\gamma)(\pi^0 \to e^+e^-\gamma)$	2×10^5
$\pi^+\pi^-$	1×10^8
$\pi^+\pi^-(\pi^0 \to \gamma\gamma)$	1×10^8
$\pi^+\pi^-(\pi^0 \to e^+e^-\gamma)$	4×10^6
sum	5.17×10^8

Chapter 6

Identification of the $\eta \to e^+e^-e^+e^-$ Events

6.1 Particle selection

There are two positrons and two electrons in the final state of the $\eta \to e^+e^-e^+e^-$ decay. For that reason, the first analysis step is to check whether the event has at least two positively and two negatively charged particles, measured with the CD. Each particle must have a cluster in the Mini Drift Chamber (MDC), since for these particles both the momenta and the sign of their electric charge is available. To ask for the minimum number of positively charged ($N_+ \geq 2$) and negatively charged ($N_- \geq 2$) particles reduces the number of preselected events to approximately 4 %: In case of the 2008 (2009) data from around 1.5×10^8 to 2130098 events (2.5×10^8 to 4450594 events). The reason why it is not requested that the event should have exactly two positively and two negatively charged particles is that an double Dalitz decay event candidate should be not rejected due to the occurrence of random coincidences.

The selection criteria which are described in this section check the basic properties of all of these tracks. If one particle fulfills the requirements of the cut it is accepted, otherwise it is rejected. After each cut it is checked if the event has still at least two positively and two negatively charged particles which were not rejected by the previous cuts. If not, the event is rejected.

At first, it is demanded that the charged particles have a scattering angle which lies within the geometrical acceptance of the CD. For that reason, particles with a scattering angle $\theta < 20°$ or $\theta > 169°$ are rejected. These are particles where the scattering angle was obviously wrongly reconstructed. The scattering-angle distribution of the charged particles in the CD and the used cuts are shown in Fig. 6.1. This distribution is obtained from the analysis of the 2009 data set.

The next analysis step is a cut on the time difference between the ^{3}He nucleus in the FD and each charged particle in the CD. This cut is used to check if the particles in the CD belong to the same reaction as the ^{3}He nucleus in the FD and helps to get rid of background coming from chance coincidences. For the particles in the CD the time signal can come from the PSB or from the comparatively slow SEC. For that reason, it is first checked if the particle has a cluster either in the PSB, or in the SEC. If PSB, the PSB time information is taken. This is the case for 93 % of the charged particles in the CD. Otherwise, the time information is taken from the SEC. Figure 6.2 shows the distribution of the time difference between the ^{3}He

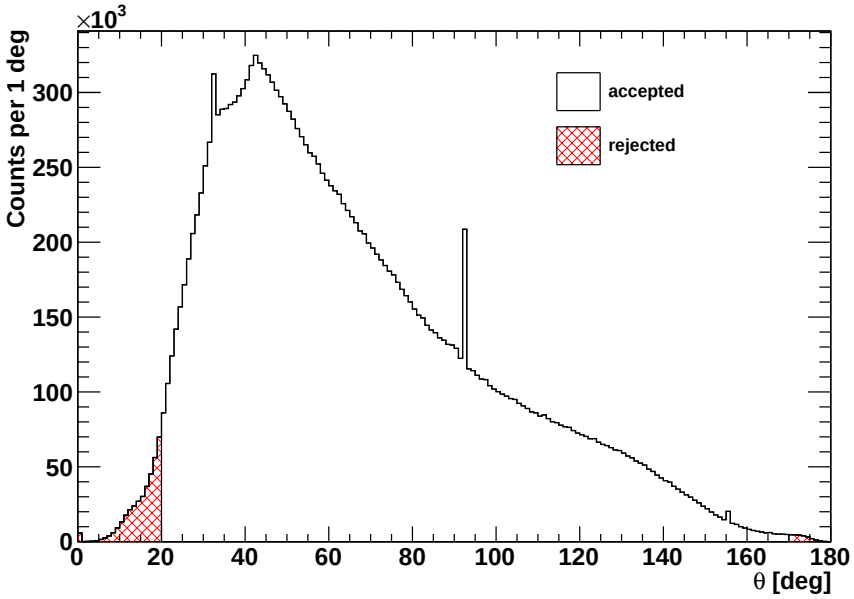

Figure 6.1: Scattering-angle distribution of the charged particles in the CD (2009 data). Particles with a scattering angle which is outside the geometrical acceptance are rejected. The spikes at 32.5°, 92.5°, and 155.5° are artifacts which disappear in the course of the further analysis by cuts on the minimum particle energies.

nucleus and the particles in the CD, which have a time signal from the PSB. Particles which lie within a time window of ±10 ns around the peak center are accepted. For the analysis of the 2008 data the used time window is ±15 ns. This is due to the fact that the width of the peak is wider (Gaussian fit of the peak: $\sigma \approx 2$ ns) compared with the peak in the distribution from the 2009 data (Gaussian fit of the peak: $\sigma \approx 1.5$ ns).

Figure 6.3 shows the time-difference distribution for particles in the CD without a cluster in the PSB, but with a SEC cluster providing the time signal. Since the time resolution of the SEC is much worse compared with the time resolution of the PSB, particles which lie within a time window of ±40 ns around the peak center are accepted for the further analysis. In case of neutral particles the time information always comes from the SEC. For that reason, the same cut is used for the photons in the analysis chain of the normalization channels $\eta \to e^+e^-\gamma$ and $\eta \to \pi^+\pi^-(\pi^0 \to e^+e^-\gamma)$.

The next analysis step is a cut on the closest distance between the trajectory of a particle and the point with the coordinates $(0, 0, 0)$, which is the assumed decay vertex. The coordinates of this point refer to the coordinate system which is described in Sect. 2.2.5. In order to get rid of particles which belong to products of secondary interactions, particles with a closest distance to the vertex in the xy-plane larger than 15 mm are rejected. The distance to the vertex is calculated in xy-plane since the helix parameters which describe the movement in this plane are more precise compared to the resolution of the parameters which describe the movement in the z-direction.

The closest approach distributions which are obtained from the analysis of the 2009 data and simulated $\eta \to e^+e^-e^+e^-$ events are shown in Fig. 6.4. The cut rejects 28 % of the charged particles of the 2009 data (27 % for the 2008 data), while only 3.6 % particles of the simulated

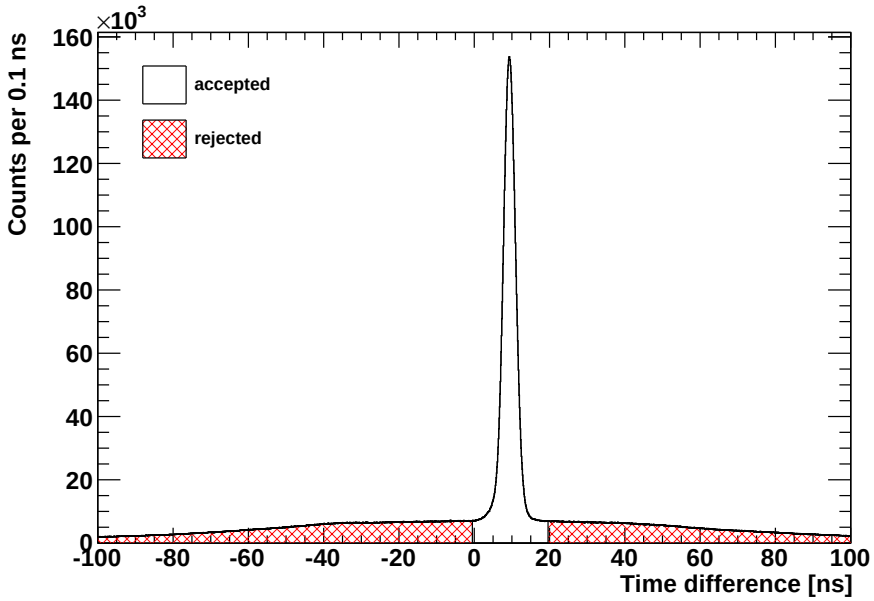

Figure 6.2: Distribution of the time difference between the ^{3}He nucleus in the FD and the particles in the CD, which have a time signal from the PSB (2009 data). Particles which lie within a time window of ±10 ns around the peak center are accepted. The cut is used to suppress background from chance coincidences.

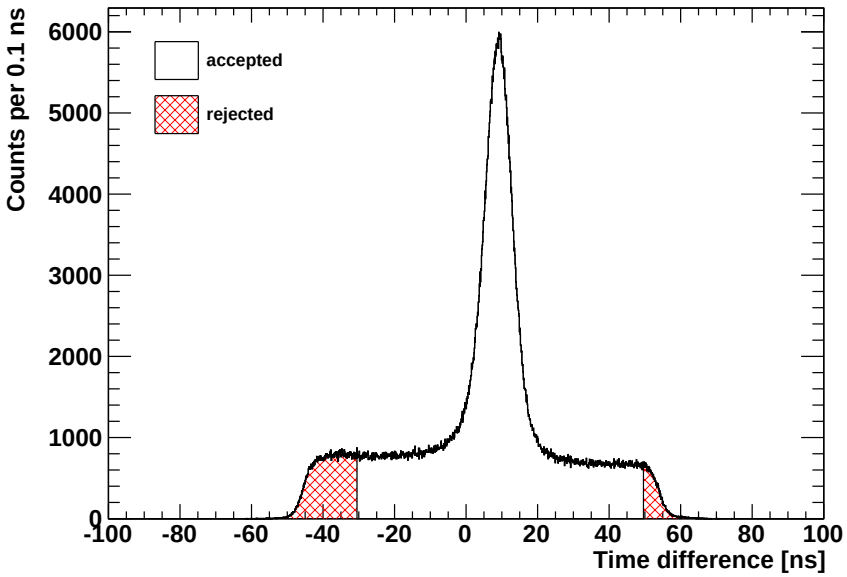

Figure 6.3: Distribution of the time difference between the ^{3}He nucleus in the FD and the particles in the CD, which have a time signal from the SEC (2009 data). Particles which lie within a time window of ±40 ns around the peak center are accepted. The cut is used to suppress background from chance coincidences.

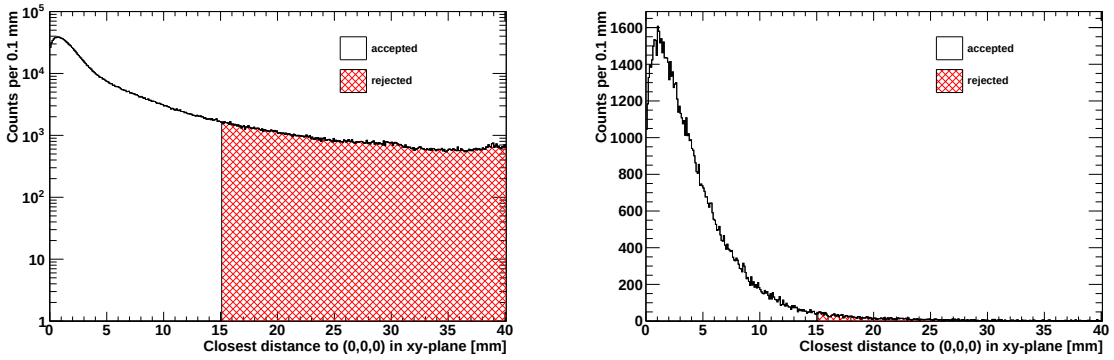

(a) 2009 data

(b) MC simulation for $\eta \to e^+e^-e^+e^-$

Figure 6.4: Closest distance in xy-plane between the trajectory of a particle and the assumed interaction vertex. Particles with a closest distance to the vertex larger than 15 mm are rejected. The cut is used to reject particles which belong to products of secondary interactions. The two spectra show a different shape since on this stage of the analysis the distribution from data is dominated by background events.

particles of the signal channel are rejected. Since an event which should be considered for the further analysis must have at least two positively and two negatively charged particles, around 60 % of the ^{3}He-tagged events in data are rejected by this cut, while only 11 % of the signal events are rejected.

6.2 Particle identification

More than 97 % of the charged decay modes of the η meson contain $\pi^+\pi^-$ pairs [11]. In order to suppress this huge amount of events with pions, a method to discriminate electrons (positrons) against pions is needed. In this analysis, artificial neural networks (ANN) are used for particle identification (PID). They will be introduced and explained in the first part of this section. Afterwards, it will be shown how the ANNs can be used at WASA to distinguish between electrons (positrons) and pions. Finally, the performance of the ANNs will be demonstrated. The PID algorithm judges for every particle whether it is an electron (positron) or a pion, independent of the decay channel which is investigated and of other particles from the same event.

6.2.1 Neural networks

A neural network is a system of connections which are made of nerve cells. They can be found in the brain of animals and human beings, where the human brain consists of several billions of such nerve cells [87]. This complex structure enables us to learn new abilities and to abstract and generalize from the learned to unknown situations.

An artificial neural network (ANN) is a mathematical abstraction of such a network structure. In 1943, the idea for an ANN was first proposed by W. S. McCulloch and W. H. Pitts in the article “A logical calculus of the ideas immanent in nervous activity” [88]. In the

meantime, ANNs are one important field in the research area of artificial intelligence. The applications reach, for example, from pattern recognition tasks, optimization processes, steering of robots, or for the prediction of stock prices [87]. Within the framework of this thesis, ANNs are used for particle identification in order to separate electrons (positrons) from pions.

Multilayer perceptrons, which are simple feed-forward networks, belong to the commonly used neural networks [89]. Such a network consists of neurons which are arranged in several layers. The first layer is named the input layer, whereas the last one is named the output layer. The other layers are called hidden layers. Each neuron in a certain layer is connected to each neuron from the previous and the subsequent layers. The strength of the links is characterized by weights. Following the structure of a brain, the weighted links are named synapses.

The dataflow through an ANN can be described as follows: The neurons of the input layer normalize their input values and forward them to the first hidden layer. Each neuron in any subsequent layer first computes a linear combination

$$x_i = \sum_{j=1}^{n} w_{ij} x_j \tag{6.1}$$

which is the sum of the outputs x_j for all n neurons of the previous layer times the weighting factor w_{ij}. x_i is then the argument of an activation function f, which returns the output y_i of the neuron, *i.e.*

$$y_i = f(x_i) = f\left(\sum_{j=1}^{n} w_{ij} x_j\right) . \tag{6.2}$$

f is a linear function for the output neurons of the last layer, while it is a sigmoid function (function of the form $f(x) = 1/(1 + e^{-x})$) for the neurons of the hidden layers.

Before the ANN can be used, the weighting factors w_{ij} must be determined with a learning algorithm. Here, a training set is needed consisting of events, which contain – for a given set of input values – the output values, which the network should ideally provide. With the learning algorithm the total error

$$\Delta = \frac{1}{2}\sqrt{\sum_i \Delta_i^2} \tag{6.3}$$

is minimized, where Δ_i is the error on each output neuron [89, 90].

In this analysis, the `TMultiLayerPerceptron` class of ROOT [69, 90] is used for the implementation of the multilayer perceptrons. To distinguish between electrons (positrons) and pions, the measured quantities of the three sub-detectors of the WASA CD are used: the momentum from the MDC, the specific energy loss in the PSB, and the energy deposit in the SEC.

Figure 6.5 shows the simulated distribution of the specific energy loss in the PSB for electrons, and positrons, and pions against the momentum times the charge of the particle. The specific energy loss is the energy deposit in the PSB, which is corrected for the path length of each particle through this detector. There is a separation between electrons (positrons) and pions especially for small momenta, while for larger momenta the bands overlap. Figure 6.6 shows energy deposits in the SEC against the momenta of the particles. The electrons and positrons create an electromagnetic shower in the calorimeter crystals and deposit their total energy in the SEC. Since for high energetic electrons and positrons the energy is approximately equal to the absolute value of the momentum, they lie on straight bands with the slope +1 for

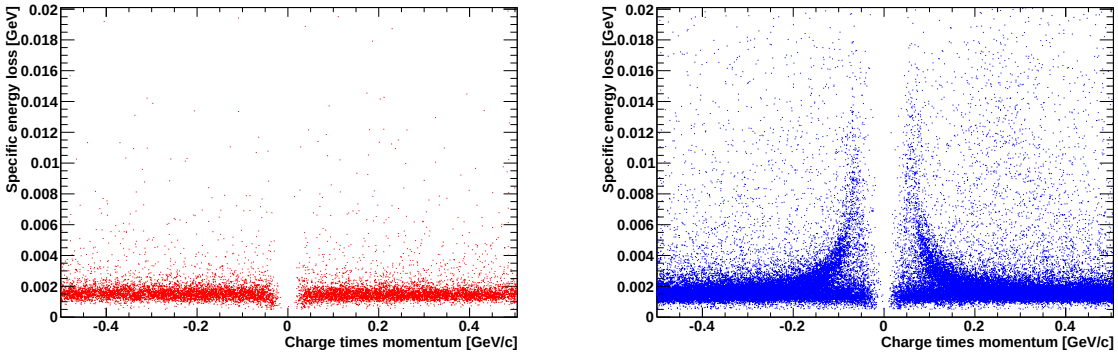

(a) MC simulation for $e^{\pm}$

(b) MC simulation for $\pi^{\pm}$

Figure 6.5: Simulated distribution of the specific energy loss in the PSB against the momentum times the charge of the particle. The distributions are obtained from Monte Carlo single-track events.

positrons and -1 for electrons. Compared to these leptons, pions deposit a smaller amount of energy for a given momentum.

In both PID plots there are spots which are more populated by electrons (positrons) compared to pions and vice versa. These distinct structures make it possible to distinguish between the two particle types.

The three measured quantities (momentum, specific energy loss in the PSB, energy deposit in the SEC) are the input values for the ANN. The output classifies every particle as an electron (positron) or pion. Since electrons and positrons on the one hand, and positively charged pions and negatively charged pions on the other hand have slightly different energy losses in the detectors, the ANNs are trained separately for positively and for negatively charged particles, respectively.

For some particles just the momentum information and the energy loss in the PSB, or the momentum and the energy deposit in the SEC is available. The first case occurs if a particle has a very small kinetic energy and is already stopped in the PSB. The second case occurs because of holes in the PSB material, or because of detection inefficiencies. Additionally, it is possible that a particle deposits only a small amount of energy in one of the detector elements. If this value is below the threshold which must be exceeded to be identified as a cluster, it will later not be considered in the track finder routine. For these two cases ANNs were created with only two neurons in the input layer. 55 % of all particles at this stage of the analysis have a cluster in all three CD sub-detectors (MDC-PSB-SEC class). Around 35 % of the particles are from the MDC-PSB class, and around 10 % of the particles are from the MDC-SEC class.

All mentioned network types consist of two hidden layers. The first hidden layer has five neurons, whereas the second hidden layer consists of three neurons. Figure 6.7 shows the structure of the multilayer perceptron for positively charged particles of the class MDC-PSB-SEC.

For each particle the output P of the ANN is a number "around" one if it is more likely a signal particle (electron/positron) or a number "around" zero if it is more likely a background

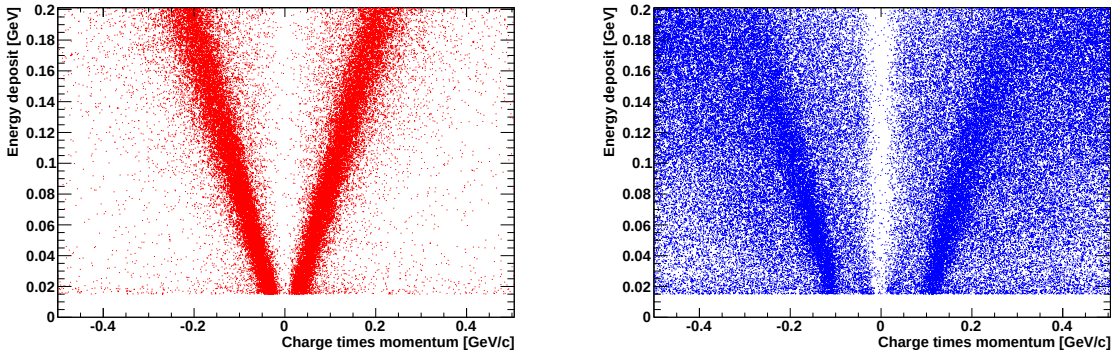

(a) MC simulation for $e^{\pm}$

(b) MC simulation for $\pi^{\pm}$

Figure 6.6: Simulated distribution of the energy deposit in the SEC against momentum times the charge of the particle. The distributions are obtained from Monte Carlo single-track events.

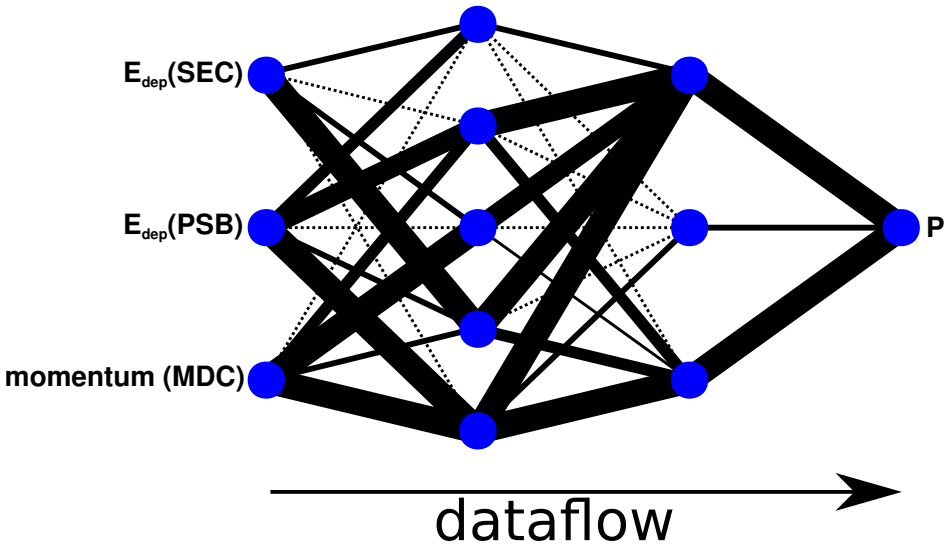

Figure 6.7: Multilayer perceptron for positively charged particles of the class MDC-PSB-SEC. The input layer consists of three neurons. There are two hidden layers with five and three neurons, respectively. The output neuron returns a value P which characterizes a particle to be more likely a positron or π^{+}. The different width of the connection lines between the neurons of the different layers denote the different strength of the connections, which is expressed by the weights w_{ij}.

particle (pion). These values can be smaller than zero or larger than one. Figure 6.8 shows the distributions of the ANN output values for e^- and π^- with a MDC, PSB, and SEC cluster.

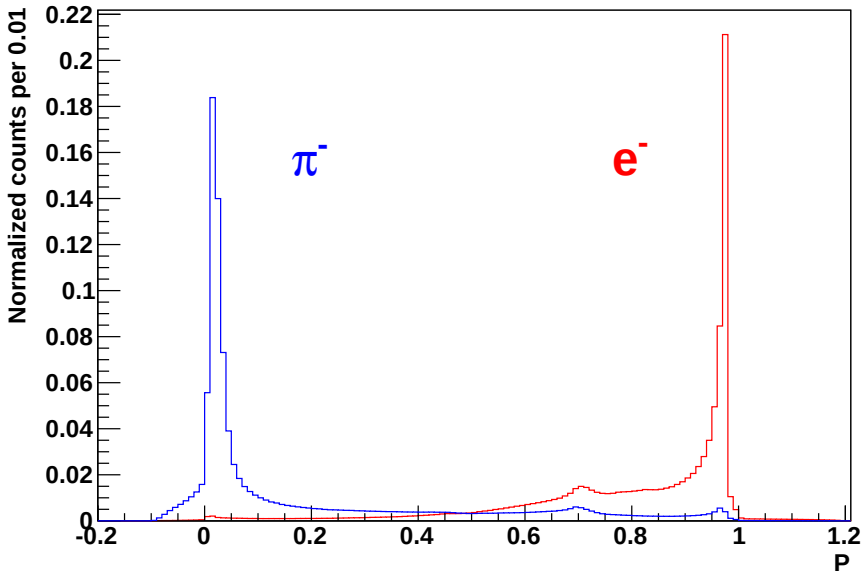

Figure 6.8: Normalized distributions of the ANN output values for simulated e^- and π^-. The particles have a MDC, PSB, and SEC cluster.

In order to constrain the ANN return value to lie in the range between zero and one, the value

$$L(P) = \frac{f_{e^\pm}(P)}{f_{e^\pm}(P) + f_{\pi^\pm}(P)} \tag{6.4}$$

is calculated for each particle which is processed through the ANN. $f_{e^\pm}(P)$ is the probability of a signal particle to get P, while $f_{\pi^\pm}(P)$ is the probability for a background particle to get P. The probability distributions $f_{e^\pm}(P)$ and $f_{\pi^\pm}(P)$ are obtained from Monte Carlo single-track events (*cf.* Fig. 6.8 for e^- and π^- from the MDC-PSB-SEC class). Since they are normalized such that their return values are in the range between zero and one, $L(P)$ is also constrained to this range.

The electron (positron) efficiency is a measure of the probability that an electron (positron) is correctly identified. The smallest value for L which a particle must have to be treated as an electron (positron) in order to achieve a certain $\varepsilon_{e^\pm}$ is determined by Monte Carlo single-track events. Related to the electron (positron) efficiency is the pion efficiency $\varepsilon_{\pi^\pm}$ which is the fraction of pions which are misidentified as electrons (positrons).

6.2.2 PID performance

Table 6.1 lists the ANN cut parameters $L_{\min}$ and the pion efficiencies for $\varepsilon_{e^\pm} = 95\,\%$ for the different networks for positively charged particles and negatively charged particles, respectively. The particle identification works the best for particles which have a signal in all three CD elements. For this class of particles around 80 % of the pions are rejected, and only 20 % are misidentified as electrons (positrons). For the other two classes roughly 50 % of the

pions are rejected. However, this means that 50 % of the pions are misidentified and wrongly treated as electrons (positrons).

Table 6.1: ANN cut parameter and pion efficiencies for $\varepsilon_{e^\pm} = 95\,\%$.

class	$L_{\min}$	ε_{π^+}	$L_{\min}$	ε_{π^-}
MDC-PSB	0.315	0.556	0.335	0.596
MDC-SEC	0.265	0.456	0.235	0.428
MDC-PSB-SEC	0.355	0.181	0.345	0.205

Figure 6.9 illustrates the specific energy loss in the PSB against the momentum times the charge of the particle for simulated $\eta \to \pi^+\pi^-(\pi^0 \to e^+e^-\gamma)$ and $\eta \to e^+e^-e^+e^-$ events before the PID and after the PID. And Fig. 6.10 shows the energy deposit in the SEC against the momentum obtained from the same decays. The distributions after the PID are filled with the particles which were identified as electrons (positrons). In the distributions from $\eta \to \pi^+\pi^-(\pi^0 \to e^+e^-\gamma)$ before the PID there are areas which are more populated by electrons (positrons) and pions, respectively. After the PID, the areas where pions are expected are significantly less populated, while the electrons (positrons) are more pronounced. In the distributions from $\eta \to e^+e^-e^+e^-$ there is nearly no loss of electrons (positrons) meaning that the signal particles are correctly identified.

The distribution for the specific energy loss in the PSB against the momentum of a particle times its charge before and after the PID can be seen in Fig. 6.11. Both plots are obtained from the analysis of the 2009 data. In addition to electrons, positrons and pions, there are also protons visible (especially in the distribution before the PID). They are located in the quadrant of the positively charged particles and have mostly a large specific energy loss compared with the other particle types. Additionally, they are spread over a larger area.

The distribution for the energy loss in the SEC against the momentum of the particle times its charge before and after the PID is shown in Fig. 6.12. It is obtained from the analysis of the 2009 data.

In both figures after the PID the spots where electrons (positrons) are expected to be are more pronounced, and pions have been successfully suppressed. The advantage of using ANNs for the PID over using, for example, a graphical cut on the PID plots is that all measured quantities from the CD sub-detectors are considered to distinguish between the particle types where the selection criteria can be expressed in one parameter.

6.3 Event selection

In this section, the event selection criteria for the $\eta \to e^+e^-e^+e^-$ events are presented. The charged particles which on this stage of the analysis are interpreted as electrons and positrons are combined to the electron-positron pairs each originating from one of the two virtual photons. In the first part of the analysis, the cuts evaluate whether the assigned electron-positron pairs can actually originate from one virtual photon. In the final step, a cut on the total invariant mass of the four particles significantly reduces the remaining amount of background.

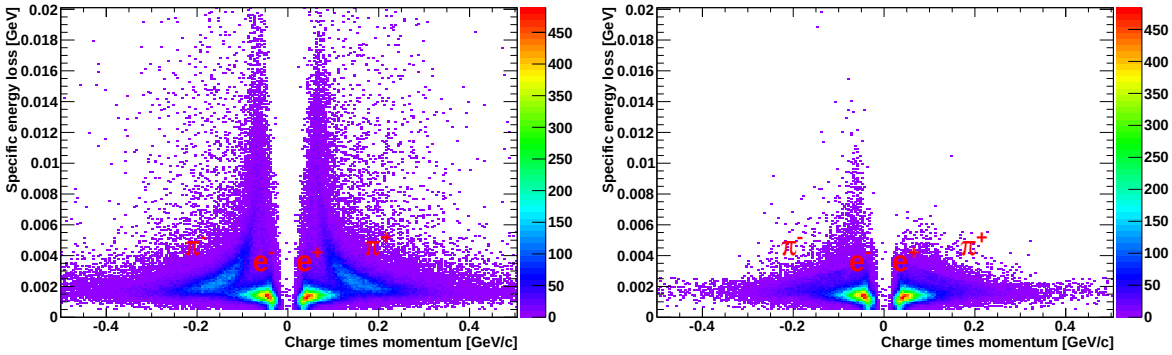

(a) $\eta \to \pi^+\pi^-(\pi^0 \to e^+e^-\gamma)$, before PID

(b) $\eta \to \pi^+\pi^-(\pi^0 \to e^+e^-\gamma)$, after PID

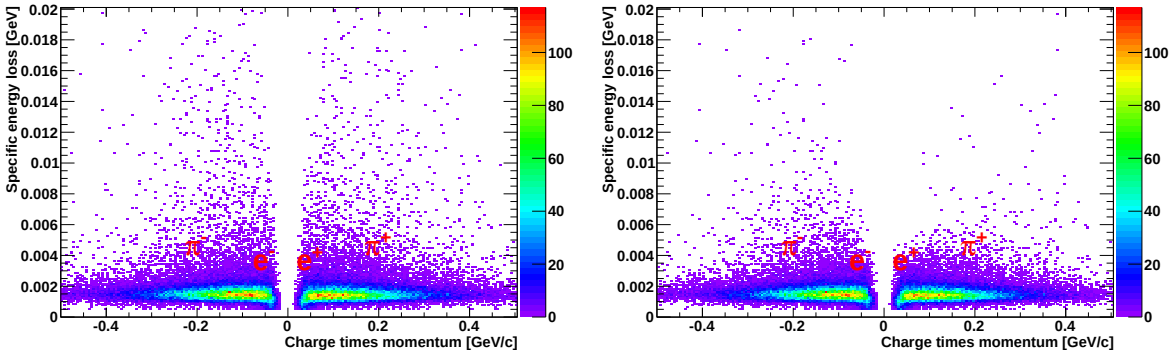

(c) $\eta \to e^+e^-e^+e^-$, before PID

(d) $\eta \to e^+e^-e^+e^-$, after PID

Figure 6.9: Specific energy loss in the PSB against the momentum times the charge of the particle for simulated $\eta \to \pi^+\pi^-(\pi^0 \to e^+e^-\gamma)$ and $\eta \to e^+e^-e^+e^-$ events.

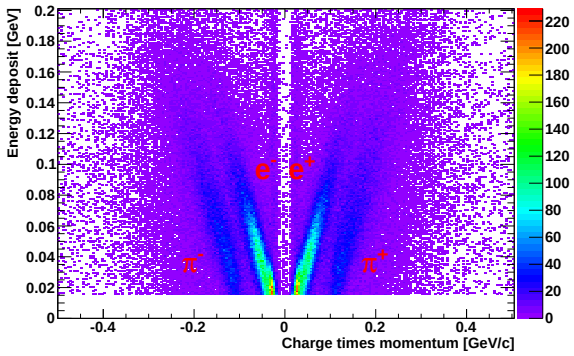

(a) $\eta \to \pi^+\pi^-(\pi^0 \to e^+e^-\gamma)$, before PID

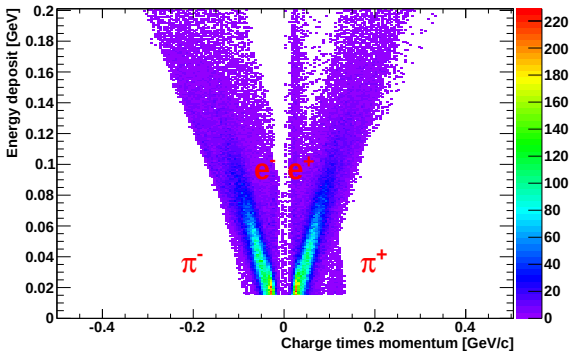

(b) $\eta \to \pi^+\pi^-(\pi^0 \to e^+e^-\gamma)$, after PID

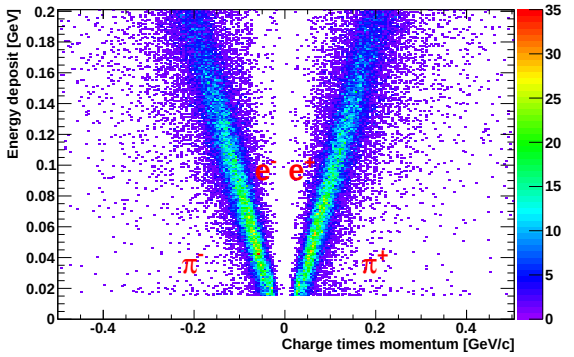

(c) $\eta \to e^+e^-e^+e^-$, before PID

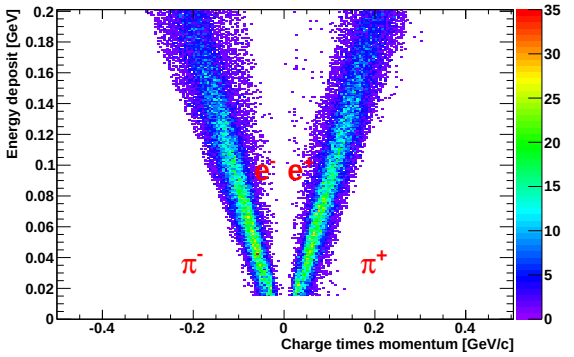

(d) $\eta \to e^+e^-e^+e^-$, after PID

Figure 6.10: Energy deposit in the SEC against the momentum times the charge of the particle for simulated $\eta \to \pi^+\pi^-(\pi^0 \to e^+e^-\gamma)$ and $\eta \to e^+e^-e^+e^-$ events.

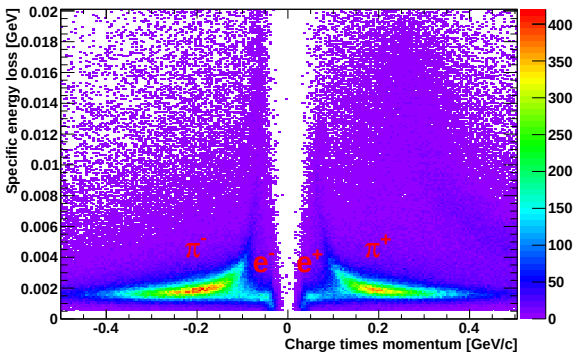

(a) before PID

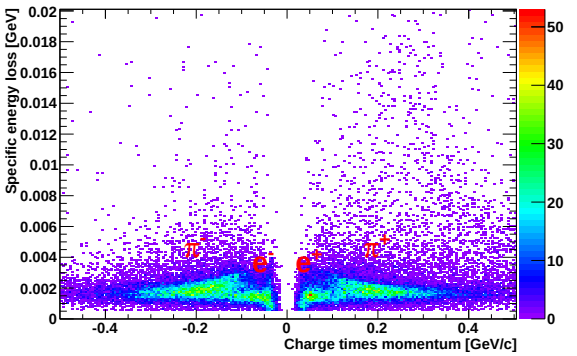

(b) after PID

Figure 6.11: Specific energy loss in the PSB against the momentum times the charge of the particle (2009 data).

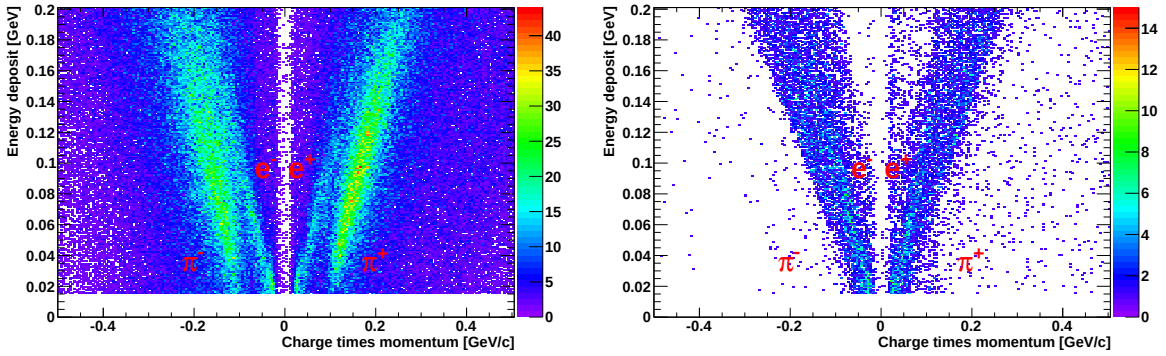

(a) before PID

(b) after PID

Figure 6.12: Energy deposit in the SEC against the momentum times the charge of the particle (2009 data).

6.3.1 Particle assignment

On this stage of the analysis an event has at least two positively and two negatively charged particles, which were not rejected by the previous selection criteria. These particles were identified as electrons (positrons) by the ANN. Every positively charged particle is now combined with every negatively charged particle as a candidate for the first or the second electron-positron pair. An electron-positron pair is the decay product of one of the virtual photons. There are

$$N = \frac{N_+ \times N_- \times (N_+ - 1) \times (N_- - 1)}{2} \tag{6.5}$$

possibilities to assign the particles to the two electron-positron pairs. N_+ is here the number of positively charged particles, and N_- is the number of negatively charged particles. Since it is arbitrary which electron-positron pair is named the first pair and which one is named the second, there is a factor 2 in the denominator. The assignment of the identified electrons and positrons to the virtual photons is demonstrated in Fig. 6.13.

In the following, it is checked for each of those N combinations whether it can be an $\eta \to e^+e^-e^+e^-$ double Dalitz decay event candidate or not. If one of the cut conditions is not fulfilled, only the track combination is rejected, not the entire event. This is demonstrated by Fig. 6.14.

Each distribution which will be shown to demonstrate the selection criteria (like opening-angle distribution) is filled with all track combinations which have fulfilled the previous cut conditions.

6.3.2 Electron-positron opening angle

The first selection criterion in order to identify $\eta \to e^+e^-e^+e^-$ events is based on the opening angle α between the electron and the positron which are treated as the decay products of the same virtual photon. Figure 6.15 illustrates the simulated opening-angle distribution for the signal channel with correctly assigned electron-positron pairs (red solid histogram), wrongly assigned electron-positron pairs (red dashed histogram), and for $\pi^+\pi^-$ pairs from

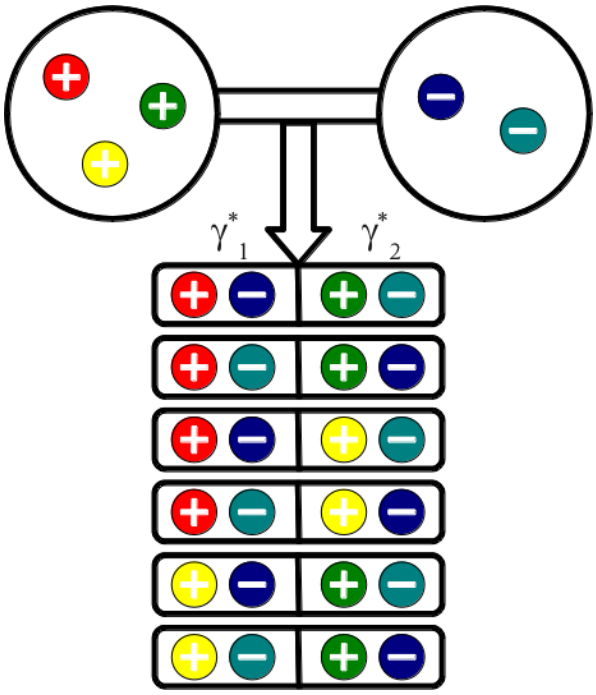

Figure 6.13: Every positively charged particle is combined with every negatively charged particle to one electron-positron pair from one of the two virtual photons (here γ_1^* and γ_2^*). As an example, the combination is demonstrated for three positively charged particles ($N_+ = 3$) and two negatively charged particles ($N_- = 2$).

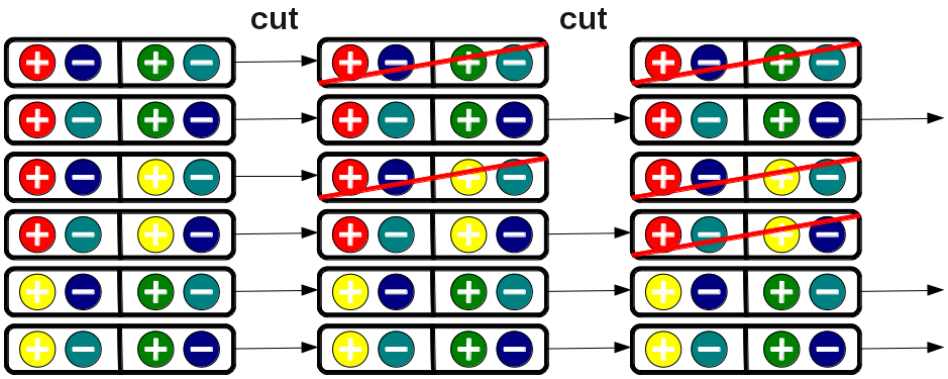

Figure 6.14: For every particle combination it is checked if the cut condition is fulfilled. If one cut condition is not fulfilled, only the track combination is rejected, not the entire event.

$\eta \to \pi^+\pi^-\pi^0$ reactions (blue solid histogram). The different histograms are normalized to the same integral.

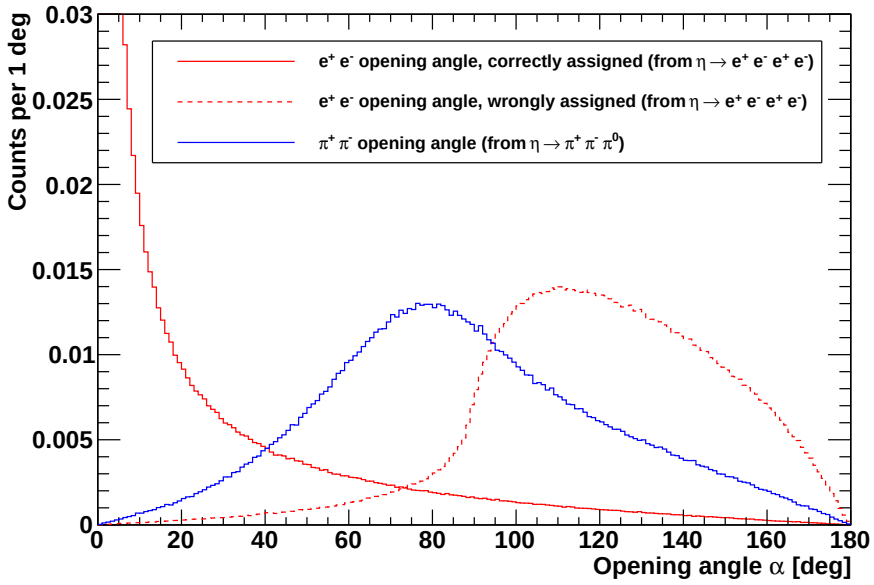

Figure 6.15: Simulated distribution of the opening angle α between the positively and negatively charged particles from the signal channel with correctly assigned electron-positron pairs (red solid histogram), wrongly assigned electron-positron pairs (red dashed histogram), and for $\pi^+\pi^-$ pairs (blue solid histogram). α is calculated in the laboratory frame. The pions are from $\eta \to \pi^+\pi^-\pi^0$ reactions. This reaction (with a subsequent single Dalitz decay of the pion) is one of the main background channels. All histograms are normalized to the same integral. The simulation is not a full WMC detector simulation, but a simulation with the event generator Pluto.

The opening angle is regarded in the laboratory frame and should be in this analysis for both electron-positron pairs smaller than or equal to 40°. This cut has two advantages: First, on this stage of the analysis there is still a huge contribution from η-decay channels with $\pi^+\pi^-$ pairs in the final state. As discussed earlier, the ANN has at best a pion-reduction factor of around

$$1 - \varepsilon_{\pi^-} = 1 - 0.2 = 80\,\% \tag{6.6}$$

which means that around 20 % of the pions are misidentified and wrongly treated as electrons (positrons). This reduction is obtained for particles with a MDC, PSB, and SEC cluster. The reduction factor for particles of the other two classes is roughly 50 %. Hence, not all of the η-decay channels with $\pi^+\pi^-$ pairs are suppressed so far. A cut on small opening angles between the positively and the negatively charged particle, which have been assigned to be the decay products of the same virtual photon, reduces the amount of pions significantly. For instance, according to simulations the number of $\eta \to \pi^+\pi^-\pi^0$ events is reduced to approximately 8 % by demanding $\alpha \leq 40°$.

The reason for a small opening angle α between the electron and the positron is that they originate from an off-shell photon with a small virtuality. The energy-momentum four-vector

for a dilepton is

$$\underline{\mathrm{p}}_{\gamma^*} = \underline{\mathrm{p}}_{e^+} + \underline{\mathrm{p}}_{e^-} \tag{6.7}$$

where $\underline{\mathrm{p}}_{e^+}$ is the energy-momentum four-vector of the positron and $\underline{\mathrm{p}}_{e^-}$ of the electron, respectively. Here, the energy of the leptons $E_{e^\pm}$ is much larger compared with their mass $m_{e^\pm}$ times the speed of light squared (*i.e.* $E_{e^\pm} \gg 0.511\,\mathrm{MeV}$). For that reason, the approximation can be made that the energy of the electrons (positrons) is proportional to their momenta. Squaring of Eq. 6.7 and using $E_{e^\pm} \approx p_{e^\pm} c$ leads to

$$m_{\gamma^*}^2 c^2 = 2 p_{e^+} p_{e^-} (1 - \cos\alpha) \tag{6.8}$$

where m_{γ^*} is the virtuality of the off-shell photon (mass of the dilepton), $p_{e^\pm}$ is the absolute value of the momentum of the positron and the electron, respectively. Equation 6.8 can be rewritten as

$$\cos\alpha = 1 - \frac{m_{\gamma^*}^2 c^2}{2 p_{e^+} p_{e^-}} \,. \tag{6.9}$$

Figure 6.16 illustrates the simulated dilepton-mass distribution from the reaction $\eta \to (\gamma^* \to e^+e^-)(\gamma^* \to e^+e^-)$. The insert shows the range of small masses. Due to energy conservation, the distribution starts at two times the electron mass and rises sharply towards large m_γ^*. Until the maximum of the distribution is reached, the phase-space and p-wave contribution dominate the virtual photon propagator. For larger m_{γ^*}, the contribution of the photon propagator dominates and leads to a rapid drop-off of the number of events with large values of m_{γ^*}. As a result of the fact that most of the dileptons have a mass close to threshold, the right part of Eq. 6.9 is mostly close to one, and therefore the opening angle is mostly small.

The second advantage of demanding small opening angles α is that most of the particle combinations with wrongly assigned electron-positron pairs from the signal channel are rejected (*cf.* Fig. 6.15). The opening angle β between the two virtual photons from the reaction $\eta \to (\gamma^* \to e^+e^-)(\gamma^* \to e^+e^-)$ in the laboratory system is mostly large. This is due to the fact that the two virtual photons are emitted "back-to-back" in the center-of-mass system, where the opening angle is always 180°. The boost into the laboratory system broadens the opening angle distribution and shifts the maximum to a smaller value. The simulated distribution of the opening angle β between the two virtual photons from the reaction $\eta \to (\gamma^* \to e^+e^-)(\gamma^* \to e^+e^-)$ can be seen in Fig. 6.17. Together with the previously discussed distribution for the opening angle α between the electron and the positron which originate from the same virtual photon, the opening angle between wrongly assigned electron-positron pairs must therefore be mostly large.

The distribution of the opening angle α is shown in Fig. 6.18. The histogram is obtained from the analysis of the 2009 data. Track combinations are accepted if α is for both electron-positron pairs smaller than or equal to 40°. On this stage of the analysis there is still a huge contribution from $\pi^+\pi^-$-pairs. This is why the distribution peaks at opening angles of around 80° as it is the case of the simulated distribution for $\eta \to \pi^+\pi^-\pi^0$ shown in Fig. 6.15. By using the marked cut events with pions are effectively suppressed.

6.3.3 Suppression of conversion events

The next cut suppresses events where a photon converts in the beam pipe into an electron-positron pair. The same method was already used by the KLEO collaboration in their analyses for the measurements of the $\eta \to e^+e^-e^+e^-$ and $\eta \to \pi^+\pi^-e^+e^-$ decays (*cf.* Refs. [9, 91]).

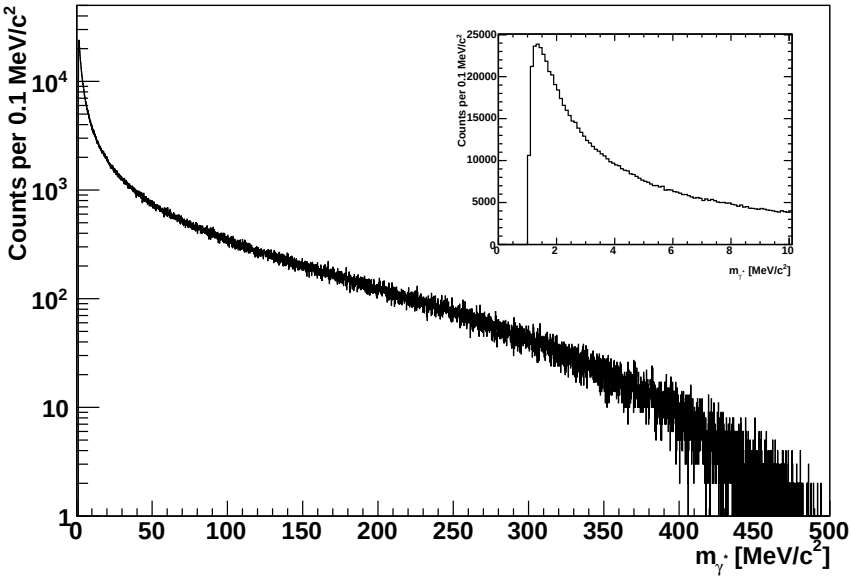

Figure 6.16: Simulated mass distribution of the virtual photons from the reaction $\eta \to (\gamma^* \to e^+e^-)(\gamma^* \to e^+e^-)$. The insert shows the range of small masses. The distribution begins at a mass of the virtual photon which is two times the electron mass. The simulation is not a full WMC detector simulation, but a simulation with the event generator Pluto.

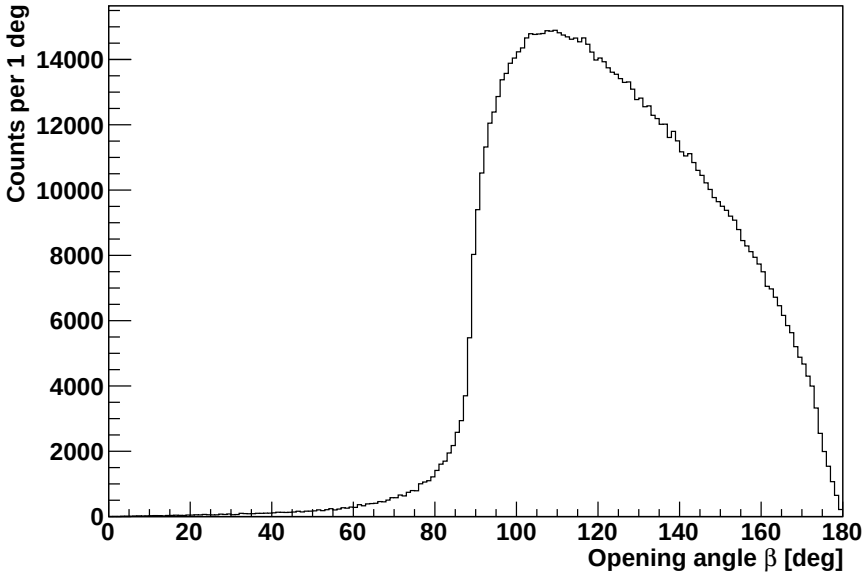

Figure 6.17: Simulated distribution of the opening angle β between the two virtual photons from the reaction $\eta \to (\gamma^* \to e^+e^-)(\gamma^* \to e^+e^-)$ in the laboratory frame. The two virtual photons are emitted "back-to-back" in the center-of-mass system, where the opening angle is always 180°. The boost into the laboratory system broadens the distribution. The simulation is not a full WMC detector simulation, but a simulation with the event generator Pluto.

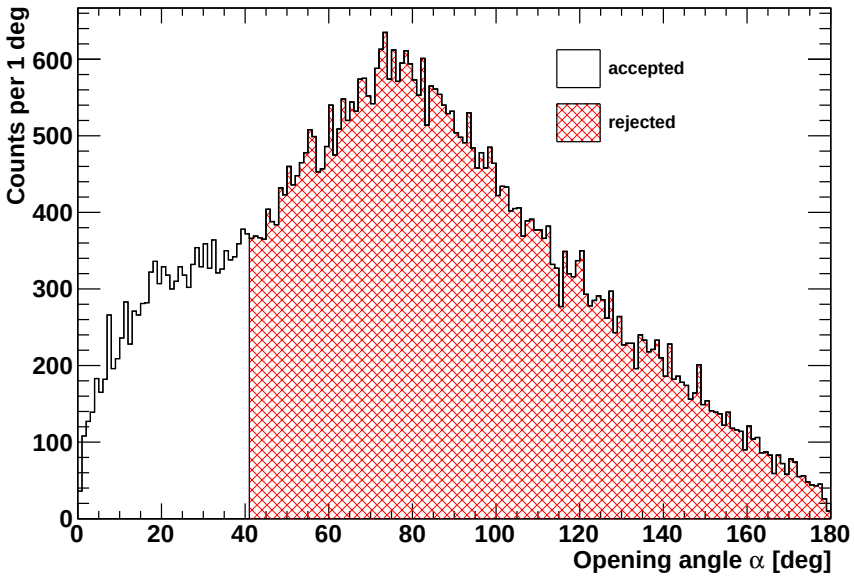

Figure 6.18: Opening-angle distribution between the positively and negatively charged particles which are treated as the electron and positron which originate from the same virtual photon (2009 data). Since on this stage of the analysis there is still a huge contribution from $\pi^+\pi^-$-pairs, the distribution peaks at opening angles of around 80°.

Although the probability that a photon converts in the WASA beam pipe (made of beryllium with a wall thickness of 1.2 mm) into an electron-positron pair is only 3×10^{-3} [92], events with conversion play a non-neglectable role when a rare decay channel is analyzed. For example, if the two real photons of the decay $\eta \to \gamma\gamma$ convert, there are the same particles as in case of the signal channel. This is also true if the real photon of the channel $\eta \to e^+e^-\gamma$ converts into an electron-positron pair. The simulated ratio between events with $\eta \to (\gamma \to e^+e^-)_{\text{conversion}}(\gamma \to e^+e^-)_{\text{conversion}}$ and the signal channel is 0.14. Whereas the ratio between the events with $\eta \to e^+e^-(\gamma \to e^+e^-)_{\text{conversion}}$ and the signal channel is 0.81[1].

The identification of events with photon conversion is based on two measured quantities. At first, the vertex of the electron-positron pair is determined by calculating the point of the closest distance between the reconstructed helices of the electron and the positron. Is in case of a conversion event, the distance in the xy-plane between this point and the beam-pellet interaction point is within the detector resolution equal to the radius of the beam pipe. For a signal event, however, the vertex of the electron-positron pair is close to the primary vertex, which means that the distance between the two points is small (close to zero). The corresponding cut variable will be named in the following as "radius of closest approach".

The other cut variable is the invariant mass of the electron-positron pair which is calculated from their energy-momentum four-vectors at the points where they traverse the beam pipe. This cut variable will be named as "invariant mass at beam pipe". The decay products of non-conversion events originate from a virtual photon which decays in the direct vicinity

[1]For the calculations of the ratios $\mathcal{BR}(\eta \to e^+e^-e^+e^-) = 2.6 \times 10^{-5}$ is used, which is the theoretical prediction based on QED calculations [3].

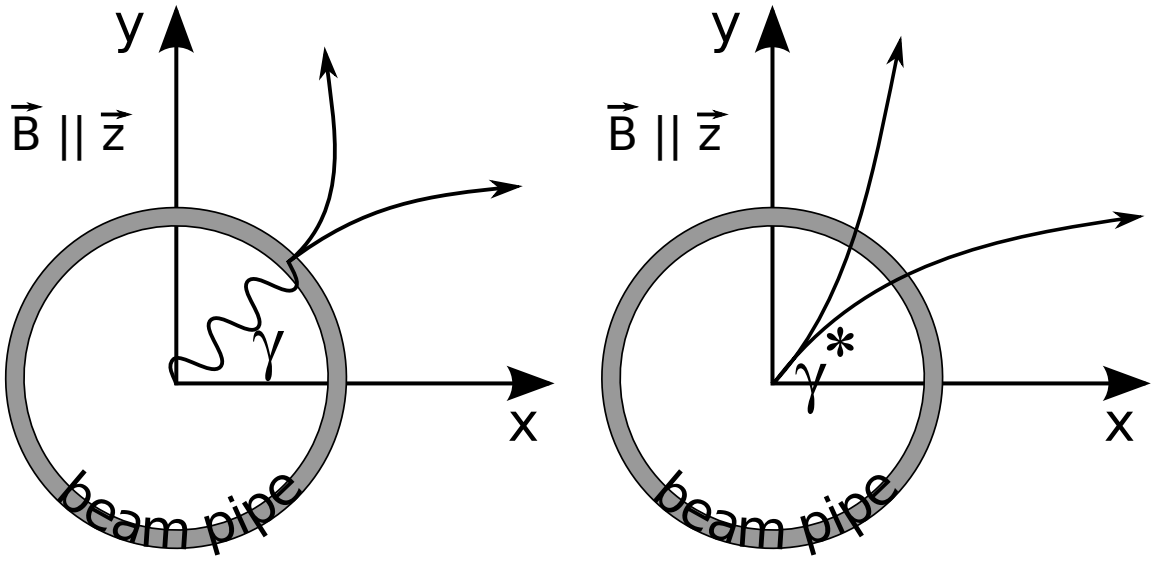

(a) conversion event (b) non-conversion event

Figure 6.19: Illustration of the method applied to suppress events where a photon converts in the beam pipe. The arrows denote the momenta of the electron and the positron, respectively. In case of conversion of a real photon the closest distance between the reconstructed electron and positron helices is reached at the radius of the beam pipe. The invariant mass of the particles, calculated from their energy-momentum four-vectors at the beam pipe, is around two times the electron mass. For non-conversion events the closest distance distance between the reconstructed electron and positron helices is reached close the the beam target interaction point, while the invariant mass (calculated from their energy-momentum four-vectors at the beam) is large. This is due to a large opening angle between the electron and the positron which they have when they traverse the beam pipe after their flight through the magnetic field within the MDC.

to the beam-pellet interaction point into an electron-positron pair. During the flight of the two leptons through the magnetic field within the MDC, their opening angle increases. This results in larger values for their invariant mass at the beam pipe compared to their true invariant mass. For conversion events, however, this value is around two times the electron mass.

The two cut conditions are illustrated by Fig. 6.19.

A simulated distribution for the radius of the closest approach against the invariant mass of the lepton pair calculated from their energy-momentum four-vectors at the beam pipe for the signal channel and for the reaction $\eta \to \gamma\gamma$ can be seen in Fig. 6.20. There is a densely populated region at small invariant masses around the radius of closest approach of 30 mm, which is the radius of the beam pipe. For non-conversion events the radius is mostly smaller and their invariant mass at the beam pipe is larger.

Electron-positron pairs are accepted if they lie in the rectangle area, meaning that the radius of the closest approach must be smaller than or equal to 25 mm. Their invariant mass at the beam pipe must be larger than or equal to $0.01\,\mathrm{GeV}/c^2$. The two conditions must

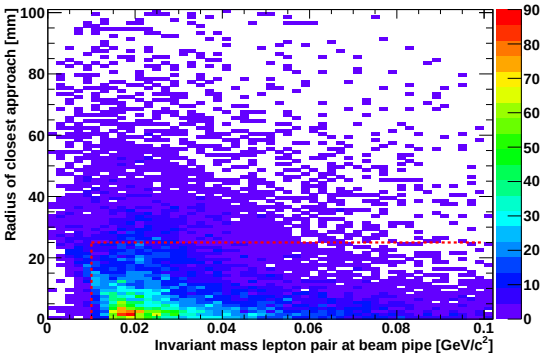

(a) Simulated $\eta \to e^+e^-e^+e^-$ events

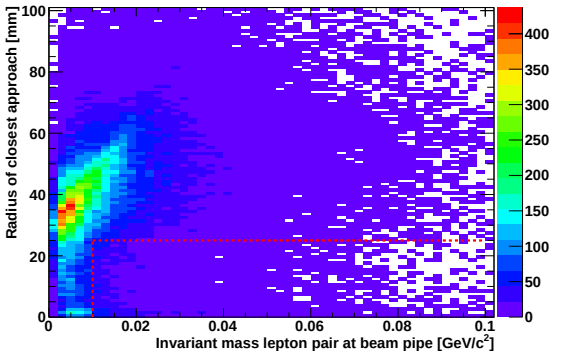

(b) Simulated $\eta \to \gamma\gamma$ events

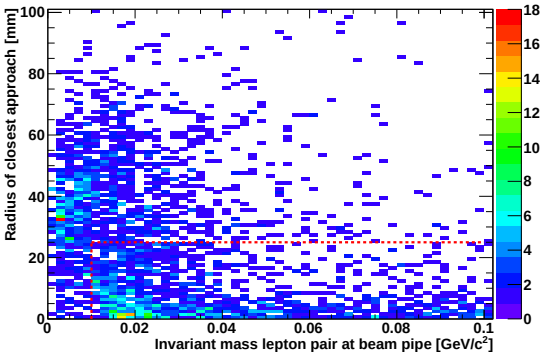

(c) 2009 data, analysis chain for the signal channel $\eta \to e^+e^-e^+e^-$

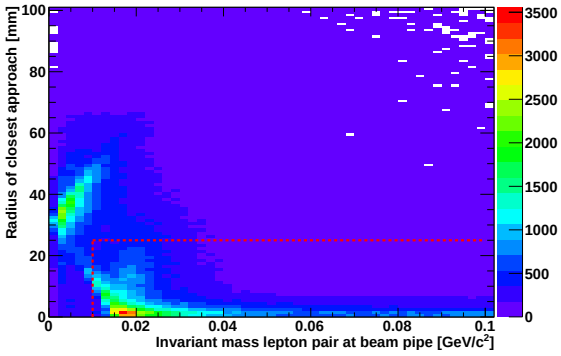

(d) 2009 data, analysis chain for the monitoring channel $\eta \to e^+e^-\gamma$

Figure 6.20: Radius of the closest approach against the invariant mass of the lepton pair calculated from their energy-momentum four-vectors at the beam pipe. Electron-positron pairs are accepted if the radius of the closest approach is smaller than or equal to 25 mm. The invariant mass must be larger than or equal to 0.01 GeV/c^2. The cuts are marked by the two red dashed lines.

be fulfilled by both electron-positron pairs which are assigned to an $\eta \to e^+e^-e^+e^-$ event candidate. By demanding these conditions the number of $\eta \to e^+e^-\gamma$ events is reduced to 7 %, $\eta \to \gamma\gamma$ to 2 %, and $\eta \to (\pi^0 \to \gamma\gamma)(\pi^0 \to \gamma\gamma)(\pi^0 \to \gamma\gamma)$ to 3 %. By achieving these large reduction factors it must be accepted that 44 % of signal events are rejected.

Figure 6.20 shows the distribution for the radius of the closest approach against the invariant mass at the beam pipe which is obtained from the analysis of the 2009 data. Since the distribution on this stage of the analysis is already sparsely populated, Fig. 6.20 also shows the distribution from the analysis chain of the monitoring channel $\eta \to e^+e^-\gamma$. In this plot the two regions with conversion events and non-conversion events can be seen as it was illustrated with the simulated distributions.

6.3.4 Invariant mass

Figure 6.21 shows the development of the efficiency times the branching ratio for all simulated η-decay channels after every selection criterion. Here, the branching ratio of the signal channel $\eta \to e^+e^-e^+e^-$ is assumed to be $\mathcal{BR}(\eta \to e^+e^-e^+e^-) = 2.6 \times 10^{-5}$, which is the theoretical prediction based on QED calculations [3]. The plot already includes the last cut on the invariant mass of the decay products, which is discussed in this subsection. After the previous cuts there is still a contribution from η decays with a single Dalitz decay of the pion. Especially the decay $\eta \to (\pi^0 \to \gamma\gamma)(\pi^0 \to e^+e^-\gamma)(\pi^0 \to e^+e^-\gamma)$ is not sufficiently suppressed (blue dotted line). The signal to background ratio is on this stage of the analysis $S/B = 0.46$. This ratio is the efficiency times the branching ratio of the signal channel divided by the sum of the efficiency times the branching ratio of the other η-decay channels.

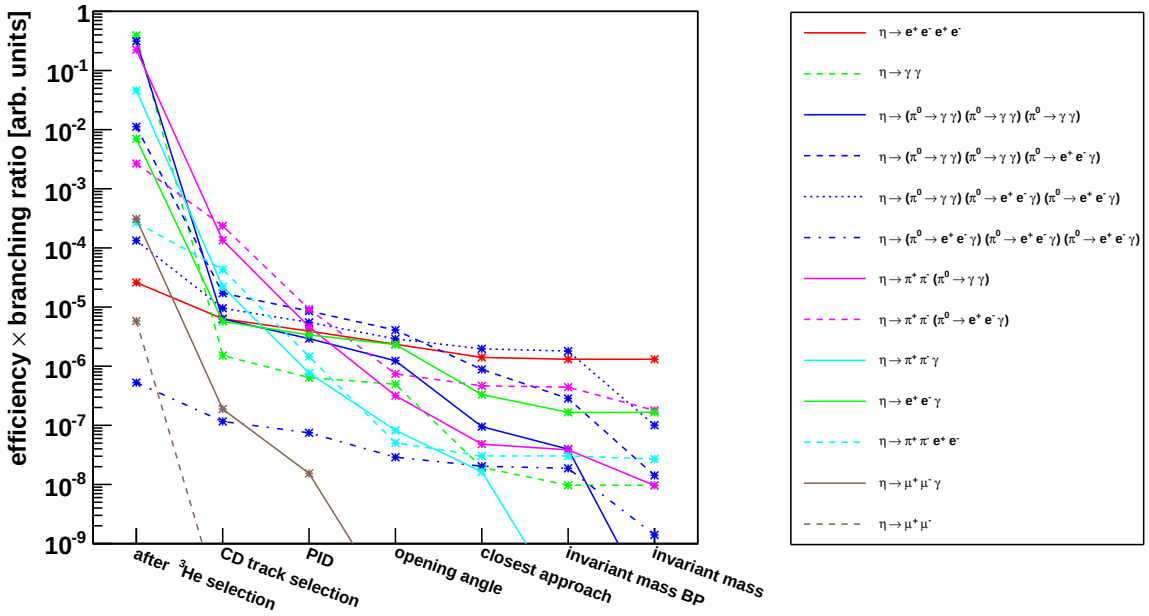

Figure 6.21: Development of the efficiency times the branching ratio for all simulated η decay channels after every selection criterion. This plot already includes the last cut on the invariant mass of the decay products, which is discussed within this subsection. The values for the efficiency times the branching ratio after a selection criterion is independent of the sequence of the previously applied cuts.

The simulated invariant $e^+e^-e^+e^-$ mass distribution for the channels $\eta \to e^+e^-e^+e^-$ and $\eta \to (\pi^0 \to \gamma\gamma)(\pi^0 \to e^+e^-\gamma)(\pi^0 \to e^+e^-\gamma)$ can be seen in Fig. 6.22. The invariant mass of four charged particles from the decay $\eta \to (\pi^0 \to \gamma\gamma)(\pi^0 \to e^+e^-\gamma)(\pi^0 \to e^+e^-\gamma)$ is smaller compared with the invariant mass of the four charged particles from the signal decay, since not all particles of the reaction are considered. Event candidates are accepted where the invariant mass of the four leptons is larger than or equal to $0.275\,\mathrm{GeV}/c^2$. By using this cut the number of $\eta \to (\pi^0 \to \gamma\gamma)(\pi^0 \to e^+e^-\gamma)(\pi^0 \to e^+e^-\gamma)$ events is reduced to 6 %, whereas there is nearly no loss of signal events (approximately 0.1 %, *cf.* Fig. 6.21). The signal to background ratio rises from $S/B = 0.46$ to $S/B = 2.6$.

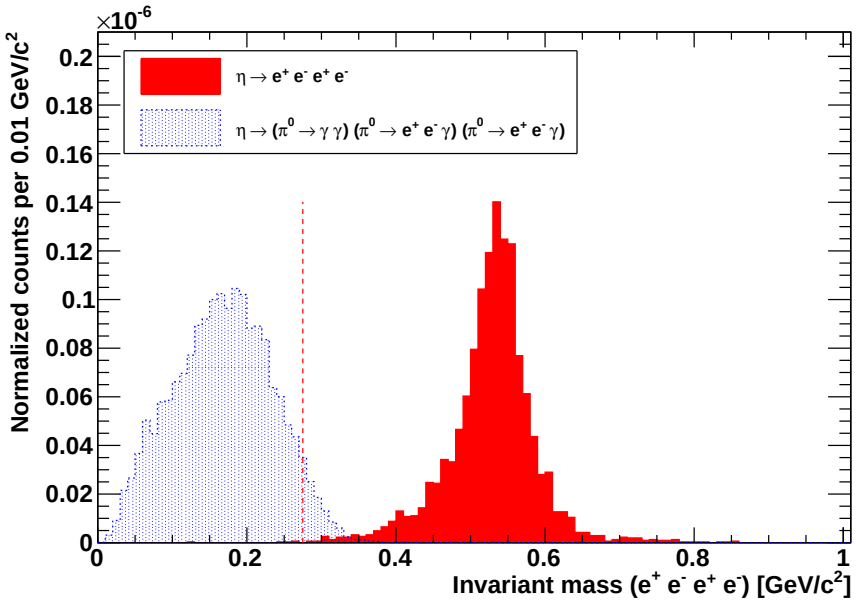

Figure 6.22: Simulated distribution of the invariant mass of the four charged particles from the decays $\eta \to e^+e^-e^+e^-$ and $\eta \to (\pi^0 \to \gamma\gamma)(\pi^0 \to e^+e^-\gamma)(\pi^0 \to e^+e^-\gamma)$. The histograms are normalized that their integrals are proportional to the number of expected events on this stage of the analysis. Event candidates with an invariant mass equal to or larger than $0.275\,\mathrm{GeV}/c^2$ are accepted. This cut is marked by the red dashed line.

The distribution of the invariant mass of the four identified leptons against the ^{3}He-missing mass can be seen in Fig. 6.23. The plot is obtained from the analysis of the 2009 data. In case of the η-decay channels (events where the ^{3}He-missing mass is in the range of the η mass), the decay $\eta \to (\pi^0 \to \gamma\gamma)(\pi^0 \to e^+e^-\gamma)(\pi^0 \to e^+e^-\gamma)$ contributes the most to the bin with the maximum contend. The reactions with the direct production of two neutral pions which decay via the single Dalitz decays have a similar signature and also end up in the same range of the invariant mass. However, they have a wider spread in the ^{3}He-missing mass distribution, which makes it possible to describe this background with a continuous function and subtract it from the final ^{3}He-missing mass distribution. This is not possible for $\eta \to (\pi^0 \to \gamma\gamma)(\pi^0 \to e^+e^-\gamma)(\pi^0 \to e^+e^-\gamma)$ events. For that reason, these events need to be suppressed which is achieved by the cut (marked by the red dashed line).

The second most populated bin in Fig. 6.23 comprises exactly the range where the $\eta \to e^+e^-e^+e^-$ events are supposed to lie.

6.4 Results

In this section, the results of the analysis of $\eta \to e^+e^-e^+e^-$ and the monitoring channels will be presented, and the systematical error on the branching ratio will be discussed.

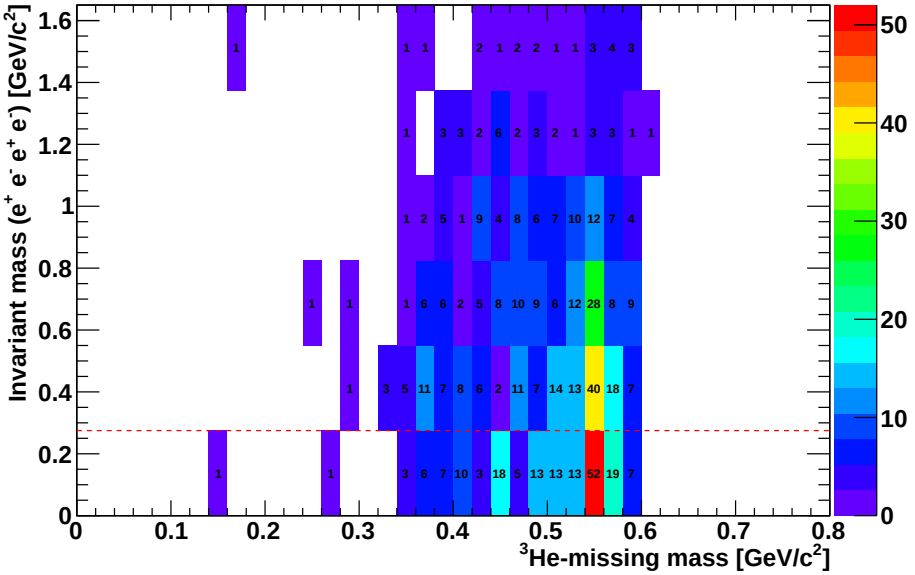

Figure 6.23: Invariant mass of the four identified decay particles against the ^{3}He-missing mass (2009 data). Event candidates with an invariant mass above $0.275\,\mathrm{GeV}/c^2$ are accepted. This cut is marked by the red dashed line.

6.4.1 Determination of the number of $\eta \to e^+e^-e^+e^-$ events

The ^{3}He-missing mass distribution is the monitoring spectrum, which is filled for every event which passed a given cut and all the previous selection criteria. Figure 6.24 shows the development of the ^{3}He-missing mass distribution after every cut which are used to select the $\eta \to e^+e^-e^+e^-$ decay channel for the 2008 and 2009 data. It is important to mention that every event is assigned at maximum to one ^{3}He candidate. For that reason, the final ^{3}He-missing mass distributions have at maximum one entry per event. In contrast to this, the distribution which were shown to demonstrate the used cuts were filled with all track combinations which have fulfilled the previous selection criteria. This is due to the fact that this analysis evaluates every track combination if it could be a double Dalitz decay or not. This means that if the ^{3}He-missing mass spectrum is filled, there must be at least one double Dalitz decay event candidate.

The final ^{3}He-missing mass distributions (these are the black histograms in Fig. 6.24) are used to extract the number of identified signal events. The histograms are fitted with the sum of a Gaussian function for the η peak and a polynomial function of order two for the continuous background from reactions with direct-pion production. The parameters for the peak center of the Gaussian function and its standard deviation are fixed according to the fit values from the initial ^{3}He-missing mass distribution after the selection of the ^{3}He nuclei (*cf.* Fig. 4.11).

Since the shape of the background from the reactions with direct-pion production should be in both cases the same, the histograms are fitted with the same quadratic function in the same range. The only difference between the two functions is a scaling factor which considers the different number of entries in the two histograms. Figure 6.25 shows the final ^{3}He-missing

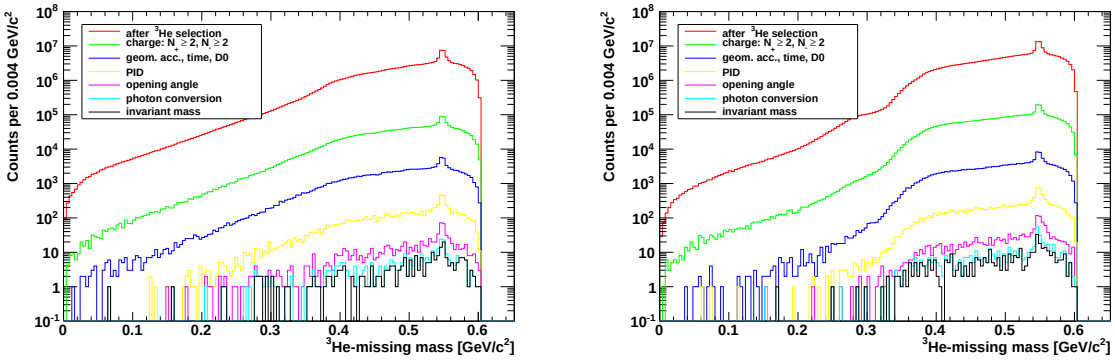

(a) 2008 data

(b) 2009 data

Figure 6.24: Development of the ^{3}He-missing mass distribution during the different stages of the analysis chain to identify $\eta \to e^+e^-e^+e^-$ events.

mass spectrum and the fit from the 2008 and 2009 data. The black solid curve is the sum of the Gaussian function and the polynomial function, while the green dashed curve is just the polynomial function. Due to the poor statistics, the fit of the histograms is based on the likelihood method. This technique assumes a Poisson probability function for each bin and considers also empty bins, which is not the case for a χ^2-fit [93].

The number of η events in the final ^{3}He-missing mass distribution is extracted by counting the background subtracted entries which lie within a $\pm 3\sigma$ range around the center of the η peak. In case of the 2008 data there are $N_{\eta,\mathrm{f}} = 21.5 \pm 7.7_{\mathrm{stat}}$ remaining events from η decays, and in case of the 2009 data there are $N_{\eta,\mathrm{f}} = 43.7 \pm 9.9_{\mathrm{stat}}$ remaining events from η decays.

The number of signal events is the difference between $N_{\eta,\mathrm{f}}$ and the sum of all η decay background channels which are expected to end up in the η peak of the final ^{3}He-missing mass distribution. This number is

$$N_{\eta,\mathrm{bgd}} = N_{\eta,0} \times \left(\sum_i \varepsilon_i \times \mathcal{BR}_i \right) \tag{6.10}$$

where $N_{\eta,0}$ is the number of identified η events after the ^{3}He selection. It was shown in Sect. 4.6 how this number is extracted. $N_{\eta,0} = (11.26 \pm 0.01_{\mathrm{stat}}) \times 10^6$ events were found in the 2008 data set and $N_{\eta,0} = (19.32 \pm 0.01_{\mathrm{stat}}) \times 10^6$ in the 2009 data set.

The sum in Eq. 6.10 is over all considered η background channels. ε_i is the efficiency and $\mathcal{BR}_i$ is the known branching ratio of the ith channel, which is taken from the PDG [94][2]. The efficiency of a channel is the number of events which reach the final ^{3}He-missing mass distribution divided by the number of events after the ^{3}He-selection cuts, which is on the same stage of the analysis where $N_{\eta,0}$ is extracted. These values are obtained from Monte Carlo simulations.

The efficiency times the branching ratio of the background channels and the development after the different cuts was already discussed in Sect. 6.3.4 and is shown in Fig. 6.21. In case

[2] In this analysis the values from Ref. [94] were taken with $\mathcal{BR}(\eta \to e^+e^-\gamma) = (7.0 \pm 0.7) \times 10^{-3}$ instead of the value $\mathcal{BR}(\eta \to e^+e^-\gamma) = (6.9 \pm 0.4) \times 10^{-3}$ from Ref. [11]

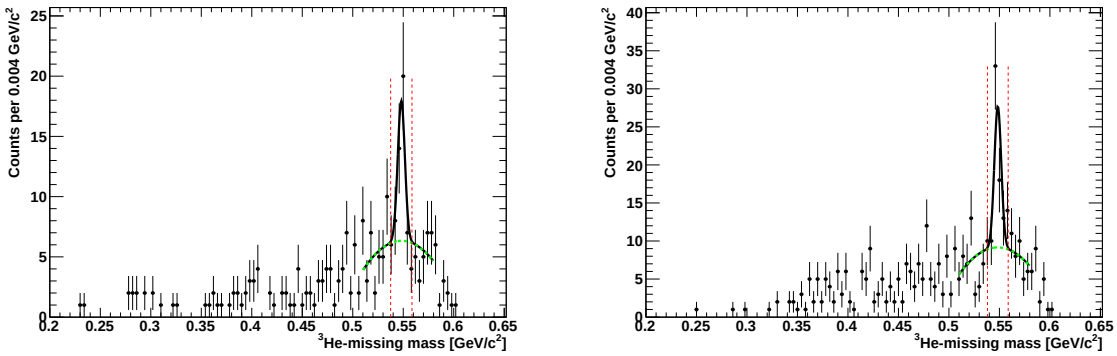

(a) 2008 data (b) 2009 data

Figure 6.25: Final ^{3}He-missing mass spectrum and the fit. The black solid curve is the sum of the Gaussian function and the polynomial function, while the green dashed line is just the polynomial function, which describes the background from reactions with direct-pion production. The red dashed lines mark the $\pm 3\sigma$ environment around the η-peak position.

of the 2008 data there are $N_{\eta,\mathrm{bgd}} = 5.7$ events in the final ^{3}He-missing mass spectrum, and $N_{\eta,\mathrm{bgd}} = 9.8$ events in case of the 2009 data. The statistical errors on these values, which are the propagated statistical errors of $N_{\eta,0}$, are neglected. The background is dominated by the three channels $\eta \to e^+e^-\gamma$ with a contribution of around 33 % to the sum of all η-background channels, $\eta \to \pi^+\pi^-(\pi^0 \to e^+e^-\gamma)$ with 35 %, and $\eta \to (\pi^0 \to \gamma\gamma)(\pi^0 \to e^+e^-\gamma)(\pi^0 \to e^+e^-\gamma)$ with 20 %.

The number of signal events can be calculated with the following formula

$$N_{\eta\to e^+e^-e^+e^-} = N_{\eta,\mathrm{f}} - N_{\eta,\mathrm{bgd}} \; . \tag{6.11}$$

This leads to $N_{\eta\to e^+e^-e^+e^-} = 15.8 \pm 7.7_{\mathrm{stat}}$ identified signal events in the 2008 data set and $N_{\eta\to e^+e^-e^+e^-} = 33.9 \pm 9.9_{\mathrm{stat}}$ signal events in the 2009 data set. The total number of identified $\eta \to e^+e^-e^+e^-$ double Dalitz decays is

$$\boxed{N_{\eta\to e^+e^-e^+e^-,\mathrm{tot}} = 49.7 \pm 12.5_{\mathrm{stat}}}$$

with a statistical significance of $4\,\sigma$. The ratio between the number of signal events and the number of background events coming from other η decays is $S/B = 3.2$.

Figure 6.26 shows the final ^{3}He-missing mass distribution after the subtraction of the background from reactions with direct-pion production for the 2008 data and the 2009 data, respectively. The red histogram is the contribution of the signal channel, and the blue histogram is the contribution of the remaining η-background channels. The yellow histogram is the sum of the signal and background channels.

Finally, the final ^{3}He-missing mass distribution after the subtraction of the background from reactions with direct-pion production from both data sets can be seen in Fig. 6.27.

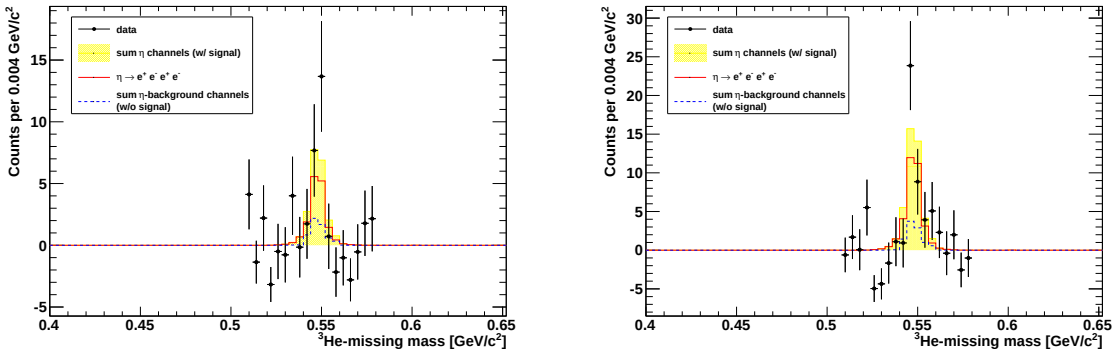

(a) 2008 data (b) 2009 data

Figure 6.26: Final ^{3}He-missing mass distribution after the subtraction of the background from reactions with direct-pion production. The red histogram is the contribution of the signal channel, and the blue histogram is the contribution of the η-background channels. The yellow histogram is the sum of the signal and background channels.

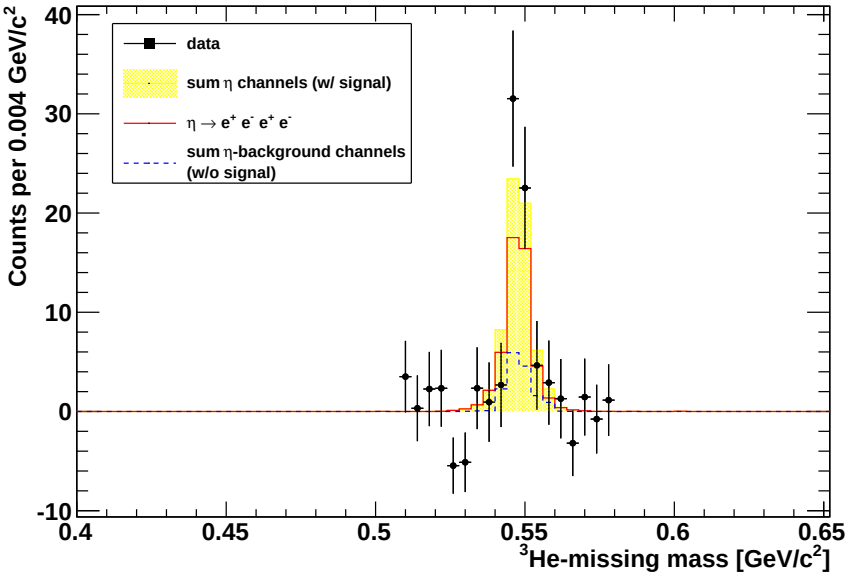

Figure 6.27: Final ^{3}He-missing mass distribution after the subtraction of the background from reactions with direct-pion production from both data sets. The total number of identified $\eta \to e^+e^-e^+e^-$ double Dalitz decays is $N_{\eta\to e^+e^-e^+e^-,\mathrm{tot}} = 49.7 \pm 12.5_{\mathrm{stat}}$. The ratio between the number of signal events and the number of background events coming from other η decays is $S/B = 3.2$. The sum of the η-background channels mainly consists of $\eta \to e^+e^-\gamma$, $\eta \to \pi^+\pi^-(\pi^0 \to e^+e^-\gamma)$, and $\eta \to (\pi^0 \to \gamma\gamma)(\pi^0 \to e^+e^-\gamma)(\pi^0 \to e^+e^-\gamma)$.

6.4.2 $\eta \to e^+e^-e^+e^-$ branching ratio

The branching ratio of a particle decay is the fraction of this decay probability into a certain final state relative to all possible decay modes:

$$\mathcal{BR}(\eta \to e^+e^-e^+e^-) = \frac{N_{\eta\to e^+e^-e^+e^-,0}}{N_{\eta,0}} \tag{6.12}$$

where $N_{\eta\to e^+e^-e^+e^-,0}$ is the initial number of signal events which were produced in total during the experiment. This number can be calculated as

$$N_{\eta\to e^+e^-e^+e^-,0} = \frac{N_{\eta\to e^+e^-e^+e^-}}{\varepsilon_{\eta\to e^+e^-e^+e^-}} \tag{6.13}$$

where $\varepsilon_{\eta\to e^+e^-e^+e^-}$ is the reconstruction efficiency for the signal channel. This number is generally based on Monte Carlo simulations and, in our case, is the number of signal events in the final ^{3}He-missing mass distribution divided by the number of events which fulfill the ^{3}He-selection criteria. In the present analysis, the reconstruction efficiency for the signal channel is 5 %.

Combining Eqs. 6.12 and 6.13, the branching ratio can be written as

$$\mathcal{BR}(\eta \to e^+e^-e^+e^-) = \frac{N_{\eta\to e^+e^-e^+e^-}}{\varepsilon_{\eta\to e^+e^-e^+e^-} \times N_{\eta,0}} \,. \tag{6.14}$$

The result for the branching ratio of the double Dalitz decay $\eta \to e^+e^-e^+e^-$ based on the present analysis of the 2008 data is $\mathcal{BR}(\eta \to e^+e^-e^+e^-) = (2.8 \pm 1.4_{\text{stat}}) \times 10^{-5}$. The same data set was earlier analyzed within a framework of a PhD thesis by L. Yurev, where $\mathcal{BR}(\eta \to e^+e^-e^+e^-) = (2.9 \pm 1.1_{\text{stat}}) \times 10^{-5}$ with a signal to background ratio of $S/B = 1/1$ was determined [10]. Both results are in a good agreement. Since the two analysis chains differ (the analysis in Ref. [10] is more based on the decay topology, without a PID), the agreement of the final results emphasize that the data set and the used cuts are well understood.

The result based on the analysis of the 2009 data is $\mathcal{BR}(\eta \to e^+e^-e^+e^-) = (3.5 \pm 1.0_{\text{stat}}) \times 10^{-5}$. This data set was not analyzed before.

The weighted mean of the present analysis of the two beam times and its standard deviation is

$$\boxed{\mathcal{BR}(\eta \to e^+e^-e^+e^-) = (3.2 \pm 0.8_{\text{stat}}) \times 10^{-5}} \,.$$

This value is, within less than one standard deviation, in agreement with the theoretical prediction for the branching ratio of $\mathcal{BR}(\eta \to e^+e^-e^+e^-) = 2.6 \times 10^{-5}$ which is based on QED calculations [3]. It is also in agreement with the measured value $\mathcal{BR} = (\eta \to e^+e^-e^+e^-) = (2.4 \pm 0.2_{\text{stat}}) \times 10^{-5}$ which comes from the KLOE collaboration [9].

6.5 Monitoring channels

The monitoring channels are studied and analyzed for two reasons. First, the influence of the different cuts can be tested based on a decay which has a known and well understood branching ratio. Since the branching ratio of such a monitoring channel is larger compared with the signal channel, the study enables to evaluate the cuts based on a data sample containing more events which are of interest. Additionally, the simulated distributions on

which the cuts are based on can be tuned to the measured data. In doing so, the simulated reconstruction efficiencies are brought in agreement with the "true" efficiencies. Second, in contrast to a calculation of the branching ratio based on an the identified η events in the initial ^{3}He-missing mass distribution (absolute normalization), the branching ratio can be also calculated relative the monitoring channel. By using the known branching fraction of the normalization channel, the relative branching ratio can be extrapolated to an absolute branching ratio. Any significant deviation between the results from the different calculation methods would be a sign for systematic effects.

In this analysis, the reactions $\eta \to e^+e^-\gamma$ and $\eta \to \pi^+\pi^-(\pi^0 \to e^+e^-\gamma)$ are used as monitoring channels, since they are the most contributing background channels in the final ^{3}He-missing mass distribution from the measurement of $\eta \to e^+e^-e^+e^-$. $\eta \to e^+e^-\gamma$ is closely related to the signal channel, since like in case of the double Dalitz decay the η meson couples to two photons. However, in case of the single Dalitz decay there is only one virtual photon which decays into an electron-positron pair. The other photon is real and can be identified with the detector. The $\eta \to e^+e^-\gamma$ decay is around 270 times more frequent than the double Dalitz decay[3].

The other monitoring channel is $\eta \to \pi^+\pi^-(\pi^0 \to e^+e^-\gamma)$. Like in case of the double Dalitz decay there are four charged particles in the final state. It is the second most contributing background channel in the final ^{3}He-missing mass distribution from the analysis of $\eta \to e^+e^-e^+e^-$. This decay is around 100 times more frequent than the double Dalitz decay[4].

Both analysis chains are very similar to that of the signal channel. Thus, systematic effects in the analysis of the main channel can easily be recognized.

6.5.1 Monitoring channel $\eta \to e^+e^-\gamma$

In this analysis chain, the event must have at least one positively charged particle ($N_+ \geq 1$), one negatively charged particle ($N_- \geq 1$), and one neutral particle ($N_0 \geq 1$). The charged particles must fulfill the same basic requirements for properly reconstructed particles as the decay particles of the signal channel $\eta \to e^+e^-e^+e^-$, and they must be also identified as electrons (positrons) according to the same selection criterion (*cf.* Sects. 6.1 and 6.2).

The neutral particle has solely a cluster in the SEC. Its minimum energy must be above 0.09 GeV. This threshold suppresses so-called splitoffs. These are fake photon candidates, which have the following origin. Normally, a shower of a particle in the calorimeter spreads over several crystals. It can happen that all the hits in the different crystals are not matched to one cluster, while the remaining hits are combined into a new cluster which is treated as an additional particle. Typically, these "particles" have small energies and are effectively rejected by this cut. Studies about splitoffs can be found in Refs. [10, 95], where $\eta \to e^+e^-\gamma$ is analyzed with WASA-at-COSY data.

The time difference between the ^{3}He nucleus in the FD and the time signal of the neutral particle in the CD must lie in the same window as for the charged particles with a time information from the SEC.

[3] The branching ratio of the single Dalitz decay is $\mathcal{BR}(\eta \to e^+e^-\gamma) = 7.0 \times 10^{-3}$ (PDG value from Ref. [94]), and the branching ratio of the double Dalitz decay is $\mathcal{BR}(\eta \to e^+e^-e^+e^-) = 2.6 \times 10^{-5}$ (based on QED calculations [3]). This leads to $\mathcal{BR}(\eta \to e^+e^-\gamma)/\mathcal{BR}(\eta \to e^+e^-e^+e^-) \approx 270$.

[4] The branching ratio of the decay $\eta \to \pi^+\pi^-\pi^0$ is $\mathcal{BR}(\eta \to \pi^+\pi^-\pi^0) = 0.2274$, and the branching ratio of the single Dalitz decay of the pion is $\mathcal{BR}(\pi^0 \to e^+e^-\gamma) = 0.01174$ (PDG values from Ref. [94]). The branching ratio of the double Dalitz decay is $\mathcal{BR}(\eta \to e^+e^-e^+e^-) = 2.6 \times 10^{-5}$ (based on QED calculations [3]). This leads to $\mathcal{BR}(\eta \to \pi^+\pi^-(\pi^0 \to e^+e^-\gamma))/\mathcal{BR}(\eta \to e^+e^-e^+e^-) = (0.2274 \times 0.01174)/(2.6 \times 10^{-5}) \approx 100$.

After the track selection and particle identification, the particles which are still accepted are combined to

$$N = N_+ \times N_- \times N_0 \tag{6.15}$$

single Dalitz decay event candidates. For each of these N combinations it is checked if the contributing particles could have been originated from the $\eta \to e^+e^-\gamma$ decay or not. The electron-positron pairs, which are supposed to come from the same virtual photon, must fulfill the same selection criteria as each of the electron-positron pairs in the analysis chain for $\eta \to e^+e^-e^+e^-$. This includes the opening angle, the radius of the closest approach, and the invariant mass at the beam pipe. Finally, the invariant mass of the particles which are treated as the electron, positron, and photon is calculated. It must lie in the same range as the invariant mass of the four charged particles which are regarded in the double Dalitz decay analysis.

Figure 6.28 shows the final ^{3}He-missing mass distribution after the subtraction of the background from reactions with direct-pion production from the analysis of the 2008 and 2009 data. 77.1 % of the peak consists of $\eta \to e^+e^-\gamma$ events. 9.8 % of the entries are from the channel $\eta \to (\pi^0 \to \gamma\gamma)(\pi^0 \to \gamma\gamma)(\pi^0 \to e^+e^-\gamma)$, and 5.4 % are from $\eta \to \pi^+\pi^-(\pi^0 \to \gamma\gamma)$. The other η channels contribute less than 5 % to the peak. These events are all summed up and build the blue solid histogram. The yellow histogram is the sum of all simulated η channels, including the contribution from $\eta \to e^+e^-\gamma$. From the distributions, the number of initial η events (which is named as $N_{\eta,0}$) can be determined with the equation

$$N_{\eta,0} = \frac{N_{\eta,\mathrm{f}}}{\sum_i \varepsilon_i \times \mathcal{BR}_i} \tag{6.16}$$

where $N_{\eta,\mathrm{f}}$ is the number of events which lie within a $\pm 3\sigma$ environment around the peak center of the background subtracted ^{3}He-missing mass distribution (*cf.* Fig. 6.28), which can be described by a Gaussian function. The sum in Eq. 6.16 goes over all the simulated η channels, whereas the contribution of $\eta \to e^+e^-e^+e^-$ is neglected. The efficiencies ε_i are obtained from Monte Carlo simulations, and the branching ratios $\mathcal{BR}_i$ are from the PDG [94].

In case of the 2008 data, the calculated number of initial η events is $N_{\eta,0} = (10.1 \pm 0.1_{\mathrm{stat}}) \times 10^6$, while for the 2009 data $N_{\eta,0} = (17.9 \pm 0.1_{\mathrm{stat}}) \times 10^7$. In Sect. 6.5.3 these values will be used to calculate again the branching ratio of $\eta \to e^+e^-e^+e^-$ and to compare this result with the branching ratio which was obtained by using the the $N_{\eta,0}$ from the fit of the initial ^{3}He-missing mass distribution.

Figures 6.29, 6.30, 6.31, and 6.32 show the different distributions on which the cuts are based for the 2009 data. Additionally, the composition of the distributions is illustrated with simulated spectra. Here, the contributions of the different η-decay channels are fixed according to their branching fraction times their reconstruction efficiencies. The total number of expected η events in every distribution is also fixed. This value is extracted from a fit of the ^{3}He-missing mass distributions which is filled with the same events as in the individual distributions. Only the simulated distributions from the reactions with direct-pion production are fitted to the data, since their cross sections are unknown. If the contribution of an η-decay channel or a reaction with direct-pion production is larger than 5 %, they are displayed in the distributions. Otherwise they are added up and the sum of these histograms is shown.

All spectra are very well described by the simulated decays and reactions over the entire scale. The only deviation between data and simulation is visible in the invariant mass distribution. As from approximately 0.2 GeV/c^2 to the end of the scale, the histogram which shows

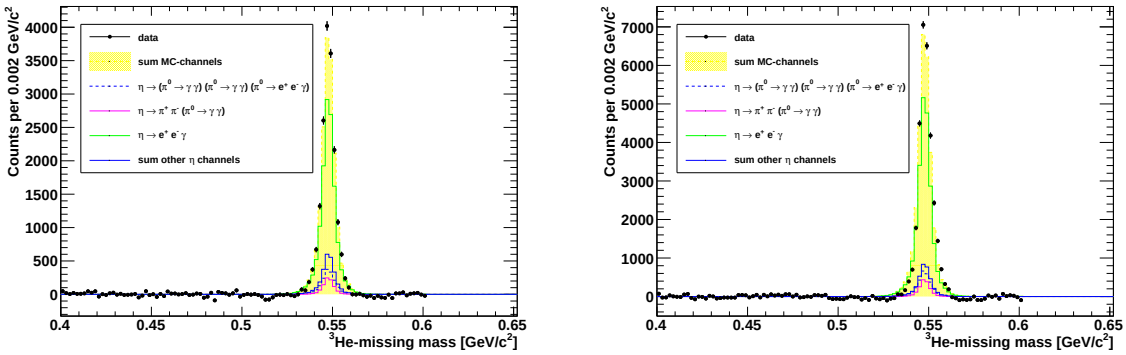

(a) 2008 data (b) 2009 data

Figure 6.28: Final ^{3}He-missing mass distribution after the subtraction of the background from reactions with direct-pion production (from the analysis of $\eta \to e^+e^-\gamma$). 77.1 % of the peak consists of $\eta \to e^+e^-\gamma$ events. 9.8 % of the entries are from the channel $\eta \to (\pi^0 \to \gamma\gamma)(\pi^0 \to \gamma\gamma)(\pi^0 \to e^+e^-\gamma)$, and 5.4 % are from $\eta \to \pi^+\pi^-(\pi^0 \to \gamma\gamma)$. Each other η channel contributes less than 5 % to the peak. These events are all summed up and build the blue solid histogram. The yellow histogram is the sum of all simulated η channels.

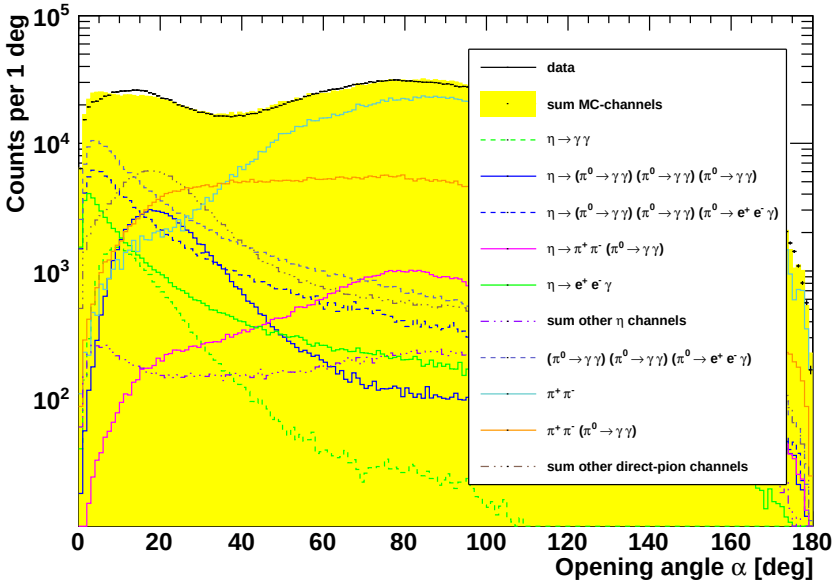

Figure 6.29: Distribution of the opening angle α between the positively and negatively charged particle, which are treated as the electron and positron which originated from the virtual photon.

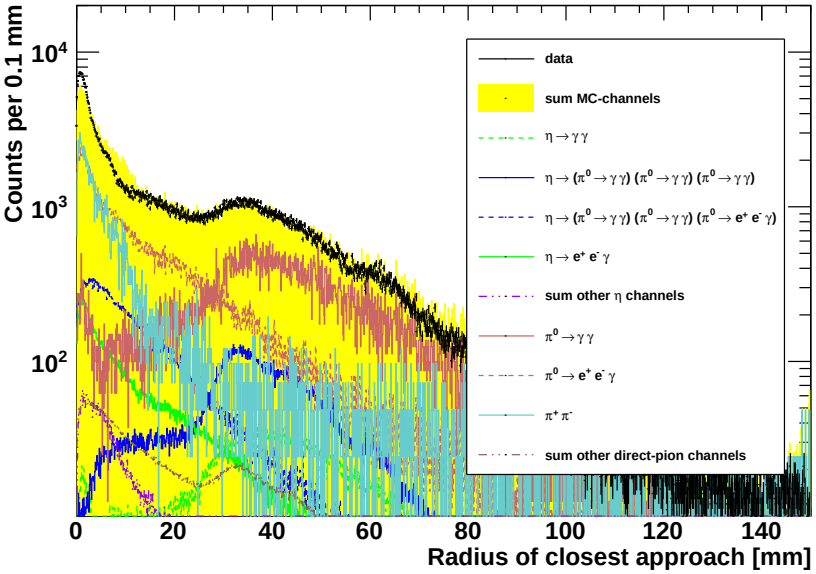

Figure 6.30: Radius of the closest approach between the positively and negatively charged particle, which are treated as the electron and positron which originated from the virtual photon.

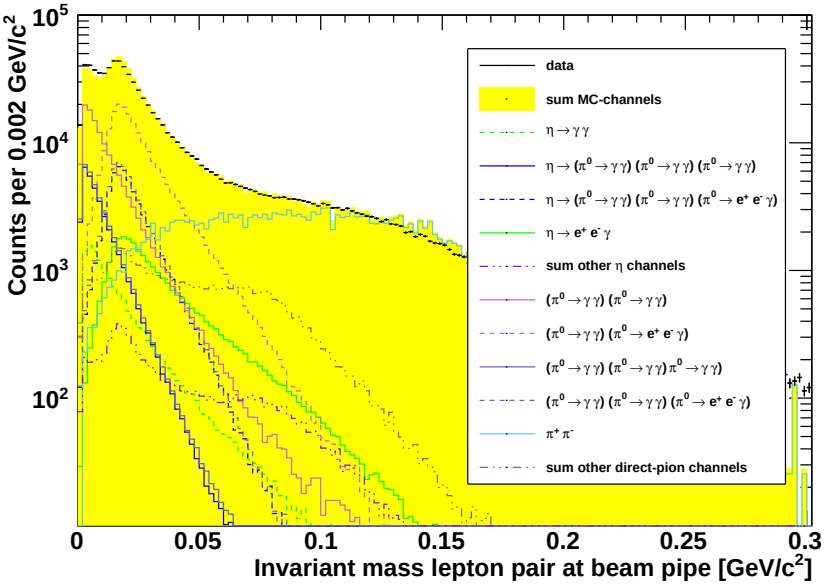

Figure 6.31: Invariant mass distribution of the positively and negatively charged particle, which are treated as the electron and positron from the virtual photon. The invariant mass is calculated from the energy-momentum four-vectors at the beam pipe.

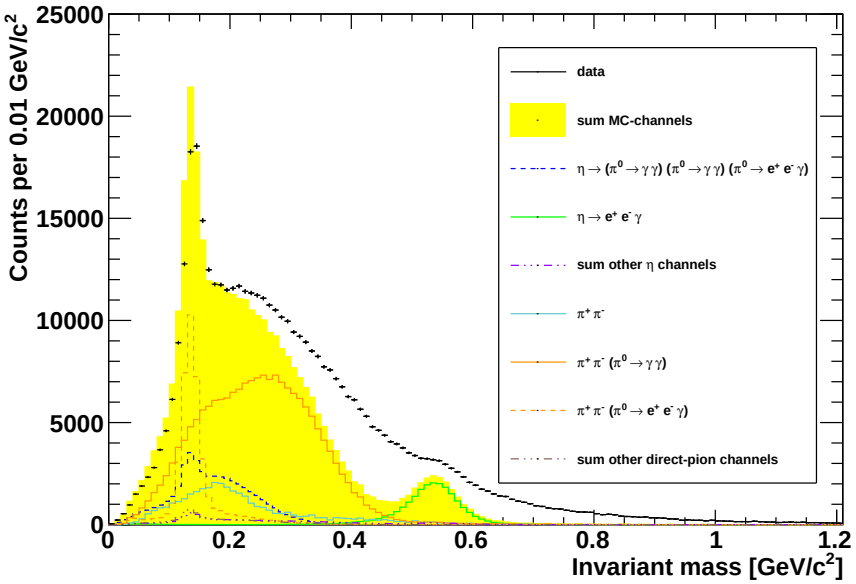

Figure 6.32: Invariant mass distribution of the positively and negatively charged particle (which are treated as the electron and positron), and the neutral particle.

the sum of the Monte Carlo channels has less entries compared with the distribution obtained from experimental data. The reason for this deviation are runs with high luminosities, where multiple accidental events are combined in a single event. This effect also explains the large invariant masses above 0.61 GeV/c^2 which is the limit for the invariant mass of the system X from $p\,d \to {}^3\mathrm{He}\,X$ reactions because of energy and momentum conservation. The large values are obtained when the invariant mass is calculated from particles which belong to different events. The effects due to event overlap are not included in the simulation, and for that reason the invariant mass spectrum can not fully be reproduced by the simulated spectra.

Much effort is made within the WASA-at-COSY collaboration to get a better understanding of the effects due to event overlap and the occurrence of chance coincidence particles. However, no general approach has been found so far to correct for the deviation between the simulations and the data. In the analysis which is presented in this thesis "good" events are not discarded if there would be a chance coincidence particle, since an event must have at least the number of positively, negatively, and neutral charged particles which are needed for an exclusive measurement of a particular channel (*cf.* Sect. 6.3.1). For instance, in the analysis chain for $\eta \to e^+e^-e^+e^-$ it is asked for $N_+ \geq 2$ and $N_- \geq 2$. All combinations are built and it is checked for each if it fulfills the selection criteria. By using this strategy, the number of initial η events ($N_{\eta,0}$) measured by counting the η events in the initial ^{3}He-missing mass distribution can be reproduced by the analysis of the monitoring channels. As a consequence, the branching ratios based on the different normalization methods are consistent (see below). If in the analysis of the monitoring channel $\eta \to e^+e^-\gamma$ only events with $N_+ = 1$, $N_- = 1$, and $N_0 = 1$ are further analyzed, the measured number $N_{\eta,0}$ is smaller by a factor of 2.5 (2008 data) and 2.4 (2009 data) as compared with the number obtained from counting the η events in the initial ^{3}He-missing mass distribution. As it will be shown later, $N_{\eta,0}$ can be also reproduced from the analysis of $\eta \to \pi^+\pi^-(\pi^0 \to e^+e^-\gamma)$. However, this number can not be

reproduced if only events with $N_+ = 2$, $N_- = 2$, and $N_0 = 1$ are further analyzed. Here, the number is smaller by a factor of 2.5 (2008 data) and 2.3 (2009 data).

6.5.2 Monitoring channel $\eta \to \pi^+\pi^-(\pi^0 \to e^+e^-\gamma)$

The other monitoring channel is the decay $\eta \to \pi^+\pi^-\pi^0$ with a subsequent single Dalitz decay of the neutral pion $\pi^0 \to e^+e^-\gamma$. In this analysis chain it is at first asked for at least two positively charged particles ($N_+ \geq 2$), at least two negatively charged particles ($N_- \geq 2$), and at least one neutral particle ($N_0 \geq 1$).

The requirements on the neutral particles are the same as in case of the analysis of the other monitoring channel $\eta \to e^+e^-\gamma$. The charged particles must fulfill the same criteria as described in the sections about the particle selection of the signal channel $\eta \to e^+e^-e^+e^-$ (*cf.* Sect. 6.1. Concerning the particle identification, there must at least one positively charged particle identified as a positron ($N_{e^+} \geq 1$), and one negatively charged particle identified as an electron ($N_{e^-} \geq 1$). Additionally, at least one positively charged particle must be rejected as a positron and at least one negatively charged particle must be rejected as an electron. These particles are then treated as pions, where the conditions $N_{\pi^+} \geq 1$ and $N_{\pi^-} \geq 1$ must be fulfilled. Out of the identified particles

$$N = \underbrace{N_{\pi^+} \times N_{\pi^-}}_{\pi^+\pi^- \text{pair}} \times \underbrace{N_{e^+} \times N_{e^-}}_{\text{from } \gamma^*} \times N_0 \tag{6.17}$$

event candidates can be built. Each of these N combinations is now tested if it could be an $\eta \to \pi^+\pi^-(\pi^0 \to e^+e^-\gamma)$ event or not. The electron-positron pairs, which are supposed to come from the same virtual photon, must fulfill the same selection criteria as each of the electron-positron pairs in the analysis of the main channel. This includes the opening angle, the radius of the closest approach, and the electron-positron invariant mass at the beam pipe. Finally, the invariant mass of all five particles is calculated. It must lie in the same range as the invariant mass of the four charged particles of the double Dalitz decay analysis.

Figure 6.33 shows the final ^{3}He-missing mass distribution after the subtraction of background from reactions with direct-pion production from the analyses of the 2008 and 2009 data. 92.4 % of the peak consists of $\eta \to \pi^+\pi^-(\pi^0 \to e^+e^-\gamma)$ events, and 5.0 % of $\eta \to \pi^+\pi^-(\pi^0 \to \gamma\gamma)$ events. As described in the previous subsection, the number of initial η events $N_{\eta,0}$ can be determined based on these final ^{3}He-missing mass distributions (*cf.* Eq. 6.16). The calculated values are $N_{\eta,0} = (12 \pm 1_{\text{stat}}) \times 10^7$ for the 2008 data, and $N_{\eta,0} = (20 \pm 1_{\text{stat}}) \times 10^7$ for the 2009 data.

6.5.3 Different normalizations

As discussed in Sect. 6.4.2, the formula for the branching ratio of $\eta \to e^+e^-e^+e^-$ is

$$\mathcal{BR}(\eta \to e^+e^-e^+e^-) = \frac{N_{\eta,\text{f}} - N_{\eta,0} \times (\sum_i \varepsilon_i \times \mathcal{BR}_i)}{\varepsilon_{\eta \to e^+e^-e^+e^-} \times N_{\eta,0}} \,. \tag{6.18}$$

It depends on the number of initial η events $N_{\eta,0}$, where this number was previously taken from the identified η events after the ^{3}He preselection. This number can be also determined from the analysis of the monitoring channels. Table 6.2 lists the extracted numbers for $N_{\eta,0}$ for the two data sets. The given uncertainties are the statistical errors. There is a deviation

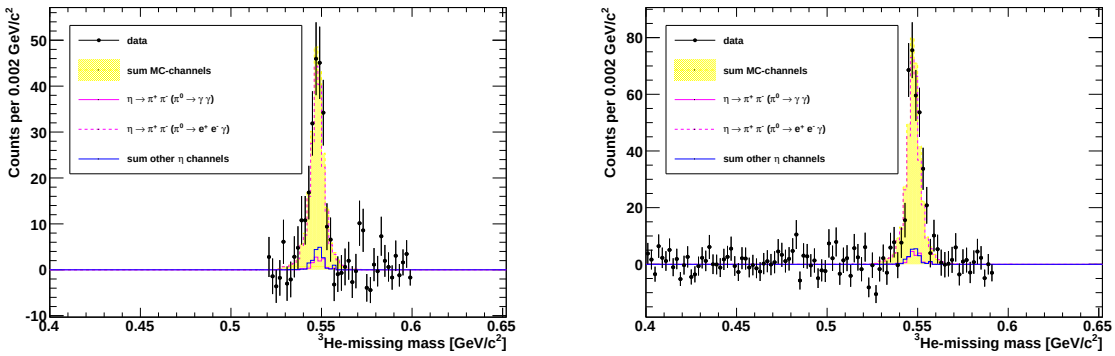

(a) 2008 data (b) 2009 data

Figure 6.33: Final ^{3}He-missing mass distribution after the subtraction of the background from reactions with direct-pion production (from the analysis of $\eta \to \pi^+\pi^-(\pi^0 \to e^+e^-\gamma)$). 92.4 % of the peak consists of $\eta \to \pi^+\pi^-(\pi^0 \to e^+e^-\gamma)$ events, and 5.0 % of $\eta \to \pi^+\pi^-(\pi^0 \to \gamma\gamma)$ events. The other η-decay channels contribute less than 5 % to the peak. These events are all summed up and build the blue solid histogram. The yellow histogram is the sum of all simulated η channels.

between the values which are obtained from a fit of the initial ^{3}He-missing mass distribution and the values which are obtained from the monitoring channel $\eta \to e^+e^-\gamma$ which can not explained by the statistical error. This could be a sign for a systematical effect. The values which are obtained from the analysis of $\eta \to \pi^+\pi^-(\pi^0 \to e^+e^-\gamma)$ agree within the errors with the values which are obtained from the fit of the initial ^{3}He-missing mass distribution. However, the statistical errors are here quite large which makes it quite difficult to judge if there is a systematic effect.

Table 6.2: Initial number of η events in the two data sets. The values in the first row are obtained from a fit of the initial ^{3}He-missing mass distribution. The last two rows show the values for $N_{\eta,0}$ which are obtained from the analysis of the monitoring channels. The given uncertainties are the statistical errors.

	2009 data	2009 data
^{3}He tagged η events	$(11.26 \pm 0.01_{\text{stat}}) \times 10^6$	$(19.32 \pm 0.01_{\text{stat}}) \times 10^6$
mon. channel $\eta \to e^+e^-\gamma$	$(10.1 \pm 0.1_{\text{stat}}) \times 10^6$	$(17.9 \pm 0.1_{\text{stat}}) \times 10^6$
mon. channel $\eta \to \pi^+\pi^-(\pi^0 \to e^+e^-\gamma)$	$(12 \pm 1_{\text{stat}}) \times 10^6$	$(20 \pm 1_{\text{stat}}) \times 10^6$

The branching ratio for $\eta \to e^+e^-e^+e^-$ is again calculated with the different values for $N_{\eta,0}$, where the results are summarized in Fig. 6.34. The combined values of the branching ratios based on the same normalization method are the weighted mean values and their errors from the two individual results, where only one data set is considered. The blue point is the branching ratio from the main analysis chain. The values are all in agreement within one standard deviation. There is no systematic effect due to the choice of the normalization.

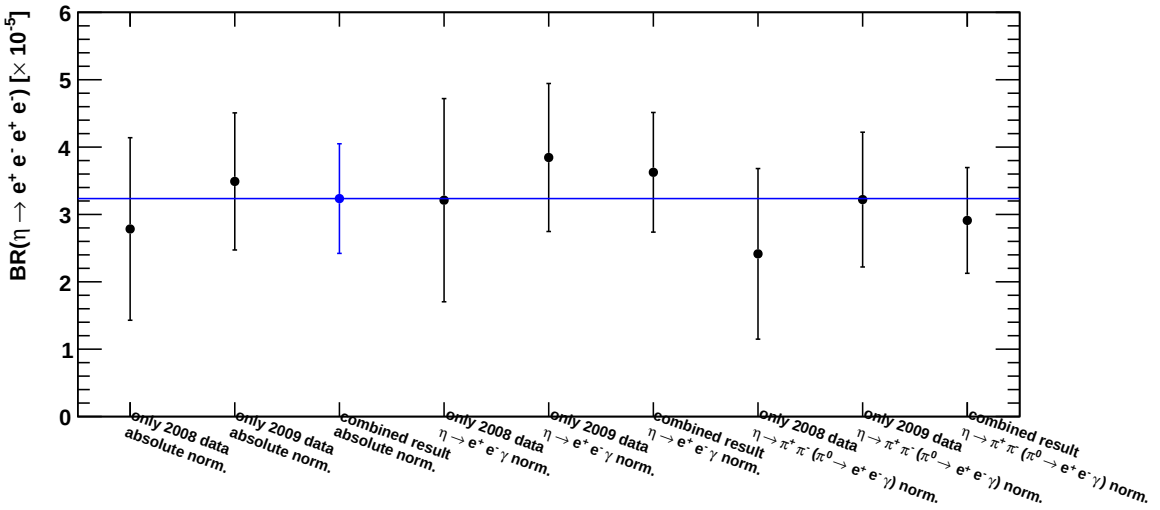

Figure 6.34: Branching ratio for $\eta \to e^+e^-e^+e^-$ based on different normalizations. The 2008 and 2009 data sets were analyzed separately. The combined values for the branching ratios based on the same normalization method are the weighted mean values and their errors of the two individual results, where only one data set is considered. The blue point is the value from the main analysis chain. The errors are statistical errors.

6.6 Systematic effects

6.6.1 Background fit

In the main analysis chain, the initial number of η events is determined from a fit of the ^{3}He-missing mass distribution after the ^{3}He selection (shown in Fig. 4.11). In order to get an estimate for the systematic error on $N_{\eta,0}$, the background from the reactions with direct-pion production is fitted with polynomial functions of different orders, the fit range is varied, and also the binning of the histogram is changed. The maximum deviation between these results for $N_{\eta,0}$ and the value for $N_{\eta,0}$ which is used in Sect. 6.4.2 for the calculation of the branching ratio is $\pm 5\,\%$. This relative uncertainty leads to an absolute uncertainty of 2×10^{-6} on the final result for the branching ratios which were obtained from the analysis of the 2008 and 2009 data.

Also the number of η events $N_{\eta,\mathrm{f}}$ in the final ^{3}He-missing mass distribution is extracted from a fit of this histogram. Again, different functions (linear and quadratic) are used, the fit range is varied, and also the binning of the histogram is changed in order to estimate the systematic uncertainty on the branching ratios due to the uncertainty on $N_{\eta,\mathrm{f}}$. Due to the poor statistics of the final distributions, the polynomial function is poorly constrained and the number of extracted η events is very sensitive to the choice of the fit function. A reasonable estimate for the absolute uncertainty on the branching ratios is 7×10^{-6}. This corresponds to a relative uncertainty of 25 % on the result from the 2008 data, and 20 % on the result from the 2009 data.

6.6.2 Branching ratios of the background channels

The determination of the number of η-background events ($N_{\eta,\mathrm{bgd}}$) depends on the branching ratios of the contributing channels. In order to get an estimate how the uncertainties on these branching ratios effect the measured $\eta \to e^+e^-e^+e^-$ branching fraction, the background branching ratios are all varied one after the other by one unit of their errors [94]. The differences between the new branching ratio and the value obtained from the main analysis are added in quadrature. This results in an absolute uncertainty of 4×10^{-7} on the branching ratios obtained from the 2008 and 2009 data.

6.6.3 Reconstruction efficiency

The reconstruction efficiency ε for a simulated η decay is the number of events m which reach the final ^{3}He-missing mass distribution divided by the number of events N which passed the ^{3}He-selection criteria. It is the probability that an event fulfills all applied cuts of the analysis. Since there are only two options – an event can either be accepted or rejected – the assumption can be made that m is a binomially distributed variable [96]. Therefore, its standard deviation is

$$\sigma_m = \sqrt{N\varepsilon(1-\varepsilon)} \tag{6.19}$$

and the estimate of the standard deviation for ε is

$$\sigma_\varepsilon = \sqrt{\frac{\varepsilon(1-\varepsilon)}{N}}\,. \tag{6.20}$$

To determine the systematic error on the branching ratio of $\eta \to e^+e^-e^+e^-$ due to the errors of the reconstruction efficiencies, the branching ratio is again calculated where the reconstruction efficiency ε_i is reduced and increased by one standard deviation $\sigma_{\varepsilon,i}$ (*i.e.* $\varepsilon_i + \sigma_{\varepsilon,i}$ and $\varepsilon_i - \sigma_{\varepsilon,i}$). This is done for every simulated η-background channel. The differences between the new branching ratio and the value obtained from the main analysis are added in quadrature. This leads to an absolute uncertainty of 1×10^{-6} on the final result for the branching ratios obtained from the 2008 and 2009 data.

6.6.4 Form factor

Due to the limited statistics, the analyzed data sets do not allow one to study the double off-shell transition form factor of the η meson. However, its influence on the result for the branching ratio of $\eta \to e^+e^-e^+e^-$ was investigated.

One model for the form factor is

$$F(q_1^2, q_2^2) = \frac{m_\rho^4}{(m_\rho^2 - q_1^2)(m_\rho^2 - q_2^2)} \tag{6.21}$$

where q_1 and q_2 are the energy-momentum four-vectors of the first and the second electron-positron pair, respectively, and $m_\rho = 770\,\mathrm{MeV}/c^2$ is the pole mass parameter, which is roughly equal to the mass of the ρ meson. This form factor is proposed in Ref. [2]. By analyzing simulated signal events where the invariant mass of the dileptons was distributed according to the form factor from Eq. 6.21, the reconstruction efficiency changes from $5.02 \pm 0.03\,\%$ (main analysis with $F(q_1^2, q_2^2) = 1$) to $4.83 \pm 0.03\,\%$. For that reason, the combined branching ratio increases by $4\,\%$, which results in $\mathcal{BR}(\eta \to e^+e^-e^+e^-) = (3.3 \pm 0.8_{\mathrm{stat}}) \times 10^{-5}$.

Equation 6.21 shows one possible parametrization of the form factor. Since its exact shape is not known, the difference between the branching ratio from the main analysis and the result which was obtained by including the form factor above is not considered as a systematic uncertainty.

6.6.5 Variation of cuts

For the determination of systematic uncertainties due to a change of the cut parameters, the analysis of $\eta \to e^+e^-e^+e^-$ is redone while at each iteration one cut parameter is changed. In doing so, the influence and the stability on the final result can be checked. Whether the difference between the results from the main analysis and after the change of one parameter is significant is judged with the method by R. Barlow [97]. The result for the branching ratio from the main analysis is $\mathcal{BR}(\eta \to e^+e^-e^+e^-) = (2.8 \pm 1.4_{\text{stat}}) \times 10^{-5}$ (2008 data), and $\mathcal{BR}(\eta \to e^+e^-e^+e^-) = (3.5 \pm 1.0_{\text{stat}}) \times 10^{-5}$ (2009 data). The new result for the branching ratio (named as $\mathcal{BR}'$ with the statistical error $\sigma'_{\mathcal{BR}}$) is calculated again and compared with the result above. The difference between the two measured values is

$$\Delta = \mathcal{BR} - \mathcal{BR}' \tag{6.22}$$

and the square of its error is

$$\sigma^2_\Delta = \sigma^2_{\mathcal{BR}'} - \sigma^2_{\mathcal{BR}} \, . \tag{6.23}$$

Here, the difference between the squares of the two errors is used, since the subset is correlated with the data set of the main analysis (*cf.* Ref. [97]). To check whether Δ is a significant difference which can not be explained by the change of the statistical error, the value

$$\kappa = \frac{\Delta}{\sigma_\Delta} = \frac{\mathcal{BR} - \mathcal{BR}'}{\sqrt{|\sigma^2_{\mathcal{BR}'} - \sigma^2_{\mathcal{BR}}|}} \tag{6.24}$$

is introduced. The distribution of κ obtained from different checks should be a standard Gaussian distribution [98]. Therefore, if a check for a systematic effect has a $\kappa < 3$, the deviation between the new value for the branching ratio and the value from the main analysis is not considered as a systematic error.

Table 6.3 lists the systematic checks, the new results for the branching ratios due to the modification of a cut parameter in the analysis chain and the κ values. There is no systematic check which results in $\kappa \geq 3$, which means that there was no systematic error found due to a change of one of the cut parameters.

6.6.6 Summary

Table 6.4 summarizes the systematic uncertainties on the final result. Since the different contributions are independent, the individual systematic errors are added in quadrature in order to obtain the total systematic error. The absolute uncertainty on the final result for the branching ratio is 8×10^{-6}, where the largest contribution comes from the fit of the final ^{3}He-missing mass distributions. This leads to the final result

$$\boxed{\mathcal{BR}(\eta \to e^+e^-e^+e^-) = (3.2 \pm 0.8_{\text{stat}} \pm 0.8_{\text{syst}}) \times 10^{-5}} \, .$$

Table 6.3: Overview of the checks for systematic effects. The result for the branching ratio from the main analysis is $\mathcal{BR}(\eta \to e^+e^-e^+e^-) = (2.78 \pm 1.36_{\text{stat}}) \times 10^{-5}$ (from the 2008 data set), and $\mathcal{BR}(\eta \to e^+e^-e^+e^-) = (3.49 \pm 1.02_{\text{stat}}) \times 10^{-5}$ (from the 2009 data set). The systematic checks are: 1) – 4) Maximum opening angle between the electron-positron which are supposed to originate from the same virtual photon. 5) – 8) Maximum radius of closest approach between the electron-positron which are supposed to originate from the same virtual photon. 9) – 12) Minimum invariant mass of the electron-positron pair which is calculated from the energy-momentum four-vectors at the beam pipe. 13) – 16) Minimum total invariant mass of the four leptons.

	systematic check	2008 data		2009 data	
		$\mathcal{BR} \pm \sigma_{\mathcal{BR}}$ $[\times 10^{-5}]$	κ	$\mathcal{BR} \pm \sigma_{\mathcal{BR}}$ $[\times 10^{-5}]$	κ
1)	$\alpha_{\max} = 36°$	1.21 ± 1.20	2.45	2.75 ± 0.95	1.99
2)	$\alpha_{\max} = 38°$	2.80 ± 1.32	−0.06	2.80 ± 0.96	2.00
3)	$\alpha_{\max} = 42°$	3.05 ± 1.39	−0.94	4.10 ± 1.06	−2.11
4)	$\alpha_{\max} = 44°$	3.15 ± 1.41	−0.99	4.35 ± 1.10	−2.09
5)	$\text{CA.}_{\max} = 20.0\,\text{mm}$	3.28 ± 1.57	−0.64	3.20 ± 1.11	0.66
6)	$\text{CA.}_{\max} = 22.5\,\text{mm}$	3.05 ± 1.44	−0.57	3.61 ± 1.06	−0.42
7)	$\text{CA.}_{\max} = 27.5\,\text{mm}$	2.98 ± 1.32	−0.61	3.30 ± 0.99	0.77
8)	$\text{CA.}_{\max} = 30.0\,\text{mm}$	3.08 ± 1.27	−0.62	3.47 ± 0.96	0.06
9)	$\text{IM.BP.}_{\min} = 5.0\,\text{MeV}/c^2$	2.45 ± 1.29	0.77	3.50 ± 0.99	−0.04
10)	$\text{IM.BP.}_{\min} = 7.5\,\text{MeV}/c^2$	2.67 ± 1.31	0.30	3.50 ± 1.00	−0.05
11)	$\text{IM.BP.}_{\min} = 12.5\,\text{MeV}/c^2$	3.33 ± 1.45	−1.09	3.74 ± 1.08	−0.70
12)	$\text{IM.BP.}_{\min} = 15\,\text{MeV}/c^2$	3.88 ± 1.64	−1.20	3.99 ± 1.20	−0.79
13)	$\text{IM.}_{\min} = 0.225\,\text{GeV}/c^2$	2.47 ± 1.43	0.70	3.11 ± 1.07	1.18
14)	$\text{IM.}_{\min} = 0.250\,\text{GeV}/c^2$	2.52 ± 1.39	0.91	3.40 ± 1.05	0.36
15)	$\text{IM.}_{\min} = 0.300\,\text{GeV}/c^2$	3.08 ± 1.34	−1.29	3.79 ± 0.99	−1.22
16)	$\text{IM.}_{\min} = 0.325\,\text{GeV}/c^2$	3.28 ± 1.33	−1.76	3.53 ± 0.95	−0.11

Table 6.4: Summary of the systematic uncertainties on $\mathcal{BR}(\eta \to e^+e^-e^+e^-)$. There is no contribution due to a variation of a cut parameter. The individual systematic errors are added in quadrature in order to obtain the total systematic error. To get a conservative estimate for the uncertainty, the value is rounded up.

source	absolute uncertainty	relative uncertainty	
		2008	2009
fit initial ^{3}He-MM	2×10^{-6}	7.1 %	5.7 %
fit final ^{3}He-MM	7×10^{-6}	25.0 %	20.0 %
branching ratios	4×10^{-7}	1.4 %	1.1 %
efficiency	1×10^{-6}	3.6 %	2.9 %
cut variation	–	–	–
sum	$7.4 \times 10^{-6} \approx 8 \times 10^{-6}$	28.6 %	22.9 %

Chapter 7

Search for $\eta \to e^+e^-$

7.1 Particle selection and identification

The decay $\eta \to e^+e^-$ is similar to $\eta \to e^+e^-e^+e^-$ since there is also an electron-positron pair in the final state. For that reason, many of the selection criteria which were used to identify double Dalitz event candidates can be used for the search for $\eta \to e^+e^-$ events. The ^{3}He-selection is exactly the same as in the analysis chain for $\eta \to e^+e^-e^+e^-$. In the present analysis chain it is requested that there is at least one positively and one negatively charged particle measured with the CD. Before it is checked whether one of the positively charged particles and one of the negatively charged particles in the CD could belong to an $\eta \to e^+e^-$ event, it is checked if the charged particles fulfill the basic requirements for properly reconstructed particles. The requirements are the same which have to be fulfilled by each charged particle in the CD from the analysis chain for the identification of $\eta \to e^+e^-e^+e^-$ events. This means that the scattering angle must be in the range of the geometrical acceptance of the CD, there must be a time correlation between the particles in the CD and the particle in the FD, and the particle must originate from a point close to the beam-pellet interaction point (see Sect. 6.1). Like in the $\eta \to e^+e^-e^+e^-$ analysis, the particles in the CD run through the particle-identification algorithm (see Sect. 6.2). In contrast to the analysis chain for the search of the double Dalitz decay, the selection criteria for electrons and positrons are here more strict. As it was shown in Sect. 6.2.2 where the performance of the PID algorithm is discussed, there is a fraction of pions which are misidentified as electrons or positrons. In the analysis chain for $\eta \to e^+e^-e^+e^-$, the amount of events with pion pairs, which are wrongly treated as electrons and positrons, is reduced by checking their opening angle. This angle is small for electrons and positrons, which originate from the same virtual photon, while it is large for pions. Due to a different decay topology, the quite effective opening-angle cut is not applicable to select electrons and positrons from $\eta \to e^+e^-$ events. By only using the same PID criteria as it is used in the analysis chain for the double Dalitz decay, there would be too many misidentified particles. To reduce these events, a particle identification based on more strict selection criteria is used in the present analysis chain. It is demanded that the charged particles in the CD must have a cluster in the MDC, the PSB, and in the SEC. In doing so, the most efficient ANN with the best discrimination between electrons (positrons) and pions can be used. The demanded electron and positron efficiency is 90 %. In doing so, the amount of positively charged pions which are wrongly identified as positrons is only 12.5 %, while 14.9 % of the negatively charged pions are misidentified as electrons.

An event which is considered for the further analysis must contain at least one positively and one negatively charged particle in the CD, where both must fulfill the selection criteria which were presented so far. The following cuts which are presented below are more related to the features of the $\eta \to e^+e^-$ decay. Some selection criteria are similar to the cuts which were used to select $\eta \to e^+e^-e^+e^-$ events. However, since the expected branching ratio for $\eta \to e^+e^-$ is around four orders of magnitude smaller than the branching ratio for $\eta \to e^+e^-e^+e^-$, stricter conditions are needed to suppress background reaction. On the one hand, the background is reduced by a cut-optimization procedure. On the other hand, the analysis chain is extended by an additional kinematic fit in order to obtain the smallest upper limit for the branching ratio of the decay $\eta \to e^+e^-$ which is feasible with the selection criteria.

7.2 Cut optimization

The upper limit for the branching ratio of the decay channel $\eta \to e^+e^-$ is calculated with the formula

$$\mathcal{UL}(\eta \to e^+e^-) = \mathcal{BR}(\eta \to e^+e^-) + \lambda \times \sigma_{\mathcal{BR}(\eta \to e^+e^-)} \tag{7.1}$$

where $\mathcal{BR}(\eta \to e^+e^-)$ is the measured branching ratio of the decay $\eta \to e^+e^-$ and $\sigma_{\mathcal{BR}(\eta \to e^+e^-)}$ is its Gaussian statistical error. The value λ depends on which confidence interval the upper limit should be calculated. For example, if the upper limit should be given at a 90 % confidence level, λ is equal to 1.28, since

$$\int_{-\infty}^{\mu+\lambda\times\sigma} \frac{1}{\sigma\sqrt{2\pi}} e^{-\frac{1}{2}\left(\frac{x-\mu}{\sigma}\right)^2} \mathrm{d}x = \frac{1}{2}\left[1 + \mathrm{erf}\left(\frac{\lambda}{\sqrt{2}}\right)\right] \stackrel{!}{=} 0.9 \tag{7.2}$$

is fulfilled for $\lambda = 1.28$. This value is independent of the mean value μ (corresponding to $\mathcal{BR}(\eta \to e^+e^-)$) and its standard deviation σ (corresponding to $\sigma_{\mathcal{BR}(\eta \to e^+e^-)}$). In this example, negative values for the branching ratio are included in the construction of the confidence interval. Later, the upper limit will be also calculated based on the confidence interval which is constructed by requiring that unphysical values are avoided. However, the general formula for the upper limit shown in Eq. 7.1 and the formulas below are not affected by this method. The two ways to construct the confidence intervals result only in different values for λ.

When using the equations for the branching ratio and its statistical error (*cf.* Sect. 6.4), the upper limit of the branching ratio for $\eta \to e^+e^-$ is

$$\mathcal{UL}(\eta \to e^+e^-) = \frac{N_{\eta,\mathrm{f}} - N_{\eta,\mathrm{bgd}}}{\varepsilon_{\eta\to e^+e^-} \times N_{\eta,0}} + \lambda \frac{\sigma_{N_{\eta,\mathrm{f}}}}{\varepsilon_{\eta\to e^+e^-} \times N_{\eta,0}} \tag{7.3}$$

where $N_{\eta,\mathrm{f}}$ is the number of η mesons in the final ^{3}He-missing mass distribution. $N_{\eta,\mathrm{bgd}}$ is the number of background events from other η decays, and $\varepsilon_{\eta\to e^+e^-}$ the efficiency for the signal channel. The latter is derived from a Monte Carlo simulation and defined as the number of simulated $\eta \to e^+e^-$ events which reach the final ^{3}He-missing mass distribution, *i.e.* $N_{\eta\to e^+e^-,\mathrm{f}}$, divided by all the simulated events which pass the ^{3}He-selection criteria. $N_{\eta,0}$ is the initial number of η events. In this equation the assumption is made that the statistical error on $\mathcal{BR}(\eta \to e^+e^-)$ is dominated by the propagated statistical error on $N_{\eta,\mathrm{f}}$, where the statistical errors on $N_{\eta,\mathrm{bgd}}$ and $N_{\eta,0}$ are neglected. For that reason, only $\sigma_{N_{\eta,\mathrm{f}}}$ is considered

in the equation. This error is equal to $\sqrt{N_\mathrm{f}}$, where N_f is the number of events in the final ^{3}He-missing mass distribution in the range of the η mass before the subtraction of the background from reactions with direct-pion production.

The number of $\eta \to e^+e^-$ signal events $N_{\eta\to e^+e^-}$ is the difference between $N_{\eta,\mathrm{f}}$ and $N_{\eta,\mathrm{bgd}}$. Thus, Eq. 7.3 can be rewritten as

$$\mathcal{UL}(\eta \to e^+e^-) = \underbrace{\frac{N_{\eta\to e^+e^-}}{\varepsilon_{\eta\to e^+e^-} \times N_{\eta,0}}}_{\approx 0} + \lambda \frac{\sqrt{N_\mathrm{f}}}{\varepsilon_{\eta\to e^+e^-} \times N_{\eta,0}} \; . \tag{7.4}$$

Since it is expected that $N_{\eta\to e^+e^-}$ is very small, the upper limit is dominated by the second term. $N_{\eta,0}$ is fixed for a given data set. If the number of signal events is neglected, the upper limit is proportional to

$$\mathcal{UL}(\eta \to e^+e^-) \propto R = \frac{\sqrt{N_\mathrm{f}}}{\varepsilon_{\eta\to e^+e^-}} \; . \tag{7.5}$$

To be most sensitive to new physics beyond the Standard Model, it is mandatory to shift the frontier of the upper limit to an as small as possible value. In this thesis, a cut-optimization procedure is used which determines the cut parameters which lead to the smallest upper bound. This is done by searching for the cut parameters which minimize the R function from Eq. 7.5. The challenge of this optimization problem is its multidimensionality. The optimization function depends on seven variables. Later, when a kinematic fit is included in the analysis chain, there are even eight parameters which have to be optimized.

The condition for a minimum of a function is that all of its first derivatives with respect to the different variables must be zero. The cut-optimization procedure searches for each variable separately the value where the first derivative vanishes. It starts with a random set of cut parameters $x_{1,0}$, $x_{2,0}$, ..., $x_{n,0}$. From the initial set of cut parameters one parameter, *e.g.* $x_{1,0}$, is varied, while the other values stay fixed. If a new minimum is found in the range where the parameter was changed, the corresponding value is taken as the new $x_{1,0}$. In the next step R is minimized with respect to x_2, which gives the new value for $x_{2,0}$. After the minimization of the function with respect to one variable, it is possible that the function is no longer minimized with respect to the other variables. For that reason, the optimization procedure is repeated until the minimum of the function with respect to all variables is found. Figure 7.1 illustrates this cut-optimization procedure. More information about this kind of function minimization can be found, for instance, in Ref. [99].

In case of the 2008 data 1178353 events are analyzed with the cut optimization algorithm, and 2301804 events in case of the 2009 data. The fraction of accepted events for the signal channel $\eta \to e^+e^-$ is calculated based on 2680956 simulated events. The applied cuts will be presented in the next subsections.

7.2.1 Energy deposit in the calorimeter

The energy deposit in the SEC of the positively and negatively charged particle must be larger than or equal to the cut parameter "minimum E_dep(SEC)". Additionally, the sum of the energy deposits must be larger than or equal to the cut parameter "sum E_dep(SEC)". Figure 7.2 shows the energy deposit in the SEC of the negatively charged particle against the energy deposit in the SEC of the positively charged particle obtained from the 2009 data and for simulated $\eta \to e^+e^-$ events. The optimization function R for different minimum energy

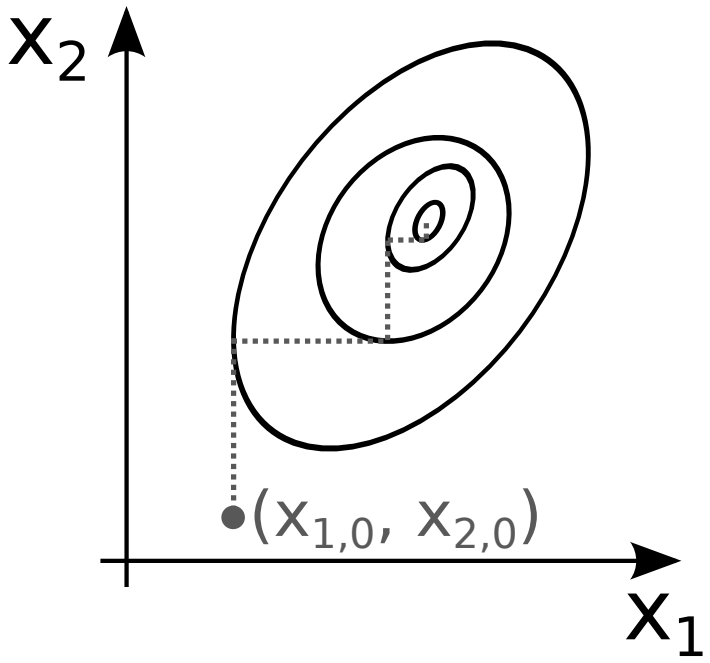

Figure 7.1: Sketch of the cut-optimization procedure (*cf.* Ref. [99]). For illustration purposes, the function which should be minimized depends only on the variables x_1 and x_2. The curves represent contour lines of the function. The dashed lines show the steps during the optimization procedure. The search for the minimum starts at the cut parameters $x_{1,0}$ and $x_{2,0}$. At first, the function value is calculated for different values of x_2 in a certain range, while $x_{1,0}$ is fixed. The x_2 value which leads to the smallest value of the function is then taken as the new $x_{2,0}$. Now, x_1 is varied in a certain range, while $x_{2,0}$ is fixed. If the minimum is found with respect to x_1, the corresponding value is taken as the new $x_{1,0}$. The optimization procedure is repeated until the minimum of the function is found with respect to both variables.

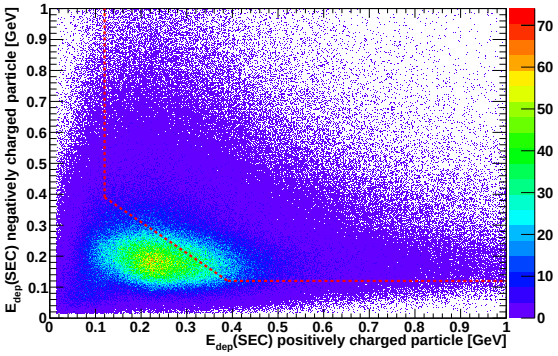

(a) Energy deposit in the SEC of the negatively charged particle against the energy deposit in the SEC of the positively charged particle (2009 data). The red dashed lines show the optimized cut parameters.

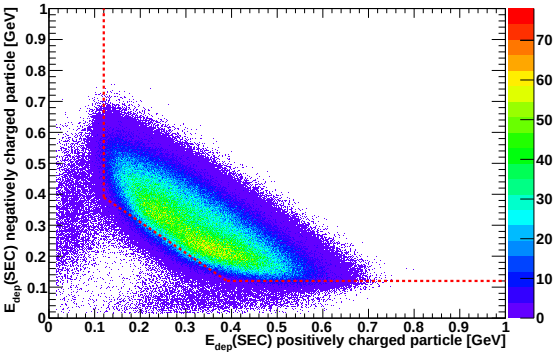

(b) Simulated energy deposit in the SEC of the negatively charged particle against the energy deposit in the SEC of the positively charged particle (from $\eta \to e^+e^-$). The red dashed lines show the optimized cut parameters.

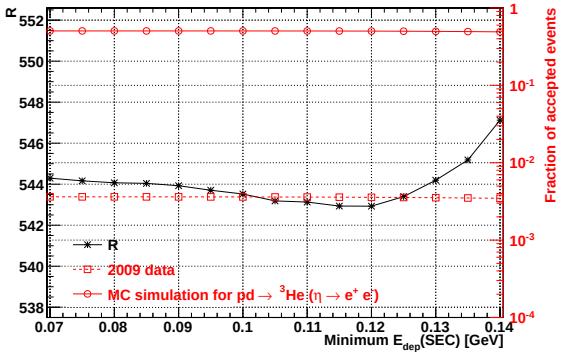

(c) Optimization of the cut parameter for the minimum energy deposit in the SEC. The minimum of R is found for $E_{\mathrm{dep}}(\mathrm{SEC}) \geq 0.12\,\mathrm{GeV}$.

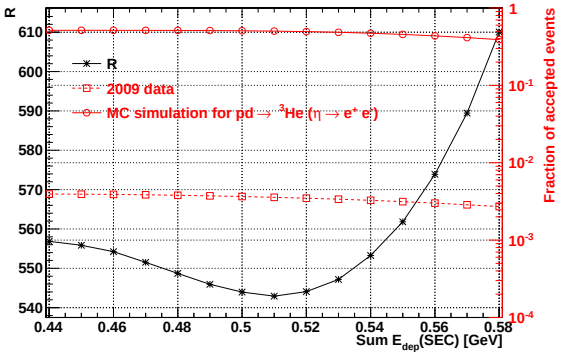

(d) Optimization of the cut parameter for the sum of the energy deposits in the SEC. The minimum of R is found if the sum of $E_{\mathrm{dep}}(\mathrm{SEC}) \geq 0.51\,\mathrm{GeV}$.

Figure 7.2: Cut optimization with respect to the energy deposit in the SEC.

deposits can also be seen in Fig. 7.2. R is plotted for the condition that the energy loss is larger than the "minimum $E_{\mathrm{dep}}(\mathrm{SEC})$" value. For the other cut parameters the optimum choice is taken. The minimum of R is found for $E_{\mathrm{dep}}(\mathrm{SEC}) \geq 0.12\,\mathrm{GeV}$. Additionally, Fig. 7.2 shows the optimization function R for different sums of the energy deposits. The minimum of R is found if the sum of $E_{\mathrm{dep}}(\mathrm{SEC}) \geq 0.51\,\mathrm{GeV}$.

Due to charge conservation, the number of produced electrons must be equal to the number of positrons. The same is true for the positively and negatively charged pions. For that reason, one would expect that the distribution in Fig. 7.2 which shows the energy deposit in the SEC for data is symmetric with respect to a line which bisects the shown quadrant. The asymmetry, however, is introduced by protons and deuterons in the CD, which on this stage of the analysis are not yet rejected.

7.2.2 Radius of closest approach

The radius of the closest approach of the positively and negatively charged particle must be smaller than or equal to the cut parameter "maximum radius of closest approach". Figure 7.3 shows the distribution of the radius of the closest approach obtained from the 2009 data and for simulated $\eta \to e^+e^-$ events. The optimization function R for different cut parameters can also be seen in Fig. 7.3. The minimum of R is found if the radius of closest approach is below 17.5 mm.

7.2.3 Invariant mass

The invariant mass of the positively and negatively charged particle must be larger than or equal to the cut parameter "minimum invariant mass". Additionally, the invariant mass must be smaller than or equal to the cut parameter "maximum invariant mass". Figure 7.4 shows the distribution of the invariant mass from the 2009 data, simulated $\eta \to e^+e^-$ events, and the optimization function R for different values of the minimum invariant mass. The minimum of R is found if the minimum invariant mass is larger than or equal to $0.51\,\mathrm{GeV}/c^2$. Figure 7.4 also shows the optimization function R for different values of the maximum invariant mass. The minimum of R is in this case found if the maximum invariant mass is smaller than or equal to $0.65\,\mathrm{GeV}/c^2$.

7.2.4 Opening angle

The opening angle β between the positively and negatively charged particle in the laboratory frame must be larger than or equal to the cut parameter "minimum opening angle β". Additionally, β must be smaller than or equal to the cut parameter "maximum opening angle β". Figure 7.5 shows the distribution of the opening angle from the 2009 data, simulated $\eta \to e^+e^-$ events, and the optimization function R for different values of the minimum opening angle. The minimum of R is found if the minimum opening angle β is larger than or equal to 92.5°. Figure 7.5 also shows the optimization function R for different values of the maximum opening angle. The minimum of R is found if the maximum opening angle β is below 180°.

7.2.5 Upper limit from analysis with conventional cuts

Table 7.1 summarizes the optimized cut parameters for the analysis of the 2008 and the 2009 data sets. The parameters are given for the analysis chain without a kinematic fit (will be later included). There are no significant differences between the determined values for the two data sets.

Figure 7.6 shows the final ^{3}He-missing mass distributions after all cuts which are obtained from the analysis of the 2008 and 2009 data. The distributions are fitted with a sum of a polynomial function which describes the background coming from reactions with direct-pion production, and a Gaussian function for a possible η peak. The mean value of the Gaussian function and its standard deviation are fixed according to the parameters which are obtained from the fit of the initial ^{3}He-missing mass distribution before all cuts (see Fig. 4.11). The parameter which describes the height of the Gaussian peak is constraint to be larger than or equal to zero. Polynomial functions of the order between one and five, and also different minimum and maximum fit ranges were used to fit the distributions. Finally, the fit with the

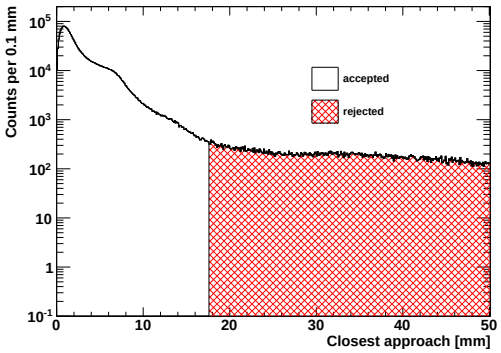

(a) Distribution of the radius of the closest approach of the positively and negatively charged particle (2009 data).

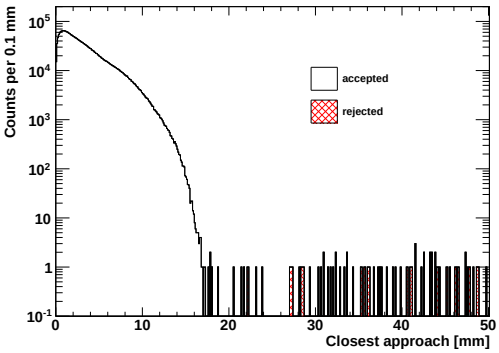

(b) Simulated distribution of the radius of the closest approach of the positively and negatively charged particle (from $\eta \to e^+e^-$).

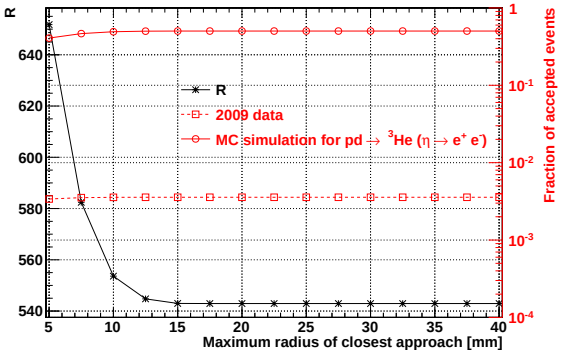

(c) Optimization of the cut parameter for the maximum radius of the closest approach of the positively and negatively charged particle. The minimum of R is found if the radius of closest approach is smaller than or equal to 17.5 mm.

Figure 7.3: Cut optimization of the radius of the closest approach of the positively and negatively charged particle.

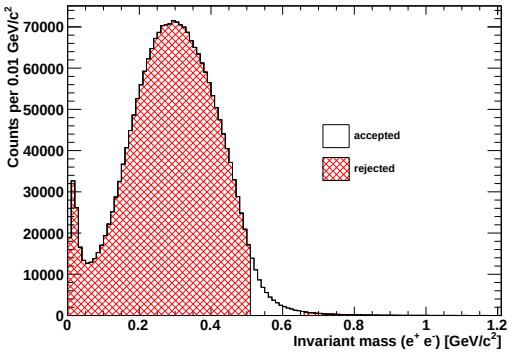

(a) Distribution of the invariant mass of the positively and negatively charged particle (2009 data).

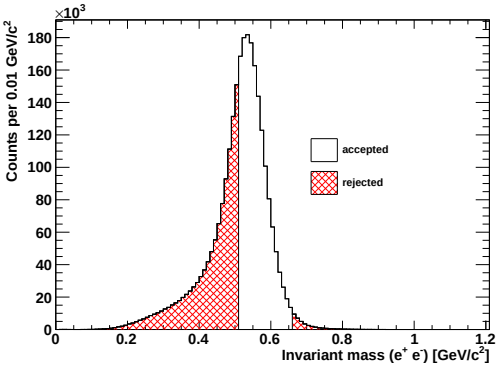

(b) Simulated distribution of the invariant mass of the positively and negatively charged particle (from $\eta \to e^+e^-$).

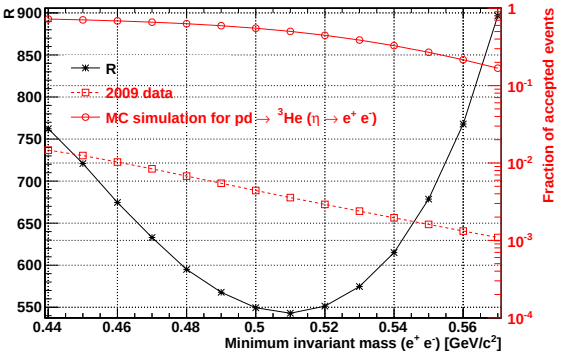

(c) Optimization of the cut parameter for the minimum invariant mass of the positively and negatively charged particle. The minimum of R is found if the minimum invariant mass is larger than or equal to $0.51\,\mathrm{GeV}/c^2$.

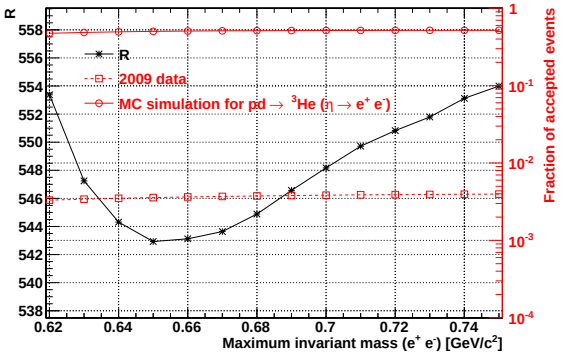

(d) Optimization of the cut parameter for the maximum invariant mass of the positively and negatively charged particle. The minimum of R is found if the maximum invariant mass is smaller than or equal to $0.65\,\mathrm{GeV}/c^2$.

Figure 7.4: Cut optimization of the invariant mass of the positively and negatively charged particle.

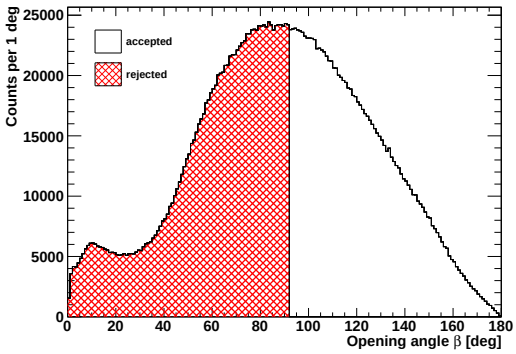

(a) Distribution of the opening angle β between the positively and negatively charged particle (2009 data).

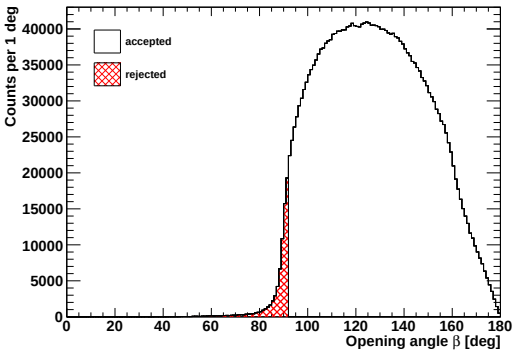

(b) Simulated distribution of the opening angle β between the positively and negatively charged particle (from $\eta \to e^+e^-$).

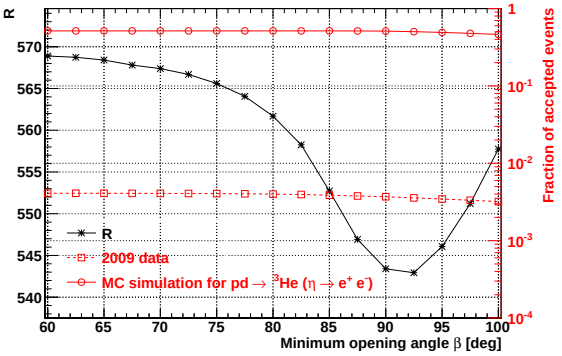

(c) Optimization of the cut parameter for the minimum opening angle between the positively and the negatively charged particle. The minimum of R is found if the minimum β is larger than or equal to 92.5°.

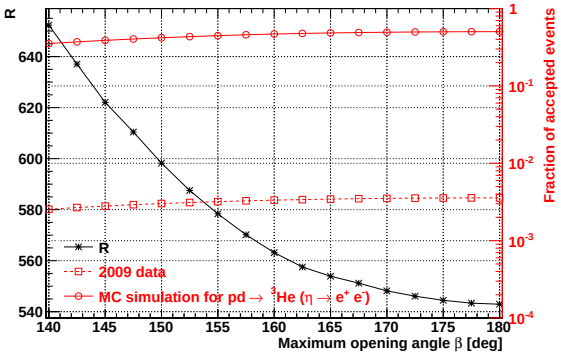

(d) Optimization of the cut parameter for the maximum opening angle between the positively and the negatively charged particle. The minimum of R is found if the maximum β is below 180°.

Figure 7.5: Cut optimization of the opening angle β between of the positively and negatively charged particle.

Table 7.1: Optimized cut parameters for the analysis of the 2008 and 2009 data. The parameters are given for the analysis chain without the kinematic fit.

cut parameter	2008 data	2009 data
min. E_{dep}(SEC) [GeV]	0.125	0.12
sum E_{dep}(SEC) [GeV]	0.52	0.51
max. radius CA. [mm]	15.0	17.5
min. inv. mass [GeV/c^2]	0.51	0.51
max. inv. mass [GeV/c^2]	0.67	0.65
min. β [°]	90.0	92.5
max. β [°]	180.0	180.0

χ^2 per degree of freedom which is the closest to one is used for the fits in Fig. 7.6. In both plots there is no indication for an η peak.

Figure 7.7 shows the ^{3}He-missing mass distributions after the subtraction of background from reactions with direct-pion production which are obtained from the analysis of the 2008 and 2009 data.

Counting the events in the range between the red dashed lines of the background subtracted ^{3}He-missing mass distribution gives the number of remaining η events, which is $N_{\eta,\mathrm{f}} = 54.8 \pm 68.2_{\mathrm{stat}}$ (2008 data), and $N_{\eta,\mathrm{f}} = -14.3 \pm 94.8_{\mathrm{stat}}$ (2009 data). Both numbers are within the given statistical errors in agreement with zero.

The yellow histogram is the sum of the η-decay background channels, which are expected in this histogram according to the simulation. It can be calculated according to the following formula

$$N_{\eta,\mathrm{bgd}} = N_{\eta,0} \times \left(\sum_i \varepsilon_i \times \mathcal{BR}_i \right) \tag{7.6}$$

where $N_{\eta,0}$ is the number of identified η events after the ^{3}He selection. $N_{\eta,0} = (11.26 \pm 0.01_{\mathrm{stat}}) \times 10^6$ was found in the 2008 data set, and $N_{\eta,0} = (19.32 \pm 0.01_{\mathrm{stat}}) \times 10^6$ in the 2009 data set (see Sect. 4.6). The expected number of η-decay background events in case of the 2008 data is $N_{\eta,\mathrm{bgd}} = 8.1$, and $N_{\eta,\mathrm{bgd}} = 14.5$ for the 2009 data. The errors on these values are neglected here. $N_{\eta,\mathrm{bgd}}$ is dominated by more than 75 % by events from $\eta \to e^+e^-\gamma$ decays.

The branching ratio of $\eta \to e^+e^-$ is calculated with equation

$$\mathcal{BR}(\eta \to e^+e^-) = \frac{N_{\eta,\mathrm{f}} - N_{\eta,\mathrm{bgd}}}{\varepsilon_{\eta\to e^+e^-} \times N_{\eta,0}} \,. \tag{7.7}$$

The reconstruction efficiency for $\eta \to e^+e^-$ is 18 %. The result for the branching ratio, based on the analysis of the 2008 data, is $\mathcal{BR}(\eta \to e^+e^-) = (2.3 \pm 3.4_{\mathrm{stat}}) \times 10^{-5}$, while the analysis of the 2009 data results in $\mathcal{BR}(\eta \to e^+e^-) = (-0.8 \pm 2.8_{\mathrm{stat}}) \times 10^{-5}$. The errors on the branching ratios are the propagated statistical errors on $N_{\eta,\mathrm{f}}$ and $N_{\eta,0}$. Both branching fractions are within less than one standard deviation in agreement with zero. For that reason, it is more reasonable to give an upper limit for the branching fraction of the decay $\eta \to e^+e^-$.

The following discussion on the determination of the upper limits is based on the publication "A Unified Approach to the Classical Statistical Analysis of Small Signals" by G. J. Feldman and R. D. Cousins [100]. Let x be the measured value of μ in an experiment, which is determined with a Gaussian resolution function with a known fixed standard deviation σ.

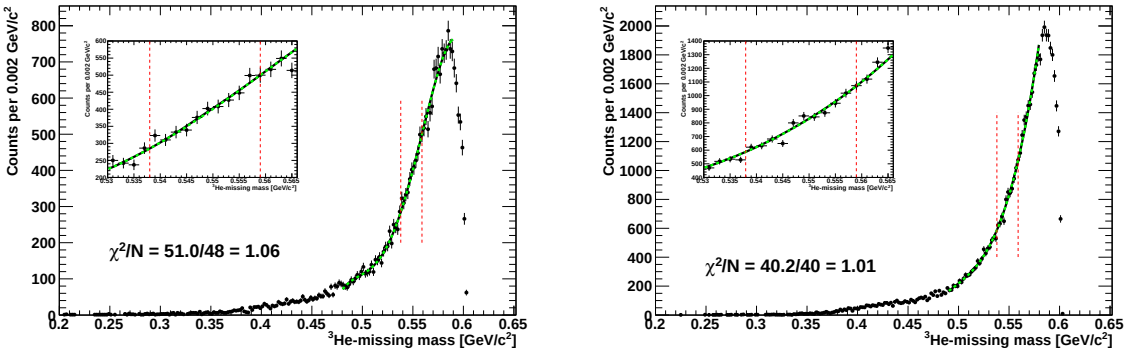

(a) 2008 data (b) 2009 data

Figure 7.6: Final ^{3}He-missing mass spectrum and the fit from the analysis without a kinematic fit. The black solid curve is the sum of the Gaussian function and the polynomial function, and the green dashed line is the polynomial function, which describes the background from reactions with direct-pion production. The red dashed lines mark the $\pm 3\sigma$ environment around the peak center of an assumed Gaussian shaped η peak. The inserts show a zoom of this range. There is no indication for an η peak.

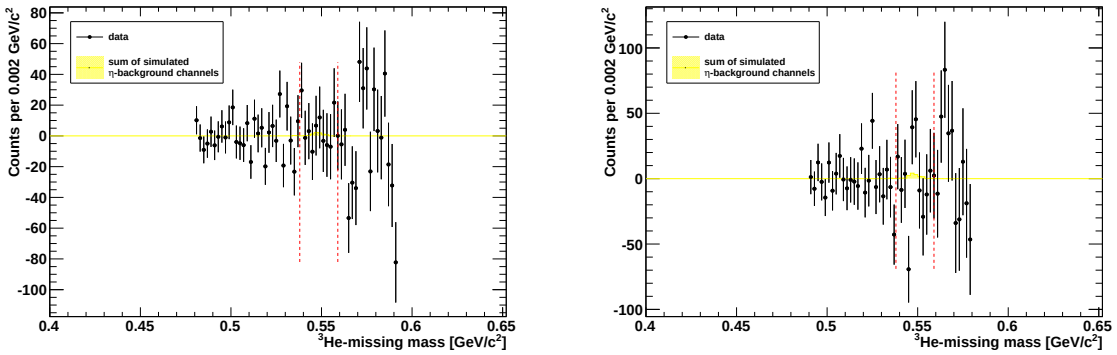

(a) 2008 data (b) 2009 data

Figure 7.7: Final ^{3}He-missing mass distribution from the analysis without a kinematic fit after the subtraction of the background from reactions with direct-pion production.

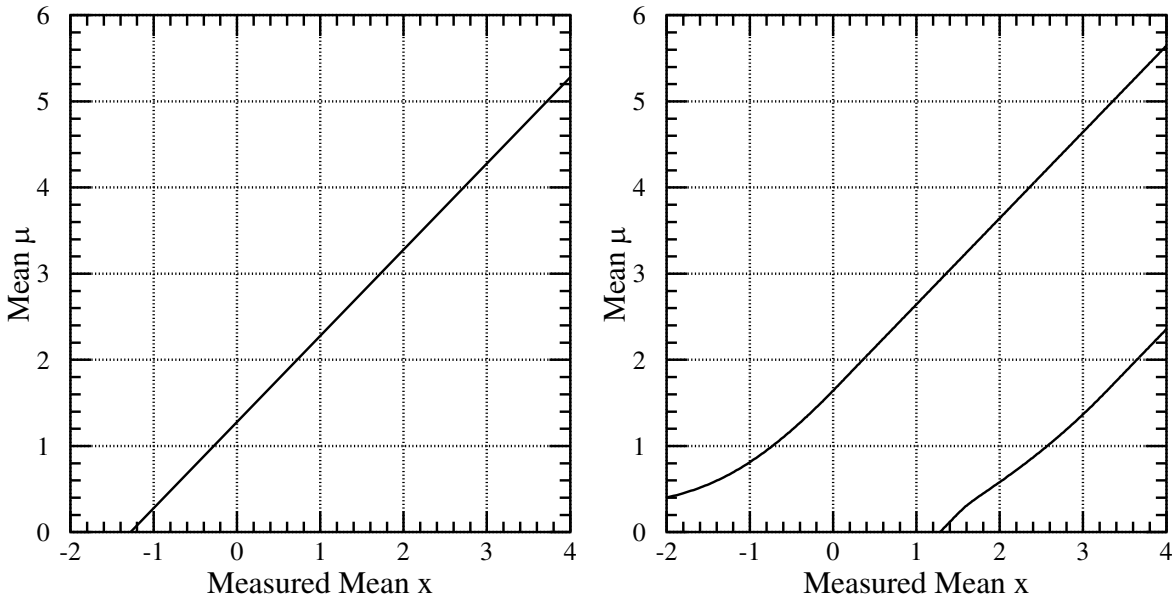

(a) Standard confidence interval

(b) μ is constrained to be non-negative

Figure 7.8: 90 % confidence intervals for the mean μ of a Gaussian. The measured mean x and μ are normalized to the standard deviation σ [100].

Figure 7.8 shows the standard confidence interval for the upper bound of μ (at the 90 % CL) as a function of the measured mean x (normalized to the standard deviation σ). The interval is calculated as described in Sect. 7.2 where the motivation of the cut parameter optimization was introduced. Using this method, the upper limit for the branching ratio of $\eta \to e^+e^-$ is 6.7×10^{-5} (2008 data) and 2.8×10^{-5} (2009 data). The upper bound for the number of signal events is $N_{\eta \to e^+e^-} < 134$ (2008 data) and $N_{\eta \to e^+e^-} < 93$ (2009 data). All values are given at the 90 % CL. The numbers are calculated based on $N_{\eta \to e^+e^-} = 46.7 \pm 68.2$ signal events (2008 data) and $N_{\eta \to e^+e^-} = -28.8 \pm 94.8$ signal events (2009 data).

The alternative method which is introduced and recommended in Ref. [100] to construct confidence intervals excludes unphysical regions. This is reasonable, since negative branching ratios do not have a physical meaning. The 90 % confidence intervals for the mean of a Gaussian, which is constrained to be non-negative, is shown in Fig. 7.8 (they are also listed in Appendix B). Using this method, the upper limit of the branching ratio for $\eta \to e^+e^-$ is 8.0×10^{-5} (based on the analysis of the 2008 data), and 3.8×10^{-5} (2009 data). The upper bound for the number of signal events is $N_{\eta \to e^+e^-} < 160$ (2008 data), and $N_{\eta \to e^+e^-} < 129$ (2009 data). All values are given at the 90 % CL.

Table 7.2 summarizes the results for the measurements of the upper limits for the branching ratio of $\eta \to e^+e^-$. As expected, the result which is obtained from the analysis of the 2008 data set is around a factor of two larger compared with the result from the 2009 data set, since the last one contains roughly twice as many η events. The result which is based on the standard confidence interval is similar to the result which is determined with the method from Ref. [100]. The results which are obtained from the analysis of the 2009 data are comparable to the upper limit from the WASA/CELSIUS measurement, which is

$\mathcal{BR}(\eta \to e^+e^-) < 2.7 \times 10^{-5}$ (at the 90 % CL) [22]. However, the determined upper limit is around one order of magnitude larger compared with the recent upper limit from the HADES collaboration with $\mathcal{BR}(\eta \to e^+e^-) < 4.9^{+0.7}_{-1.2} \times 10^{-6}$ (at the 90 % CL) [41].

Table 7.2: Results for the upper limit of the branching ratio of $\eta \to e^+e^-$ obtained from the analysis of the 2008 and 2009 data. The values are given at the 90 % CL. The analysis chains are without the usage of a kinematic fit.

	2008 data	2009 data
standard confidence interval	6.7×10^{-5}	2.8×10^{-5}
Feldman-Cousins	8.0×10^{-5}	3.8×10^{-5}

The results are the smallest upper limits which can be measured with the used set of cuts. In order to shift the upper limit so smaller values a kinematic fit has to be introduced.

7.3 Analysis including kinematic fit

A kinematic fit is a least-square fit which minimizes a χ^2 function with constraints [46, 101]. The constraints are included by means of Lagrange multipliers. The χ^2 function is parametrized as

$$\chi^2 = \sum_{i=1}^{m} \left(\frac{\epsilon_i}{\sigma_i}\right)^2 + 2\sum_{\mu} \lambda_\mu F_\mu(\epsilon_1, ..., \epsilon_m) \tag{7.8}$$

where the correction term $\epsilon_i = x_i - v_i$ is the difference between the fitted value x_i and the measured value v_i. σ_i is the uncertainty of v_i, λ_μ is a Lagrange multiplier, and $F_\mu(\epsilon_1, ..., \epsilon_m)$ is the constraint equation. The first sum goes over all m kinematic variables, while the second sum goes over the μ constraints. It is assumed that there is no correlation between the fitted values.

The constraints equation can be expanded in a Taylor series around the measured variables

$$F_\mu(x_1, ..., x_m) \approx F_\mu(v_1, ..., v_m) + \sum_{j=1}^{m} \epsilon_j \left.\frac{\partial F_\mu}{\partial x_j}\right|_{x_j = v_j} = 0 \tag{7.9}$$

where the higher order terms are here neglected. To find the correction terms ϵ_j, which minimize Eq. 7.8, the first derivative of Eq. 7.8 with respect to ϵ_j is calculated and is then set equal to zero, *i.e.*

$$2\frac{\epsilon_j}{\sigma_j^2} + 2\sum_{\mu} \lambda_\mu \left.\frac{\partial F_\mu}{\partial x_j}\right|_{x_j = v_j} = 0\,. \tag{7.10}$$

Solving this equation for ϵ_j gives

$$\epsilon_j = -\sigma_j^2 \sum_{\mu} \lambda_\mu \left.\frac{\partial F_\mu}{\partial x_j}\right|_{x_j = v_j}\,. \tag{7.11}$$

To determine the Lagrangian multipliers, ϵ_j is inserted into Eq. 7.9. ϵ_j can then be calculated with Eq. 7.11. The fit values x_j are equal to $v_j + \epsilon_j$.

In this analysis, the kinematic fit is used to check if particles fulfill a certain reaction hypothesis, namely $p\,d \to {}^3\mathrm{He}\,e^+\,e^-$. In doing so, the measured kinematic variables of the different particles are varied (limited by the experimental resolution) in order to match energy and momentum conservation. A measure of how good the fit hypothesis is fulfilled is the χ^2 value, which can be translated into a probability for the reaction hypothesis. A cut on this probability distribution will be used to further reject background events.

7.3.1 Error parametrization

In order to use the kinematic fit, the uncertainties of the measured values must be parametrized. For a particle with a known mass, the energy-momentum four-vector in the laboratory system is fully determined by three independent variables like for instance the kinetic energy E_{kin}, the polar angle θ, and the azimuthal angle ϕ. For these variables an error parametrization is needed which limits the amount of variation of the measured variables.

The error parametrization is based on Monte Carlo simulations, where the difference between the true values from single-track events and the reconstructed values is regarded:

$$\Delta E = E_{\mathrm{kin,true}} - E_{\mathrm{kin,rec}} \,, \tag{7.12}$$

$$\Delta\theta = \theta_{\mathrm{true}} - \theta_{\mathrm{rec}} \,, \tag{7.13}$$

$$\Delta\phi = \phi_{\mathrm{true}} - \phi_{\mathrm{rec}} \,. \tag{7.14}$$

The distributions are fitted with Gaussian functions, where the standard deviation is the resolution of the particular kinematic variable. This is used as the error σ_i which is needed as an input for the kinematic fit. Since the error parametrization is completely based on simulations, it is mandatory that the experimental resolution is reproduced with the Monte Carlo simulation.

Due to the rotational symmetry of the WASA detector, the error distributions are independent of the azimuthal angle ϕ. However, the errors depend on the kinetic energy and on the scattering angle θ, which means that a two-dimensional parametrization is needed, *i.e.*

$$\sigma_{E_{\mathrm{kin}}} = \sigma_{E_{\mathrm{kin}}}(E_{\mathrm{kin}}, \theta) \,, \tag{7.15}$$

$$\sigma_{\theta} = \sigma_{\theta}(E_{\mathrm{kin}}, \theta) \,, \tag{7.16}$$

$$\sigma_{\phi} = \sigma_{\phi}(E_{\mathrm{kin}}, \theta) \,. \tag{7.17}$$

In case of the error parametrization for the ^{3}He nuclei, the interval size of the kinetic energy is 0.01 GeV, and for the scattering angle the interval size is 1°. Figure 7.9 shows the error parametrization. It can be seen that $\sigma_{E_{\mathrm{kin}}}$ strongly depends on the kinetic energy, while it only slightly increases with increasing scattering angles. σ_θ and also σ_ϕ increase for decreasing kinetic energies and scattering angles.

For the error parametrization of the electrons and the positrons, the interval size in case of the kinetic energy is 0.01 GeV, and for the scattering angle the interval size is 5°. The error parametrization for these particles can be seen in Fig. 7.10. Like the error parametrization for ^{3}He, $\sigma_{E_{\mathrm{kin}}}$ strongly depends on the kinetic energy, while it only slightly increases with increasing scattering angles. For all distributions the errors increase rapidly at the edges of the geometrical acceptance of the CD. Coming into these regions, less layers of the MDC contribute to the helix reconstruction. This results in a larger uncertainty on these variables. For the ranges where the errors can not be parametrized in a reasonable way since they are

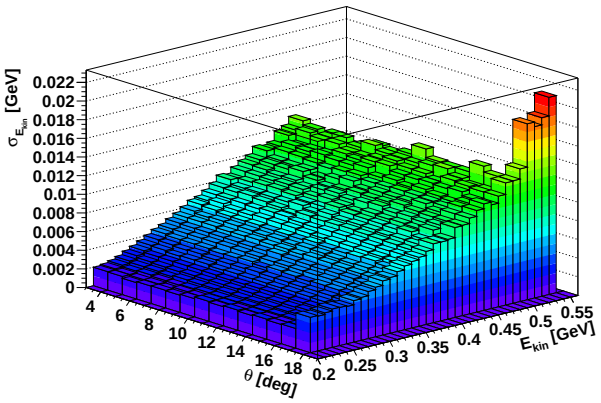

(a) Error parametrization $\sigma_{E_{\mathrm{kin}}} = \sigma_{E_{\mathrm{kin}}}(E_{\mathrm{kin}}, \theta)$

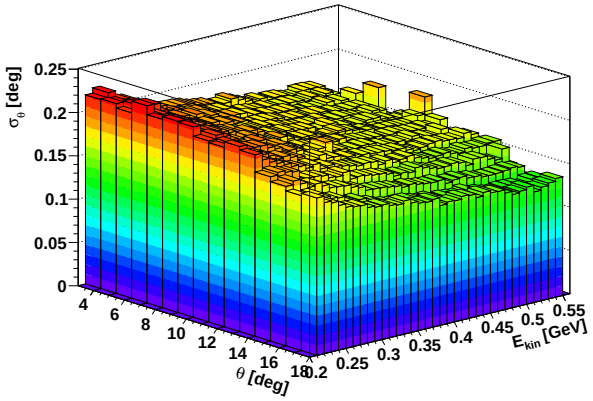

(b) Error parametrization $\sigma_\theta = \sigma_\theta(E_{\mathrm{kin}}, \theta)$

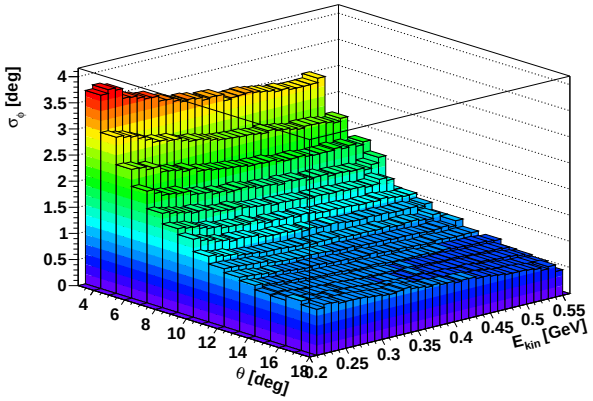

(c) Error parametrization $\sigma_\phi = \sigma_\phi(E_{\mathrm{kin}}, \theta)$

Figure 7.9: Error parametrization for the kinetic energy E_{kin}, the scattering angle θ, and the polar angle ϕ for ^{3}He. The errors depend on the kinetic energy E_{kin} and on the scattering angle θ.

obviously non-Gaussian, the errors are set equal to zero in the shown distributions. Particles with kinetic energies or scattering angles where no reasonable error parametrization exists are not considered in the kinematic fit.

Systematic effect on error parametrization

Since the error parametrization is completely based on simulations, it must be ensured that there are no systematic effects introduced due to a wrong determination of these variables. One particular effect which has to be considered concerns the reconstruction of the azimuthal angle ϕ of the particles which are measured with the FD.

The angle-reconstruction procedure assumes that particles traverse the detector on straight trajectories which have their origin at the vertex $(x, y = 0)$. However, the forward scattered particles are deflected by the magnetic field B_z of the solenoid. For that reason, the Lorentz force acts on the motion of the particle in the x- and y-direction and leads to a change of the azimuthal angle ϕ. This is illustrated in Fig. 7.11.

The change in ϕ due to the presence of the magnetic field can be corrected by adding

$$\Delta\phi = 0.3 \, \frac{q[e] \times l[\mathrm{m}] \times B[\mathrm{T}]}{p\left[\frac{\mathrm{GeV}}{c}\right] \times \cos\theta} \left(1 - \frac{l[\mathrm{m}]}{2 z_{\mathrm{FTH}}[\mathrm{m}]}\right) \tag{7.18}$$

to the reconstructed azimuthal angle [102]. q is the charge of the measured particle, l is the length of solenoid field, B is the strength of the magnetic field, p is the momentum, θ is the scattering angle, and z_{FTH} is the distance of the FTH from the origin measured along the z-axis.

In Eq. 7.18 it is assumed that the magnetic field is constant which, according to Fig. 2.15, is not the case. Nevertheless, the constant field approximation can be used to bring the true and reconstructed ϕ angle in a better agreement [102].

7.3.2 Performance

A kinematic fit can be used to suppress background reactions. This is done by rejecting events which do not fulfill an assumed reaction hypothesis. Figure 7.12 shows the χ^2 distribution which is obtained from the analysis of simulated $p\,d \to {}^3\mathrm{He}\,(\eta \to e^+e^-)$ reactions, where the reaction hypothesis $p\,d \to {}^3\mathrm{He}\,e^+\,e^-$ is assumed. Additionally, the theoretical χ^2 distribution for four degrees of freedom is plotted. The degrees of freedom N is here four, since energy and momentum conservation is demanded, without any further constraints (n_c) and no unmeasured variables (u), *i.e.*

$$N = 4 + n_c - u = 4 + 0 - 0 = 4 \tag{7.19}$$

The simulated distribution is normalized to the maximum of the theoretical χ^2 function. The discrepancies between the two distributions – especially the enhanced tail at large χ^2 values – is due to a non-perfect error parametrization for certain fit variables, where non-Gaussian errors are treated as Gaussian ones.

If events fulfill the expected hypothesis and the errors are correctly parametrized, the probability distribution

$$P(\chi^2, N) = \frac{1}{2^{\frac{N}{2}}\Gamma\left(\frac{N}{2}\right)} \int_{\chi^2}^{\infty} e^{-\frac{t}{2}} t^{\frac{N}{2}-1} \mathrm{d}t \tag{7.20}$$

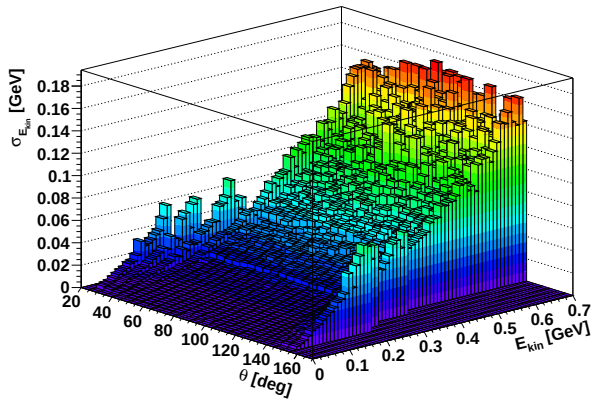

(a) Error parametrization $\sigma_{E_{\mathrm{kin}}} = \sigma_{E_{\mathrm{kin}}}(E_{\mathrm{kin}}, \theta)$

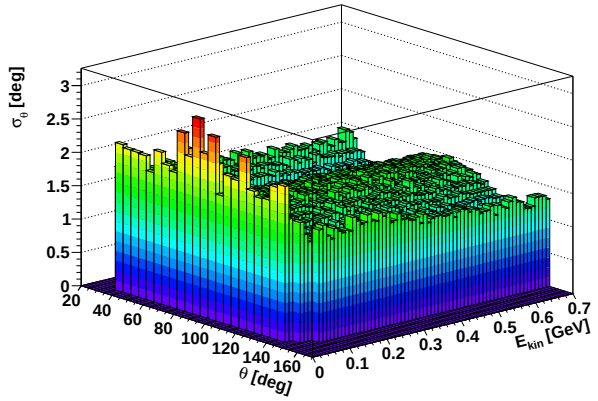

(b) Error parametrization $\sigma_\theta = \sigma_\theta(E_{\mathrm{kin}}, \theta)$

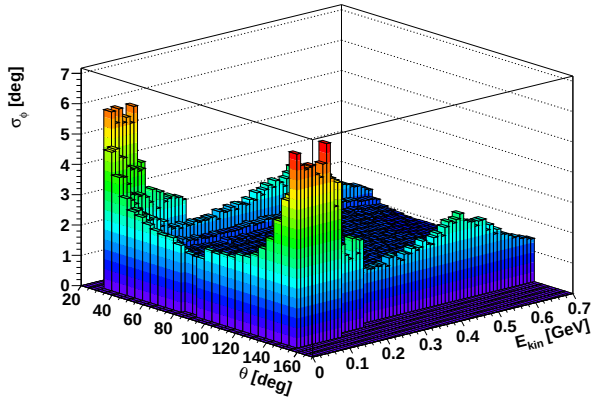

(c) Error parametrization $\sigma_\phi = \sigma_\phi(E_{\mathrm{kin}}, \theta)$

Figure 7.10: Error parametrization for the kinetic energy E_{kin}, the scattering angle θ, and the polar angle ϕ for electrons and positrons. The errors depend on the kinetic energy E_{kin} and on the scattering angle θ.

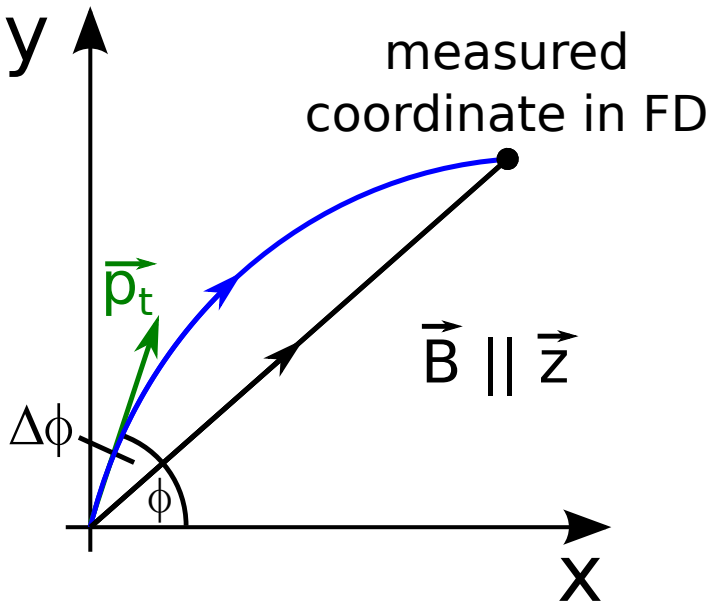

Figure 7.11: ϕ correction: The angle-reconstruction procedure assumes that particles traverse the detector on straight trajectories (shown as the black line) which have their origin at the vertex. However, the forward scattered particles are effected by the magnetic field of the solenoid which forces them on curved trajectories (blue line). This leads to a difference of $\Delta\phi$ between the true azimuthal angle and the reconstructed one.

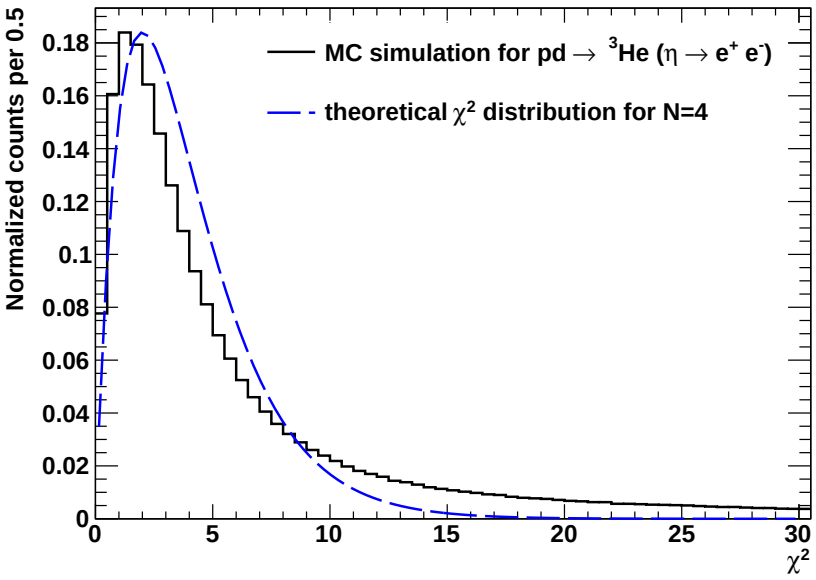

Figure 7.12: χ^2 distribution. The black solid distribution is obtained from the analysis of simulated $p\,d \to {}^3\mathrm{He}\,(\eta \to e^+e^-)$ reactions, where the reaction hypothesis $p\,d \to {}^3\mathrm{He}\,e^+\,e^-$ is assumed. The blue dashed line is the theoretical χ^2 distribution for four degrees of freedom. The simulated histogram is normalized to the maximum of the theoretical distribution.

should be uniformly distributed between zero and one [101]. For background reactions, however, the probability distribution is mostly populated at the lowest values. Figure 7.13 shows the probability distribution which is obtained from the analysis of simulated $p\,d \to {}^3\mathrm{He}\,(\eta \to e^+e^-)$ reactions and from the analysis of the 2009 data. The hypothesis $p\,d \to {}^3\mathrm{He}\,e^+\,e^-$ is assumed in the kinematic fit. The spectrum from the simulated signal reactions is reasonably flat over a wide range. The rise of the distribution at the smallest probabilities corresponds to events which lie in the tail of the χ^2 distribution (*cf.* Fig. 7.12). The distribution obtained from the analysis of the 2009 data is, as expected, not uniform. Moreover, it is mainly populated at small probabilities. This is due to the fact that the data mostly contain events for which the fit hypothesis is inappropriate.

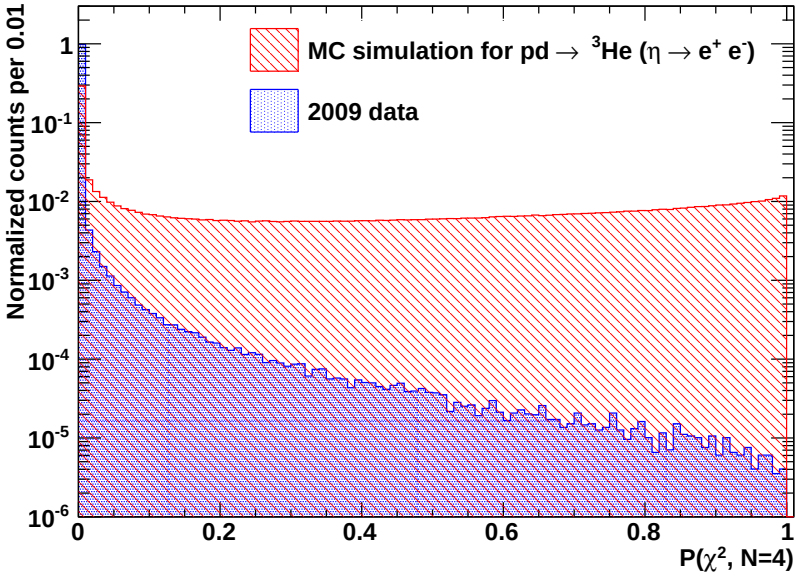

Figure 7.13: Normalized probability distributions $P(\chi^2, N = 4)$ obtained from the analysis of simulated $p\,d \to {}^3\mathrm{He}\,(\eta \to e^+e^-)$ reactions and from the analysis of the 2009 data. The fit hypothesis is $p\,d \to {}^3\mathrm{He}\,e^+\,e^-$.

Since the probability distributions for the signal channel $\eta \to e^+e^-$ and the data are fundamentally different, a cut on these distributions is used to suppress further background events. This enables to reduce again the upper limit for the branching ratio of $\eta \to e^+e^-$. Therefore, the cut optimization is redone, whereby a cut on the probability distribution is now included and "minimum $P(\chi^2, N = 4)$" is used as an additional cut parameter. The results of the cut optimization and the improved upper limit will be presented in the next subsection.

7.3.3 Upper limit from analysis with kinematic fit

Table 7.3 summarizes the optimized cut parameters for the analysis chains of the 2008 and 2009 data sets which include the kinematic fit. According to simulations, the reconstruction for the signal channel is 8.7 %.

Figure 7.14 shows the final ^{3}He-missing mass distribution obtained from the 2008 data.

Table 7.3: Optimized cut parameters for the analysis of the 2008 and 2009 data. The parameters are shown for the analysis chain with kinematic fit.

cut parameter	2008 data	2009 data
min. E_{dep}(SEC) [GeV]	0.095	0.090
sum E_{dep}(SEC) [GeV]	0.50	0.53
max. radius CA. [mm]	17.5	17.5
min. inv. mass [GeV/c^2]	0.51	0.51
max. inv. mass [GeV/c^2]	0.69	0.70
min. β [°]	85.0	85.0
max. β [°]	155.0	180.0
min. $P(\chi^2, N)$	0.60	0.55

Due to the poor statistics in the range around the η mass there is no obvious choice for a fit function which is needed for a quantitative determination of the contribution from reactions with direct-pion production. Since it is expected that there is no improvement for the upper limit from the 2008 data set, the further analysis will focus on the 2009 data set.

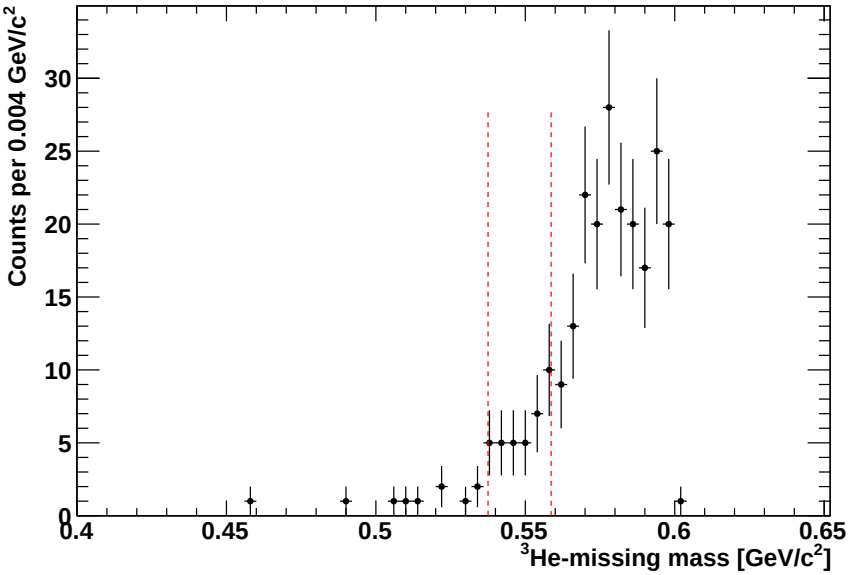

Figure 7.14: Final ^{3}He-missing mass distribution from the $\eta \to e^+e^-$ analysis (2008 data). The two red line mark the $\pm 3\sigma$ range around the peak position of a possible η signal.

The final ^{3}He-missing mass distribution from the 2009 data can be seen in Figs. 7.15 and 7.16, where also the different fit functions are shown. The range around the η mass is fitted with the sum of a polynomial function to describe the background from reactions with direct-pion production and a Gaussian function for a possible η signal. The mean value and its standard deviation are the ones which were obtained from the fit of the initial ^{3}He-missing mass distribution after the ^{3}He selection. To study the influence of the fit on the final result,

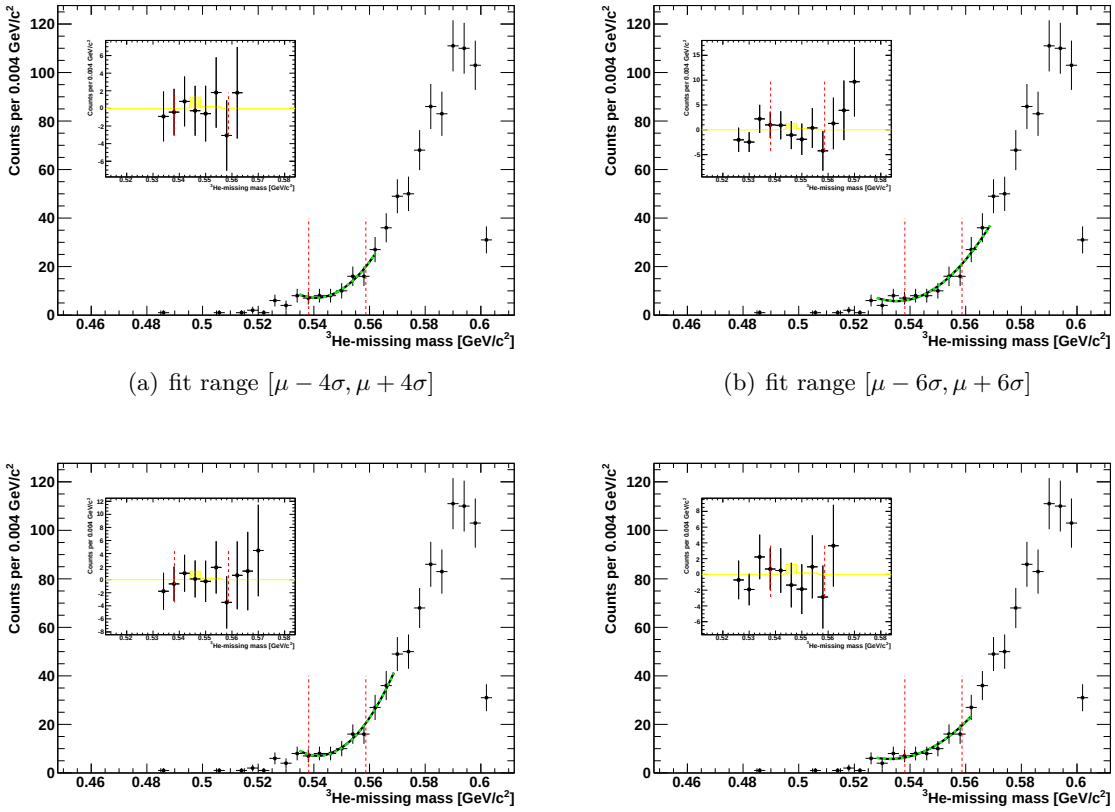

(a) fit range $[\mu - 4\sigma, \mu + 4\sigma]$

(b) fit range $[\mu - 6\sigma, \mu + 6\sigma]$

(c) fit range $[\mu - 4\sigma, \mu + 6\sigma]$

(d) fit range $[\mu - 6\sigma, \mu + 4\sigma]$

Figure 7.15: Final ^{3}He-missing mass distribution from the analysis chain which includes the kinematic fit, obtained from the 2009 data. The distributions are fitted with the sum of a polynomial function of the order two plus a Gaussian function for a possible η peak. The fit ranges are varied in the different plots.

different fit ranges and polynomial functions of the order two and three are used to describe the background. The number of remaining η events is the sum the entries in the background subtracted histograms in the missing mass distribution in the range $\mu - 3\sigma$ to $\mu + 3\sigma$ (shown in the inserts where the range is marked by the red lines). According to simulations, there are 1.5 $\eta \to e^+e^-\gamma$ and 0.2 $\eta \to e^+e^-e^+e^-$ events[1] in the final ^{3}He-missing mass distribution. These events are summed up and build the yellow histogram in the background subtracted distributions. These events are subtracted from the number of counted η events in order to determine the number of $N_{\eta \to e^+e^-}$ events. The upper limits for the $\eta \to e^+e^-$ branching ratio are calculated using the method by G. J. Feldman and R. D. Cousins from Ref. [100], which was introduced in the previous section.

Table 7.4 lists the results for $\eta \to e^+e^-$ in the 2009 data set. It shows the used fit functions, the number of extracted signal events ($N_{\eta \to e^+e^-}$), the $\eta \to e^+e^-$ branching ratio, and the upper limits of $N_{\eta \to e^+e^-}$ and $\mathcal{BR}(\eta \to e^+e^-)$. It can be seen that the (rounded)

[1] For $\eta \to e^+e^-e^+e^-$ the value $\mathcal{BR}(\eta \to e^+e^-e^+e^-) = 2.6 \times 10^{-5}$ is used for the calculation [3].

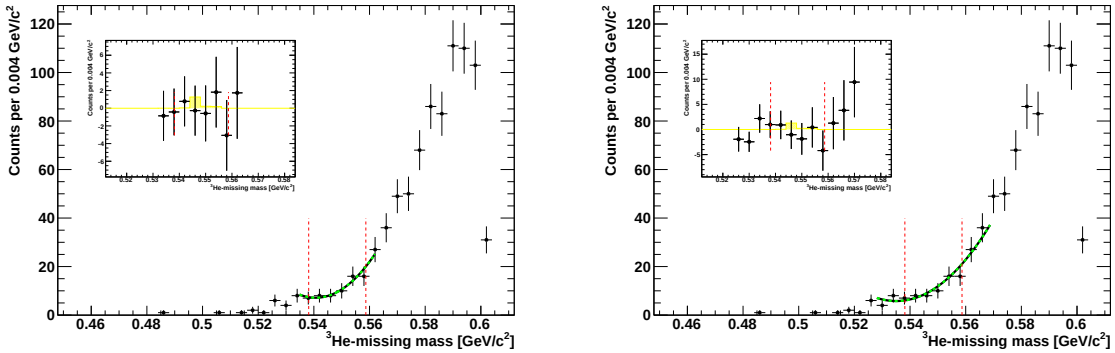

(a) fit range $[\mu - 4\sigma, \mu + 4\sigma]$

(b) fit range $[\mu - 6\sigma, \mu + 6\sigma]$

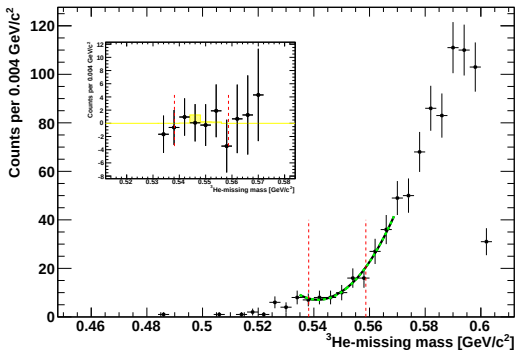

(c) fit range $[\mu - 4\sigma, \mu + 6\sigma]$

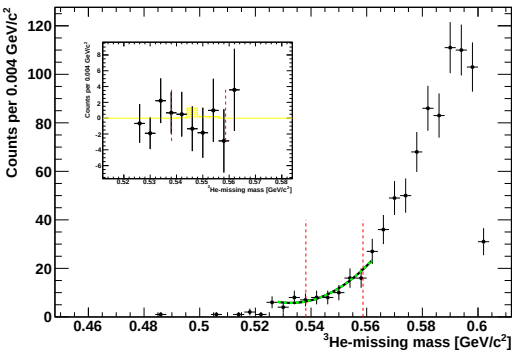

(d) fit range $[\mu - 6\sigma, \mu + 4\sigma]$

Figure 7.16: Final ^{3}He-missing mass distribution from the analysis chain which includes the kinematic fit, obtained from the 2009 data. The distributions are fitted with the sum of a polynomial function of the order three plus a Gaussian function for a possible η peak. The fit ranges are varied in the different plots.

values for the upper limits do not depend on the polynomial function, whereas they depend on the fit range. The upper limits for the $\eta \to e^+e^-$ branching ratio lie in the range between 4.55×10^{-6} and 6.08×10^{-6}. The values are significantly smaller as compared to the upper bound from WASA/CELSIUS, which is $\mathcal{BR}(\eta \to e^+e^-) < 2.7 \times 10^{-5}$ (90 % CL) [22]. The value found in this analysis are close to the recent upper limit from the HADES collaboration, which is $\mathcal{BR}(\eta \to e^+e^-) < 4.9^{+0.7}_{-1.2} \times 10^{-6}$ (at the 90 % CL) [41].

Table 7.4: Results from the search for $\eta \to e^+e^-$ in the 2009 data set from the analysis chain which includes the kinematic fit. Listed are the number of signal events, the branching ratio and their upper limits at the 90 % CL. They are calculated based on the method by G. J. Feldman and R. D. Cousins [100]. The final ^{3}He-missing mass distributions are fitted with the sum of a polynomial function and a Gaussian function for a possible η peak. The orders N of the polynomial functions are labeled as polN. Different fit ranges around the center of an possible η peak (denoted as μ with standard deviation σ) are used.

	$N_{\eta\to e^+e^-}$	$\mathcal{UL}$	$\mathcal{BR}$ $[\times 10^{-6}]$	$\mathcal{UL}$ $[\times 10^{-6}]$	
pol2, $[\mu-4\sigma, \mu+4\sigma]$	-3.5 ± 8.1	10.3	-2.08 ± 4.79	6.08	Fig. 7.15
pol2, $[\mu-6\sigma, \mu+6\sigma]$	-6.7 ± 8.1	7.7	-3.97 ± 4.79	4.55	Fig. 7.15
pol2, $[\mu-4\sigma, \mu+6\sigma]$	-3.1 ± 8.1	10.3	-1.86 ± 4.79	6.08	Fig. 7.15
pol2, $[\mu-6\sigma, \mu+4\sigma]$	-5.7 ± 8.1	8.3	-3.38 ± 4.79	4.89	Fig. 7.15
pol3, $[\mu-4\sigma, \mu+4\sigma]$	-3.5 ± 8.1	10.3	-2.07 ± 4.79	6.08	Fig. 7.16
pol3, $[\mu-6\sigma, \mu+6\sigma]$	-6.6 ± 8.1	7.7	-3.90 ± 4.79	4.55	Fig. 7.16
pol3, $[\mu-4\sigma, \mu+6\sigma]$	-3.2 ± 8.1	10.3	-1.88 ± 4.79	6.08	Fig. 7.16
pol3, $[\mu-6\sigma, \mu+4\sigma]$	-5.6 ± 8.1	8.3	-3.34 ± 4.79	4.89	Fig. 7.16

As discussed, the result for the upper limit depends on the choice of the fit function. Since it is hard to judge which function describes the histogram the best, the most conservative value for the upper limit is used as the result from this analysis:

$$\boxed{\mathcal{BR}(\eta \to e^+e^-) < 6 \times 10^{-6} \ (90\,\%\text{CL})}$$

Chapter 8

Summary and Outlook

This thesis reported on the 3×10^7 η decays from $p\,d \to {}^3\mathrm{He}\,\eta$ reactions measured with the WASA-at-COSY experiment that were analyzed in order to identify rare $\eta \to e^+e^-e^+e^-$ double Dalitz decay events. Since the ratio between the number of expected signal events and events coming from other η-decay channels in the initial data sample is around 1/40000, the challenge of this analysis was to develop selection criteria which suppress effectively the huge amount of background. The analysis focussed especially on the particle identification, where neural networks were used to distinguish between electrons (positrons) and pions based on the correlation between the momentum and the energy deposit in the electromagnetic calorimeter or in a thin plastic scintillator. The suppression of pions is mandatory in the search for $\eta \to e^+e^-e^+e^-$ decays since more than 97 % of the charged decay modes of the η meson contain $\pi^+\pi^-$ pairs.

Although WASA was designed such that the probability for photon conversion in the detector material is low, such events cannot be neglected in the study of a rare decay. For instance, if the photon in $\eta \to e^+e^-\gamma$ converts in the beam pipe, there are the same particles in the final state as in the double Dalitz decay. The expected number of such events is of the same order of magnitude as the number of signal events, but these have been suppressed successfully. The performance of the analysis method was tested on the main background reactions $\eta \to e^+e^-\gamma$ and $\eta \to \pi^+\pi^-(\pi^0 \to e^+e^-\gamma)$, which are much more frequent than the η double Dalitz decay.

In total $49.7 \pm 12.5_{\mathrm{stat}}$ $\eta \to e^+e^-e^+e^-$ double Dalitz decay candidates were identified. The absolute branching ratio for $\eta \to e^+e^-e^+e^-$ was determined to be $\mathcal{BR}(\eta \to e^+e^-e^+e^-) = (3.2 \pm 0.8_{\mathrm{stat}} \pm 0.8_{\mathrm{syst}}) \times 10^{-5}$. The measurement is in perfect agreement with various theoretical predictions and with the most recent measurements from the KLOE collaboration [9], which reported $\mathcal{BR} = (\eta \to e^+e^-e^+e^-) = (2.4 \pm 0.2_{\mathrm{stat}} \pm 0.1_{\mathrm{syst}}) \times 10^{-5}$. This value was published during the preparation of this thesis.

The new selection criteria were adapted for the search for the $\eta \to e^+e^-$ decay in the same data set. Theoretical calculations predict a the branching ratio of this channel on the order of 10^{-9}. Any significant deviation from this would be a sign for new physics beyond the Standard Model. In the analysis, the cut parameters were optimized to lower the upper limit for the branching ratio of this decay to the smallest possible value that is consistent with the current data set from *pd*-reactions. This results in an upper limit of $\mathcal{BR}(\eta \to e^+e^-) < 6 \times 10^{-6}$ at the 90 % confidence level. This upper limit is more than a factor four lower than the earlier result from the WASA/CELSIUS experiment [22], which gave $\mathcal{BR}(\eta \to e^+e^-) < 2.7 \times 10^{-5}$

at the 90 % confidence level, and is close to the upper limit recently published by the HADES collaboration which is $\mathcal{BR}(\eta \to e^+e^-) < 4.9^{+0.7}_{-1.2} \times 10^{-6}$ at the 90 % confidence level [41].

Over the last few years, WASA-at-COSY has produced more than 5×10^8 η mesons in pp-collisions and therefore has one of the largest data sets containing η-events. These data allow one to study η decays with higher precision which may eventually lead to a better understanding of the Standard Model of particle physics.

Appendix A

η-Decay Modes

In the following, the branching ratios and upper limits for the decay channels of the η meson are listed. Table A.1 shows the neutral decay modes, Table A.2 shows the charged decay modes, while Table A.3 shows the C, P, CP or LF violating modes. The upper limits are given at the 90 % CL. The values are from Ref. [11].

Table A.1: Neutral decay modes of the η meson. $(71.91 \pm 0.34)\,\%$ of the η mesons decay to solely neutral particles.

decay mode	branching ratio
$\eta \to \gamma\gamma$	$(39.31 \pm 0.20)\,\%$
$\eta \to 3\pi^0$	$(32.57 \pm 0.23)\,\%$
$\eta \to \pi^0 2\gamma$	$(2.7 \pm 0.5) \times 10^{-4}$
$\eta \to 2\pi^0 2\gamma$	$< 1.2 \times 10^{-3}$
$\eta \to 4\gamma$	$< 2.8 \times 10^{-4}$
invisible	$< 6 \times 10^{-4}$

Table A.2: Charged decay modes of the η meson. $(28.10 \pm 0.34)\,\%$ of the η mesons decay to a final state with at least one charged particle pair.

decay mode	branching ratio
$\eta \to \pi^+\pi^-\pi^0$	$(22.74 \pm 0.28)\,\%$
$\eta \to \pi^+\pi^-\gamma$	$(4.60 \pm 0.16)\,\%$
$\eta \to e^+e^-\gamma$	$(6.9 \pm 0.4) \times 10^{-3}$
$\eta \to \mu^+\mu^-\gamma$	$(3.1 \pm 0.4) \times 10^{-3}$
$\eta \to e^+e^-$	$< 5.6 \times 10^{-6}$
$\eta \to \mu^+\mu^-$	$(5.8 \pm 0.8) \times 10^{-6}$
$\eta \to e^+e^-e^+e^-$	$(2.40 \pm 0.22) \times 10^{-5}$
$\eta \to \pi^+\pi^-e^+e^-(\gamma)$	$(2.68 \pm 0.11) \times 10^{-4}$
$\eta \to e^+e^-\mu^+\mu^-$	$< 1.6 \times 10^{-4}$
$\eta \to \mu^+\mu^-\mu^+\mu^-$	$< 3.6 \times 10^{-4}$
$\eta \to \mu^+\mu^-\pi^+\pi^-$	$< 3.6 \times 10^{-4}$
$\eta \to \pi^+\pi^-2\gamma$	$< 2.0 \times 10^{-3}$
$\eta \to \pi^+\pi^-\pi^0\gamma$	$< 5 \times 10^{-4}$
$\eta \to \pi^0\mu^+\mu^-\gamma$	$< 3 \times 10^{-6}$

Table A.3: Experimental upper limits for the C, P, CP and LF violation decay modes of the η meson.

decay mode		branching ratio
$\eta \to \pi^0\gamma$	C	$< 9 \times 10^{-5}$
$\eta \to \pi^+\pi^+$	P, CP	$< 1.3 \times 10^{-5}$
$\eta \to 2\pi^0$	P, CP	$< 3.5 \times 10^{-4}$
$\eta \to 2\pi^0\gamma$	C	$< 5 \times 10^{-4}$
$\eta \to 3\pi^0\gamma$	C	$< 6 \times 10^{-5}$
$\eta \to 3\gamma$	C	$< 1.6 \times 10^{-5}$
$\eta \to 4\pi^0$	P, CP	$< 6.9 \times 10^{-7}$
$\eta \to \pi^0e^+e^-$	C	$< 4 \times 10^{-5}$
$\eta \to \pi^0\mu^+\mu^-$	C	$< 5 \times 10^{-6}$
$\eta \to \mu^+e^- + \mu^-e^+$	LF	$< 6 \times 10^{-6}$

Appendix B

Confidence Intervals

In this work, the confidence intervals for the upper limit of $\eta \to e^+e^-$ signal events and its branching ratio are calculated based on the confidence intervals determined by G. J. Feldman and R. D. Cousins [100]. Table B.1 lists the 90 % confidence intervals for the mean μ of a Gaussian for different measured means x_0. μ is constrained to be non-negative.

Table B.1: 90 % confidence intervals (determined by G. J. Feldman and R. D. Cousins [100]).

x_0	90 % CL	x_0	90 % CL	x_0	90 % CL
-3.0	0.00, 0.26	-0.9	0.00, 0.88	1.1	0,00, 2.74
-2.9	0.00, 0.27	-0.8	0.00, 0.95	1.2	0.00, 2.84
-2.8	0.00, 0.28	-0.7	0.00, 1.02	1.3	0.02, 2.94
-2.7	0.00, 0.29	-0.6	0.00, 1.10	1.4	0.12, 3.04
-2.6	0.00, 0.30	-0.5	0.00, 1.18	1.5	0.22, 3.14
-2.5	0.00, 0.32	-0.4	0.00, 1.27	1.6	0.31, 3.24
-2.4	0.00, 0.33	-0.3	0.00, 1.36	1.7	0.38, 3.34
-2.3	0.00, 0.34	-0.2	0.00, 1.45	1.8	0.45, 3.44
-2.2	0.00, 0.36	-0.1	0.00, 1.55	1.9	0.51, 3.54
-2.1	0.00, 0.38	0.0	0.00, 1.64	2.0	0.58, 3.64
-2.0	0.00, 0.40	0.1	0.00, 1.74	2.1	0.65, 3.74
-1.9	0.00, 0.43	0.2	0.00, 1.84	2.2	0.72, 3.84
-1.8	0.00, 0.45	0.3	0.00, 1.94	2.3	0.79, 3.94
-1.7	0.00, 0.48	0.4	0.00, 2.04	2.4	0.87, 4.04
-1.6	0.00, 0.52	0.5	0.00, 2.14	2.5	0.95, 4.14
-1.5	0.00, 0.56	0.6	0.00, 2.24	2.6	1.02, 4.24
-1.4	0.00, 0.60	0.7	0.00, 2.34	2.7	1.11, 4.34
-1.3	0.00, 0.64	0.8	0.00, 2.44	2.8	1.19, 4.44
-1.2	0.00, 0.70	0.9	0.00, 2.54	2.9	1.28, 4.54
-1.1	0.00, 0.75	1.0	0.00, 2.64	3.0	1.37, 4.64
-1.0	0.00, 0.81				

Symbols and Acronyms

Latin letters:

b	barn
b	bottom (beauty) quark
c	charm quark, parameter
d	deuteron
d	down quark
e	electron/positron, Euler's number
f	probability distribution
g	vectormeson coupling
i	imaginary unit, index name
j	index name
l	length
m	meter
n	nano
n_c	number of constraints
p	momentum or proton
q	arbitrary quark, four-momentum transfer, charge
s	strange quark
t	top (true) quark
u	up quark, number of unmeasured variables
v	measured value
$\vec{v}$	velocity
w	weight
w/	with
w/o	without
x	coordinate in Cartesian coordinate system, arbitrary observable
$\vec{x}$	position vector
y	coordinate in Cartesian coordinate system, output of a neuron
z	coordinate in Cartesian coordinate system
z_{FTH}	distance of the FTH from the origin along the z-axis
$\mathcal{A}$	decay amplitude
$\vec{B}$	magnetic field
$\mathcal{BR}$	branching ratio
C	C-parity quantum number
E	energy, electric field

E_{dep}	energy deposit
E_{kin}	kinetic energy
F	form factor
F_μ	constraint function
He	helium
I	isospin quantum number
I_3	third component of isospin
J	total spin quantum number
L	particle identification cut value
$\mathcal{L}$	Lagrangian
N	number of degrees of freedom, order of a polynomial function
N_C	number of colors in SM
P	P-parity quantum number, pseudoscalar field/meson, probability
Q	charge, quark-charge matrix
SU(3)	special unitary group of degree 3
T	Tesla
$\mathcal{UL}$	upper limit
V	vectormeson field
X	set of particles, axis title, real part of decay amplitude
$\vec{X}$	position vector
Y	axis title, imaginary part of decay amplitude
Z	axis title

Greek letters:

α	opening angle, fine structure constant
β	opening angle
γ	photon
γ^*	virtual photon
ϵ	correction term
ε	efficiency
η	η meson
η'	η' meson
λ	Lagrangian multiplier
μ	muon, mean value, index name
π	pion
σ	cross section, standard deviation
ϕ	phi meson
χ^2	χ^2 function
ψ	wave function
Δ	difference, total error

Other symbols and notations:

$\Box$	arbitrary symbol
$\vec{\Box}$	vector
$\bar{\Box}$	mean value
$\Box^0$	neutral charged
$\Box^+$	positively charged
$\Box^-$	negatively charged
d$\Box$	differential
$\partial\Box$	partial differential
$\Delta\Box$	difference
$\Box_x$	variable in x-direction
$\Box_y$	variable in y-direction
$\Box_z$	variable in z-direction
$\Box_{\mathrm{min}}$	minimum value
$\Box_{\mathrm{max}}$	maximum value
$\underline{\Box}$	four-vector
Re$\Box$	real part
Im$\Box$	imaginary part
Tr$\Box$	trace

Acronyms:

ANN	Artificial Neural Network
BCT	Beam Current Transformer
CA	Closest Approach
CD	Central Detector
CELSIUS	Cooling with ELectrons and Storing of Ions from the Uppsala Synchrocyclotron
CL	Confidence Level
COSY	Cooler Synchrotron Jülich
DAQ	Data Acquisition System
EMS	Experimental Message Specification
FD	Forward Detector
FF	Form Factor
FIFO	First In First Out
FRA	Forward Range Absorber
FRH	Forward Range Hodoscope
FRI	Forward Range Intermediate
FPC	Forward Proportional Chamber
FPGA	Field Programmable Gate Array
FTH	Forward Trigger Hodoscope
FVH	Forward Veto Hodoscope
FWC	Forward Window Counter
FZ	Forschungszentrum

GEANT	GEometry ANd Tracking
IKP	Institut für Kernphysik
IM	Invariant Mass
JULIC	JUelich Isochronous Cyclotron
LFQM	Light-Front Quark Model
LMD	Lowest Meson Dominance
LVDS	Low Voltage Differential Signaling
MDC	Mini Drift Chamber
MM	Missing Mass
NMSSM	Next-to-Minimal Supersymmetric Standard Model
OPE	Operator Product Expansion
PDG	Particle Data Group
PID	Particle Identification
PSB	Plastic Scintillator Barrel
QCD	Quantum Chromodynamics
QED	Quantum Electrodynamics
QFD	Quantum Flavordynamics
RAID	Redundant Array of Independent Disks
SCS	Superconducting Solenoid
SEC	Scintillator Electromagnetic Calorimeter
SI	Système international d'unités
VMD	Vector Meson Dominance
WASA	Wide Angle Shower Apparatus
WMC	Wasa Monte Carlo

Bibliography

[1] T. Petri. Anomalous decays of pseudoscalar mesons. Master's thesis, University of Bonn, Bonn, Germany, 2010.

[2] J. Bijnens and F. Persson. Effects of different Form-factors in Meson-Photon-Photon Transitions and the Muon Anomalous Magnetic Moment. *arXiv:hep-ph/0106130v1*, 2001.

[3] C. Jarlskog and H. Pilkuhn. Eta decays with e^+e^- and $\mu^+\mu^-$ pairs. *Nucl. Phys. B*, 1(5):264–268, 1967.

[4] T. Miyazaki and E. Takasugi. Internal Conversion of Pseudoscalar Mesons into Lepton Pairs. *Phys. Rev. D*, 8:2051–2062, 1973.

[5] C.-C. Lih. Study of π^0 and η decays containing dilepton. *J. Phys. G*, 38(6):065001, 2011.

[6] C. Terschluesen. Electromagnetic transition form factors of light vector mesons. Master's thesis, Justus-Liebig-Universität Gießen, Gießen, Germany, 2010.

[7] C. Terschluesen. Private communication, 2012.

[8] R. R. Akhmetshin et al. Study of conversion decays $\phi \to \eta e^+e^-$, $\eta \to e^+e^-\gamma$ and $\eta \to \pi^+\pi^-e^+e^-$ at CMD-2. *Phys. Lett. B*, 501:191–199, 2001.

[9] F. Ambrosino et al. Observation of the rare $\eta \to e^+e^-e^+e^-$ decay with the KLOE experiment. *arXiv:1105.6067v3 [hep-ex]*, 2011.

[10] L. S. Yurev. *Study of the decay $\eta \to e^+e^-e^+e^-$ with WASA-at-COSY*. PhD thesis, Universität Köln, Germany, 2011.

[11] J. Beringer et al. 2012 Review of Particle Physics. *Phys. Rev. D*, 86(7A):010001, 2012.

[12] C. Amsler. *Kern- und Teilchenphysik*. Vdf Hochschulverlag AG, 2007. ISBN: 978-3-8252-2885-9.

[13] A. Pevsner et al. Evidence for a Three-Pion Resonance Near 550 MeV. *Phys. Rev. Lett.*, 7(11):421–423, 1961.

[14] A. Bramon, R. Escribano, and M. D. Scadron. The $\eta - \eta'$ Mixing Angle Revisited. *Eur. Phys. J. C*, 7:271, 1999.

[15] J. Wess and B. Zumino. Consequences of anomalous ward identities. *Phys. Lett. B*, 37(1):95–97, 1971.

[16] E. Witten. Current algebra, baryons, and quark confinement. *Nucl. Phys. B*, 223(2):433–444, 1983.

[17] M. Benayoun et al. A Global Treatment Of VMD Physics Up To The ϕ: I. e^+e^- Annihilations, Anomalies And Vector Meson Partial Widths. *Eur. Phys. J. C*, 65:211–245, 2010.

[18] M. Benayoun et al. Upgraded breaking of the HLS model: a full solution to the τ – e^+e^- and ϕ decay issues and its consequences on $g-2$ VMD estimates. *Eur. Phys. J. C*, 72:1848, 2012.

[19] M. Benayoun et al. The dipion mass spectrum in e^+e^- annihilation and τ decay: a dynamical (ρ, ω, ϕ) mixing approach. *Eur. Phys. J. C*, 55:199–236, 2008.

[20] H. Berghäuser et al. Determination of the η-transition form factor in the $\gamma p \to p\eta \to p\gamma e^+e^-$ reaction. *Phys. Lett. B*, 701:562–567, 2011.

[21] M. F. M. Lutz and S. Leupold. On the radiative decays of light vector and axial-vector mesons. *Nucl. Phys. A*, 813:96, 2008.

[22] M. Berłowski et al. Measurement of η meson decays into lepton-antilepton pairs. *Phys. Rev. D*, 77:032004, 2008.

[23] L. G. Landsberg. Electromagnetic Decays of Light Mesons. *Phys. Rept.*, 128:301–376, 1985.

[24] T. E. Browder et al. New upper limit on the decay $\eta \to e^+e^-$. *Phys. Rev. D*, 56(9):5359–5365, 1997.

[25] A. E. Dorokhov and M. A. Ivanov. Rare decay $\pi^0 \to e^+e^-$ theory confronts KTeV data. *arXiv:0704.3498v2 [hep-ph]*, 2007.

[26] L. Bergström. Rare Decay of a Pseudoscalar Meson Into a Lepton Pair - A Way to Detect New Interactions? *Z. Phys. C*, 14:129–134, 1982.

[27] P. Fayet. Constraints on light dark matter and U bosons, from ψ, Υ, K^+, η and η' decays. *Phys. Rev. D*, 74:054034, 2006.

[28] Y. Kahn, M. Schmitt, and T. M. P. Tait. Enhanced rare pion decays from a model of MeV dark matter. *Phys. Rev. D*, 78:115002, 2008.

[29] Q. Chang and Y.-D. Yang. Rare decay $\pi^0 \to e^+e^-$ as a sensitive probe of light CP-odd Higgs in NMSSM. *arXiv:0808.2933v2 [hep-ph]*, 2008.

[30] E. Abouzaid et al. Measurement of the rare decay $\pi^0 \to e^+e^-$. *Phys. Rev. D*, 75:012004, 2007.

[31] G. B. Tupper and M. A. Samuel. π^0 and η decays into lepton pairs. *Phys. Rev. D*, 26:3302–3304, 1982.

[32] G. B. Tupper and M. A. Samuel. Reply to "Note on the $\gamma\gamma$ contribution to $\pi^0 \to e^+e^-$ and $\eta \to \mu^+\mu^-$". *Phys. Rev. D*, 29:1031–1031, 1984.

[33] M. J. Savage, M. Luke, and M. B. Wise. The Rare Decays $\pi^0 \to e^+e^-$, $\eta \to e^+e^-$ and $\eta \to \mu^+\mu^-$ in Chiral Perturbation Theory. *arXiv:hep-ph/9207233v1*, 1992.

[34] B. Margolis et al. Quark model calculation of $\eta \to l^+l^-$ to all orders in the bound-state relative momentum. *Phys. Rev. D*, 47:1942–1950, 1993.

[35] D. G. Dumm and A. Pich. Long-distance contributions to the $K_L \to \mu^+\mu^-$ decay width. *arXiv:hep-ph/9801298v2*, 1998.

[36] J. Gronberg et al. Measurements of the Meson-Photon Transition Form Factors of Light Pseudoscalar Mesons at Large Momentum Transfer. *Phys. Rev. D*, 57:33, 1998.

[37] A. E. Dorokhov, M. A. Ivanov, and S. G. Kovalenko. Complete structure dependent analysis of the decay $P \to l^+l^-$. *arXiv:0903.4249v1 [hep-ph]*, 2009.

[38] M. Knecht et al. Decay of pseudoscalars into lepton pairs and large-N_C QCD. *arXiv:hep-ph/9908283v1*, 1999.

[39] J. Davies, J. Guy, and R. Zia. Experimental limits to the $\pi^0 \to e^+e^-$ rate and their consequences for a direct electron-hadron coupling. *Nuovo Cimento A*, 24:324–332, 1974.

[40] D. B. White et al. Search for the decays $\eta \to \mu e$ and $\eta \to e^+e^-$. *Phys. Rev. D*, 53:6658–6661, 1996.

[41] G. Agakishiev et al. Inclusive dielectron spectra in $p + p$ collisions at 3.5 GeV kinetic beam energy. *Eur. J. Phys. A*, 48:64, 2012.

[42] R. Maier et al. Cooler synchrotron COSY. *Nucl. Phys. A*, 626:395c–403c, 1997.

[43] R. Maier. Cooler synchrotron COSY: Performance and perspectives. *Nucl. Instr. Meth. Phys. Res. A*, 390:1–8, 1997.

[44] WASA-at-COSY collaboration. Common material, `http://wasasrv.ikp.kfa-juelich.de/WasaWiki`.

[45] B. Lorentz et al. Status and future plans of polarized beams at COSY. *J. Phys. Conf. Ser.*, 295(1):012146, 2011.

[46] C. F. Redmer. *In search of the Box-Anomaly with the WASA facility at COSY*. PhD thesis, Bergische Universität Wuppertal, Wuppertal, Germany, 2010.

[47] Insitut für Kernphysik. `http://www.fz-juelich.de/ikp/DE/Home/home_node.html`. Retrieved 2012-02-13.

[48] H.-H. Adam et al. Proposal for the Wide Angle Shower Apparatus (WASA) at COSY-Juelich - "WASA at COSY". *arXiv:nucl-ex/0411038v1*, 2004.

[49] C. Bargholtz et al. The WASA detector facility at CELSIUS. *Nucl. Instr. Meth. Phys. Res. A*, 594(3):339–350, 2008.

[50] B. Trostell. Vacuum injection of hydrogen micro-sphere beams. *Nucl. Instr. Meth. Phys. Res. A*, 1995.

[51] A. Winnemöller. *Analyse des verbotenen η-Meson Zerfalls $\eta \to \pi^0 e^+ e^-$ am Experimentaufbau WASA-at-COSY*. PhD thesis, Westfälische Wilhelms Universität Münster, Münster, Germany, 2011.

[52] A. Pricking. *Double pionic fusion to* ^{4}He - *Kinematically complete measurements over the energy region of the ABC effect*. PhD thesis, Universität Tübingen, Tübingen, Germany, 2011.

[53] C. Pauly. *Light meson production in pp reactions at CELSIUS/WASA above the η threshold*. PhD thesis, Universität Hamburg, Hamburg, Germany, 2006.

[54] M. Zieliński. Feasibility study of the $\eta' \to \pi^+\pi^-\pi^0$ decay using WASA-at-COSY apparatus. Master's thesis, Jagiellonian University, Cracow, Poland, 2008.

[55] W. Demtröder. *Experimentalphysik 4: Kern-, Teilchen- und Astrophysik*, volume 2. Springer-Verlag Berlin Heidelberg New York, 2005. ISBN 3-540-21451-8.

[56] M. Jacewicz. *Measurement of the reaction $pp \to pp\pi^+\pi^-\pi^0$ with CELSIUS/WASA at* 1.36 GeV. PhD thesis, Uppsala Universitet, Uppsala, Sweden, 2004.

[57] P. Podkopał. Performance of the New Plastic Scintillator Barrel Detector for WASA-at-COSY. *Berichte des Forschungszentrums Jülich Jül-4282*, 2009. ISSN 0944-2952.

[58] R. J. M. Y. Ruber. *An Ultra-thin-walled Superconducting Solenoid for Meson-decay Physics*. PhD thesis, Uppsala University, Uppsala, Sweden, 1999.

[59] I. Koch. *Measurements of* $2\pi^0$ *and* $3\pi^0$ *production in proton-proton collisions at a center of mass energy of* 2.465 GeV. PhD thesis, Uppsala Universitet, Uppsala, Sweden, 2004.

[60] R. J. M. Y. Ruber. Radiation hardness test of CsI crystals for WASA. *WASA Report 2/90*, 1990.

[61] U. Schuberth. *The reaction $pp \to pp\eta$ close to threshold*. PhD thesis, Uppsala University, Uppsala, Sweden, 1995.

[62] J. Hampe. Measurements of the Response Characteristics of CsI(Na) Crystals. Master's thesis, RWTH Aachen University, Aachen, Germany, 2010.

[63] J. Zabierowski and J. Rachowski. The Light-Pulser Monitoring System for the WASA detector facility. *Nucl. Instr. Meth. Phys. Res. A*, 606(3):411–418, 2009.

[64] I. N. Bronstein, K. A. Semendjajew, G. Musiol, and H. Mühlig. *Taschenbuch der Mathematik*. Verlag Harri Deutsch, Frankfurt am Main, 6. edition, 2005. ISBN: 978-3-8171-2006-2.

[65] H. Kleines et al. The New DAQ System for WASA at COSY. *IEEE Trans. Nucl. Sci.*, 53, 2006.

[66] H. Kleines et al. Performance Issues of the New DAQ System for WASA at COSY. *IEEE Trans. Nucl. Sci.*, 55(1):261–264, 2008.

[67] M. Wolke. First Experiments with the WASA Detector. *Berichte des Forschungszentrums Jülich Jül-4262*, 2008. ISSN 0944-2952.

[68] I. Froehlich et al. Pluto: A Monte Carlo Simulation Tool for Hadronic Physics. *arXiv:0708.2382v2 [nucl-ex]*, 2007.

[69] R. Brun and F. Rademakers. ROOT - An Object Oriented Data Analysis Framework. *Proceedings AIHENP'96 Workshop, Lausanne, Sep. 1996, Nucl. Instr. Meth. Phys. Res. A*, 389:81–86, 1997.

[70] F. James. W515: N-Body Monte-Carlo Event Generator. Technical report, `http://wwwasdoc.web.cern.ch/wwwasdoc/shortwrupsdir/w515/top.html`, 1975. Retrieved 2012-08-22.

[71] Application Software Group Computing and Networks Division. GEANT - Detector Description and Simulation Tool. Technical report, `http://wwwasd.web.cern.ch/wwwasd/geant/`, CERN, Geneva, Switzerland, 1993. Retrieved 2012-08-22.

[72] K. Zwoll et al. Flexible Data Acquisition System for Experiments at COSY. *IEEE Trans. Nucl. Sci.*, 41:37–44, 1994.

[73] V. Hejny, M. Hartmann, and A. Mussgiller. RootSorter: A New Analysis Framework for ANKE. *Berichte des Forschungszentrums Jülich Jül-4052*, 2003. ISSN 0944-2952.

[74] M. Bashkanov. Internal Note. Universität Tübingen, Tübingen, Germany, 2009.

[75] M. Komogorov et al. Track recognition algorithm for WASA Mini Drift Chamber (MDC). Technical report, WASA Collaboration Internal Report, 1997.

[76] R. E. Kalman. A New Approach to Linear Filtering and Prediction Problems. *Trans. Am. Soc. Mech. Eng. – J. Basic. Eng. D*, 82:35–45, 1960.

[77] T. C. Awes et al. A simple method of shower localization and identification in laterally segmented calorimeters. *Nucl. Instr. Meth. Phys. Res. A*, 311:130–138, 1992.

[78] P. Vlasov. *Analysis of the $\eta \to 3\pi^0$ decay in the pp interaction.* PhD thesis, Ruhr-Universität Bochum, Bochum, Germany, 2008.

[79] R. Bilger et al. Measurement of the $p\,d \to {}^3\mathrm{He}\,\eta$ cross section between 930 and 1100 MeV. *Phys. Rev. C*, 65:044608, 2002.

[80] J. Banaigs et al. A study of the reactions $dp \to \tau\pi^0$ and $dp \to \tau\eta^0$. *Phys. Lett. B*, 45(4):394–398, 1973.

[81] M. Bashkanov et al. Exclusive Measurements of $pd \to {}^3\mathrm{He}\pi\pi$: the ABC Effect Revisited. *arXiv:nucl-ex/0508011v3*, 2005.

[82] K. Schoenning et al. Production of η and 3π mesons in the $pd \to {}^3\mathrm{He}X$ reaction at 1360 and 1450 MeV. *arXiv:1001.4604v2 [nucl-ex]*, 2010.

[83] E. Claiavassa et al. Measurement of the $pp \to pp\eta$ total cross section between 1.265 and 1.50 GeV. *Phys. Lett. B*, 322:270–274, 1994.

[84] C. Zheng. Matching Trigger Efficiency of Forward Detector of WASA-at-COSY. *Berichte des Forschungszentrums Jülich Jül-4282*, 2009. ISSN 0944-2952.

[85] J Złomańczuk. Internal Note: Selection of ^{3}He Events in *pd* Runs at 1 GeV. WASA-at-COSY Collaboration Internal Note, 2009.

[86] C. Amsler et al. η-decays into three pions. *Phys. Lett. B*, 346:203–207, 1995.

[87] W. Ertel. *Grundkurs Künstliche Intelligenz*. Fried. Vieweg & Sohn Verlag , GWV Fachverlage GmbH, Wiesbaden, first edition, 2008. ISBN 978-3-528-05924-8.

[88] W. S. McCulloch and W. H. Pitts. A logical calculus of the ideas immanent in nervous activity. *Bulletin of Mathematical Biophysics*, 5:115–133, 1943.

[89] The ROOT Team. *ROOT, An Object-Oriented Data Analysis Framework, Users Guide 5.21*, 2008.

[90] ROOT | A Data Analysis Framework CERN. Description of the TMultiLayerPerceptron class. `http://root.cern.ch/root/html/TMultiLayerPerceptron.html`. Retrieved 2012-08-23.

[91] F. Ambrosino et al. Measurement of the branching ratio and search for a CP violating asymmetry in the $\eta \to \pi^+\pi^- e^+ e^- (\gamma)$ decay at KLOE. *Phys. Lett. B*, 675:283, 2009.

[92] W. A. van den Bosch. Possibility to Measure $\eta \to e^+e^-e^+e^-$ using WASA. Technical report, Dep. of Radioation Sciences, Uppsala University, Sweeden, 1996.

[93] ROOT | A Data Analysis Framework - CERN. `http://root.cern.ch/root/html/TH1.html`. Retrieved 2012-07-24.

[94] K. Nakamura et al. Review of Particle Physics. *J. Phys. G.*, 37:075021, 2010.

[95] M. Hodana. *Study of the $\eta \to e^+e^-\gamma$ decay using WASA-at-COSY detector system.* PhD thesis, Jagiellonian University, Cracow, Poland, 2012.

[96] G. Cowan. Error analysis for effciency. Technical report, RHUL Physics, 2008. `http://www.pp.rhul.ac.uk/~cowan/stat/notes/efferr.pdf`. Retrieved 2012-09-03.

[97] R. Barlow. Systematic Errors: facts and fictions. *arXiv:hep-ex/0207026v1*, 2002.

[98] D. Coderre. *The branching ratio and CP-violating asymmetry of $\eta \to \pi^+\pi^- e^+ e^-$*. PhD thesis, Ruhr-Universität Bochum, Bochum, Germany, 2012.

[99] F. James. MINUIT Tutorial Function Minimization. *Reprinted from the Proceedings of the 1972 CERN Computing and Data Processing School, Pertisau, Austria, 10-24 September, 1972 (CERN 72-21)*, 2004.

[100] G. J. Feldman and R. D. Cousins. Unified approach to the classical statistical analysis of small signals. *Phys. Rev. D*, 57(7):3873–3889, 1998.

[101] A. Kupść. WASA Note on Kinematical Fit. Technical report, WASA-at-COSY Collaboration Internal Note, 1995.

[102] V. Hejny. Effects of Magnetic Field in FD. WASA-at-COSY Collaboration Internal Wiki, 2009.

Danksagung

In diesem Abschnitt möchte ich mich bei all denen bedanken, die mich in den letzten drei Jahren als Doktorand begleitet und zum Gelingen dieser Arbeit beigetragen haben.

Zunächst gilt mein Dank Prof. Dr. Hans Ströher, der es mir ermöglicht hat, meine Doktorarbeit am Institut für Kernphysik des Forschungszentrums Jülich zu schreiben.

Ich bedanke mich ganz herzlich bei Dr. Markus Büscher, der mich während dieser Zeit betreut hat und mir mit seinem großem Fachwissen immer wieder geholfen hat kleine und größere Probleme zu lösen. Vielen Dank für deine große Geduld.

Ebenso gilt mein Dank Prof. Dr. Jan Jolie, der als Zweitgutachter dieser Arbeit zur Verfügung stand. Vielen Dank auch an Prof. Dr. Alexander Altland und Prof. Dr. Detlev Gotta, die als Vorsitzender der Prüfungskommission beziehungsweise als Beisitzer zur Verfügung standen.

Ich danke den Mitgliedern der WASA-at-COSY Kollaboration für die zahlreichen Diskussionen und Ideen, die diese Arbeit vorangetrieben haben. Besonders erwähnt seien hier Dr. Volker Hejny, Dr. Andrzej Kupsc, Dr. Susan Schadmand, Dr. Andreas Wirzba, Dr. Frank Goldenbaum, Dr. Magnus Wolke, Dr. Christoph Florian Redmer, Dr. Pavel Fedorets, Dr. Pawel Podkopal, Dr. Daniel Coderre, Dr. Leonid Yurev, Dr. Malgorzata Hodana, M.Sc. Farha Anjum Kahn und Dipl.-Phys. Daniel Lersch.

Ebenso möchte ich meinen Kollegen vom IKP danken, die jederzeit offen für Fragen aller Art waren. Stets konnte ich mit euch über Probleme in immer angenehmer Atmosphäre diskutieren. Besonders erwähnen möchte ich hier Dipl.-Phys. Ilhan Engin (vielen Dank auch für das Korrekturlesen dieser Arbeit), Dr. Michael Hartmann, Dr. Henner Ohm und Dipl.-Phys. Astrid Holler.

Schließlich möchte ich meiner Familie und besonders meinen Eltern Joachim und Christiane Wurm danken. Vielen Dank für eure Unterstützung!

Erklärung

Ich versichere, dass ich die von mir vorgelegte Dissertation selbständig angefertigt, die benutzten Quellen und Hilfsmittel vollständig angegeben und die Stellen der Arbeit – einschließlich Tabellen, Karten und Abbildungen –, die anderen Werken im Wortlaut oder dem Sinn nach entnommen sind, in jedem Einzelfall als Entlehnung kenntlich gemacht habe; dass diese Dissertation noch keiner anderen Fakultät oder Universität zur Prüfung vorgelegen hat; dass sie – abgesehen von unten angegebenen Teilpublikationen – noch nicht veröffentlicht worden ist sowie, dass ich eine solche Veröffentlichung vor Abschluss des Promotionsverfahrens nicht vornehmen werde. Die Bestimmungen der Promotionsordnung sind mir bekannt. Die von mir vorgelegte Dissertation ist von Priv.-Doz. Dr. rer. nat. Markus Büscher betreut worden.

Veröffentlichungen

- P. Wurm. Search for the $\eta \to e^+e^-e^+e^-$ double Dalitz decay. *J. Phys. Conf. Ser.*, 312:102016, 2011.
- P. Wurm. Analysis of the $\eta \to e^+e^-e^+e^-$ double Dalitz decay. *Berichte des Forschungszentrums Jülich Jül-4336*, 2011. ISSN 0944-2952
- P. Adlarson, et al. Proceedings of the second International PrimeNet Workshop. *arXiv:1204.5509v1 [nucl-ex]*, 2012
- P. Wurm. Measurement of the double Dalitz decay $\eta \to e^+e^-e^+e^-$ with WASA-at-COSY. *Berichte des Forschungszentrums Jülich Jül-4349*, 2012. ISSN 0944-2952

Weitere Veröffentlichungen

- P. Adlarson, et al. (WASA-at-COSY collaboration). Abashian-Booth-Crowe Effect in Basic Double-Pionic Fusion: A New Resonance?. *Phys. Rev. Lett.*, 106:242302, 2011.
- P. Adlarson, et al. (WASA-at-COSY collaboration). $\pi^0\pi^0$ Production in Proton-Proton Collisions at $T_p = 1.4\,\mathrm{GeV}$. *Phys. Lett. B*, 706:256–262, 2012.
- P. Adlarson, et al. (WASA-at-COSY collaboration). Exclusive measurement of the decay $\eta \to \pi^+\pi^-\gamma$. *Phys. Lett. B*, 707:243–249, 2012.
- P. Adlarson, et al. (WASA-at-COSY collaboration). Abashian-Booth-Crowe resonance structure in the double pionic fusion to ^{4}He. *Phys. Rev. C*, 86:032201, 2012.
- P. Adlarson, et al. (WASA-at-COSY collaboration). Isospin Decomposition of the Basic Double-Pionic Fusion in the Region of the ABC Effect. *arXiv:1212.2881 [nucl-ex]*, 2012.
- P. Adlarson, et al. (WASA-at-COSY collaboration). Search for the η-mesic ^{4}He with WASA-at-COSY detector. *arXiv:1301.0843 [nucl-ex]*, 2013.

Konferenzbeiträge

- Analysis of the $\eta \to e^+e^-e^+e^-$ double Dalitz decay. *International Nuclear Physics Conference 2010.* 4.–9. Juli 2010, Vancouver, Kanada. 2010. (Poster)
- Analysis of the $\eta \to e^+e^-e^+e^-$ double Dalitz decay. *Canadian Institute of Nuclear Physics Workshop on Fundamental Symmetries.* 9.–10. Juli 2010, Vancouver, Kanada. 2010. (Poster)
- Analysis of the $\eta \to e^+e^-e^+e^-$ double Dalitz decay. *DPG Frühjahrstagung 2011.* 21.–25. März 2011, Münster, Deutschland. 2011. (Vortrag)
- Analysis of the $\eta \to e^+e^-e^+e^-$ double Dalitz decay. *Les-Nabis School on Amplitude Analysis 2011.* 1.–5. August 2011, Bad Honnef, Germany. (Poster)
- Analysis of the $\eta \to e^+e^-e^+e^-$ double Dalitz decay. *PrimeNet Workshop 2011.* 26.–28. September 2011, Jülich, Germany. 2011. (Poster)
- Hadron physics with WASA-at-COSY. *DPG Frühjahrstagung 2012.* 19.–23. März 2012, Mainz, Deutschland. 2012. (Gruppenvortrag)